Mathematical and numerical modeling of bilipid membrane electroporation : A phase ordering kinetics approach

Pedro Jaramillo

THÈSE PRÉSENTÉE

POUR OBTENIR LE GRADE DE

DOCTEUR
DE L'UNIVERSITÉ DE BORDEAUX

ECOLE DOCTORALE DE MATHÉMATIQUES ET

D'INFORMATIQUE

SPÉCIALITÉ : MATHÉMATIQUES APPLIQUÉES

Par **Pedro JARAMILLO**

Modélisation mathématique de l'électroporation des membranes bilipidiques : une approche par champ de phase

Sous la direction de :
Co-directrice: **Annabelle COLLIN**
Co-directeur: **Clair POIGNARD**

Soutenue le 8 décembre 2023

Membres du jury :

M. Hatem ZAAG	Directeur de Recherche	CNRS	Rapporteur
M. Matthieu ALFARO	Professeur des Universités	Université de Rouen	Rapporteur
Mme. Florence HUBERT	Professeure des Universités	Université d'Aix-Marseille	Examinatrice
Mme. Magali RIBOT	Professeure des Universités	Université d'Orléans	Présidente
M. Lluis M. MIR	Directeur de Recherche	CNRS	Examinateur
Mme. Annabelle COLLIN	Maîtresse de conférences	Bordeaux INP	Directrice de thèse
M. Clair POIGNARD	Directeur de Recherche	Inria	Directeur de thèse

Abstract

This thesis deals with the modeling of electroporation of a bilipid membrane. Electroporation uses strong, short electrical pulses to create pores in cell membranes. Reversible electroporation allows non-permeable molecules to enter cells without killing them, while irreversible electroporation results in cell death in the target area. Because of the size of the cells (diameter of 20 [μm]) and the duration of the pulse (10 [ns] to 100 [μs]), a precise study of this phenomenon experimentally is practically impossible, therefore a model based approach is necessary. Many models have been proposed, but none of them could satisfactorily explain the many features of the experimentally observed phenomenon.

The aim of this thesis is to present a new phase field model of electroporation. This physically based model consists of the Allen-Cahn equation for the membrane water content and a nonlocal differential equation for the transmembrane voltage.

We first mathematically study our model. A fine analysis of the involved nonlocal Dirichlet-to-Neumann operators in two simple configurations (a spherical membrane and a flat periodic membrane) allows us to compare the time constants of the phenomenon between spherical and flat membranes. In addition, we perform a linear stability analysis of our model which relates pore creation in the membrane to concavity condition in our model. the effects of the equations coupling of our model. To estimate the parameters of the model, we also compare the energy functional of our model with the energy functionals of other physical models that currently represent the state of the art.

Second, we design a numerical scheme of order 2 in time. It is based on a Fast Fourier Transform and a well-designed Strang Splitting scheme. This method, which is very powerful in terms of computational time, is used to perform a sensitivity analysis of the parameters of the model.

Finally, we compare our model with the most popular model of electroporation in a realistic scenario and with experimental data in the case of nanosecond pulses applied to a cell suspension.

Keywords: Mathematical modeling; Electroporation; Fractional step numerical scheme; Elliptic problem; Linear stability analysis; Phase ordering kinetics.

Résumé

Cette thèse est dédiée à la modélisation de l'électroporation d'une membrane bilipidique. L'électroporation consiste à créer des pores dans les membranes cellulaires à l'aide d'impulsions électriques intenses et brèves. L'électroporation réversible permet l'entrée de molécules non perméables dans le cytoplasme des cellules sans les tuer, tandis que l'électroporation irréversible entraîne la mort cellulaire dans la zone ciblée. En raison de la taille des cellules (diamètre de 20 [μm]) et de la durée de l'impulsion (10 [ns] à 100 [μs]), une étude expérimentale précise de ce phénomène est pratiquement impossible, ce qui justifie l'introduction de modèles mathématiques. Bien que de nombreux modèles aient été proposés, aucun n'a réussi à expliquer de manière complète les multiples caractéristiques observées expérimentalement. L'objectif de cette thèse est de présenter un nouveau modèle de champ de phase pour l'électroporation. Ce modèle physique comprend l'équation d'Allen-Cahn pour la teneur en eau de la membrane et une équation aux dérivées partielles non locale pour le potentiel transmembranaire. Dans un premier temps, nous procédons à une analyse mathématique approfondie de notre modèle. Cela inclut une étude détaillée des opérateurs Dirichlet-to-Neumann non locaux impliqués dans deux configurations simples (une membrane sphérique et une membrane périodique plate), permettant ainsi une comparaison des constantes des temps entre les deux. De plus, nous effectuons une analyse de stabilité linéaire de notre modèle, mettant en évidence les effets du couplage des équations du modèle. Pour estimer les paramètres du modèle, nous comparons également la fonctionnelle d'énergie de notre modèle avec celles d'autres modèles physiques correspondant actuellement l'état de l'art. Dans un deuxième temps, nous concevons un schéma numérique d'ordre 2 en temps. Ce schéma repose sur une transformée de Fourier rapide et une méthode de splitting de Strang. Cette méthode est très puissante en termes de temps de calcul et nous permet de réaliser une analyse de sensibilité des paramètres du modèle. Enfin, nous confrontons notre modèle au modèle d'électroporation le plus populaire dans un scénario réaliste ainsi qu'à des données expérimentales concernant des impulsions de l'ordre de la nanoseconde appliquées à une cellule en suspension.

Mots clés : Modélisation mathématique ; Électroporation ; Champs de phase.

Contents

Acknowledgements

Thank you, Annabelle Collin and Clair Poignard for all the support and guidance you gave me during these past few years. I will always fondly remember our discussions in front of the chalk board. They were not only mathematically stimulating but a source of motivation which made me remember why I love mathematics.

This work was quite challenging for me and it would not have been possible without the support of my co-workers: Virginie, the best office partner one could ask for; Sergio, 'mbare for life; Cédrick, who always took the time to answer all my pesky questions, and the best boardgame player one could ask for (specially in co-op games); Simone, ciccio, I enjoyed talking maths with you while using the whiteboard; Béatrice, the coffe break we took during the Fortran courses would always lift my spirit; Alexis, who was effortlessly the best dressed Phd student I knew; Eloïse, the safest choice when looking to enjoy a meal with an interesting conversation; Julien, who sends the best memes and makes the best jokes; and the rest of the MONC team (Kylian, Khaoula, Simon, Giorgia, Florian, Linh, Guillaume).

From my personal life, I would like to thank Sébastien, a friend for life who was particularly helpful during the hard times and someone who calls you just to check how you are doing.

Thank you Daniela, the love of my life. You make the tough times tolerable and the good times amazing. I always appreciate you hearing me talk about any little victory I managed to get. Also, thank you for being a constant source of motivation to better myself.

Finally, I thank my parents Jacqueline Aguayo and Efrén Jaramillo. Your support was invaluable, and I am so lucky to have you as my parents. Were it not for you mom, I would have never come to France. Were it not for you dad, I would have never chosen to study Mathematics.

Résumé long (en français)

L'électroporation consiste à soumettre les cellules à des champs électriques pulsés de forte intensité et de courte durée dans le but de créer des pores dans leur membrane. Ces pores permettent d'introduire des molécules non perméables dans les cellules vivantes sans les tuer (électroporation réversible), ou de provoquer la mort des cellules dans la zone visée (électroporation irréversible).

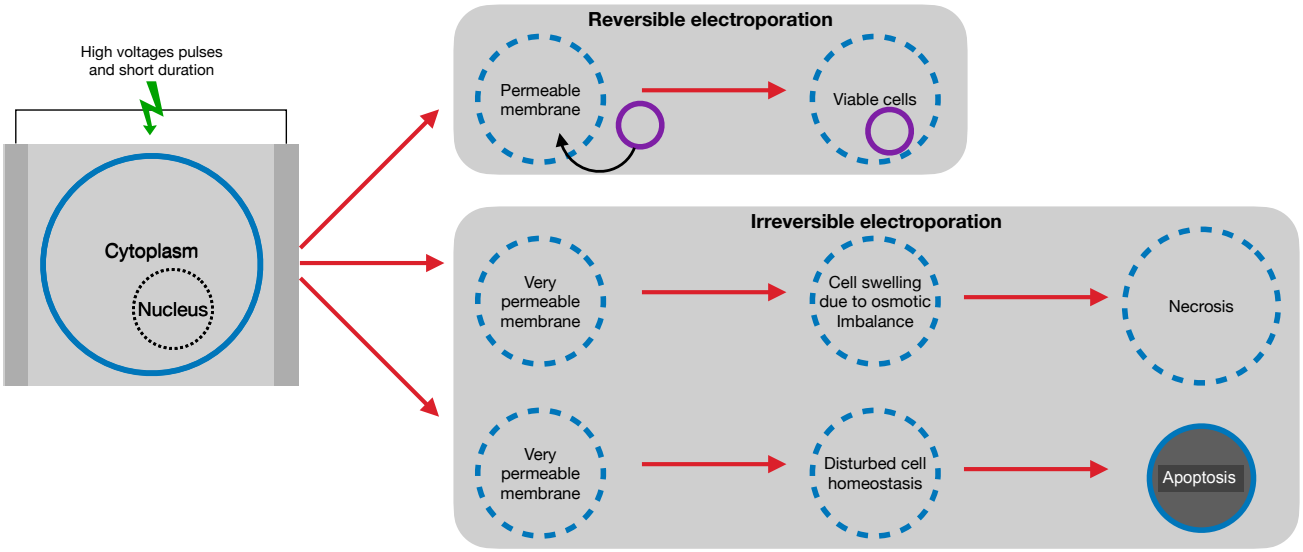

Figure 1: Schéma représentant l'électroporation d'une cellule, montrant à la fois les aspects réversibles et irréversibles.

Cette thèse se concentre sur le développement d'outils mathématiques novateurs pour la modélisation de l'électroporation à l'échelle cellulaire. Le modèle d'électroporation que nous proposons combine un modèle quasistatique du potentiel électrique autour de la membrane cellulaire avec un modèle de champ de phase basé sur une version modifiée de l'équation d'Allen-Cahn, qui décrit l'état de la membrane. Nous justifions physiquement ce modèle du point de vue de la modélisation et démontrons son comportement en le simulant dans un scénario approprié.

Contributions

Objectifs de la thèse

La première contribution est le développement d'un nouveau modèle mathématique basé sur la physique pour l'électroporation à l'échelle cellulaire.

Actuellement, il existe plusieurs modèles d'électroporation cellulaire, généralement répartis en deux catégories : les modèles phénoménologiques et les modèles basés sur la physique. Les modèles phénoménologiques reposent principalement sur des intuitions et contiennent des paramètres ajustés par des expériences, ce qui les rend descriptifs plutôt que prédictifs. En revanche, les modèles basés sur la physique sont mieux justifiés, mais ils doivent faire face à la complexité accrue de la modélisation ce qui amène parfois à simplifier excessivement le phénomène et ainsi à perdre certains aspects clés observés dans les expériences. Jusqu'à présent, aucun modèle n'a été entièrement satisfaisant, et un consensus définitif au sein de la communauté concernant le modèle d'électroporation cellulaire adéquat n'a pas été atteint.

Dans cette thèse, nous présentons un modèle mathématique d'électroporation cellulaire, où tous les paramètres ont une interprétation physique.

Le modèle mathématique que nous proposons est donné par un système d'équations aux dérivées partielles (EDP). Il prend la forme d'une équation semilinéaire de réaction-diffusion d'ordre 2 agissant sur ϕ qui modélise l'état de la membrane couplée à une EDP non locale ayant pour inconnue la différence de potentiel à travers la membrane notée v. Il s'écrit :

$$\begin{cases} \partial_t \phi - D\Delta_\Gamma \phi = -\alpha \mathcal{W}'(\phi) + \frac{\alpha}{2} C_m'(\phi) v^2, \ \forall x \in \Gamma, \ t > 0, \\ \phi(0, \cdot) = 0, \end{cases} \tag{1a}$$

$$\begin{cases} C_m(\phi)\partial_t v + (S_m(\phi) + \Lambda)v = g, \ \forall x \in \Gamma, \ t > 0 \\ v(0, \cdot) = 0, \end{cases} \tag{1b}$$

où D correspond à la diffusion latérale des lipides dans la membrane, $\mathcal{W}$ le potentiel double puits de l'énergie libre associée à la membrane (voir Figure 3), Λ l'opérateur pseudodifferentiel nonlocal composé de deux opérateurs Dirichlet-to-Neumann, S_m la conductance électrique de la membrane, C_m la capacitance électrique de la membrane et g est un terme source qui représente l'application du champ électrique.

Les deux équations sont définies sur une surface compacte et lisse $\Gamma \subset \mathbb{R}^3$ qui représentent la membrane (voir Figure 2).

La deuxième contribution consiste à l'étude mathématique des propriétés qualitatives du modèle

Le système couplé est une EDP quasi-linéaire en la variable (ϕ, v). Nous procédons à une analyse mathématique approfondie de notre modèle. En effet nous montrons que ce modèle possède de bonnes propriétés qualitatives pour notre problème et nous comparons son comportement dans deux cas importants: $\Gamma = \mathbb{S}^2$ and $\Gamma = \mathbb{T}^2 = (\mathbb{R}/\mathbb{Z})^2$ (une membrane

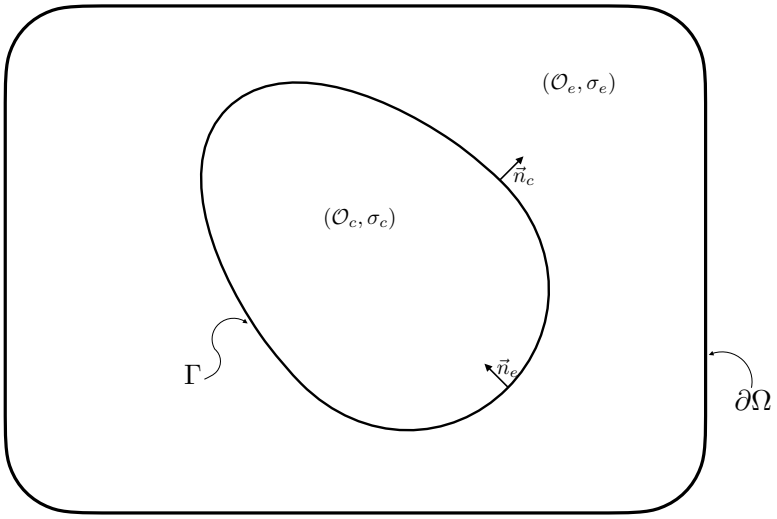

Figure 2: Représentation d'une cellule du point de vue de notre modèle. Le domaine intracellulaire est représenté par $\mathcal{O}_c$, la membrane est représentée par Γ, et le domaine extracellulaire par $\mathcal{O}_e$. L'union des trois ensembles correspond au domaine Ω.

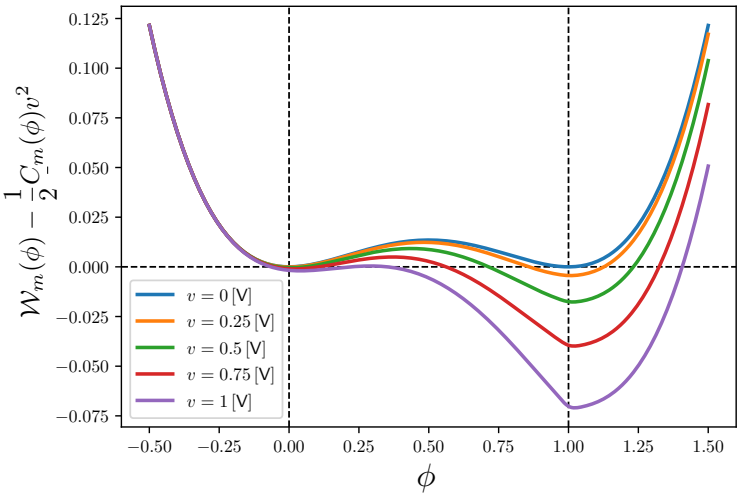

Figure 3: Potentiel énergétique associé à la membrane cellulaire sous l'influence d'un voltage transmembranaire (TMV) v, $\mathcal{W}_m(\phi) - C_m(\phi)v^2/2$. Les deux états stables sont donnés par $\phi = 0$ pour une membrane parfaite et $\phi = 1$ pour un défaut dans la membrane (pore contenant de l'eau). Le champ électrique favorise l'entrée d'eau dans la membrane en faisant de la phase $\phi = 1$ le seul point stable pour le potentiel énergétique de la membrane.

sphérique et une membrane périodique plate) à travers une étude détaillée des opérateurs Dirichlet-to-Neumann non locaux correspondants. Cette étude permet une comparaison des constantes de temps entre les membranes sphériques et plates. De plus, nous effectuons une analyse de stabilité linéaire de notre modèle, mettant en évidence les effets du couplage des équations du modèle. Pour estimer les paramètres du modèle, nous comparons également la fonctionnelle énergétique de notre modèle avec celles d'autres modèles physiques qui représentent actuellement l'état de l'art.

La troisième contribution est le développement d'un schéma numérique performant pour résoudre le modèle

Résoudre (1) numériquement n'est pas un problème trivial. La taille caractéristique associée à l'équation (1a) est de l'ordre de grandeur de quelques nanomètres tandis que la taille characteristique de la membrane cellulaire es de l'ordre de quelques dizaines de micromètres. Par conséquent, indépendamment du schéma numérique utilisé pour résoudre le problème, on doit utiliser un résolution spatiale très fine. De même, le temps caractéristique associé à l'équation (1b) est de l'ordre de grandeur de la nanoseconde (dans le cas d'une membrane électroporée). Ainsi, une haute résolution temporelle est nécessaire pour simuler le phénomène, indépendamment du schéma numérique utilisé. Ces contraintes impliquent le développement d'un schéma rapide et stable pour simuler le système.

Parmi les autres difficultés que nous repérons, il y a la propriété nonlocale de l'opérateur Λ, le fait qu'il ne commute pas avec les opérateurs $f \to \frac{f}{C_m(\phi)}$ et $f \to S_m(\phi)f$, et la dépendance en temps de l'opérateur $f \to \frac{1}{C_m(\phi)}\Lambda f$ (à travers la fonction $t \to \phi(t, \cdot)$).

Nous développons un schéma numérique efficace qui surmonte l'ensemble de ces difficultés, au moins dans le cas particulier de $\Gamma = (\mathbb{R}/\mathbb{Z})^2$. Il est basé sur une transformation de Fourier rapide pour diagonaliser les opérateurs Λ et le laplacien, un solveur numérique itératif de type gradient conjugué, et un schéma à pas fractionnaire de type splitting de Strang, pour obtenir un schéma d'ordre 2 en temps.

Avec ce schéma, nous pouvons simuler un morceau de membrane de taille $4 \cdot 10^4[\text{nm}^2]$, ce qui correspond à plus de trois ordres de grandeur par rapport à la taille d'une membrane dans les cas des simulations de dynamiques moléculaires actuellement considérées comme dans [85, 81].

L'efficacité de ce schéma numérique nous donne l'opportunité d'effectuer une analyse de sensibilité pour les paramètres et de faire des comparaisons avec le modèle d'électroporation le plus populaire dans un scénario réaliste et avec des données expérimentales dans le cas d'impulsions nanosecondes appliquées à une suspension cellulaire.

Structure de la thèse

Dans le **premier chapitre**, nous faisons un résumé de l'état actuel de l'art dans la modélisation de l'électroporation cellulaire. Nous commençons par décrire la structure biologique et la fonctionnalité de la membrane cellulaire, ce qui nous amène à examiner le comportement

électrique de la membrane et à justifier ainsi sa modélisation sous l'angle électrique. Ensuite, nous passons en revue les modèles les plus représentatifs de l'électroporation disponibles dans la littérature. Au fil des dernières décennies, plusieurs modèles ont été proposés, certains s'appuyant sur des principes physiques, d'autres étant des combinaisons de différents modèles, et quelques uns étant des extensions de modèles établis précédemment.

Malgré cette diversité de modèles, aucun d'entre eux n'a pu expliquer intégralement le phénomène d'électroporation, bien qu'ils montrent généralement un accord qualitatif raisonnable avec les observations expérimentales. Cela soulève des questions importantes pour les scientifiques utilisant l'électroporation dans leurs recherches, telles que l'identification de la fréquence optimale de délivrance d'impulsions pour maximiser l'électroporation d'une cellule, ainsi que les valeurs idéales pour l'intensité du champ ou la durée de l'impulsion électrique.

Actuellement, ces questions dépassent les possibilités des modèles existants. Les modèles que nous rappelons dans cette thèse :

- Le modèle de pore aqueux transitoire, initialement proposé par Chizmadzhev *et al.* qui a joué un rôle crucial dans la compréhension actuelle de l'électroporation. Désigné sous le nom de modèle PCA, ses concepts ont eu une influence significative sur le paysage des modèles proposés depuis plus de quarante ans.

- Le modèle KN, développé par Neu et Krassowska, est une simplification du modèle de Chizmadzhev. Il améliore le modèle initial en le rendant plus simple grâce à une analyse asymptotique rigoureuse, qui remplace une équation aux dérivées partielles par une équation différentielle ordinaire. Cette simplification facilite les simulations numériques et a depuis lors fait du modèle KN le plus largement utilisé dans la communauté de recherche.

- Le modèle développé par Leguèbe *et al.* est phénoménologique, combinant des idées physiques avec certains comportements intuitifs hypothétiques de la membrane. Contrairement aux deux modèles précédents, celui-ci distingue explicitement la conductivité électrique membranaire de la perméabilité membranaire. Bien qu'il ne fasse pas référence explicitement aux pores membranaires, puisqu'il est phénoménologique, il n'est pas nécessairement en opposition avec cette notion.

- Nous présentons brièvement les résultats issus des simulations de dynamique moléculaire, qui constituent actuellement les représentations les plus détaillées de la membrane. Cependant, ces simulations sont extrêmement limitées en raison de leur cout de calcul. Par conséquent, elles ne permettent de simuler que de petites portions de membrane à la fois, d'environ 100 [nm^2] chacune.

Le **deuxième chapitre** est dédié à la présentation et à la justification de notre modèle, qui se compose de trois parties principales. Dans la première partie, nous introduisons la ligne de niveau ϕ, qui décrit l'état de la membrane cellulaire. Son évolution est contrôlée à

travers la minimisation d'une fonctionnelle énergétique s'écrivant sous la forme suivante

$$\mathcal{E}(\phi, v) = \kappa \int_\Gamma \|\nabla\phi\|^2 + \int_\Gamma \mathcal{W}(\phi) - \frac{1}{2}\int_\Gamma C_m(\phi)v^2$$

pour un potentiel transmembranaire v donné. Cela amène à l'équation d'évolution 1a. Qualitativement, quand $v \equiv 0$, ce problème modélise bien le comportement de la membrane.

Concernant la modélisation électrique de la membrane, nous proposons aussi une approche pour comparer les deux cas $\Gamma = \mathbb{S}^2$ et $\Gamma = \mathbb{T}^2 = (\mathbb{R}/\mathbb{Z})^2$ nous permettant de mieux comprendre l'impact de certains paramètres du système.

Nous présentons aussi des choix de modélisation raisonnables pour les fonctions $\phi \to S_m(\phi)$ et $\phi \to C_m(\phi)$, puis, à travers une analyse de stabilité linéaire, nous identifions une condition suffisante pour $\mathcal{W}$ et $\phi \to C_m(\phi)$ pour générer des instabilités. Ces instabilités conduisent à la formation de pores sous l'influence du champ électrique. Notamment, nous démontrons qu'en prenant C_m comme une fonction affine, cette condition n'est pas en général verifiée. La dernière partie de ce chapitre est dédiée à l'estimation des paramètres. Nous attribuons une signification physique à tous les coefficients utilisés dans notre modèle et nous estimons approximativement chaque paramètre en fonction des quantités physiques connues de la membrane cellulaire.

Enfin nous montrons que notre modèle représente une généralisation naturelle du modèle proposé par Chizmadzhev *et al.* en identifiant les termes dans notre fonctionnelle énergétique qui sont analogues à ceux présents dans leur modèle énergétique.

Dans le **troisième chapitre**, nous procédons à la validation numérique de notre modèle et présentons les résultats obtenus. Nous exposons en détail les défis auxquels nous avons dû faire face et le schéma numérique mis en place pour y répondre. Tout d'abord, nous proposons un schéma initial naïf qui s'avère raisonnablement efficace dans le contexte de notre problème. Ensuite, nous l'améliorons pour avoir une précision d'ordre deux en temps.

Pour éviter de discrétiser les opérateurs linéaires non bornés, nous exploitons le fait que ces opérateurs peuvent être diagonalisés dans la même base de fonctions propres. Nous validons cette approche numériquement en effectuant un test de convergence sur notre modèle, démontrant ainsi une convergence d'ordre deux. Parmi les différents tests numériques que nous effectuons, nous présentons une simulation impliquant l'application d'une impulsion électrique de 12 [ns]. Cette simulation est basée sur une configuration similaire à celle utilisée dans des expériences et dans les simulations de dynamique moléculaire. Dans ces conditions, nous parvenons à électroporer un patch carré de membrane et à obtenir un comportement qualitatif cohérent concernant les temps de charge et de décharge de la membrane, ainsi que la durée de vie attendue des pores créés.

Nous procédons également à des tests de sensibilité pour évaluer l'influence des valeurs des paramètres de notre modèle. Cela s'avère particulièrement intéressant en raison de la nature quasi-linéaire de notre modèle, ce qui rend complexe une analyse mathématique approfondie de l'équation (1). Parmi les paramètres que nous testons, nous prenons en compte la conductivité électrique associée aux pores à l'intérieur de la membrane, la tension superficielle de la membrane et le bruit, qui modélise les fluctuations thermiques naturelles du système.

Dans le **quatrième chapitre**, nous conduisons des expériences numériques en utilisant notre modèle dans le but de le comparer à des données expérimentales dans différents contextes. Enfin, nous confrontons notre modèle au modèle d'électroporation le plus populaire – c'est-à-dire le modèle de KN – dans un scénario réaliste. L'objectif est de comprendre comment notre modèle se distingue du modèle le plus couramment utilisé en électroporation, d'identifier ses avantages potentiels par rapport à ce dernier, et de déterminer les limites qu'il doit surmonter.

Introduction

This thesis is part of a long standing project with the objective of understanding physically and quantitatively the phenomenon of electroporation. The work included was done at the Institut Mathématiques de Bordeaux (IMB), within the Inria team Monc. The funding for this project came from the Contrat Doctorale Spécifiques Normaliens (CDSN), a doctoral scholarship from the Ecole Normale Supérieure de Lyon (ENS Lyon).

Some context

Electroporation is the application of pulsed electric fields of high intensity and short duration to cells. The goal is to create defects – called pores – in the cell membrane [7]. Reversible electroporation allows the introduction of non-permeable molecules into living cells without directly killing them, while irreversible electroporation leads to the death of cells in the target area.

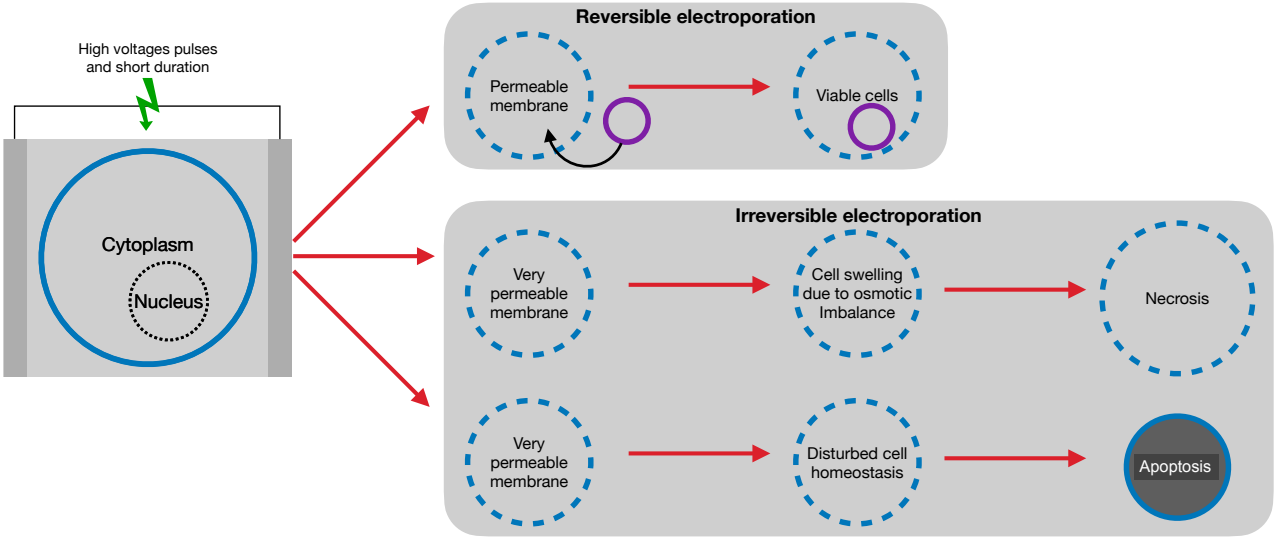

Figure 4: Diagrammatic representation of the electroporation of a cell, both reversible and irreversible.

Although, this phenomenon was discovered decades ago [91], the development of new technologies based on this phenomenon is still new. In fact, it has applications in current

research in a variety of fields. Ranging from gene therapy [24, 34] and cancer treatment [21] to treatment of cardiac arrhythmias [32, 82] and even in the food industry [53], the development of techonology based in electroporation is more active than ever before.

An important example: in cancer alone, there is a promising niche for electroporation. It turns out that in an important number of cases, the size of a tumor is not the most important factor determining the type of treatment a patient receives. In fact, if a small tumor is placed near a sensitive part of the body (near the aorta, for example), then it is likely that such a patient would no longer be a candidate for surgery. Other options are also discarded, as an example, radiofrequency therapy or other thermal ablation therapies are automatically out of consideration. The heat produced from these therapies can diffuse to the sensitive tissue surrounding the tumor and so there is big potential of causing collateral damage. Electroporation provides an ideal treatment in this scenario. Currently, non-invasive and non-thermal therapies which do not damage the structure of the tissue (the extracellular matrix) based on electroporation, are being developed exactly for these types of scenarios : tumor ablation via irreversible electroporation [71, 38, 55], electrochemotherapy [14], calcium electroporation [29], among others. The short explanation of what these therapies consist of is a local application of a short electric pulse to the tissue containing a tumor, then, depending on the therapy, the corresponding agent is introduced into it. As the cancer cells in the tumor have been electroporated, the injected agent can easily enter the cell and have an effect on the tumor. This shows the particular allure of electroporation as it can boost the effectiveness of other more traditional treatments (as in the case of electrochemotherapy, for example). There is a real societal benefit to developing all these therapies in oncology as cancer is a principal cause of death in Europe [8].

Similarly, in the treatment of cardiac arrhythmias [66], electroporation plays an important role and for some of the same reasons as in cancer treatment. This treatment basically consists of electrically isolating problematic tissue in the heart so that that it does not interact erratically with the cardiac conduction system.

Other applications, like in the food industry, are usually related to facilitating the extraction of the contents (juice, water, oil, etc) of certain biological mass [70]. Examples of this can be seen in wine production, juice extraction, olive oil extraction, drying of herbs and fruit, etc. So far, the benefits concern not only the quantity that can be extracted but the quality of the final products as well. The electroporated biomass can more easily release its contents and so less intense procedures (meaning they apply less energy, or take less time, etc) are used to extract them, thereby better preserving the quality of extracted material.

Electroporation is also frequently used in the electrotransfer of DNA. Application of this can be found in the fields working with genetically modified organisms, gene therapy [58], electrotransfer of DNA vaccines [86], etc.

All these applications showcase the potential of this technology and motivate the need to further understand this phenomenon. This need becomes more apparent when we consider the number of parameters that play a role in electroporation: electrical conductivity of the medium, intensity of the electric pulse, shape and size of the targeted cells, duration of the pulse, mean cell orientation, number of pulse repetitions, frequency of pulses, etc. The

nonlinearity of this phenomenon in addition to the number of parameters affecting it, make it practically impossible to quantitatively understand this phenomenon by just trial and error in experimentation. Additionally, it also owes its complexity, in part, to the different scales of time involved (membrane changes can happen within nanoseconds and can persists for minutes), and in part, to the biological context naturally included. As a result, modeling and testing is the only way to push forward the understanding. In fact, depending on the scale of the application (electroporation of some tissue, a suspension of cells in a fluid, a single cell, or even just a very small part of the cell membrane), completely different models are used to describe it. However, as is the case in a lot of biological settings, many mathematical models (at all scales) can be made to fit the behaviour observed in experiments. This poses the problem of choosing the "correct" model, and so physically based and predictive models are of prime interest.

The work presented in this thesis targets the development of mathematical innovative tools to model electroporation at the cellular scale. We construct an electroporation model which couples an quasistatic model of the electric potential surrounding the cell membrane and a phase-field model based on a modified version of the Allen-Cahn equation which describes the state of the membrane. From a modeling point of view, we physically justify this model and showcase its behavior by simulating it in a relevant scenario.

PhD Objectives

Main contributions

There are three main contributions of my work:

(1) The development of a new physically based mathematical model of electroporation at cellular scale.

(2) The mathematical study of the qualitative properties of this model.

(3) The development of a very efficient numerical scheme to solve the PDE system corresponding to our model.

Modeling Currently there are a several models of cellular electroporation. They roughly fall into two categories: first, the phenomenological models and then the physically based models. The phenomenological models are mainly based in intuition, and contain parameters which have to be fitted for experimentally. As a result, by their nature, they are descriptive and not predictive. On the other hand, the physically based models are better justified however they have to deal with the increased complexity involved in this type of modeling. Their fault tends to be the oversimplification of the phenomenon which then fails to capture some key aspects, some of which have been witnessed in experimentation. So far, no model has been satisfactory, in the sense that no definitive consensus in the community has been

reached as to the correct model of cell electroporation. We introduce a mathematical model of cell electroporation whose parameters all have a physical interpretation.

The mathematical model we propose is a system of partial differential equations (PDE). It takes the form of a semilinear reaction-diffusion equation acting on a membrane order parameter ϕ coupled with a linear parabolic and nonlocal PDE acting on the difference of electric potential v across the cell membrane. Both equations are defined over a closed surface Γ representing the membrane

$$\begin{cases} \partial_t \phi - D\Delta_\Gamma \phi = -\alpha \mathcal{W}'(\phi) + \frac{\alpha}{2} C_m'(\phi) v^2, \ \forall x \in \Gamma, \ t > 0, \\ \phi(0, \cdot) = 0, \end{cases} \tag{2a}$$

$$\begin{cases} C_m(\phi)\partial_t v + (S_m(\phi) + \Lambda)v = g, \ \forall x \in \Gamma, \ t > 0 \\ v(0, \cdot) = 0, \end{cases} \tag{2b}$$

where D corresponds to the lipid lateral diffusion in the membrane, $\mathcal{W}$ is a double well energy potential, the nonlocal pseudodifferential operator Λ corresponds to the composition of two Dirichlet-to-Neumann operators, S_m denotes the electric conductance of the membrane, C_m the electric capacitance of the membrane and g represents a source term associated to the application of an electric pulse to the cell.

Mathematical study The complete system is a quasi-linear PDE on the joint unknown (ϕ, v). We perform an in-depth mathematical analysis of our model. Indeed, we show that this model has good qualitative properties for our problem. We compare its behavior in two important cases: $\Gamma = \mathbb{S}^2$ and $\Gamma = \mathbb{T}^2 = (\mathbb{R}/\mathbb{Z})^2$ (a spherical membrane and a flat periodic membrane) through a detailed study of the corresponding nonlocal Dirichlet-to-Neumann operators. This study allows a comparison of the time constants between spherical and flat membranes. We also perform a linear stability analysis of our model, highlighting the effects of coupling the model equations. In order to estimate the model parameters, we also compare the energy functional of our model with that of other physical models that currently represent the state of the art.

Numerical scheme Numerically solving (2) is not trivial. The characteristic length associated to (2a) is on the order of magnitude of a few nanometers and so any reasonable numerical scheme needs to handle a high resolution in space. On the other hand, the characteristic time in (2b) is smaller than one nanosecond and so, again, any numerical schemes for this equation needs to be quick enough to handle a high resolution in time. These constraints naturally require fast and stable numerical schemes. Other difficulties arise from the nonlocal nature of the operator Λ, the fact that it does not commute with the linear operators $f \to \frac{f}{C_m(\phi)}$ and $f \to S_m(\phi)f$, and finally the fact that the unbounded operator $f \to \frac{1}{C_m(\phi)}\Lambda f$ depends on time (through $t \to \phi(t, \cdot)$). We developed an efficient numerical scheme which manages to overcome these difficulties, at least in the case of $\Gamma = (\mathbb{R}/\mathbb{Z})^2$. The scheme uses a mix of Fast Fourier Transform (FFT) to diagonalize the laplacian and Λ, a Conjugate gradient (CG) algorithm to invert the non-commuting operators, and a Strang

splitting scheme to obtain a numerical scheme of order two in time. With it, we can simulate a square patch of membrane of size $4 \cdot 10^4[\text{nm}^2]$, which is three orders of magnitude bigger of what is currently possible in molecular dynamic simulations.

The efficiency of this numerical scheme gives us the opportunity to perform a sensitivity analysis for the parameters and to make comparisons with the most popular model of electroporation in a realistic scenario and with experimental data in the case of nanosecond pulses applied to a cell suspension.

Outline of the thesis:

The **first chapter** presents a summary of the current state of the art in cell electroporation modeling. First we present the biological structure and functionality of the cell membrane. This justifies the next section where we present the electrical behavior of membrane which later on motivates its modeling from an electric point of view. After this, we show the most representative models of single cell electroporation currently available in the literature. In fact, over the past few decades, several models have been proposed. Some models are inspired from physical principles, others are a combination of different models, and a few are extensions of previously established models. With all these available models, it is natural to wonder what is the need for another one. Well, for the most part, all these models show, to one degree or another, reasonable qualitative agreement with the phenomenon of electroporation, but no single model has been able to fully explain it. By this, we mean that so far, no model captures most of the qualitative observations that have been seen in experiments. In fact, many of the questions of interest to scientists using electroporation in experiments, are out of reach of the current models. As an example of questions: what is the optimal frequency of pulse delivery to maximize electroporation of a cell? Or similarly, the optimal values for the field strength or the electric pulse duration in order to obtain a desired outcome in experiments? These types of questions are important to understand in order to develop better electroporation strategies and protocols. It is therefore vital to present the most representative current models, showcase their ideas and highlight their limitations, to motivate the need for a new model. The models we present are:

- The first transient aqueous pore model, introduced by Chizmadzhev *et al.*, which paved the way for the current understanding of electroporation. This model is denoted here as the PCA-model. The history of this model spans more than forty years and its ideas have had considerable influence in the current landscape of models available.

- A simplification of the Chizmadzhev model, developed by Neu and Krassowska and denoted here as the KN-model. This model improved upon the first model in the sense that it simplified it by means of a mathematical rigorous asymptotic analysis thereby replacing a PDE by an ODE. This made it easier to simulate from a numerical standpoint and has since become the most popular model used in the research community.

- A phenomenological model developed by Leguèbe *et al.* It presents a mix of physical ideas and some hypothesized intuitive behavior of the membrane. Compared to the two models above, it is the only one to explicitly differentiate between membrane electrical conductivity and membrane permeability. The notion of membrane pores is not part of this model however as it is phenomenological it does not really oppose this notion.

- We quickly describe some of the results obtained in molecular dynamic simulations. These simulations are the most detailed representations we currently posses of the membrane. They are however, extremely limited due to their computationally complexity. As a result only small patches of membrane can be simulated at a time around 100 [nm^2].

The **second chapter** presents and gives the physical grounds of the model. There are three main parts to it. The first part introduces the order parameter ϕ that describes state of the cell membrane. This mainly concerns its evolution as it minimizes an energy functional of the form

$$\mathcal{E}(\phi, v) = \kappa \int_\Gamma \|\nabla\phi\|^2 + \int_\Gamma \mathcal{W}(\phi) - \frac{1}{2}\int_\Gamma C_m(\phi)v^2$$

given a prescribed transmembrane potential v and results in Equation (2a). We show that in the case of $v \equiv 0$ this model behaves as one would expect of a cell membrane. The next part concerns the electric modeling of the membrane. In this part, we show the appropriate way to compare two important settings $\Gamma = \mathbb{S}^2$ and $\Gamma = \mathbb{T}^2$. We present reasonable modeling choices for the functions $\phi \mapsto S_m(\phi)$ and $\phi \mapsto C_m(\phi)$ and, through a linear stability analysis, find a necessary key condition concerning $\mathcal{W}$ and $\phi \mapsto C_m(\phi)$ for instabilities. This translates into the creation of pores as a result of these instabilities due to influence of the electric field. In particular, we show that, for example taking $\phi \mapsto C_m(\phi)$ as an affine function cannot produce pores in the membrane. The last part of this chapter concerns parameter estimation. It gives physical sense to all the coefficients used in our model and gives an approximate value to each parameter in terms of known physical quantities of the cell membrane. We also make the case that our model is a natural generalization of the transient aqueous pore model proposed by Chizmadzhev *et al.* By this, we mean that we manage to identify terms in our energy functional analogous to the energy functional they proposed in their model.

The **third chapter** validates our model numerically and shows some numerical results we have obtained. It is a detailed presentation of the challenges we needed to overcome and the numerical scheme that answers to them. We first propose a naive first scheme which works reasonably well in the context of our problem. We then improve upon this scheme and show that it is of order two accuracy in time. We do not discretize the unbounded linear operators, because we exploit the fact that these operators can be diagonalized and in the same basis of eigenfunctions. We numerically validate our claim by running a convergence test on our model and we show that we actually do obtain a convergence of order two. Among the numerical tests we do, we show a simulation which consists of an application of one 12 [ns]

electric pulse. This simulation shares a similar setup used in experiments and in molecular dynamics simulations. Under these conditions we manage to electroporate a square patch of membrane and get some qualitative behavior regarding the membrane charge and discharge times, in addition to the expected lifetime of the pores created. Furthermore, we test the sensibility of our model to the values of the its parameters. This is particularly interesting as the quasilinear nature of our model (2) makes it difficult to make a fine mathematical analysis of the equation. Among the parameters we test for, we consider the electric conductivity associated to pores inside the membrane, the surface tension of the membrane and noise (which models the natural thermal fluctuations of the system).

In the **fourth chapter**, we perform numerical experiments with our model to compare it with experimental data in different contexts. Finally, we confront our model with the most popular electroporation model – the model of KN – in a realistic scenario. The goal is to understand how our model differs from the most commonly used model for electroporation, identify its potential advantages over the latter, and determine the limitations it must overcome.

In the last chapter, a conclusion is made and some perspectives are given.

Main contributions

To conclude this introduction, a review of the publications that illustrate the work produced in this thesis is made. Conferences were also an opportunity to present this work. I also implemented the different numerical schemes and models presented in this thesis.

Publications

1. P. Jaramillo, A. Collin, and C. Poignard. Phase-field model of bilipid membrane electroporation. JOMB 2023 (in press). Mostly Chapter 2.

2. P. Jaramillo, A. Collin, and C. Poignard. Numerical scheme for Phase-field Electroporation model. Currently under editing. Mostly Chapter 3.

Conferences

1. Conference Core To Core – Osaka – 23-27/03/2020 - `http://web.apollon.nta.co.jp/jsps/index.html`

2. Conference CIRM 2396 (Non-Local Models Arising from Biology) – 11–15/10/2021 – `https://conferences.cirm-math.fr/2396.html`

3. Congrès des Jeunes Chercheuses et Chercheurs en Mathématiques Appliquées (CJC–MA 2021) – 27–29/10/2021 – `https://cjc-ma2021.github.io/`

4. Workshop ECMTB 2022 – 12th Electroporation Conference on Mathematical and Theoretical Biology.– 17–24/09/2022 – `https://ecmtb2022.org/`

5. 4th World Congress on Electroporation and Pulsed Electric fields in Biology, Medicine and food & environmental Technologies – 09–13/10/2022 – `https://wc2022.electroporation.net/`

Software Development

For the simulations presented in this thesis around 2500 lines of FreeFem++ code where written. This includes the numerical scheme we presented, mixing the Fast Fourier Transform and the Conjugate gradient iterative solver for linear systems of equations. This also includes, testing the code and convergence analysis, managing different simulation protocols, and comparing different schemes for solving ordinary differential equations which results from our numerical scheme.

Chapter 1

State of the art of electroporation modeling at cellular scale: biological and mathematical descriptions

In this chapter we first give a brief description of a cell membrane from a biological and electrical point of view. This includes a description of the electrostatic model for electric potential surrounding the cell membrane. Next, we present what the current understanding of electroporation is and how it is modeled. This includes, the classical theory of transient aqueous pores in the cell membrane, and a brief presentation of the rest of the state of the art from a modeling point of view. Lastly, we present some of the limitations associated to these models and finish the chapter with some remarks motivating the work present in the subsequent chapters of this thesis.

1.1 Cell Membrane Biology

A biological description of a cell tends to include the cell membrane, the cytoplasm, nucleus organelles, etc, each of which involve complex structures themselves. In this section, we will limit ourselves to describing only the biological structure and functionality of the membrane of a cell as it is the main object of interest, at least from a modeling standpoint. A more in-depth study of the cell could be useful for other purposes, for example, when modeling electroporation of organelles inside the cell. These considerations are out of the scope of this thesis. It is important to note that the contents of this section apply to all animal cells and so we will always reference a generic cell, without entering into further detail on the type of cell it is. The presentation of the material below is mainly a summary of the physiology of a cell membrane. We present only the most important factors that will enter into play in the later modeling section of this chapter. A more detailed presentation of this material can be easily found in other sources, for example, a lot of the material presented below is taken from [54, 43].

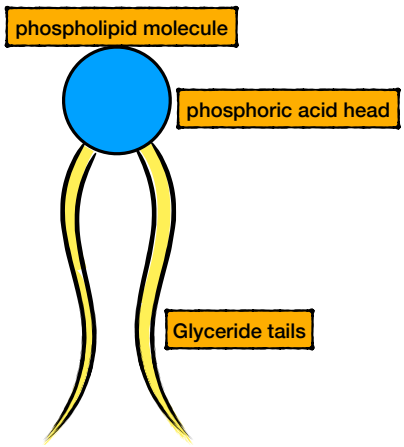

Figure 1.1: Simple representation of a generic phospholipid making up the cell membrane. Examples of phospholipids are shown in Figure 1.2.

1.1.1 Membrane Structure

As a whole, from a structural point of view, the membrane is very thin layer surrounding the cytoplasm and organelles of the cell. In fact, its thickness is usually between 5 and 10 [nm] while the diameter of its cell can easily reach 10 [μm]. The cell membrane is mainly composed of fatty acids called phosphoglycerides or phospholipids.

These phosphoglyrecides are made from phosphoric acid and glycerides, which take the form of a hydrophilic fatty acid head and hydrophobic glyceride tails, see Figure 1.1. They are part of a general type of compound known as amphiphiles, which are chemical compounds possessing both hydrophilic (water-loving) and lipophilic (fat-loving) properties. As a result, when placed in water, these phosphoglycerides spontaneously rearrange themselves into configurations which minimize exposure of the hydrophobic acid chains to the water molecules. In other words, into configurations where the acid heads are in contact with the water molecules while the tails are away from them. Figure 1.3 shows some of the possible configurations that result from this spontaneous rearrangement. One of these arrangements takes the form of a lipid bilayer. This lipid bilayer is the basic structure of the cell membrane.

The cell membrane (also known as plasma membrane), see Figure 1.4, contains in it different types of other structures like proteins, ion channels, enzyme, receptors, etc. However, it is important to note that the plasma membrane is not a static structure. Both lipids and proteins in the plasma membrane can rotate and diffuse laterally. For example, in the bilayer, cholesterol is also present, and it is known to affect the membrane fluidity. When they accumulate together they form a structure known as a lipid raft which floats freely within the membrane. Some of these structures will play a role in the modeling of the membrane as we will show in the following sections.

Remark 1. *From here on, the terms lipid bilayer, plasma membrane and cell membrane are used interchangeably.*

Among the proteins found in the cell membrane we highlight two important types. The

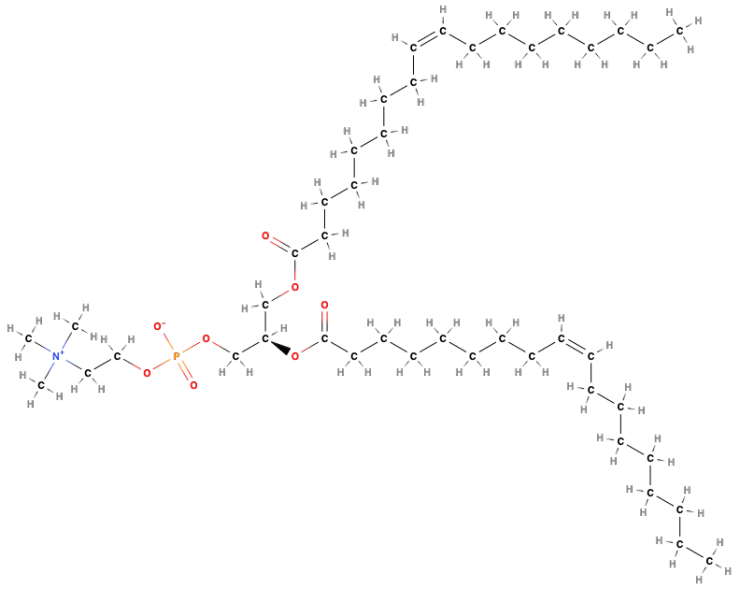

(a) Structural formula of 1,2-dioleoyl-sn-glycero-3-pphosphatidylcholine (DOPC).

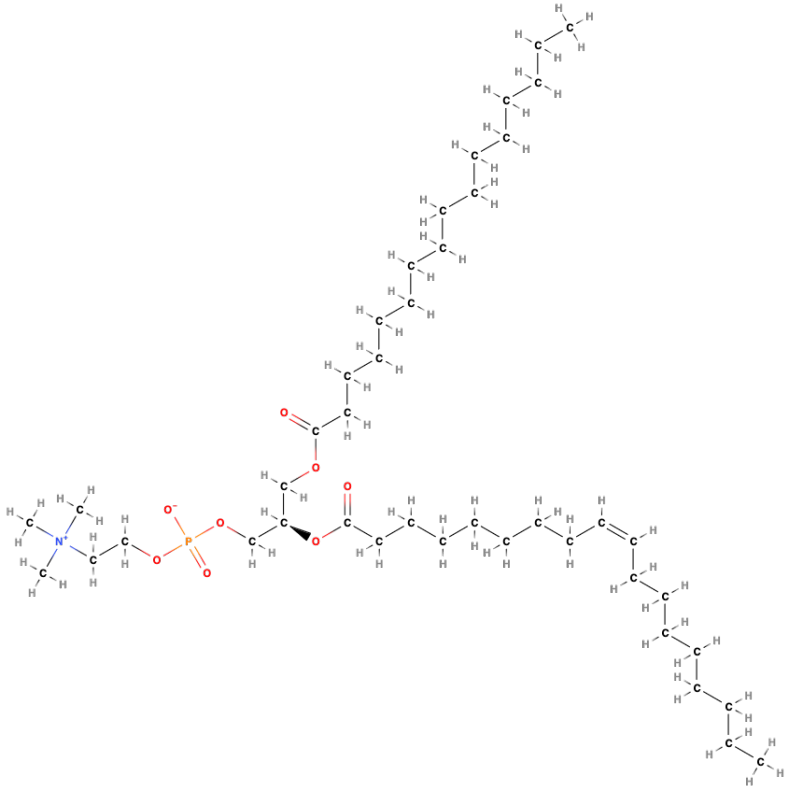

(b) Structural formula of 1-palmitoyl-2-deoyl-sn-glycero-3-phosphatidylcholine (POPC).

Figure 1.2: Two examples of phospholipids present in the cell membrane and used in molecular dynamics simulations [47]. Images found in [60].

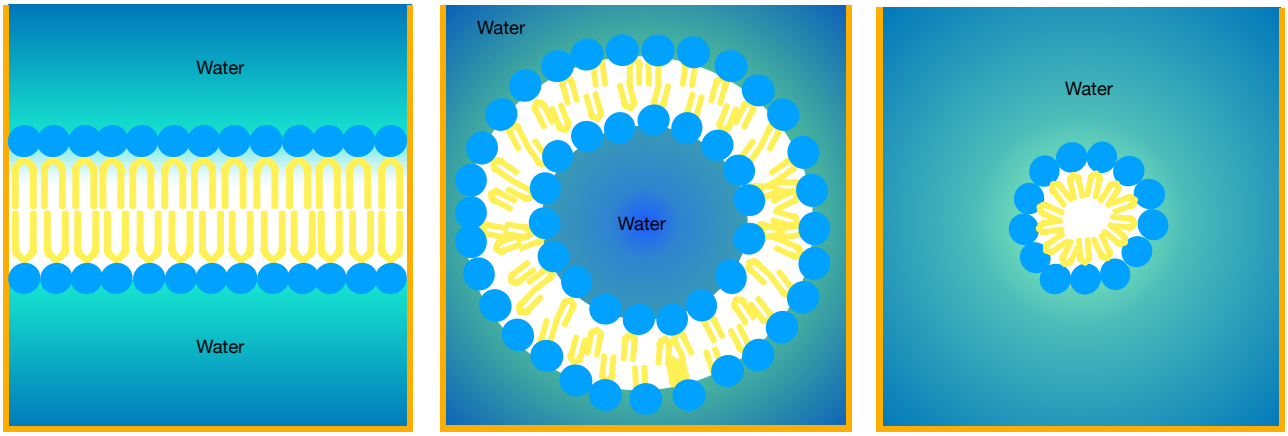

(a) Bilayer configuration. (b) Liposome configuration. (c) Micelle configuration.

Figure 1.3: Typical configurations into which lipids naturally rearrange themselves when immersed in water.

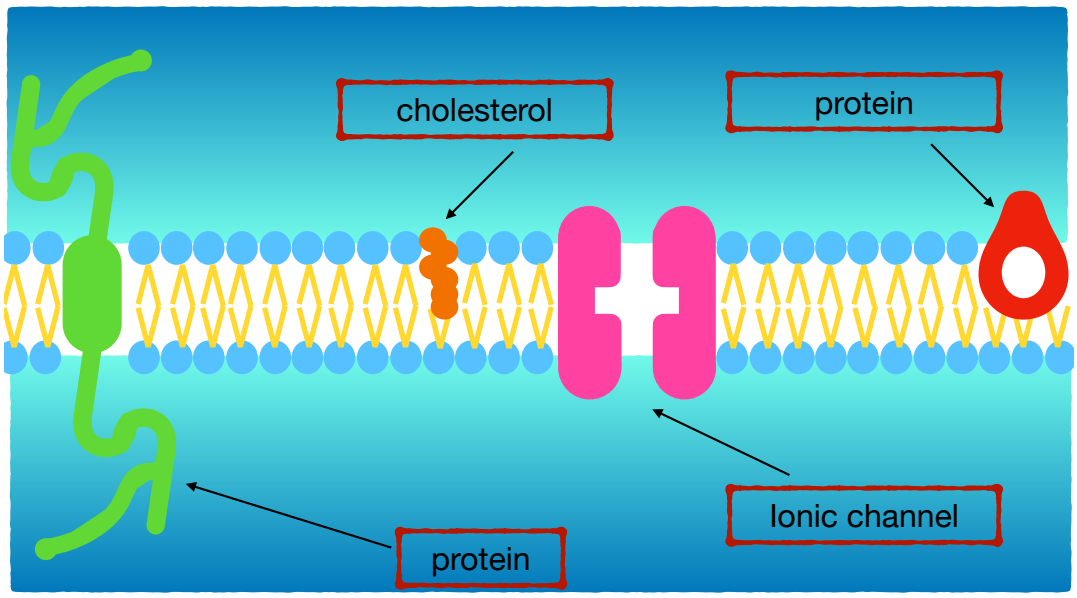

Figure 1.4: Simple diagram showing structures that can be found in the membrane of a cell.

first is ion channels. They form water filled pores in the membrane which are highly selective in what they allow to pass through them. They allow passive transport (this process does not consume energy) of only certain ions, depending on their size and charge. In fact, ion channels are charge specific, which means that channels for anions (which are negatively charged ions) have positively charged side chains in the pore, and vice versa for cations (ions with positive charge). Furthermore, depending on the type of ion channel, they can open and close as a consequence of different stimuli (light, mechanical stress, etc). Related to our study, the important examples include the voltage-gated sodium channels, the voltage-gated potassium channels and the voltage-gated calcium channels.

The second important type of proteins are lipoproteins. They are highly selective protein carriers within the membrane, just like ion channels, however they use ATP as an energy source in order to exercise active (energy consuming) transport of ions. Two important examples are the Ca^{2+}-ATPase and Na^+/K^+-ATPase pumps that mediate this active transport (see [78, 63, 17, 15] for a more detailed description). There are additional components in the membrane, but these elements are sufficient to give us a good idea of how to model a membrane.

1.1.2 Membrane functionality

From a biological point of view, the membrane plays an important regulating role. The hydrophobic interior of the bilayer, composed of fatty acid chains, makes the membrane impermeable to water-soluble molecules and so helps maintain the concentration of different ions inside the cell.

Additionally, the membrane regulates the exchange of ions between a cell and its exterior medium. The ion channels in the cell membrane allow the passage of only certain ions (primarily Na^+, K^+, Ca^{2+} and Cl^-) down their electrochemical gradient (from high to low concentrations), thus giving the plasma membrane its semipermeable characteristic. If the channels are open then this means that only certain ions can permeate across the membrane by passive mechanisms, like diffusion.

Another important regulating function of the membrane is exercised by the lipoproteins contained in it. For example, Na^+/K^+-ATPase controls the concentration gradients of Na^+ and K^+ across the membrane. This is done by active transport, enabling the cell to move solutes up a concentration gradient (from low to high concentrations) across its membrane. In general, because of this, it is not uncommon for the different ion concentrations inside the cell to differ greatly from the concentrations in its exterior medium. In fact, the Na^+ concentration tends to be higher outside the cell while the K^+ concentration is higher inside it. Functionally, this helps control the size of the cell and the water distribution on both sides of the membrane.

These properties of the membrane have an important biological role, but more importantly, they also give rise to some key electrical properties of the membrane.

1.2 Electrical properties of the cell membrane

1.2.1 Resting potential of the cell membrane

Due to the semipermeable nature of the cell membrane as described above, there is a concentration gradient for the different ions the membrane is selectively permeable to. This creates an ion flux as a result of diffusion which acts on the ions, forcing them to cross the cell membrane. This effect tends to accumulate ions at the inner and outer walls of the cell membrane. An electric field across the membrane is thus created which in turn exerts a force on the ions crossing the membrane as they have an electric charge. As a result, two forces act on ions moving across a cell membrane, diffusive forces and electric forces. This condition can be expressed in terms of net flux of ions, as in the following relation

$$J = J_D + J_E, \tag{1.1}$$

where J_D is the ionic flux due to diffusion and J_E is the ionic flux due to the electric field influence (both in units [mol.m^{-2}.s^{-1}]). The ionic flux due to diffusion is given by Fick's law, and takes the following form

$$J_D = -\frac{u_m RT}{|z|F}\nabla c,$$

where u_m is ionic mobility in the medium (units in [m^2.V^{-1}.s^{-1}]), $R = 8.314$ [J.mol^{-1}.K^{-1}] is the gas constant, T (units in [K]) is the temperature of the system, z is the valence of the type of ion, $F = 9.649 \times 10^4$ [C.mol^{-1}] is Faraday's constant, and c is the ion concentration in units [mol.m^{-3}].

The flux due to the electric field is given by:

$$J_E = -u_m \frac{z}{|z|} c \nabla U,$$

where U is the electric potential (in units [V]), $z/|z|$ gives the sign of the force affecting the ions, and $-u_m z/|z|$ is the mean velocity achieved by these types of ions in a unit electric field.

Replacing the expressions for J_E and J_D in (1.1) results in the Nernst-Planck equation

$$J = -u_m \left(RT \frac{z}{|z|} \nabla c + c|z|F\nabla U \right).$$

Consider the case of a membrane separating two media (inside the cell and outside it) containing a mix of different types of ions with no total net charge. If the membrane is only permeable to one specific type of ion then by diffusion there is a net flow of this type of ion in one direction across the membrane. This in turn, creates an imbalance in the charge and so a transmembrane voltage is created. As more and more ions flow across the membrane, the electric potential across the membrane increases until an equilibrium is reached (when

diffusive and electric forces balance out). There is a transmembrane potential associated to this equilibrium, it is known as the resting potential of the cell membrane. This process reaches stability fairly quickly and so we assume that there is a negligible effect on the initial ion concentrations on either side of the membrane. The equilibrium transmembrane voltage V is given by the Nernst equation 1.2, which is derived from the Nernst-Planck equation above by taking a null net ionic flux:

$$RT\frac{z}{|z|}\nabla c = -c|z|F\nabla U.$$

Since the membrane is extremely thin we consider any small patch to be planar and describe any variation across its perpendicular axis. This results in the following one-dimensional problem

$$\partial_x c = -\frac{zF}{RT}\partial_x U c,$$

integrating this equation across the membrane results in

$$c_i = c_o e^{-\frac{zF}{RT}(U_i - U_o)},$$

where U_i and U_o are the electric potentials near the inside and outside wall of the cell membrane, so that

$$\ln\left(\frac{c_i}{c_o}\right) = -\frac{zF}{RT}V,$$

finally resulting in

$$V = -\frac{RT}{zF}\ln\left(\frac{c_i}{c_o}\right), \tag{1.2}$$

where c_i and c_o are, respectively, the inner and outer concentrations of the type of ion the membrane is permeable to.

We denote the difference in electric potential across the plasma membrane as the transmembrane voltage (TMV) of the membrane. We follow the convention of defining the TMV as the difference between the potential at the interior wall of the cell membrane minus the potential at the exterior wall.

Remark 2. *A generalization of this expression, in the case when the membrane is permeable to multiple types of monovalent ions, is given by the Goldman-Hodgkin-Katz (see [54] for more in-depth presentation of both equations):*

$$V = -\frac{RT}{F}\ln\left(\frac{\sum_k P_k^+ c_{k,o}^+ + \sum_j P_j^- c_{j,i}^-}{\sum_k P_k^+ c_{k,i}^+ + \sum_j P_j^- c_{j,o}^-}\right),$$

where $P_k^\pm$, denotes the membrane permeability (in $[m.s^{-1}]$) to k^{th} positive or negative ion (respectively) and $c_{k,i}^\pm$ and $c_{k,o}^\pm$ are the intracellular and extracellular concentrations of the k^{th} positive or negative ion, respectively.

Taking account for different types of ions and membrane permeabilities is a natural second step when modeling the electric behavior of the cell membrane. An example of this can be seen in [19, 20].

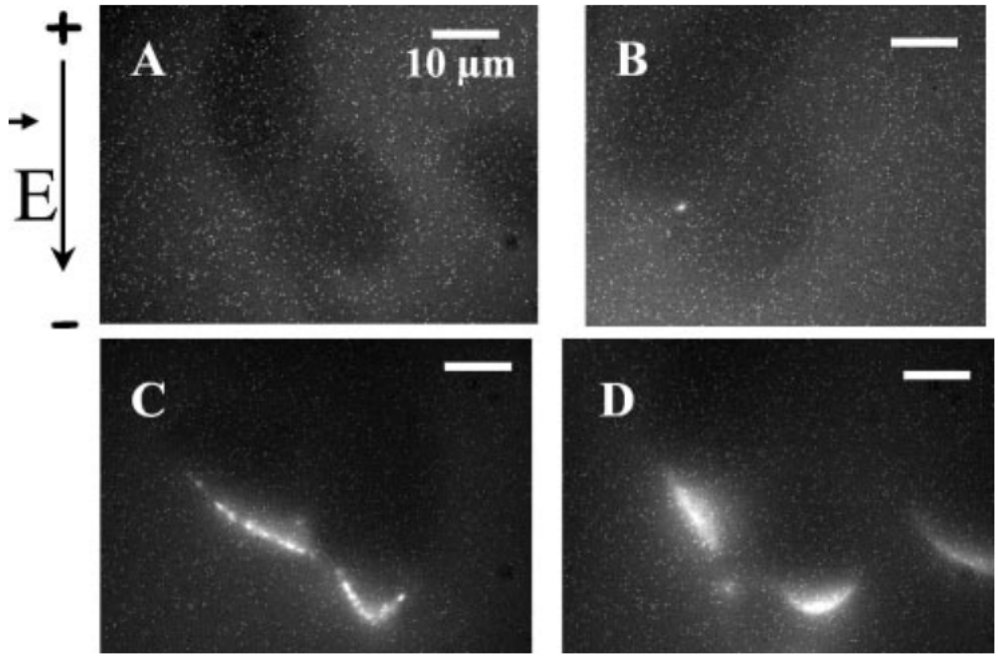

Figure 1.5: Fluorescent plasmid DNA is inserted into the environment surrounding Chinese hamster ovary cells, to visualize the mechanism of gene transfer with electroporation. Plasmid-DNA accumulation on the cell membrane for PEF with different intensities is shown. Ten pulses of 5 ms (1 Hz) were applied at 3×10^4 V.m^{-1} in **(A)**, 5×10^4 V.m^{-1} in **(B)**, 7×10^4 V.m^{-1} in **(C)** and 9×10^4 V.m^{-1} in **(D)**. Image taken from [31].

.

1.2.2 Electric potential surrounding the cell membrane

We now consider the case where the cell is immersed in an externally applied electric field. Of course, given that cell electroporation is a response to an electric stimulus applied to the cell, usually in the form of a pulsed electric field (PEF), it is natural to study the electric properties of the cell membrane. However, it has been shown that after PEF treatment, the permeabilization of the cell membrane is not uniform across its surface, see Figure 1.5. For example, evidence of this phenomenon can be seen (at least qualitatively) in experiments where measurements Propidium-iodide intake of a Chinese hamster ovary cell after PEF treatment. Imaging data clearly shows that the permeability of the membrane seems to be higher at the sides of the cell facing the electrodes applying the treatment (for example, see [31]). This supports the idea that electroporation is a physical phenomenon as opposed to a biological response of the cell to an electric field. Therefore, it is sensible to model this phenomenon by studying the TMV at each point of the cell membrane. To this end, we study the electric potential surrounding the cell membrane.

Before detailing how the electric potential is modeled, we fix some notations.

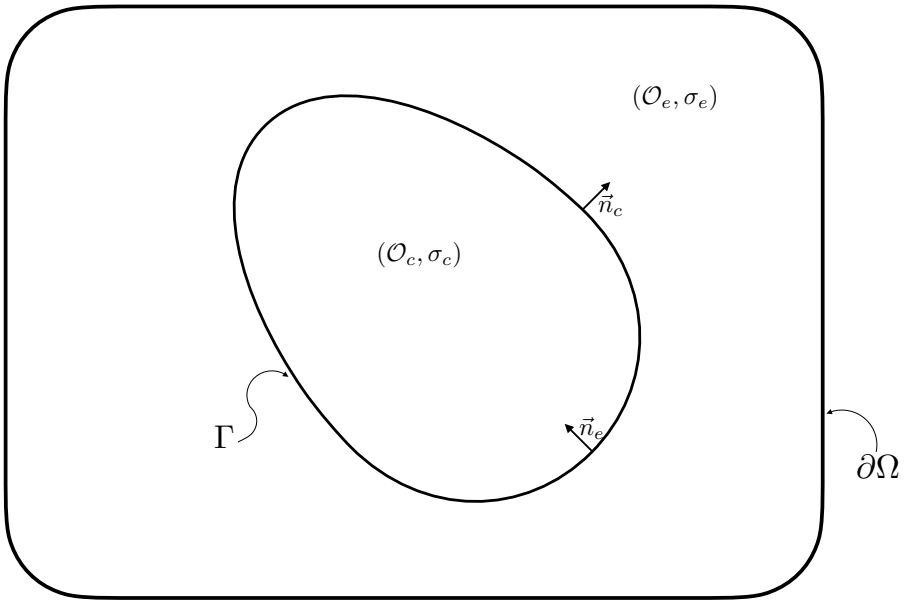

Figure 1.6: Diagram representing a cell $\mathcal{O}_c$, its membrane Γ and its external environment $\mathcal{O}_e$. The union of all three sets makes up the whole system Ω.

Notation

- $\mathcal{O}_c$ and $\mathcal{O}_e$ denote two connected smooth domains representing the interior and exterior of the cell, respectively.
- $\Gamma := \partial\mathcal{O}_c$ is the cell membrane itself (see Figure 1.6 for a clear representation).
- $\Omega := \bar{\mathcal{O}}_c \cup \mathcal{O}_e$ denotes the entire system and $\bar{\Omega}$ is its outside border.
- σ_e and σ_c are the electric conductivities of the exterior and interior media respectively. Additionally, $\sigma : \mathcal{O}_c \cup \mathcal{O}_e \to \mathbb{R}$ is a piecewise function defined by $\sigma_{|\mathcal{O}_c} := \sigma_c$ and $\sigma_{|\mathcal{O}_e} := \sigma_e$.
- $\vec{n}_c : \Gamma \to R^3$ is the unitary normal vector to Γ pointing towards the exterior of the cell
- Similarly, $\vec{n}_e : \Gamma \to R^3$ the normal pointing to the interior of the cell. Therefore, $\vec{n}_e(x) = -\vec{n}_c(x)$, for all x in Γ.
- The electric potential surrounding the cell membrane is represented by a piecewise function $U : \mathcal{O}_c \cup \mathcal{O}_e \to \mathbb{R}$.
- Following the same convention as in [54], we define the TMV on Γ to be

$$[U]_\Gamma(x) := U_{|\Gamma^-}(x) - U_{|\Gamma^+}(x),\ \forall x \in \Gamma,$$

where $U_{|\Gamma^\pm}(x) := \lim_{\tau \to 0^+} U(x \pm \tau\vec{n}_c)$.

Remark 3. *The cell membrane is modeled as a two dimensional surface even though in reality it has a non-zero thickness. This is naturally justified by its small thickness (relative to the size of the cell), but it has also been mathematically validated in [69].*

Electric potential in the quasi-static regime

As the cell membrane is mainly composed of a lipid bilayer, it prevents the passage of ions, and so it behaves like an electric insulator between two conductive media. Therefore charge accumulates on either side of the of the cell membrane. This gives rise to a change in the TMV (it is no longer equal to the resting potential). A standard approach to modeling the membrane in this scenario is to think of it as a leaky capacitor, due to its semipermeable nature. The electric potential inside and outside the cell is given by the solution to the Laplace equation where we consider both the interior and exterior of the cell to be source-free environments (no net charge) [19]. Therefore, given an initial electric potential $U_0 \colon \mathcal{O}_e \cup \mathcal{O}_c \to \mathbb{R}$, the electric potential U is modeled as the solution to the following PDE

$$\nabla \cdot (\sigma \nabla U) = 0, \ \text{ in } \mathcal{O}_e \cup \mathcal{O}_c,\ t \geq 0, \tag{1.3a}$$

$$U(0,\cdot) = U_0(\cdot), \ \text{ in } \mathcal{O}_e \cup \mathcal{O}_c, \tag{1.3b}$$

$$U_{|_{\partial\Omega}}(t,\cdot) = g(t,\cdot), \ \text{ in } \partial\Omega,\ t \geq 0, \tag{1.3c}$$

$$\sigma_c \vec{n}_c \cdot \nabla U_{|_{\Gamma^-}} = \sigma_e \vec{n}_c \cdot \nabla U_{|_{\Gamma^+}},\ t \geq 0, \tag{1.3d}$$

$$\sigma_e \vec{n}_e \cdot \nabla U_{|_{\Gamma^+}}(t,x) = C_m \partial_t [U]_\Gamma(t,x) + I_{\text{ion}}(t,x),\ \forall x \in \Gamma,\ t > 0, \tag{1.3e}$$

where $g \colon \mathbb{R}^+ \times \partial\Omega \to \mathbb{R}$ prescribes an external electric field and C_m is the capacitance of the membrane.

Equation (1.3d) is the condition of conservation of charge for the current density traversing the cell membrane. The membrane electrical model is then expressed in Equation (1.3e), as the current density passing trough the membrane. It is composed of a capacitive current term, represented by $C_m \partial_t [U]_\Gamma$, and an ionic current term, represented by I_{ion}. The ionic current term describes the passive dynamics of the cell membrane, meaning, the ion channels which allow the transport of certain ions through the membrane. It is usually defined as

$$I_{\text{ion}} := S_m([U]_\Gamma - V_{\text{resting}}),$$

where S_m corresponds to the specific membrane conductance, and V_{resting} corresponds to the natural resting potential of the membrane.

Remark 4. *We consider from now on that $V_{resting}$ is identically zero. This choice is made only to simplify notation as this parameter does not play an important role in the mathematical description of electroporation models. That is to say, all the results obtained with this choice of modeling can be easily modified to take into account a non-zero resting potential.*

We highlight the fact that so far, the electroporation phenomenon has not been taken into account in the above model. That is, we consider in the above model that the membrane capacitance and conductance are constant and unchanged by the application of an electric

field. We know that when a strong enough electric field is applied then the permeability and conductance of the membrane drastically increases, and so the above model no longer yields a faithful representation of the electric potential U. We address this point in Section 1.3, where we present some models of electroporation. For now, we also ignore the question of wellposedness of the above system. This question will be addressed in a more general scenario in the next chapter.

1.2.3 Stationary TMV equation

In the above model (1.3), the TMV $[U]_\Gamma$ (as well as the surrounding electric potential) approaches a stationary state in the idealized scenario where the applied electric field E is constant in time and the electric properties of the membrane do not change over time. This involves solving a static version of (1.3), which takes the form of

$$\nabla \cdot (\sigma \nabla U) = 0, \quad \text{in } \mathcal{O}_e \cup \mathcal{O}_c, \tag{1.4a}$$

$$U_{|\partial\Omega}(\cdot) = g(\cdot), \quad \text{in } \partial\Omega, \tag{1.4b}$$

$$\sigma_c \vec{n}_c \cdot \nabla U_{|\Gamma^-} = \sigma_e \vec{n}_c \cdot \nabla U_{|\Gamma^+}, \tag{1.4c}$$

$$\sigma_e \vec{n}_e \cdot \nabla U_{|\Gamma^+}(x) = S_m(x)[U]_\Gamma(x), \ \forall x \in \Gamma. \tag{1.4d}$$

This determines the maximum TMV attained by the cell membrane for a given an external electric field E (prescribed by the Dirichlet boundary condition g on $\partial\Omega$). This is of particular interest as the characteristic time of charge of a membrane is less than 1 [μs] [33], while electric field pulse delivery which cause electroporation usually have pulses of widths in the range of $1 - 100$ [μs] or longer. This tool also helps in determining (at least intuitively) whether or not a particular PEF application should cause electroporation in a cell.

Well-posedness result

A well-posedness result for (1.4) can be obtained from a direct application of a result in [37]. For completeness we add a short but different proof of well-posedness. It will use the following theorem which is derived from the classic Banach-Necas-Babuska theorem, see [23] for a clear presentation of the Banach-Necas-Babuska theorem.

Theorem 5. *Let X and M be two Hilbert spaces, we denote by X' and M' their duals. Let $a\colon X \times X \to \mathbb{R}$, $b\colon X \times M \to \mathbb{R}$ be two continuous bilinear forms, $L \in X'$ and $G \in M'$ and let $Z_b = \{\tau \in X \,|\, b(\tau, q) = 0, \forall q \in M\}$ be the kernel of b. If a is coercive over Z_b (with coercivity constant α) then the following variational problem*

$$\text{find } (\xi, p) \in X \times M \text{ such that, } \begin{cases} a(\xi, \tau) + & b(\tau, p) = L(\tau), \ \forall \tau \in X, \\ & b(\xi, q) = G(q), \ \forall q \in M, \end{cases} \tag{1.5}$$

is well-posed if and only if

$$\exists \beta > 0, \ \inf_{q \in M} \left(\sup_{\tau \in X} \frac{b(\tau, q)}{\|\tau\|_X \|q\|_M} \right) \geq \beta.$$

Furthermore, the unique solution (ξ, p) depends continuously on the problem data as follows

$$\|\xi\|_X \leq \frac{\|L\|_{X'}}{\alpha} + \frac{1}{\beta}\left(1 + \frac{\|a\|}{\alpha}\right)\|G\|_{M'},$$
$$\|p\|_M \leq \left(1 + \frac{\|a\|}{\alpha}\right)\left(\frac{1}{\beta}\|L\|_{X'} + \frac{\|a\|}{\beta^2}\|G\|_{M'}\right).$$

Proof. See Chapter 1 of the Franck Boyer's course notes [9] (in french). □

Remark 6. *The above variational formulation is easily transformed into the usual variational formulation used in the classic Banach-Necas-Babuska theorem by considering the following continuous bilinear form*

$$c\colon (X \times M) \times (X \times M) \to \mathbb{R}$$
$$((\xi, p), (\tau, q)) \mapsto a(\xi, \tau) + b(\tau, p) - b(\xi, q),$$

which translates the problem (1.5) into finding $(\xi, p) \in X \times M$ such that

$$c((\xi, p), (\tau, q)) = L(\tau) - G(q),\ \forall (\tau, q) \in X \times M.$$

To use the above theorem we transform (1.4) into a variational formulation as in (1.5). First, we split (1.4a) by introducing a new unknown ξ and then we replace (1.4) with this new system of equations

$$\sigma^{-1}\xi - \nabla U = 0, \text{ in } \mathcal{O}_e \cup \mathcal{O}_c, \tag{1.6a}$$
$$-\nabla \cdot \xi = 0, \text{ in } \mathcal{O}_e \cup \mathcal{O}_c, \tag{1.6b}$$
$$U_{|\partial\Omega}(\cdot) = g(\cdot), \text{ in } \partial\Omega, \tag{1.6c}$$
$$\vec{n}_c \cdot \xi_{|\Gamma^-} = \vec{n}_c \cdot \xi_{|\Gamma^+}, \text{ in } \Gamma, \tag{1.6d}$$
$$\vec{n}_e \cdot \xi_{|\Gamma^+} = S_m[U]_{|\Gamma}, \text{ in } \Gamma. \tag{1.6e}$$

Next, we translate this into a variational formulation. For this we need a pair of Hilbert spaces X and M as in (1.5).

Let $\gamma_\Gamma^\pm : H_{\text{div}}(\mathcal{O}_c \cup \mathcal{O}_e) \to H^{-1/2}(\Gamma)$ be two continuous trace operators on $H_{\text{div}}(\mathcal{O}_c \cup \mathcal{O}_e)$ given by

$$\gamma_\Gamma^+ \colon \tau \mapsto \vec{n}_e \cdot (\tau_{|\mathcal{O}_e})_{|\Gamma}, \text{ and } \gamma_\Gamma^- \colon \tau \mapsto \vec{n}_c \cdot (\tau_{|\mathcal{O}_c})_{|\Gamma}$$

To take into account the condition (1.6d) we consider the following Hilbert space

$$X := H_{\text{div}}(\mathcal{O}_c \cup \mathcal{O}_e) \cap \left(\gamma_{\text{Tr}}^+\right)^{-1}(L^2(\Gamma)) \cap \left(\gamma_{\text{Tr}}^-\right)^{-1}(L^2(\Gamma)) \cap \text{Ker}(\gamma_{\text{Tr}}^- - \gamma_{\text{Tr}}^+),$$
$$\|\tau\|_X^2 := \|\tau\|_{L^2(\Omega)}^2 + \|\nabla \cdot \tau\|_{L^2(\Omega)}^2.$$

Remark 7. *The operators $\gamma_\Gamma^\pm$ were introduced just to show the construction of X while being extremely obvious in the fact that it is a Hilbert space (closed subspace of the Hilbert space $H_{div}(\mathcal{O}_c \cup \mathcal{O}_e)$ made up of intersections of closed subspaces). When dealing with elements of X we will not make a difference between these two operators and just use the notation of restricting a function to Γ. The small abuse we make is done just to simplify notation.*

If we take $M := L^2(\Omega)$, then we obtain the following result by a direct application of Theorem 5. The following result was not found in the literature, however it has a classic proof.

Corollary 8. *Using the definitions of X and M given above, Equation (1.6) can be written in a variational form as in (1.5), where U plays the role of p and the linear and bilinear forms are*

$$
\begin{aligned}
a\colon (\xi,\tau) &\mapsto \int_\Omega \sigma^{-1}\xi\cdot\tau + \int_\Gamma \frac{(\vec{n}_e\cdot\xi_{|\Gamma})(\vec{n}_e\cdot\tau_{|\Gamma})}{S_m},\ \forall \tau,\xi\in X,\\
b\colon (\tau,q) &\mapsto \int_\Omega (\nabla\cdot\tau)q,\ \forall \tau\in X, q\in M,\\
G\colon q &\mapsto 0,\ \forall q\in M,\\
L\colon \tau &\mapsto \int_{\partial\Omega} g\vec{n}_\Omega\cdot\tau,\ \forall\tau\in M,\ \textit{where } \vec{n}_\Omega\colon \partial\Omega\to\mathbb{R}^3,\ \textit{is the unit outward normal vector at } \partial\Omega.
\end{aligned}
$$

Furthermore, this problem is well-posed.

Proof. First, we detail the calculation which transforms (1.6) into (1.5). We multiply (1.6a) by a test function $\tau\in X$ and then do an integration by parts on the second term:

$$
\begin{aligned}
\int_\Omega \sigma^{-1}\xi\cdot\tau - \int_\Omega \nabla U\cdot\tau &= 0,\\
\int_\Omega \sigma^{-1}\xi\cdot\tau - \int_{\mathcal{O}_e\cup\mathcal{O}_c} \nabla U\cdot\tau &= 0,\\
\int_\Omega \sigma^{-1}\xi\cdot\tau + \int_{\mathcal{O}_e\cup\mathcal{O}_c} U\nabla\cdot\tau - \int_\Gamma \vec{n}_c\cdot\tau_{|\Gamma}U_{|\Gamma^-} - \int_\Gamma \vec{n}_e\cdot\tau_{|\Gamma}U_{|\Gamma^+} &= \int_{\partial\Omega} U_{|\partial\Omega}\vec{n}_\Omega\cdot\tau,\\
\int_\Omega \sigma^{-1}\xi\cdot\tau + \int_\Gamma \vec{n}_e\cdot\tau_{|\Gamma}[U]_{|\Gamma} + \int_\Omega (\nabla\cdot\tau)U &= \int_{\partial\Omega} U_{|\partial\Omega}\vec{n}_\Omega\cdot\tau,\\
\underbrace{\int_\Omega \sigma^{-1}\xi\cdot\tau + \int_\Gamma \vec{n}_e\cdot\tau_{|\Gamma}\frac{\vec{n}_e\cdot\xi_{|\Gamma}}{S_m}}_{a(\xi,\tau)} + \underbrace{\int_\Omega (\nabla\cdot\tau)U}_{b(\tau,U)} &= \underbrace{\int_{\partial\Omega} U_{|\partial\Omega}\vec{n}_\Omega\cdot\tau}_{L(\tau)}.
\end{aligned}
$$

The second equation in (1.5) is then recovered by multiplying (1.6b) by a test function $q\in M$. Now, to prove well-posedness we only need to prove the inf-sup condition from Theorem 5.

We prove that there exists a $\beta>0$ such that for all $q\in M$, there exists $\tau\in X$ for which $b(\tau,q)/\left\|\tau\right\|_X \geq \beta\left\|q\right\|_M$.

Let $q\in M := L^2(\Omega)$ we construct an element $\tau\in X$ as follows. Let $\phi_c\in H^2(\mathcal{O}_c)$ be the solution to the following problem

$$
\begin{aligned}
-\triangle\phi_c &= q,\ \text{in } \mathcal{O}_c\\
\phi_c &= 0,\ \text{in } \Gamma,
\end{aligned}
$$

let $\phi_e \in H^2(\mathcal{O}_e)$ be the solution of the following problem

$$\begin{aligned} -\triangle\phi_e &= q, \text{ in } \mathcal{O}_e \\ \vec{n}_e \cdot \nabla\phi_e &= -\vec{n}_c \cdot \nabla\phi_c, \text{ in } \Gamma, \\ \phi_e &= 0, \text{ in } \partial\Omega, \end{aligned}$$

and finally let $\tau := -\mathbb{1}_{\mathcal{O}_c}\nabla\phi_c - \mathbb{1}_{\mathcal{O}_e}\nabla\phi_e$. By construction, $\tau \in X$ and

$$b(\tau, q) = \int_\Omega (\nabla \cdot \tau)q = \int_\Omega q^2.$$

Furthermore,

$$\|\tau\|_X^2 = \|\nabla\phi_c\|_{L^2(\mathcal{O}_c)}^2 + \|\nabla\phi_e\|_{L^2(\mathcal{O}_e)}^2 + \|q\|_{L^2(\Omega)}^2 .$$

Using the Poincaré inequality we obtain the last inequality in the following calculation

$$\|\nabla\phi_c\|_{L^2(\mathcal{O}_c)}^2 = -\int_{\mathcal{O}_c} \triangle\phi_c\phi_c = \int_{\mathcal{O}_c} q\phi_c \le \|q\|_{L^2(\mathcal{O}_c)} \|\phi_c\|_{L^2(\mathcal{O}_c)} \le C_c \|q\|_{L^2(\mathcal{O}_c)} \|\nabla\phi_c\|_{L^2(\mathcal{O}_c)} ,$$

where the constant C_c depends on the domain $\mathcal{O}_c$. We thus obtain $\|\nabla\phi_c\|_{L^2(\mathcal{O}_c)} \le C_c \|q\|_{L^2(\mathcal{O}_c)}$. Similarly,

$$\begin{aligned} \|\nabla\phi_e\|_{L^2(\mathcal{O}_e)}^2 &= \int_{\mathcal{O}_e} -\triangle\phi_e\phi_e + \int_\Gamma \vec{n}_e \cdot \nabla\phi_e\phi_e \\ &= \int_{\mathcal{O}_e} q\phi_e + \int_\Gamma \vec{n}_e \cdot \nabla\phi_e\phi_e \\ &\le C_e \|q\|_{L^2(\mathcal{O}_e)} \|\nabla\phi_e\|_{L^2(\mathcal{O}_e)} + \int_\Gamma \phi_e\vec{n}_e \cdot \nabla\phi_e \\ &\le C_e \|q\|_{L^2(\mathcal{O}_e)} \|\nabla\phi_e\|_{L^2(\mathcal{O}_e)} + \|\vec{n}_e \cdot \nabla\phi_c\|_{H^{-1/2}(\Gamma)} \|\phi_e\|_{H^{1/2}(\Gamma)} \\ &\le C_e \|q\|_{L^2(\mathcal{O}_e)} \|\nabla\phi_e\|_{L^2(\mathcal{O}_e)} + C_e' \|\phi_c\|_{H^1(\mathcal{O}_c)} \|\phi_e\|_{H^1(\mathcal{O}_e)} \\ &\le C_e \|q\|_{L^2(\mathcal{O}_e)} \|\nabla\phi_e\|_{L^2(\mathcal{O}_e)} + C_e'' \|\nabla\phi_c\|_{L^2(\mathcal{O}_c)} \|\nabla\phi_e\|_{L^2(\mathcal{O}_e)} \\ &\le C_e''' \|q\|_{L^2(\Omega)} \|\nabla\phi_e\|_{L^2(\mathcal{O}_e)} , \end{aligned}$$

where C_e''' is a constant which depends only on the domains $\mathcal{O}_e$ and $\mathcal{O}_c$. As a result of the above calculations we obtain the following bound

$$\|\tau\|_X \le \sqrt{1 + C_c^2 + C_e'''^2}\, \|q\|_{L^2(\Omega)}$$

and so taking $\beta := 1/\sqrt{1 + C_c^2 + C_e'''^2}$ we have the desired result:

$$\frac{b(\tau, q)}{\|\tau\|_X} \ge \beta \|q\|_{L^2(\Omega)}$$

□

Remark 9. *This proves that* $PH^1(\Omega) = \{u \in L^2(\Omega) \colon u_{|\mathcal{O}_e} \in H^1(\mathcal{O}_e),\, u_{|\mathcal{O}_c} \in H^1(\mathcal{O}_c)\}$ *armed with the norm* $\|u\| = \int_{\mathcal{O}_e \cup \mathcal{O}_c} |u|^2 + \int_{\mathcal{O}_c} |\nabla u|^2 + \int_{\mathcal{O}_e} |\nabla u|^2 + \int_\Gamma [u]^2$ *is a Banach space.*

Schwan's equation

An important example of a solution to the stationary problem above, is the case of a spherical cell with constant conductance $S_m \ll 1$ (meaning S_m is a constant which we will make tend to zero) and under the influence of a constant (in space and time) electric field. It shows the maximum TMV that can be reached given an electric field magnitude. Let $R_0 > 0$ denote the radius of the cell, so that

$$\mathcal{O}_c = B_{R_0} := \{x \in \mathbb{R}^3 \mid \|x\| = \sqrt{x_1^2 + x_2^2 + x_3^2} < R_0\}$$

and let $R_{\text{ext}} \gg 1$ denote the radius of the entire system, $\Omega = B_{R_{\text{ext}}}$. Given an electric field $\vec{E} = |E|\vec{e}_z$, a boundary condition which results in this field is given in spherical coordinates by $g(\theta, \varphi) = -|E|R_{\text{ext}}\cos(\theta)$, where $\varphi \in [0, \pi]$ and $\theta \in [0, 2\pi]$ denotes the angle of between a point in $\partial B_{R_{\text{ext}}} = \mathbb{S}^2_{R_{\text{ext}}}$ and $\vec{e}_z$ (see Figure 1.7). An explicit solution to (1.4) can be obtained by the method of separation of variables.

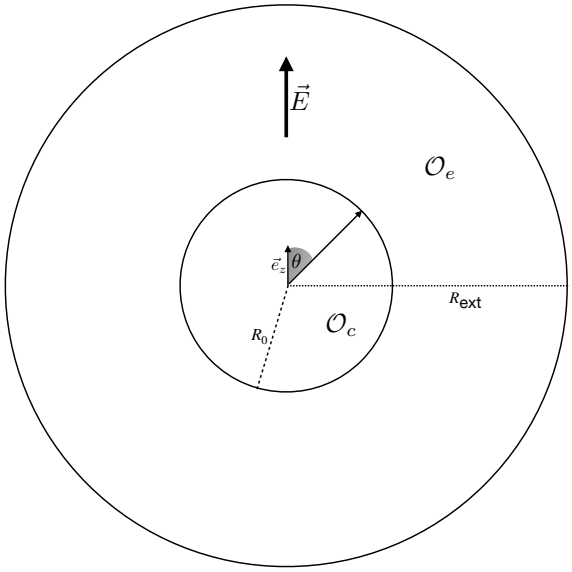

Figure 1.7: Spherical cell under the influence of a constant (in space and time) electric field $\vec{E}$.

This type of calculation will be further detailed in the next chapter, so in this part we

will only present the resulting formula, known as steady state Schwan's equation [87]

$$
\begin{aligned}
[U]_\Gamma(\theta) &= \frac{\frac{\sigma_c\sigma_e}{R_0^2}(R_{\text{ext}}/R_0)^2\frac{3}{(R_{\text{ext}}/R_0)^3-1}}{\left(\frac{\sigma_c}{R_0}+\frac{\sigma_e}{R_0}\frac{1+2(R_{\text{ext}}/R_0)^3}{(R_{\text{ext}}/R_0)^3-1}\right)S_m+\left(\frac{\sigma_e\sigma_c}{R_0^2}\frac{1+2(R_{\text{ext}}/R_0)^3}{(R_{\text{ext}}/R_0)^3-1}\right)}R_{\text{ext}}|E|\cos(\theta),\\
&\xrightarrow[R_{\text{ext}}\to\infty]{} \frac{3\frac{\sigma_e\sigma_c}{R_0}|E|\cos(\theta)}{\frac{\sigma_c+2\sigma_e}{R_0}S_m+\frac{2\sigma_e\sigma_c}{R_0^2}},\\
&\xrightarrow[S_m\to 0]{} \frac{3}{2}R_0|E|\cos(\theta),\\
[U]_\Gamma^{\text{Schwan}}(\theta) &= \frac{3}{2}R_0|E|\cos(\theta),\ \text{(steady state Schwan's equation)}.
\end{aligned}
$$

This result is what is most often cited in the literature (both experimental and theoretical, [87, 24, 19]) as it provides a simple relation between the electric field magnitude $|E|$ and the resulting TMV in a round cell. For now this ends the presentation of the electric behavior of the cell membrane. We continue with the mathematical modeling of single cell electroporation and present the current state of the art.

1.3 Modeling electroporation of the membrane

Before the presentation of the most classical mathematical models of electroporation we first present some of the aspects of this phenomenon which motivate the theories that have been developed.

1.3.1 Experimental observations

In the presence of an electric field, the TMV of a cell increases (in absolute value) due to charge accumulating at each wall of the cell membrane. When the TMV is large enough then the following changes have been observed [81] (non-exhaustive list):

1. The membrane permeability is affected. There is now entry and exit of molecules that would not normally be able to pass through the cell membrane.

2. Membrane electrical conductivity dramatically increases. This is also referred to as dielectric breakdown. In particular, there is an increased exchange of ions between the cell and its environment.

3. The TMV drops to near zero. This is linked with the increased membrane electrical conductivity.

4. Some of the lipids in the lipid bilayer are oxidized, changing the composition of the membrane.

5. Phosphatidylserine (PS) inside the cell is externalized. This is known as PS translocation.

6. ATP and potassium ions (K^+) exit the cell and calcium ions (Ca^+) enter it.

7. The osmotic balance of a cell is disrupted.

8. If the electric field is not too strong then the cell may repair its membrane (meaning it becomes semipermeable once again) and continue on living. Otherwise, the cell may be greatly affected by the above changes or it may suffer too much physical damage and, as a result, die. These two scenarios are known as reversible and irreversible electroporation respectively.

It is important to note that even though the above changes are related, they are distinct phenomena, happening at different time scales and depending on different factors. For instance, the increased permeability allowing transit of molecules across the membrane is an effect that has been detected up to milliseconds after the delivery of a strong electric pulse on a cell (for example, see [89]). In contrast, the increased conductivity of the membrane, allowing the exchange of ions of the cell with its exterior medium, happens within a few microseconds of the start of an electroporating electric pulse.

In practice, the way experiments are setup to observe these types of behaviors, is that one (or a few) pulsed electric field is delivered to a bath of suspended cells. After this, the evolution of the system of cells is studied, for example, via imaging data, and then conclusions follow. Experimentally, the main difficulty tends to be measuring a particular effect of electroporation on a cell. This is usually done in indirect ways as it is difficult to see the cell membrane up close with the necessary resolution to clearly study effects on the cell membrane that happen on the time scales of microseconds, see [33], for a more detailed account of experimental advances in this field.

Remark 10. *Contrary to the rest of the points in the above list, the last point is often difficult to quantify or model properly as it depends on the bath surrounding the cell (relating sucrose and ions uptake, for example), not only the membrane state. As a result, the representation of cell death is usually not addressed in most electroporation models. This is due to it being a biological phenomenon, and the actual mechanisms which determine cell death not always include physical damage of the cell membrane (membrane rupture). For example, cell apoptosis (programmed cell death) can be an indirect consequence of electroporation.*

We highlight that in practice the state of the membrane is difficult to measure experimentally. As a result, in most models, the electroporated state of the membrane (of increased permeability to most molecules) is tacitly equated with its high conductivity state. However, it is important to note that in reality membrane permeability and conductivity are two different concepts. Membrane conductivity is an intrinsic property of the membrane to allow the passage of current. Membrane permeability is a property of the membrane with respect to a specific molecule.

1.3.2 Transient aqueous pore theory

So far the most used physically based theory explaining the sudden increase in membrane permeability as a result of electric field influence is the creation of transient aqueous pores

inside the membrane. Through these pores, the exchange between the cell and its environment takes place. A detailed presentation of this theory (and other less successful ones) can be found in [91]. In the next section we present a quick summary of this theory and a couple of models which are based on it.

Types of pores

This first model of electroporation explaining the dielectric breakdown of the cell membrane by means of the creation of membrane defects was proposed by Chizmadzhev *et al.* [1, 67]. The idea is to explain the dielectric breakdown of the membrane by the creation of defects which are assumed to be circular pores that do not interact with each other (as such, they are described only by their radius). The dynamics of a pore of radius r are then driven by the energy associated to the creation of such a pore in the membrane. The most common model of this energy functional (see [64, 91]) requires the distinction between two different types of pores: hydrophilic pores (conducting pores) and hydrophobic pores (non conducting pores).

- Hydrophilic pores are assumed to be round (of toroidal shape) with the lipid heads of the lipid bilayer covering the outer surface of the membrane (see Figure 1.8). Of course, their hydrophilic nature will then affect the conductivity of the membrane.

  The energy associated to such a pore is given by

  $$E_1(r) := 2\pi\gamma r - \pi\sigma r^2 + \left(\frac{C_1}{r}\right)^4, \; r > 0,$$

  where γ is the linear tension of a pore (also known as pore edge-energy per unit of length) and σ is the surface tension of the membrane (or energy per unit of surface). The third term, represents the steric repulsion resulting from the packing of the lipid heads lining the defect (the value of C_1 used in [64] is 9.67×10^{-15} [$\mathrm{J}^{1/4}$.m]). Another way to think about it is that considering a constant linear tension γ is too simplistic to capture the mechanical constraints on the membrane when creating a pore. In other words, as the radius of a hydrophilic pore goes to zero, the increased membrane distortion leads to an increased mechanical strain of the membrane also known as the steric hindrance of the lipids making up the cell membrane (or steric repulsion).

- On the other hand, hydrophobic pores are assumed to be cylindrical in shape (see Figure 1.8). Their non conducting nature is a result of the their shape and the fact that lipid tails in the cell membrane are hydrophobic. The energy associated to the creation of these hydrophobic pores is given by [30]

  $$\tilde{E}_0(r) = 2\pi h \varkappa r \frac{I_1(r/r^*)}{I_0(r/r^*)},$$

  where $h = 5$ [nm] is the membrane thickness, $\varkappa = 0.05$ [$\mathrm{N.m}^{-1}$] is the interface tension between the hydrophobic lipid tails and the water, r^* represents the characteristic

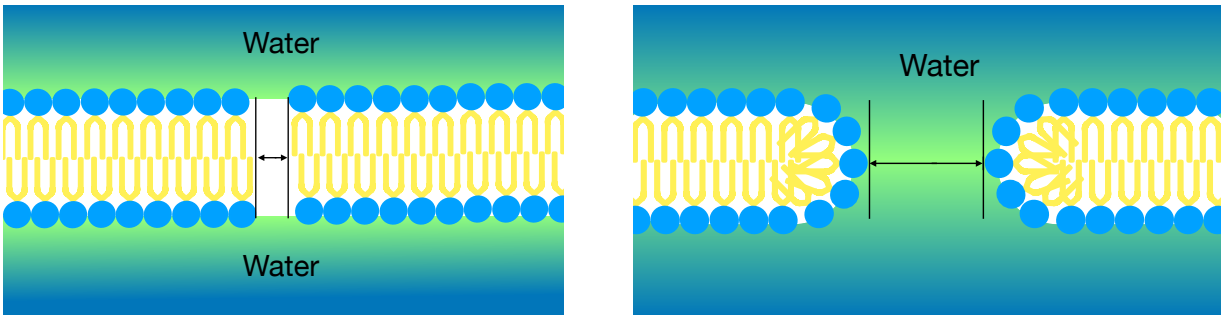

(a) Hydrophobic pore.

(b) Hydrophilic pore.

Figure 1.8: Simple representation of the two types of pores in a lipid bilayer.

	Value	Description
h	5×10^{-9} [m]	membrane thickness
E_*	45 [kT]	maximum energy associated to a hydrophobic pore
r_*	0.5 [nm]	maximal radius associated to a hydrophobic pore
σ	10^{-3} [J.m^{-2}]	energy of an intact membrane (its surface tension)
γ	1.8×10^{-11} [J.m^{-1}]	edge energy of a pore
C_1	9.67×10^{-15} [J$^{1/4}$.m]	Constant coefficient in hydrophobic energy pore.
ϵ_w	80	dielectric coefficient of water
ϵ_l	2	dielectric coefficient of lipid
ϵ_0	8.85×10^{-12} [F.m^{-1}]	permittivity of the vacuum

Table 1.1: Parameters used in the energy functional associated to a lipid bilayer. These values have been taken from [64].

length of these pores (it is usually around 0.5 [nm]) and I_0 and I_1 are modified Bessel functions (of order 0 and 1 respectively). For the sake of simplicity, instead of the above formula, we use the following quadratic function which appropriately approximates the hydrophobic free energy of a pore [64]

$$E_0(r) := E_*(r/r_*)^2,\ r \geq 0,$$

where r_* is the characteristic radius of at which a hydrophilic pore becomes more energetically favorable than its current hydrophobic configuration. E_* is the energy associated to a hydrophobic pore of such a radius. These values can be found in Table 1.1.

The energy of any pore of a radius $r \geq 0$ is then defined by

$$\mathcal{E}(r) := \min(E_0(r), E_1(r)).$$

As a result, the distinction of between hydrophobic and hydrophilic pores comes down to the size of the radius after which hydrophilic pores are more energetically favorable than hydrophobic ones. A graphical representation of this can be seen in Figure 1.9.

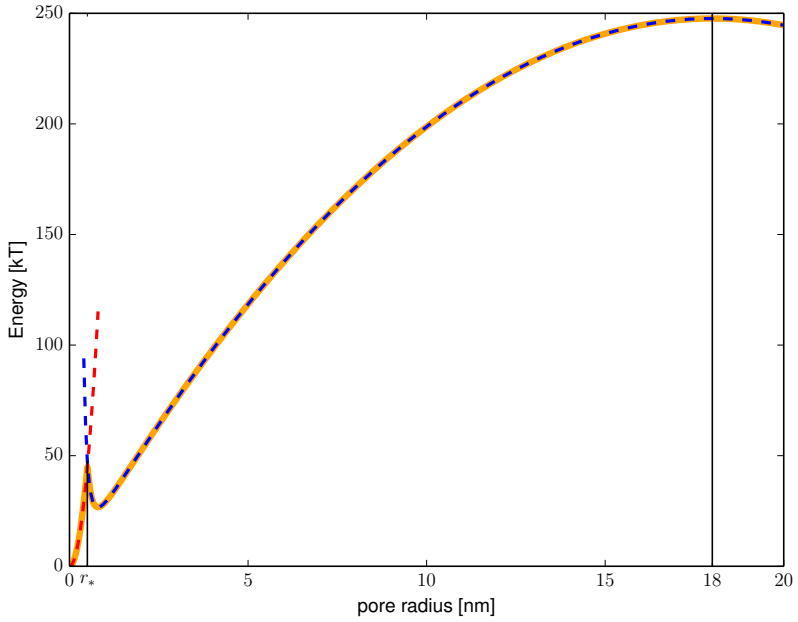

Figure 1.9: The hydrophobic pore energy $r \mapsto E_0(r)$ is in red, hydrophilic pore energy $r \mapsto E_1(r)$ is in blue and the minimum of both energies $r \mapsto \mathcal{E}(r)$ is in orange. The point at which the hydrophilic configuration becomes more energetically favorable is $r_* = 0.5$ [nm]. This energy functional is the same as the one presented in [64]. The parameters associated to this plot can be found in Table 1.1.

When a pore radius r is big enough, the quadratic term (due to surface tension) is more relevant than the other two terms in E_1. We can see that past a certain size it is more energetically favorable for a pore to keep growing, than to reseal (negative slope of the energy functional at this point). This usually is interpreted as the breakdown of a lipid bilayer by means of rupture. It is one of the reasons that can lead to irreversible electroporation in living cells and membrane rupture in artificial lipid bilayers.

Remark 11. *The modeling of the electrical breakdown of a membrane due to membrane rupture has been naturally inspired by the modeling of soap films and their rupture. This is based on the assumption that a membrane pore grows like a pore in a soap film. For example, see [95, 42].*

Electric field influence on the membrane

In the presence of transmembrane potential $v : \Gamma \to \mathbb{R}$, its influence on the lipid bilayer is taken into account by adding an additional term to each of the energy functionals E_0 and E_1:

$$E_0(r, v) = E_*(r/r_*)^2 - \frac{1}{2}\left(\frac{(\epsilon_w - \epsilon_l)\epsilon_0}{h}\right)\pi r^2 v^2, \quad \forall r \geq 0, \forall x \in \Gamma,$$

$$E_1(r, v) = 2\pi\gamma r - \pi\sigma r^2 + \left(\frac{C_1}{r}\right)^4 - \frac{1}{2}\left(\frac{(\epsilon_w - \epsilon_l)\epsilon_0}{h}\right)\pi r^2 v^2, \quad \forall r \geq 0, \forall x \in \Gamma,$$

where ϵ_0 is the electrical permittivity of the vacuum, and ϵ_w and ϵ_l are the dielectric constants of water and of the membrane respectively. This additional term can be interpreted as the electrical energy of a capacitor with a permittivity equal to the change in permittivity between the two media, see [1]. Another interpretation, which comes from [33], is that this additional term corresponds to the Born energy of the membrane, which is the energy associated to moving a unit of charge from a medium of high permittivity and to one with low permittivity. In the case of an intact membrane, the Born energy would be equal to this additional term and so the energy needed to create a pore is equated to this Born energy.

Remark 12. *The energy needed to create a pore under the influence of an electric field (by means of the resulting transmembrane voltage) is thus given by*

$$\mathcal{E}(r, v) = \min(E_0(r, v), E_1(r, v)), \tag{1.7}$$

see Figure 1.10 for a visual representation of this energy functional.

Pore conductivity

As hydrophobic pores allow water enter into the membrane, they affect its conductivity. The conductivity of a pore denoted by S_p, is given by (see [30, 18]) the following formula

$$S_p \colon \mathbb{R} \to \mathbb{R}_*^+ \tag{1.8a}$$

$$v \mapsto \frac{\frac{1}{2}\pi h\sigma_w\left(e^{\frac{ve_c}{kT}} - 1\right)}{e^{\frac{ve_c}{kT}}\frac{\left(w_0 e^{w_0 - l_p\frac{ve_c}{kT}} - l_p\frac{ve_c}{kT}\right)}{w_0 - l_p\frac{ve_c}{kT}} - \frac{w_0 e^{w_0 + l_p\frac{ve_c}{kT}} + l_p\frac{ve_c}{kT}}{w_0 + l_p\frac{ve_c}{kT}}} \tag{1.8b}$$

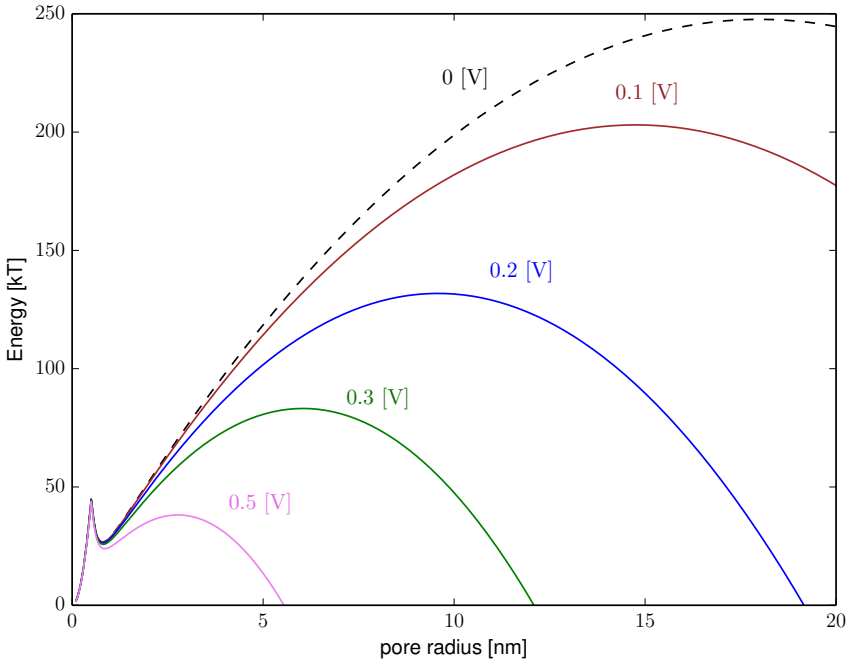

Figure 1.10: Energy needed to create a pore in a lipid bilayer under the influence of different transmembrane voltages.

	Value	Description
l_p	0.15	relative entrance length of pores
σ_w	1.30 [S.m^{-1}]	conductivity of aqueous solution in pores
w_0	2.65	nondimensionalized energy barrier within a pore

Table 1.2: Values used in the modeling of the pore conductivity. They were taken from [18, 19]

where l_p is the relative entrance length of a pore, w_0 is the energy barrier inside a pore and e_c is the electric charge of an electron. Typical values of the constants in the above expression found in the literature are in Table 1.2.

This expression is derived from the Nernst-Planck equation presented in Section 1.2.1. In fact, (1.8) is obtained from the integration of the Nernst-Planck equation describing the movement of ions in an orthogonal direction across the membrane. This calculation is done in [5].

1.3.3 PCA-model

In this section we present the first model involving transient aqueous pores in the membrane presented by Pastushenko, Chizmadzhev and Arakelyan in [67]. The main idea consists in describing the state of the cell membrane by means of a pore density distribution

	Value	Description
D	5×10^{-14} [$\mathrm{m}^2.\mathrm{s}^{-1}$]	diffusion coefficient
ν_c	2×10^{38} [$\mathrm{s}^{-1}.\mathrm{m}^{-3}$]	attempt rate density
ν_d	10^{11} [s^{-1}]	fluctuation rate per lipid molecule

Table 1.3: Parameters used in the definition of the PCA-model. Values taken from [64].

$n : \mathbb{R}^+ \times \mathbb{R}^+ \times \Gamma \to \mathbb{R}$ such that

$$N_{r_0}(t,x) := \int_{r_0}^{+\infty} n(r,t,x)dr$$

is the number of pores (per unit area of the membrane) of radius bigger than $r_0 \geq 0$, at time t and at position x in Γ. If there is a transmembrane voltage $v\colon \Gamma \to \mathbb{R}$ acting on the cell membrane, the evolution of the distribution $(r,t) \mapsto n(r,t)$ is given by a Fokker-Planck equation [91] with an additional source term [64] representing the creation and destruction of pores.

$$\partial_t n - D\partial_r\left(\frac{1}{kT}n\partial_r\mathcal{E} + \partial_r n\right) = \nu_c\frac{h}{kT}e^{-E_0/(kT)}\partial_r E_0 - \nu_d n H(r_* - r),\ \forall r \geq 0, \forall x \in \Gamma, \quad (1.9a)$$

$$n(t=0,\cdot) = n_0, \quad (1.9b)$$

$$n(\cdot, r=0) = 0, \quad (1.9c)$$

where D is an abstract diffusion constant for pores in pore-radius space (in units [$\mathrm{m}^2.\mathrm{s}^{-1}$]), k is the Boltzmann constant, T is the temperature of the system, ν_c is the attempt rate density [92] (units in [$\mathrm{s}^{-1}.\mathrm{m}^{-3}$]), ν_d is the fluctuation rate per lipid molecule (units in [s^{-1}]), h is the membrane thickness, H is the Heaviside's function, and lastly n_0 is the initial state of the cell membrane.

Remark 13. *Equation (1.9) is also known as the Smoluchowski equation. Strictly speaking, this only consists of half of the model, as we still need the coupling with the model determining the TMV. We present a way of coupling both problems (which also applies to this model) in the next section where we present the KN-model. There is more than one way to do this, for instance see [80] where they show a different way than the one we present here.*

1.3.4 KN-model

We now present a second model based on the same transient aqueous pore theory. It is the most commonly used model of single cell electroporation and it was first introduced by Krassowska *et al.* in [18, 64].

The approach taken by Neu and Krassowska consists of making an asymptotic analysis of (1.9) in order to reduce it to the study of an ordinary differential equation which determines

	Value	Description
α	10^9 m^2.s^{-1}	pore creation rate coefficient
q	2.56	coefficient linked to pore creation
N_{m}	1.5×10^9 m^{-2}	equilibrium pore density at zero TMV
V_{ep}	0.258 V	characteristic voltage of electroporation

Table 1.4: Parameters used in the KN-model. These values were taken from [65].

the evolution of the total density of (hydrophilic) pores at each point of the cell membrane

$$N(t,x) := \int_{r_*}^{+\infty} n(r,t,x)dr, \quad t \geq 0,\ x \in \Gamma,$$

where r_* is the minimal radius a hydrophilic pore can have, see Figure 1.9.

Given an initial state of the cell membrane, given by $N_0 : \Gamma \to \mathbb{R}^+$, and an initial potential electric potential $U_0 : \mathcal{O}_e \cup \mathcal{O}_c \to \mathbb{R}$, the complete single cell electroporation model is given by the couple $(t,x) \in \mathbb{R}^+ \times \Gamma \mapsto (N(t,x), [U]_\Gamma(t,x))$ which is determined from the solution to the following system of coupled partial differential equations

$$\begin{cases} \nabla \cdot (\sigma \nabla U) = 0, \ \text{ in } \mathcal{O}_e \cup \mathcal{O}_c,\ t \geq 0, \\ U(0,\cdot) = U_0, \ \text{ in } \mathcal{O}_e \cup \mathcal{O}_c, \\ U_{|\partial\Omega}(t,\cdot) = g(t,\cdot), \ \text{ in } \partial\Omega,\ t \geq 0, \\ \sigma_c \vec{n}_c \cdot \nabla U_{|\Gamma^-} = \sigma_e \vec{n}_c \cdot \nabla U_{|\Gamma^+},\ t \geq 0, \\ \sigma_e \vec{n}_e \cdot \nabla U_{|\Gamma^+}(t,x) = C_m \partial_t [U]_\Gamma(t,x) + S_m [U]_\Gamma(t,x) + I_{\mathrm{ep}}(N, [U]_\Gamma),\ \forall x \in \Gamma,\ t > 0. \end{cases} \tag{1.10a}$$

$$\begin{cases} \dot{N} = \alpha e^{([U]_\Gamma / V_{\mathrm{ep}})^2} \left(1 - \frac{N}{N_m e^{q([U]_\Gamma / V_{\mathrm{ep}})^2}}\right), \quad t > 0,\ x \in \Gamma, \\ N(0,\cdot) = N_m, \ \text{ in } \Gamma, \end{cases} \tag{1.10b}$$

where α, q, V_{ep} and N_m are constants whose values and interpretation can be found in Table 1.4. There is an additional term I_{ep} in the description of the current density crossing then membrane. It represents the component of the current density due to electroporation I_{ep}, meaning the current traversing pores induced by electroporation. It is given by the following expression [18]

$$I_{\mathrm{ep}}(N, [U]_\Gamma) := S_p([U]_\Gamma) \cdot N(t,x) \cdot [U]_\Gamma.$$

where $S_p : \mathbb{R} \to \mathbb{R}_*^+$ is the conductivity of a pore as a function of the TMV from (1.8).

Remark 14. *One of the reasons for the success of this model is that simulating the ODE on N is computationally less expensive compared to the PDE it was derived from. As it turns out, in the original transient aqueous pore model, the disparate scales in time and space naturally occurring in the model make it difficult to obtain numerical solutions. This aspect,*

is not particular to this model, but the use of an ordinary differential equation helps manage this problem. In fact, it is a key feature of this phenomenon in general. For example, PEF treatments typically last less than 100 $[\mu s]$*, yet membrane permeability can easily last several seconds (and even minutes) after the PEF treatment is over.*

As this model is derived from the original model proposed by Chizmadzhev *el al.*, it inherits from that model. For example, just like before, all pores are assumed to behave as a singular toroidal default in a sea of lipids, as a result they are independent from each other. In other words, interaction between pores is non-existent in this model.

Additionally, the long life of pores is driven by the shape of the energy valley in the pore energy functional (1.7) (see Figure 1.10). Qualitatively, the model predicts the following chain of events. First, the PEF treatment increases the cell's TMV. Then, the number of pores in the cell membrane increases as a result. This discharges the membrane TMV (near the regions of the membrane where pores were created), and so the pore sealing mechanism enters into play. Pores (hydrophilic) decrease in size down to a certain radius, where they remain as further sealing would be more energetically costly due to steric repulsion. This is the energy valley which can be seen in the energy functional in Figures 1.9 and 1.10. Eventually, because of thermal fluctuations, these pores trapped in said configuration manage to completely reseal (this means they turn into hydrophobic pores and then close up).

Since the introduction of this model, other models have been developed, partly to take into account aspects of electroporation that are not captured by this model, and partly to further understand or to verify the validity of this model.

1.3.5 LP-model (phenomenological) to account for lipid oxidation

Even though the KN-model describes quite well the initiation of the electroporation in a cell, it fails to describe the influence of pulse repetition rate and the medium conductivity influence as observed by Mir's group *et al.* [75]. Poignard's group proposed a phenomenological model, called here LP-model, to account for the lipid oxidation, pore creationdue to high electric field and the change in lipid configuration [46, 37]. The main feature of the LP model consists in reducing the number of parameters of the KN-model and adding a reaction-diffusion equation to describe the lipid oxidation due to the strong electric field.

In this model, the state of the membrane is described via two functions

$$X_1, X_2 : \mathbb{R}^+ \times \ \Gamma \ \rightarrow \ [0,1],$$

which describe the degrees of porosity and permeability (to some particular test molecule) of the cell membrane, respectively. These two membrane parameters will follow different models. The membrane porosity follows, what is known and as a sliding door model, and which naturally mimics the expected behavior of pores in a membrane being created and re-sealing. The membrane permeability follows a reaction-diffusion partial differential equation which models the alteration (oxidation) of phospholipids in the membrane and their lateral diffusion inside it.

Let $\beta_1, \beta_2 : \mathbb{R} \to [0,1]$ be two smooth sigmoid functions (their explicit formula is not necessary to present the model, but they can be found in [46]). The LP-model takes the following form

$$\begin{cases} \triangle U = 0, \text{ in } \mathcal{O}_e \cup \mathcal{O}_c, t \geq 0, \\ U(0,\cdot) = U_0(\cdot), \text{ in } \mathcal{O}_e \cup \mathcal{O}_c, \\ U_{|\partial\Omega}(t,\cdot) = g(t,\cdot), \text{ in } \partial\Omega, \\ \sigma_c \vec{n}_c \cdot \nabla U_{|\Gamma^-} = \sigma_e \vec{n}_c \cdot \nabla U_{|\Gamma^+}, \text{ in } \Gamma, t \geq 0, \\ \sigma_e \vec{n}_e \cdot \nabla U_{|\Gamma^+} = C_m \partial_t [U]_\Gamma + S_m [U]_\Gamma + (X_1 S_1 + X_2 S_2)[U]_\Gamma, \text{ in } \Gamma, t > 0, \end{cases} \tag{1.11a}$$

$$\partial_t X_1 = \frac{\beta_1([U]_\Gamma) - X_1}{\tau_1}, \text{ in } \Gamma, \tag{1.11b}$$

$$\partial_t X_2 - d_m \triangle_\Gamma X_2 = (\beta_2(X_1) - X_2)\left(\frac{1}{\tau_{2,\text{perm}}} + \mathbb{1}_{\{\beta_2(X_1) \geq X_2\}}\left(\frac{1}{\tau_{2,\text{rec}}} - \frac{1}{\tau_{2,\text{perm}}}\right)\right), \text{ in } \Gamma, \tag{1.11c}$$

$$X_1(0,\cdot) = 0, \quad X_2(0,\cdot) = 0, \tag{1.11d}$$

where $\triangle_\Gamma$ denotes the Laplace-Beltrami operator on Γ, d_m is the lateral diffusion coefficient of the lipids inside the membrane, S_1 and S_2 are the conductivites associated to a porated and permeable membrane respectively, τ_1 is the characteristic time of the poration process, $\tau_{2,\text{perm}}$ is the characteristic time of the permeabilization of the membrane, and $\tau_{2,\text{rec}}$ is the characteristic recovery time of the membrane.

Remark 15. *This model explicitly differentiates between membrane conductivity and permeability. This distinction, in addition to the incorporation of membrane diffusion, helps explain a phenomenon reported in [75, 4, 45] where PEF treatment has a higher efficiency at lower frequency of pulse repetition. We denote this phenomenon as pulse accumulation.*

1.3.6 Molecular dynamics

Further confirmation for the aqueous pore theory has been shown by means of molecular dynamics simulations. These are sophisticated numerical simulations which model a lipid bilayer and its surrounding environment by considering all the molecules making up the system. Due to the huge computational cost of this approach, only small patches of a lipid bilayer can be simulated, and for a short amount of time. The usual characteristic length of the simulation box is on the order of 10 [nm] and the length of time simulated tends to be smaller than 100 [ns]. Under these constrained conditions, Tarek, Vernier, Tieleman and others (for example, see [88, 11, 83, 81]) have shown that it is possible to create aqueous pores in the membrane with a strong enough electric field influence. They have also shown the active transport of molecules across the membrane through an aqueous pore (such as the electrotransfer of siRNA for nano-second PEF treatment [11]).

For the most part this approach is particularly useful as it presents an extremely rich representation of the membrane and manages to show pore creation naturally appearing from

simulations. Most other models, rely on unconfirmed, "cookie-cutter" notions (description taken from [91], in regards to the first energy model proposed for the aqueous pore theory), which are difficult validate (even though they may be intuitive to the point of being easily convincing).

1.4 Extensions and Limitations

1.4.1 Extensions

The above list of models is not exhaustive, however it faithfully represents the most important ideas that other approaches use to model the electroporation phenomenon. For example, Miklavcic and Towhidi (see [57]), proposed a model where pore creation is described as a four-stage process. Each stage is modeled by a density (like in the KN-model), all of which form a system of ordinary differential equations which is coupled to the usual Laplace equation which describe the TMV. Another example comes from [41, 49], where they construct a model based on the KN-model above. In it, the evolution of the radii of pores created by electroporation is taken into account, however their evolution is described by a system of ordinary differential equations as opposed to using the Smoluchowski partial differential equation (as in the PCA-model).

Instead of making a detailed account of all the existing models and their variations, we limited ourselves to just the three models presented above. However, for the interested reader, many other recent models can be found in [72].

1.4.2 Limitations

So far, among all the proposed models, there is no clear universally accepted model of electroporation. In fact, among the three approaches to modeling electroporation presented here (PCA-model, KN-model, LP-model and molecular dynamics), all have different problems or limitations, some of which we list below.

PCA-model:

- The interaction between pores is neglected as pores are only characterised by their radii and are independent to one another.
- The notion of hydrophobic pore is difficult to validate from an experimental point of view. It is not clear if this is a pertinent notion when modeling electroporation.

KN-model:

- It requires many parameters, some of which are difficult to measure (for example, N_0 and r_*). Even the expression of S_{p} depends on parameters which are known only up to order of magnitude.

- It contains parameters with no clear physical interpretation, like q and α, which have to be fitted to experimental data.
- The dynamics of creation of pores involves the characteristic TMV of electroporation V_{ep} ($V_{\text{ep}} \sim 0.256$ [V] in the literature [64, 65]). This is an artifact, result of the asymptotic analysis done to the Smoluchowski equation and it does not have a solid physical basis. The characteristic TMV of electroporation should ideally be expressed as a function of the intrinsic physical properties of the membrane. It should not itself be part of the model describing the membrane.
- It is based on the original model proposed by Chizmadzhev *et al.* and therefore inherits from its limitations.
- Some experimentally observed behaviors, like pulse accumulation, are not captured by this model.
- The mechanism by which it explains the long time scale of the duration of high membrane permeability is in contradiction with what we actually see in molecular dynamics simulations [94, 11]. Basically, the KN-model predicts that after the membrane TMV discharges there is rapid (hydrophilic) pore resealing until a certain radius at which pores remain open due to the energy rearrangement cost to go back to a hydrophobic pore configuration. This cost is eventually paid due to thermal fluctuations, thus giving the long duration to the electroporated state of the membrane. However, molecular dynamic simulations do not seem to replicate this behavior. In fact, (hydrophilic) pores tend to close up within nano-seconds of membrane discharge.

LP-model:

- It is phenomenological in nature and therefore it cannot be predictive. In other words, an important number of parameters of this model have to be fitted to each experiment.
- Even though this model does fit experimental data (at least qualitatively), it lacks some physical basis.

Molecular dynamics simulations:

- The results coming from these simulations are rich and detailed, however, this approach is not scalable to bigger patches of lipid bilayers.
- The constraints due to the small size of the simulation box result in unrealistic physical scenarios. In fact, a consequence of this can be seen in the strength of the electric field needed to create pores (it differs from experimental data by two to three orders of magnitude). The results from these numerical experiments are therefore mostly qualitative.

- Regardless of the points above, experimentation with this model requires considerable computationally resources which are not easily available and which require some sophisticated engineering to use.

This concludes the presentation of the current state of the art in electroporation modeling. All of the above limitations motivated the need for another model. We present this new model in the next chapter.

Chapter 2

Phase-field model of bilipid membrane electroporation

This chapter is an excerpt from our article [36] (Sections 1 to 5).

2.1 Introduction

Electroporation is a microscopic phenomenon that consists in imposing high and short electric pulses to biological cells in order to weaken the structure of the plasma membrane. Biologically active molecules that otherwise cannot diffuse through the membrane (e.g. hydrophilic compounds such as bleomycin or DNA) may then spread through the cell membrane. If the pulses are short enough the process is reversible: the membrane is not destroyed and reseals within minutes. The cell therefore can internalise external active molecules without losing its viability. The interest for the phenomenon has increased constantly until recently with the emergence of therapeutic strategies based on it, in oncology and also in cardiology.

Even though the phenomenon has been discovered in the late 60's, the ways the membranes become permeable by the effect of an intense electric field is still not well understood. In the late 90's, the teams of Chizmadzhev and Weaver [16, 91] proposed a description of the emergence of water pores in a sea of lipids, under very constraint geometries (the pores are cylindrical). Then Krassowska and Neu proposed a Smoluchowski equation for the population of cylindrical pores $n(r,t)$ of radius $r > 0$ at the time t, and they derived an asymptotic analysis to link the transmembrane potential to the total density of pores $N(t) = \int_{\mathbb{R}^+} n(r,t)dr$, which satisfies an ordinary differential equation [64, 18]. From these times, only slight modifications of the models have been proposed by Weaver [93, 79]. Kavian *et al.* proposed then a phenomenological version of the Krassowska and Debruin model, by limiting the number of parameter [37]. Leguèbe *et al.* proposed in [46] an extension by introducing the surface reaction-diffusion of oxidised lipids. This last model seems closer to the observations but it is phenomenological and lacks of any physical basis.

The aim of this paper is to propose a new model of membrane electroporation that

combines membrane water content (initially 0 for non porated membrane) and transmembrane voltage. Our approach enables to make a link between the physics-based membrane free-energy approaches of Chizmadzhev and Weaver and the reaction diffusion model of the phenomenological model of Leguèbe *et al.* In particular, our model, which consists in Allen-Cahn equation for the water content of the membrane, and a nonlocal differential equation on the transmembrane voltage (TMV) is a generalisation of the previous approaches in the context of phase ordering kinetics.

More precisely, given the free-energy $\mathcal{E}$ of the membrane as a functional depending on the water content of the membrane ϕ and the transmembrane voltage v, our model of membrane electropermeabilisation is a system of time evolution non local equation on the membrane Γ:

$$\begin{cases} \partial_t \phi = -\alpha \frac{\partial \mathcal{E}}{\partial \phi} \quad \forall x \in \Gamma, \forall t > 0, \\ \\ C_m(\phi)\partial_t v + (S_m(\phi) + \Lambda)v = G, \quad \forall x \in \Gamma, \forall t > 0, \\ \\ v|_{t=0} = v_\diamond, \quad \phi|_{t=0} = \phi_\diamond, \text{on } \Gamma, \end{cases} \tag{2.1}$$

where $\frac{\partial \mathcal{E}}{\partial \phi}$ is the Fréchet derivative of the functional $\mathcal{E}$ with respect to ϕ, Λ a pseudodifferential elliptic operator of order 1, which is a combination of Dirichlet to Neumann maps and C_m and S_m the capacitance and conductance of the membrane. This full model is presented in details in Section 2.3 but before that, we will start in Section 2.2 to present the choice of the free-energy $\mathcal{E}$ as a function of ϕ and v. In particular we somehow generalise the approach of Chizmadzhev and Weaver, getting rid of the geometrical cylindrical assumption. We then study the phase ordering Allen-Cahn model for the evolution of water content in the membrane. Section 2.3 focuses on the electric part of the model, that is the non local equation on the TMV.

We perform a fine analysis of the involved Dirichlet-to-Neumann nonlocal operators in two simple configurations (a spherical membrane and a flat periodic membrane) that enables us to compare the time constants of the phenomenon in spherical and flat membranes. These two simple geometrical configurations are of high importance because on the one hand, the shapes of cell in suspension and lipid vesicles in suspension are close to a sphere, while in some experiments flat film of lipid is used to investigate electroporation [22]. In addition most of the dynamic simulations on electroporation are performed in a flat geometrical setting [85, 88, 11, 84]. Section 2.4 is devoted to the linear stability analysis of the coupled problem. In Section 2.5, we present the choice of the parameters. Interestingly, we are able to make a link between our approach and the approach of Chizmadzhev and Weaver in terms of free-energy of the membrane. We also present the models of the membrane capacitance and conductance. The concluding section presents the perspectives of this research.

2.2 A mathematical model of membrane electropermeabilization

2.2.1 Free-energy of membrane subjected to a voltage

The membrane is considered as a combination of two mutually exclusive phases (lipid membrane and water filled pores) and its state is described through the continuous phase order parameter $x \in \Gamma \mapsto \phi(x) \in [0,1]$, see Cahn [13, 10]. This order parameter is somehow related to the volume fraction of water that enters the membrane thanks to electroporation. The state $\phi = 0$ represents the ideal pure lipid phase and $\phi = 1$ the ideal pure water phase. The free-energy $\mathcal{E}$ of the membrane subjected to a transmembrane voltage v is the functional energy, the so-called Gibbs energy, given in [39]

$$\mathcal{E}(\phi, v) = \frac{\kappa}{2}\int_\Gamma |\nabla\phi|^2\, ds + \int_\Gamma \mathcal{W}_m(\phi)\, ds - \frac{1}{2}\int_\Gamma C_m(\phi)v^2\, ds, \tag{2.2}$$

where $\kappa > 0$ is linked with the interfacial tension [28] and $\mathcal{W}_m$ is the double-well potential energy that describes the stable states of the membrane. The term $|\nabla\phi|^2$ regularises ϕ and helps control the thickness of the water-lipid interface, as explained by Bray [10].

From the physical view point, the gradient term in (2.2) describes the fact the interfaces water-lipid cost energy, and then two neighbouring pores will tend to merge to minimize the energy. This term enables thus to describe the interactions between neighbouring pores, which was not described by Weaver and Chizmadzhev approach. The term $\frac{1}{2}C_m(\phi)v^2$ is the electrostatic energy. It is worth noting that Weaver and Chizmadzhev considered the same electrostatic energy, which affects the potential energy to favor the phase $\phi = 1$ as described by Figure 2.1. Weaver and Chizmadzhev proposed to use a linear capacitance $C_m(\phi) = C_l(1-\phi) + C_w\phi$, $C_{l,w}$ being the capacitance of pure lipid and water phases respectively [1, 16, 91]. However the linear stability analysis provided in Section 2.4 shows that linear capacitance prevents the emergence of instabilities, as observed in a different context by Fraggedakis *et al.* in [28]. In this paper we choose to use the mixture model of Looyenga [52]

$$C_m : \quad \phi \mapsto \frac{\epsilon_0}{h}\left(\left[\epsilon_l^{1/3} + \phi(\epsilon_w^{1/3} - \epsilon_l^{1/3})\right]^3 \vartheta_1(\phi) + \epsilon_w\vartheta_2(\phi)\right), \tag{2.3}$$

where

$$\vartheta_i(\phi) = \frac{1 + \tanh(k_i(\phi - \phi_i^{\text{th}}))}{2}, \qquad i = 1, 2,$$

are smooth cutoff functions. In the following, we set $k_1 = -15$, $k_2 = 13$ and $\phi_1^{\text{th}} = \phi_2^{\text{th}} = 1$.

As the water volume fraction is not conserved (defects can be created and disappear from the membrane), we consider the non-conserved dynamics associated to this energy functional (also called model-A by Bray [10]). The evolution of ϕ is determined by the L^2–gradient flow associated with the energy functional above. It corresponds to the Euler-Lagrange equation for the energy $\phi \mapsto \mathcal{E}(\phi, v)$. In other words, for a given kinetics coefficient $\alpha > 0$ – also called

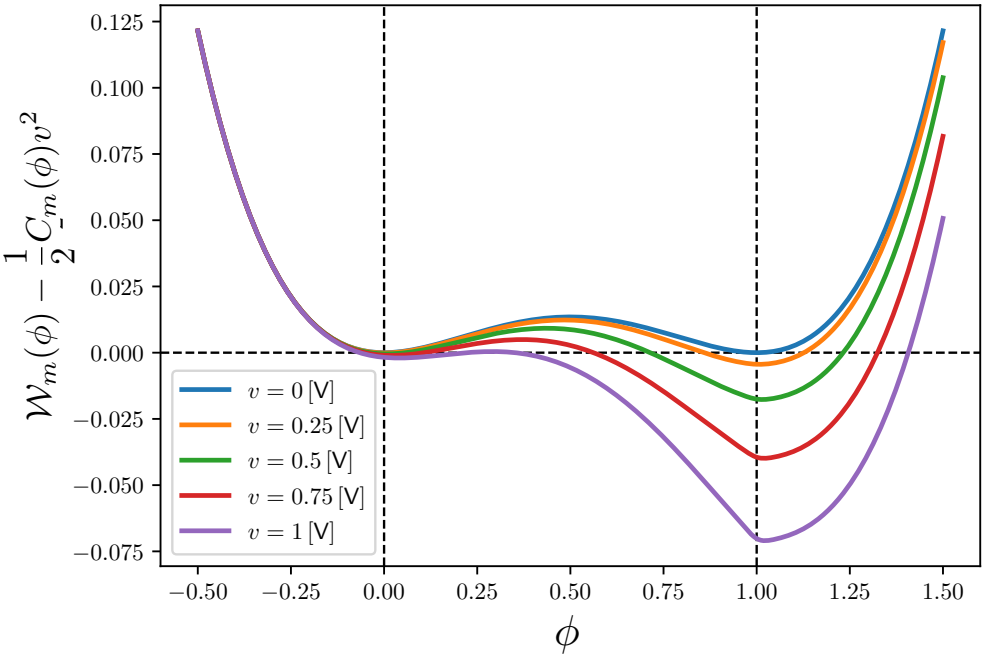

Figure 2.1: Influence of a given constant transmembrane voltage (TMV) v on the potential energy $\mathcal{W}_m(\phi) - C_m(\phi)v^2/2$. One can see that the TMV tends to tilt the double-well potential to favor the phase $\phi = 1$, favoring thus the entry of water in the membrane. The parameters are given in Tables 2.1 and 2.2.

phase field mobility – the order parameter ϕ satisfies the following Allen-Cahn equation on the membrane surface Γ [3, 10, 13]:

$$\partial_t \phi - D_0 \Delta_\Gamma \phi = -\alpha \frac{\partial \mathcal{W}_m}{\partial \phi}(\phi) + \frac{\alpha}{2} \frac{\partial C_m}{\partial \phi}(\phi) v^2, \quad \forall t > 0,$$
$$\phi(0, \cdot) = \phi^0(\cdot),$$

where $D_0 := \alpha\kappa$ is the lateral diffusion coefficient of lipids in $[\mathrm{m}^2.\mathrm{s}^{-1}]$, and α is in $[\mathrm{m}^2.\mathrm{J}^{-1}.\mathrm{s}^{-1}]$.

2.2.2 On the choice of the double well potential $\mathcal{W}_m$

The simplest double well potential[1] considered in Bray's book is $\phi \to \phi^2(1-\phi)^2$, for which the pure phases $\phi = 0$ and $\phi = 1$ are global minima and the mixed phase $\phi = 1/2$ is the local maximum [10]. The energy barrier to pass from the phase $\phi = 0$ to the phase $\phi = 1$ is then defined as the height $\mathcal{W}_m(1/2) - \mathcal{W}_m(0)$. Even though the qualitative behavior is included in this simple form of potential, it is necessary to introduce a parametrisable double well potential to make the link with the free-energy introduced by Weaver and Chizmadzhev [16, 91].

Throughout the paper, the double-well potential $\mathcal{W}_m$ is set as :

$$\mathcal{W}_m(\phi) := a_1 \phi^2 (1-\phi)^2 + a_2 (\phi + \frac{1}{2})(\phi - 1)^2, \quad \forall \phi \in [0,1], \tag{2.5}$$

where $a_1 > \frac{3}{2}|a_2|$, so that $\mathcal{W}_m$ satisfies

$$\mathcal{W}_m(0) = \frac{a_2}{2}, \quad \mathcal{W}_m(1) = 0, \quad \mathcal{W}_m'(1) = \mathcal{W}_m'(0) = 0, \quad \mathcal{W}_m''(0) > 0, \quad \text{and} \quad \mathcal{W}_m''(1) > 0.$$

The above energy potential describes the fact that the pure lipid ($\phi = 0$) and pure water ($\phi = 1$) phases are the only two stable phases. The energy barrier to pass from lipid to water equals $\mathcal{W}_m(1/2) - a_2/2$. Note that unlike the symmetrical potential of Bray's book, the energy barrier to pass from the pure water phase to the pure lipid phase equals $\mathcal{W}_m(1/2)$. Thus it requires more energy to pass from the pure water to the pure lipid phase than the opposite. Section 2.5 is dedicated to a fine analysis of the energy to choose the parameters a_1 and a_2 in adequation with Weaver and Chizmadzhev's work.

It is however important to keep in mind that a_2 mainly controls the value of the first local minimum ($\mathcal{W}_m(0) = a_2/2$) and a_1 the size of the local maximum (at $\phi_0 := 1/2 - 3a_2/(4a_1)$) which is the height of the energy barrier to pass from 0 to 1.

The following lemma states the well-posedness of the phase-field model of the membrane submitted to a given transmembrane voltage.

Lemma 16. *Let $s \geq 3$, $T > 0$, $C_m \in \mathcal{C}^{s+2}(\mathbb{R})$, $v \in \mathcal{C}([0,T[, H^s(\Gamma))$ and $\phi_\diamond \in H^s(\Gamma)$. Then there exists a unique mild solution $\phi \in \mathcal{C}([0,T], H^s(\Gamma))$ to*

$$\partial_t \phi - D_0 \Delta_\Gamma \phi = -4\alpha a_1 \phi(\phi - 1)(\phi - 1/2 + \frac{3a_2}{4a_1}) + \frac{\alpha}{2} C_m'(\phi) v^2, \ \textit{in }]0, +\infty[\times \Gamma, \tag{2.6a}$$
$$\phi|_{t=0} = \phi_\diamond, \quad \textit{on } \Gamma. \tag{2.6b}$$

[1] It is the polynomial with the lowest degree that describes the phase separation phenomenon.

Even though the result of the above lemma is quite standard, we give the proof to make the paper self-contained.

Proof. We use the semi-group theory combined with Picard fixed-point argument to prove this result. Let $S(t)$ be the contractive semigroup in $H^s(\Gamma)$ generated by the operator $f \mapsto D_0 \Delta_\Gamma f$, then we can rewrite our problem in its mild formulation as

$$\phi(t) = S(t)\phi_\diamond + \int_0^t S(t-\tau)F(\tau,\phi)\,d\tau$$

where

$$\begin{aligned} F(\tau,\phi) &:= F_1(\phi) + F_2(\tau,\phi), \\ F_1(\phi) &:= -4\alpha a_1 \phi(\phi-1)(\phi - \frac{1}{2} + \frac{3a_2}{4a_1}), \\ F_2(\tau,\phi) &:= \frac{\alpha}{2} C_m'(\phi) v^2. \end{aligned}$$

We know that $\phi \mapsto F(\tau,\phi)$ is a Lipschitz function (uniformly on $[0,T]$) on bounded sets of $H^s(\Gamma)$. In fact, $H^s(\Gamma)$ is an algebra given that $s \geq 3$ and $\dim(\Gamma) = 2$ and so F_1 is Lipschitz on bounded sets (it is a polynomial). A similar argument shows that $\phi \mapsto \frac{\alpha}{2} C_m'(\phi) v^2$ is Lipschitz if $\phi \mapsto C_m'(\phi)$ is Lipschitz on bounded sets of $H^s(\Gamma)$, which occurs thanks to the regularity of C_m.
Let $\mathcal{E} := \mathcal{C}^0\big([0,T], H^s(\Gamma)\big)$ provided with the following norm

$$\|u\|_{\mathcal{E}} := \sup_{\tau\in[0,T]} e^{-\beta\tau} \|u(\tau)\|_{H^s(\Gamma)}, \text{ where } \beta > 0,$$

and consider the following function

$$\begin{aligned} \Psi : \mathcal{E} &\to \mathcal{E} \\ \phi &\mapsto S(t)\phi_\diamond + \int_0^t S(t-\tau)F(\tau,\phi)d\tau. \end{aligned}$$

Let C be a generic constant which takes other constants into account then for $\phi_1, \phi_2 \in B(0,R) \subset \mathcal{E}$,

$$\begin{aligned} \|\Psi(\phi_1) - \Psi(\phi_2)\|_{H^s(\Gamma)} &\leq \int_0^t \|F(\tau,\phi_1) - F(\tau,\phi_2)\|_{H^s(\Gamma)}\,d\tau, \\ &\leq C\int_0^t e^{\beta\tau} e^{-\beta\tau} \|\phi_1 - \phi_2\|_{H^s(\Gamma)}\,d\tau, \\ &\leq C\frac{1}{\beta} e^{\beta t} \|\phi_1 - \phi_2\|_{\mathcal{E}}, \end{aligned}$$

and so

$$\|\Psi(\phi_1) - \Psi(\phi_2)\|_{\mathcal{E}} \leq \frac{C}{\beta} \|\phi_1 - \phi_2\|_{\mathcal{E}},$$

where the constant C depends on v, $\mathcal{O}_e$ and $\mathcal{O}_c$. By taking β large enough, Ψ is a contractive map and we can conclude the proof. □

2.2.3 Qualitative properties of the membrane order parameter at null TMV

This section is devoted to the membrane order parameter at null TMV. The aim is twofold. On the one hand, we exhibit the qualitative properties of our model in a general geometric setting, thanks to the results of Farina *et al.* [26]. On the other hand, we apply the results of Alfaro *et al.* [2] and the references therein for the case of a **flat torus** – $\Gamma = (\mathbb{R}/\mathbb{Z})^2$ – to obtain the orders of magnitude of the model parameters – a_1, a_2 and α, with D_0 being fixed to the lateral diffusion of the lipids.

In this section we summarize the existing mathematical results on the solution to Problem (2.6) (with $v \equiv 0$). There is an extensive literature studying the qualitative mathematical properties of (2.6). One can cite, for example [3, 25, 2]. All the following results are related to the following equation

$$\partial_t \phi - D_0 \Delta_\Gamma \phi = -4\alpha a_1 \phi(\phi - 1)(\phi - 1/2 + \frac{3a_2}{4a_1}), \text{ in }]0, +\infty[\times\Gamma, \tag{2.7a}$$

$$\phi|_{t=0} = \phi_\diamond, \quad \text{on } \Gamma. \tag{2.7b}$$

General qualitative properties of the order parameter ϕ

Property 17. *If the initial state of the membrane $\phi_\diamond$ is smooth enough ($\mathcal{C}^2(\Gamma)$ for example) and verifies $0 \leq \phi_\diamond(s) \leq 1$ for almost any $s \in \Gamma$ then, the solution ϕ to (2.7) satisfies the same bounds*

$$0 \leq \phi \leq 1, \qquad a.e \text{ on } (0, +\infty) \times \Gamma.$$

The next property is due to Farina *et al.*, see [26]. To reference it, we first need to introduce the following notion of stability.

Definition 18. *We say that a stationary solution ϕ to (2.7) is stable if*

$$\int_\Gamma \left(\kappa |\nabla \xi|^2 + \mathcal{W}_m''(\phi)\xi^2 \right) dx \geq 0$$

for every smooth function $\xi \in \mathcal{C}^\infty(\Gamma)$. This quadratic form is called the second variation of the energy functional (2.2) (with $v \equiv 0$) .

Property 19. *Let Γ be a smooth closed compact manifold (with nonnegative Ricci curvature), then the only stable solutions of (2.7) are constant.*

Remark 20. *This means that for the considered potential $\mathcal{W}_m$, any porated membrane will either reseal to a non porated state ($\phi \equiv 0$) or disappear ($\phi \equiv 1$).*

Asymptotic behavior of the order parameter in the case of a flat membrane

Assume in this paragraph that $\Gamma = (\mathbb{R}/\mathbb{Z})^2$. The following property is due to Theorem 1.3 due to Alfaro *et al.* [2]. Before stating the result, we first introduce some notations.

Notation 21. *Let $(a_n)_{n\in\mathbb{N}}, (b_n)_{n\in\mathbb{N}} \in \mathbb{R}$ be 2 sequences of $\mathbb{R}$.*

- *We write*

$$a_n \lesssim b_n$$

if there is a constant $C > 0$ such that for all $n \geq 0$, we have $a_n \leq C b_n$.

- *Similarly, we write*

$$a_n \ll b_n$$

if there is a sequence $\varepsilon_n \to_{n\to+\infty} 0$ such that $a_n \leq \varepsilon_n b_n$.

Property 22. *Assume that $\Gamma = (\mathbb{R}/\mathbb{Z})^2$. Let $L > 0$ denote the characteristic length scale of Γ and let $(D_{0,n})_{n\in\mathbb{N}}$, $(a_{1,n})_{n\in\mathbb{N}}$, $(a_{2,n})_{n\in\mathbb{N}}$ be three sequences strictly positive sequences. Let ϕ_n be the solution to the rescaled (in time) equation (2.7)*

$$\partial_\tau \phi_n - \Delta_\Gamma \phi_n = \frac{-4a_{1,n}\alpha L^2}{D_{0,n}} \phi_n(\phi_n - 1)\left(\phi_n - \frac{1}{2} + \frac{3a_{2,n}}{4a_{1,n}}\right), \tag{2.8}$$

$$\phi_n(t = 0, \cdot) = \phi_\diamond, \tag{2.9}$$

where $\tau := \frac{L^2}{D_{0,n}}$ is the rescaling time.

Assume that $(D_{0,n})_{n\in\mathbb{N}}$, $(a_{1,n})_{n\in\mathbb{N}}$ and $(a_{2,n})_{n\in\mathbb{N}}$ satisfy the following asymptotic behaviour

$$\frac{3a_{2,n}}{4a_{1,n}} \lesssim \sqrt{\frac{D_{0,n}}{4a_{1,n}\alpha L^2}} \ll 1.$$

1. *Given any smooth initial condition $\phi_\diamond \in [0, 1]$, the typical profile of a solution to (2.8) involves different regions where $\phi_n \simeq 1$ and $\phi_n \simeq 0$ and transition interfaces between them of size*

$$\delta_n \lesssim \sqrt{\frac{D_{0,n}}{4a_{1,n}\alpha}} \quad [m]. \tag{2.10}$$

   The time needed for the solution associated to ϕ_0 to take above description is

$$\mathcal{T}_n \lesssim \frac{1}{4a_{1,n}\alpha} \left|\log\left(\frac{D_{0,n}}{4a_{1,n}\alpha L^2}\right)\right| \quad [s]. \tag{2.11}$$

2. *The evolution of the transition interfaces can be described by the evolution of the level set $\{x \in \Gamma \mid \phi(x) = 1/2\}$. In the asymptotic regime described above, the motion of this interface is primarily determined by mean-curvature flow [25, 2].*

Remark 23. *In this work, we will use Inequality (2.10) to determine the parameters of our model. We are convinced that this is a reasonable approximation since the pores sizes are very small compared to the size of the cell (the cell radius is around $10 - 50$ $[\mu m]$ and the pore radii smaller than 50 $[nm]$). It is therefore natural to consider the membrane as a flat surface when studying the development of a single pore.*

Some remarks on the non flat case

The rigorous mathematical derivation of the above results for the non flat case is out of the scope of the present work. However, we want to present the main ideas that need to be developed in order to adapt the proof of Alfaro *et al.* [2]. Let Γ be a smooth compact manifold of dimension 2 without boundary embeddded in $\mathbb{R}^3$. We consider the Allen-Cahn equation as written in Alfaro *et al.*

$$\partial_t u^\varepsilon - \Delta_\Gamma u^\varepsilon = \frac{1}{\varepsilon^2} f(u^\varepsilon) := -\frac{1}{\varepsilon^2} u^\varepsilon (u^\varepsilon - 1/2)(u^\varepsilon - 1), \tag{2.12a}$$

$$u^\varepsilon|_{t=0} = u_0. \tag{2.12b}$$

1. The problem without diffusion is obviously the same as in the flat case and thus the sub- and super solutions $w_\varepsilon^\pm$ of Problem (2.12) in $\Gamma\times]0, 4\varepsilon^2|\ln(\varepsilon)|[$ –since here $\mu = f'(1/2) = 1/4$– are given by

$$w_\varepsilon^\pm(x,t) = Y\left(t/\varepsilon^2; u_0(x) \pm \varepsilon^2 C_6\left(e^{t/(4\varepsilon^2)} - 1\right)\right),$$

where Y is the solution to the ODE with parameter ξ given in Eq. (3.5) of [2]:

$$\begin{cases} \partial_\tau Y(\tau,\xi) = f(Y(\tau,\xi)), & \tau > 0, \\ Y(\tau = 0, \xi) = \xi. \end{cases}$$

Then one infers

$$(\partial_t - \Delta_\Gamma) w_\varepsilon^\pm - \frac{1}{\varepsilon^2} f(w_\varepsilon^+) = \frac{1}{\varepsilon^2}(\partial_\tau Y - f(Y)) + \partial_\xi Y \left(\frac{C_6}{4} e^{t/(4\varepsilon^2)} - \Delta_\Gamma u_0 - \frac{\partial_\xi^2 Y}{\partial_\xi Y} |\nabla_\Gamma u_0|\right) \partial_\xi Y.$$

One just has to modify the constant C_0 defined in Eq. (1.8) of [2] into

$$C_0 := \|u_0\|_{C^0(\Gamma)} + \|\nabla_\Gamma u_0\|_{C^0(\Gamma)} + \|\Delta_\Gamma u_0\|_{C^0(\Gamma)},$$

to show that w_ε^+ is a supersolution, similarly to the proof of Lemma 3.8 of [2]. Therefore the time of generation of the interface is of order $\varepsilon^2|\ln(\varepsilon)|$ as in the flat case. This means that Inequality (2.11) of the above Property 22 should also hold in this more general setting.

2. In order to get formally the equation of the motion of the interface, we can proceed similarly as in de Mottoni and Schatzmann [61], by replacing the Euclidean distance Λ^0 of Eq. (1.11) of [61] by the distance dist_g associated to the metric tensor g as defined in [44]. Concretely, let $M_t := \{x \in \Gamma | u^\varepsilon(x,t) = 1/2\}$, $\Gamma_t^+ := \{x \in \Gamma | u^\varepsilon(x,t) > 1/2\}$, and $\Gamma_t^- := \{x \in \Gamma | u^\varepsilon(x,t) < 1/2\}$, then the signed distance to M_t is given by

$$d_g(x,t) = \begin{cases} \mathrm{dist}_g(x, M_t),\ x \in \Gamma_t^+ \\ -\mathrm{dist}_g(x, M_t),\ x \in \Gamma_t^-. \end{cases}$$

Performing formally the same asymptotic expansion as in [61], we get the following equation of the motion of the interface M_t

$$\partial_t d_g - \Delta_\Gamma d_g = 0, \tag{2.13a}$$
$$|\nabla_\Gamma d_g| = 1, \tag{2.13b}$$
$$d_g|_{t=0} = \mathrm{dist}_g(x, M_0). \tag{2.13c}$$

It is worth noting that unlike the flat case, the motion is no longer driven by the mean curvature. This means that the second point of Property 22 should change in this more general setting.

3. Since we are considering only a compact smooth manifold Γ, the estimate of the thickness of the interface remains of size $O(\varepsilon)$. Indeed, first note that the profiles U_0 and U_1 given by Eqs. (2.5) and (2.15) of [2] are exactly the same. Then the solution u_ε is approximated in the vicinity of the interface M_0 by

$$u_\varepsilon = U_0(d_g(x,t)/\varepsilon^2) + \varepsilon U_1(d_g(x,t)/\varepsilon^2) + \cdots$$

One can then define the function $H^\pm$ given in page 543 of [2] similarly, by modifying the Euclidean distance $d_0(x)$ into $\mathrm{dist}_g(x, M_0)$ and the proof of Theorem 1.3 given at page 543 of [2] should follow similarly. This means that Inequality (2.10) of the above Property 22 should also hold in this more general setting.

In the next section, we present the equation satisfied by the transmembrane potential.

2.3 Transmembrane voltage in a membrane

2.3.1 Electric field around membranes

Throughout the paper, Γ is a closed 2D-surface without boundary. We denote by Ω the bounded domain of $\mathbb{R}^3$ in which Γ is embedded, and let $\mathcal{O}_e$ and $\mathcal{O}_c$ be the 2 connected components subsets of Ω and separated by Γ. Let σ_e (resp. σ_c) be the constant conductivities of $\mathcal{O}_e$ (resp. $\mathcal{O}_c$), and let $C_m : \phi \to C_m(\phi)$, $S_m : \phi \to S_m(\phi)$ be the surface capacitance and conductance of Γ, strictly positive bounded smooth functions of the order parameter ϕ.

Let $v_\diamond$ be a regular enough function of Γ. We assume that it belongs at least to $H^1(\Gamma)$. The electric potential U around the membrane Γ verifies the following partial differential equation (PDE)

$$[U]_\Gamma(t = 0, \cdot) = v_\diamond(\cdot), \quad \text{on} \quad \Gamma, \tag{2.14a}$$

and for any time $t > 0$:

$$\begin{cases} \nabla \cdot (\sigma_e \nabla U) = 0, \quad \text{in} \quad \mathcal{O}_e, \\ \nabla \cdot (\sigma_c \nabla U) = 0, \quad \text{in} \quad \mathcal{O}_c, \\ U(t,\cdot) = g(t,\cdot), \text{ on } \partial\Omega, \\ \sigma_c \vec{n}_c \cdot \nabla U_{|_{\Gamma^-}} + \sigma_e \vec{n}_e \cdot \nabla U_{|_{\Gamma^+}} = 0, \text{ on } \Gamma, \\ \sigma_e \vec{n}_e \cdot \nabla U_{|_{\Gamma^+}} = C_m(\phi)\partial_t [U]_\Gamma + S_m(\phi)[U]_\Gamma, \quad \text{in} \quad \Gamma, \end{cases} \tag{2.14b}$$

where $[U]_\Gamma = U_{|_{\Gamma^-}} - U_{|_{\Gamma^+}}$ and $U_{|_{\Gamma^\pm}} : x \mapsto \lim_{\tau \to 0^+} U(x \mp \tau \vec{n}(x))$ and $\vec{n}(x) := \vec{n}_c(x)$ denotes the unitary normal vector to Γ directed towards $\mathcal{O}_c$ at any point $x \in \Gamma$, while $\vec{n}_e(x) = -\vec{n}_c(x)$ is the normal vector to Γ directed towards $\mathcal{O}_e$.

Remark 24. *It is worth noting that only the initial value of the transmembrane voltage $[U]_\Gamma(t = 0, \cdot)$ is required and not the value of the initial potential everywhere in the domain. This is due to the fact that in the domains $\mathcal{O}_e$ and $\mathcal{O}_c$, we have neglected the displacement currents and only the conductive currents are considered, leading to an elliptic equation in the inner and outer domains.*

Interestingly, the above volume PDE can be rewritten in terms of Dirichlet-to-Neumann operators. Denote by Λ_c, Λ_e and Λ_o the three following Dirichlet-to-Neumann operators

$$\Lambda_c : \begin{array}{c} H^{1/2}(\Gamma) \to H^{-1/2}(\Gamma) \\ f \mapsto \vec{n_c} \cdot (\sigma_c \nabla v_c)_{|_{\Gamma^-}} \end{array} \text{,where } v_c \text{ is the solution to } \begin{cases} \nabla \cdot (\sigma_c \nabla v_c) = 0, \text{ in } \mathcal{O}_c, \\ v_{c|_\Gamma} = f, \end{cases} \tag{2.15a}$$

$$\Lambda_e : \begin{array}{c} H^{1/2}(\Gamma) \to H^{-1/2}(\Gamma) \\ f \mapsto \vec{n_e} \cdot (\sigma_e \nabla v_e)_{|_{\Gamma^+}} \end{array} \text{, where } v_e \text{ is the solution to } \begin{cases} \nabla \cdot (\sigma_e \nabla v_e) = 0, \text{ in } \mathcal{O}_e, \\ v_{e|_\Gamma} = f, \\ v_{e|_{\partial\mathcal{O}_e \setminus \Gamma}} = 0, \end{cases} \tag{2.15b}$$

$$\Lambda_o : \begin{array}{c} H^{1/2}(\partial\Omega) \to H^{-1/2}(\Gamma) \\ g \mapsto \vec{n_e} \cdot (\sigma_e \nabla v)_{|_{\Gamma^+}} \end{array} \text{, where } v_b \text{ is the solution to } \begin{cases} \nabla \cdot (\sigma_e \nabla v_b) = 0, \text{ in } \mathcal{O}_e, \\ v_{|_\Gamma} = 0, \\ v_{|_{\partial\Omega}} = g. \end{cases} \tag{2.15c}$$

Following [37], it is equivalent to solve the volume equation (2.14) for U or the following nonlocal equation on the surface Γ for the transmembrane voltage (TMV), $v = [U]_\Gamma$,

$$C_m(\phi)\partial_t v + (S_m(\phi) + \Lambda)v = G, \tag{2.16a}$$

$$v(t = 0, \cdot) = v_\diamond(\cdot), \tag{2.16b}$$

where

$$\Lambda = \Lambda_c(\Lambda_e + \Lambda_c)^{-1}\Lambda_e \tag{2.16c}$$

$$G = \Lambda_c(\Lambda_e + \Lambda_c)^{-1}\Lambda_o g. \tag{2.16d}$$

Remark 25 (Invertibilty of $\Lambda_e + \Lambda_c$)**.** *The fact that the operator $\Lambda_e + \Lambda_c$ is invertible is proven in Kavian et al. (see Lemma 8 of [37]). Its comes from the fact that Λ_e is invertible that Λ_c is a non negative self-adjoint operator.*

Proposition 26. *Problem (2.16) is equivalent to Problem (2.14) in the following sense:*

- *If U is solution to (2.14), then $[U]_\Gamma : \mathbb{R}^+ \times \Gamma \to \mathbb{R}$ is solution to (2.16).*
- *If v solution to (2.16) then the piecewise function $\tilde{U} : \mathbb{R}^+ \times \mathcal{O}_e \cup \mathcal{O}_c \to \mathbb{R}$, defined on $\mathcal{O}_e$ as the solution to*

$$\begin{cases} \nabla \cdot \left(\sigma_e \nabla \tilde{U}\right) = 0, \ \forall x \in \mathcal{O}_e, \ t \geq 0, \\ \tilde{U}_{|\partial\Omega} = g, \ \forall t \geq 0, \\ \sigma_e \partial_{n_e} \tilde{U}_{|_{\Gamma^+}} = C_m(\phi)\partial_t v + S_m(\phi)v, \ \forall x \in \Gamma, \ t > 0, \\ \tilde{U}_{|_{\Gamma^+}}(0, \cdot) = -(\Lambda_e + \Lambda_c)^{-1}(\Lambda_0 g + \Lambda_c v_\diamond), \ \forall x \in \Gamma. \end{cases}$$

and defined on $\mathcal{O}_c$ as the solution to

$$\begin{cases} \nabla \cdot \left(\sigma_c \nabla \tilde{U}\right) = 0, \ \forall x \in \mathcal{O}_c, \ t \geq 0 \\ \tilde{U}_{|_{\Gamma^-}} = (\Lambda_c + \Lambda_e)^{-1}(\Lambda_e v - \Lambda_0 g), \ \forall x \in \Gamma, \ t \geq 0. \end{cases}$$

is solution to (2.14).

Proof. This proof is taken from [37]. Using the definition of our Dirichlet-to-Neumann operators we can see that U is a solution to (2.14) if and only if it verifies the following equations

$$\begin{cases} -\Lambda_c U_{|_{\Gamma^-}} = C_m(\phi)\partial_t [U]_\Gamma + S_m(\phi)[U]_\Gamma, \\ \Lambda_c U_{|_{\Gamma^-}} + \Lambda_e U_{|_{\Gamma^+}} + \Lambda_0 g = 0. \end{cases}$$

Applying the operator $(\Lambda_e + \Lambda_c)^{-1}$ to the second equation and rearranging the terms results in the following relation

$$-U_{|_{\Gamma^-}} = -(\Lambda_c + \Lambda_e)^{-1}(\Lambda_e [U]_\Gamma - \Lambda_0 g).$$

Injecting this expression into the first equation shows the first point, with initial condition $v_\diamond := [U_0]_\Gamma$. The second point follows similarly. □

Well-posedness of the transmembrane potential

The following result extends the well-posedness results of Kavian *et al.* [37] to time-varying and space dependent capacitance.

Lemma 27. *Let $T > 0$, $s \geq 3$, $\beta_0, \beta_1 \in (0,1]$, $G \in \mathcal{C}^{\beta_0}([0,T[, H^s(\partial\Omega))$ and $\phi \in \mathcal{C}^{1,\beta_1}([0,T], H^s(\Gamma))$. Then for every initial condition $v_\diamond \in L^2(\Gamma)$ there exists a unique classical solution*

$$v \in \mathcal{C}^1([0,T], L^2(\Gamma)) \cap \mathcal{C}((0,T], D(\Lambda))$$

to

$$\begin{aligned} &C_m(\phi)\partial_t v + (S_m(\phi) + \Lambda)v = G \\ &v(t=0) = v_0. \end{aligned}$$

Proof. This result is a direct application of Theorem 6.1 and Theorem 7.1 from Pazy book [68, Chapter 5]). In order to apply these results, let us first define

$$\underline{\mathrm{v}} := \sqrt{C_m(\phi)}v,$$

which satisfies

$$\partial_t \underline{\mathrm{v}} + \underbrace{\left(\frac{S_m(\phi) - \frac{1}{2}C_m'(\phi)\partial_t\phi}{C_m(\phi)}\right)}_{=:M(t)}\underline{\mathrm{v}} + \underbrace{\frac{1}{\sqrt{C_m(\phi)}}\Lambda\frac{1}{\sqrt{C_m(\phi)}}}_{=:\tilde{\Lambda}(t)}\underline{\mathrm{v}} = \underbrace{\frac{G}{\sqrt{C_m(\phi)}}}_{=:f(t)}.$$

For all $t \geq 0$ the operator $\tilde{\Lambda}(t)$ is selfadjoint in $L^2(\Gamma)$ and monotone (Λ is monotone, see [37]). The function $M(t)$ is bounded and so we can always change the unknown we are solving for by $\underline{\mathrm{v}}_k(t) := e^{-kt}\underline{\mathrm{v}}(t)$ for large enough $k > 0$ and just consider $M(t) > 2$ and bounded. To match the same notation used in [68], we define $A(t) = M(t) + \tilde{\Lambda}(t)$. This operator is also selfadjoint and monotone. Once this setting in place, we need to verify three conditions to apply both theorems:

- The domain of $D(A(t))$ is dense in $L^2(\Gamma)$ and is independent of $t \in [0,T]$.
- For $t \in [0,T]$, the resolvent $R(\lambda : A(t))$ exists for all $\lambda \in \mathbb{C}$, $Re(\lambda) \leq 0$ and there exists $C > 0$ such that

$$\|R(\lambda : A(t))\|_{L^2(\Gamma)} \leq \frac{C}{|\lambda| + 1}, \quad \forall t \in [0,T], \quad Re(\lambda) \leq 0.$$

- There exists a constant C' and $0 < \zeta \leq 1$ such that

$$\left\|(A(t) - A(s))A(\tau)^{-1}\right\|_{L^2(\Gamma)} \leq C'|t-s|^\zeta, \quad \forall s,t,\tau \in [0,T].$$

The first point only depends on the domain of $\tilde{\Lambda}(t)$ as $v \mapsto M(t)v$ is bounded on $L^2(\Gamma)$. As $\phi \mapsto C_m(\phi)$ is strictly positive and smooth, we obtain the following equality

$$D(A(t)) = D(\Lambda) = \{u \in H^{\frac{1}{2}}(\Gamma) | \Lambda u \in L^2(\Gamma)\},$$

where the graph norm of Λ is equivalent to the graph norm of $\tilde{\Lambda}(t)$ for all $t \in [0,T]$. In fact the domain of Λ is $H^1(\Gamma)$ (see [37]) and so the norm equivalence results from the open mapping theorem. The second point results from the following calculation

$$\left\| \left(\lambda - A(t)\right)^{-1} \right\|_{L^2(\Gamma)} = \left\| \left(\lambda - 1 - (M(t)-1) - \tilde{\Lambda}(t)\right)^{-1} \right\|_{L^2(\Gamma)} \leq \frac{1}{\sqrt{|\lambda|^2 + 1 - \Re\lambda}} \leq \frac{2}{|\lambda|+1}$$

where we exploit the fact that $A(t) - 1$ is still a selfadjoint monotone operator. The third point is just a consequence of the Hölder continuity of $\partial_t \phi$, and the second point. Due the smoothness in time of $t \mapsto \phi(t)$, we can take $\zeta = 1$. □

In the subsections, we characterize the operator Λ in two important configurations: a spherical membrane and a flat torus, see Figure 2.2. These two cases are of importance, because cells in suspension are mostly round, while molecular dynamic simulations deal mostly with flat membrane. It is thus important to compare these two settings, in particular to understand the main differences in terms of order of magnitude of the time constants.

2.3.2 Spherical and flat membranes

As stated in the introduction, understanding the specificities of spherical and flat membranes is motivated by the fact that in the experiments cell and vesicle in suspension are mostly rounded, while molecular dynamic simuations are mostly performed in a flat periodic setting [22, 84]. In particular we propose in this section to perform a fine analysis of the nonlocal operator Λ to provide quantitative criteria to compare the flat and the spherical settings, see Figure 2.2.

The operator Λ in the case of a spherical membrane

We consider Γ and $\partial\Omega$ two spheres of radius R_0 and R_1 respectively where $R_1 > R_0$ (see Figure 2.2). The interior of the cell $\mathcal{O}_c = B(R_0)$ being the inner ball of radius R_0 and $\mathcal{O}_e = B(R_1) \setminus (\Gamma \cup B(R_0))$ the rest of the domain.

The operator Λ of (2.16)–denoted by $\Lambda^{\mathbb{S}}$ in the spherical setting– can be explicitly diagonalised in terms of the eigenfunctions of the Laplace-Beltrami operator on the unit sphere denoted by $\mathbb{S}^1$.

More precisely, the spectrum of the Laplace-Beltrami operator $-\Delta_{\mathbb{S}}$ is the set $\{\ell(\ell+1),\ \ell \in \mathbb{N}\}$, each eigenvalue $\ell(\ell+1)$ being of multiplicity $2\ell+1$, and the eigenfunctions are the well-known spherical harmonics (see Muller's book [62]).

As a result we get the following lemma.

Lemma 28 (Eigenmodes of the operator $\Lambda^{\mathbb{S}}$ for the sphere of radius R_0)**.** *The operator $\Lambda^{\mathbb{S}}$ from Equation (2.16) is diagonalisable in the same basis as the sphere Laplace-Beltrami operator $-\Delta_{\mathbb{S}^1}$. Let $\omega_{\lambda^{\mathbb{S}^1}_\Delta}$ be an eigenfunction of $-\Delta_{\mathbb{S}^1}$ associated with the eigenvalue $\lambda^{\mathbb{S}^1}_\Delta \in$*

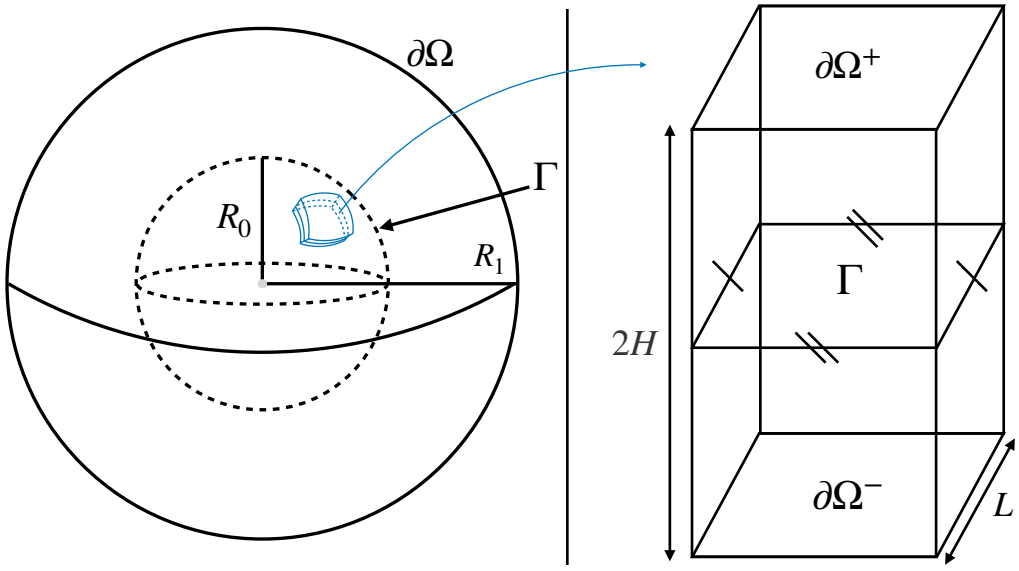

Figure 2.2: Two situations of membrane considered in this paper. On the left, the cell membrane separates the inner of the cell to the bath. The cell membrane Γ is the sphere of radius R_0 and the boundary condition at $\partial\Omega$ describes the effect of the electric field applied. On the right, a flat bi-periodic patch of the membrane placed between two charged planes $\partial\Omega^{\pm}$.

$\{\ell(\ell+1),\, \ell \in \mathbb{N}\}$.

$$
\begin{aligned}
k_\Delta^{\pm} &:= \frac{-1 \pm \sqrt{1+4\lambda_\Delta^{\mathbb{S}^1}}}{2}, \qquad \textit{with } \lambda_\Delta^{\mathbb{S}^1} \in \{\ell(\ell+1),\, \ell \in \mathbb{N}\}\ , \\
\lambda^{c,\mathbb{S}} &:= \frac{\sigma_c k_\Delta^+}{R_0}, \\
\lambda^{e,\mathbb{S}} &:= \frac{\sigma_e}{R_0} \frac{\left(k_\Delta^+ - k_\Delta^- \left(\frac{R_1}{R_0}\right)^{\sqrt{1+4\lambda_\Delta^{\mathbb{S}^1}}}\right)}{\left(\frac{R_1}{R_0}\right)^{\sqrt{1+4\lambda_\Delta^{\mathbb{S}^1}}} - 1}, \\
\lambda^{o,\mathbb{S}} &:= \frac{-\sigma_e}{R_0} \left(\frac{R_1}{R_0}\right)^{-k_\Delta^-} \frac{\sqrt{1+4\lambda_\Delta^{\mathbb{S}^1}}}{\left(\frac{R_1}{R_0}\right)^{\sqrt{1+4\lambda_\Delta^{\mathbb{S}^1}}} - 1},
\end{aligned}
$$

then

$$
\Lambda^{\mathbb{S}} \omega_{\lambda_\Delta^{\mathbb{S}^1}} = \frac{\lambda^{e,\mathbb{S}} \lambda^{c,\mathbb{S}}}{\lambda^{c,\mathbb{S}} + \lambda^{e,\mathbb{S}}} \omega_{\lambda_\Delta^{\mathbb{S}}}.
$$

In other words, if $(\omega_{\lambda_\Delta^{\mathbb{S}^1}}, \lambda_\Delta^{\mathbb{S}^1})$ *is the couple eigenvector/eigenvalue of* $-\Delta_{\mathbb{S}^1}$ *, then* $(\omega_{\lambda_\Delta^{\mathbb{S}^1}}, \lambda^{\mathbb{S}})$ *is a couple eigenvector/eigenvalue of the operator* $\Lambda^{\mathbb{S}}$ *where*

$$\lambda^{\mathbb{S}} = \frac{\lambda^{e,\mathbb{S}}\lambda^{c,\mathbb{S}}}{\lambda^{c,\mathbb{S}} + \lambda^{e,\mathbb{S}}}.$$

Remark 29. *As both operators* $\Lambda^{\mathbb{S}}$ *and* $-\triangle_{\mathbb{S}}$ *are diagonalisible in the same basis, which is a Hilbert basis of smooth functions in* $L^2(\mathbb{S})$*, the above list of eigenvalues for* $\Lambda^{\mathbb{S}}$ *is exhaustive.*

Proof. To prove the lemma, we diagonalise the three operators $\Lambda_o^{\mathbb{S}}$, $\Lambda_e^{\mathbb{S}}$ and $\Lambda_c^{\mathbb{S}}$ and then conclude by using the above relations. First, we change to spherical coordinates. As σ_c and σ_e are constant coefficients, given an interval $I = (a, b)$ $(b > a \geq 0)$, each Problem (2.15a)–(2.15b)–(2.15c) can be rewritten as

$$\left\{\begin{array}{c} (\frac{2\partial_r}{r} + \partial_r^2)U + \frac{1}{r^2}\Delta_{\mathbb{S}^1}U = 0, \ \forall (r,\theta) \in I \times \mathbb{S}^1, \\ U_{|_{\partial I \setminus \{r=0\}}}(\theta) = f(\theta), \quad \forall \theta \in \mathbb{S}^1 \end{array}\right\}$$

We take $f = \omega_{\lambda_\Delta^{\mathbb{S}^1}}$ and then we proceed by separation of variables. We assume the solution has the following ansatz $U(r,\theta) = h(r)\omega_{\lambda_\Delta^{\mathbb{S}^1}}(\theta)$. This implies that h verifies the following second order ODE

$$\frac{2}{r}h' + h'' - \frac{\lambda_\Delta^{\mathbb{S}^1}}{r^2}h = 0,$$

whose solutions are given by

$$h(r) = Ar^{k_\Delta^+} + Br^{k_\Delta^-}, \text{ where } k_\Delta^\pm = \frac{-1 \pm \sqrt{1 + 4\lambda_\Delta^{\mathbb{S}^1}}}{2},$$

for some coefficients $A, B \in \mathbb{R}$ to be determined. We determine the coefficients according to each Dirichlet boundary condition:

- By definition of the operator $\Lambda_c^{\mathbb{S}}$, $r \in (0, R_0)$ and $h(R_0) = 1$, hence $B = 0$ and $A = R_0^{-1}$ and therefore
$$\Lambda_c^{\mathbb{S}}(\omega_{\lambda_\Delta^{\mathbb{S}^1}}) = \frac{\sigma_c k_\Delta^+}{R_0}\omega_{\lambda_\Delta^{\mathbb{S}^1}}.$$
- By definition of the operator $\Lambda_e^{\mathbb{S}}$, $r \in (R_0, R_1)$, $h(R_0) = 1$ and $h(R_1) = 0$, simple calculations lead to
$$\Lambda_e^{\mathbb{S}}(\omega_{\lambda_\Delta^{\mathbb{S}^1}}) = \frac{\sigma_e}{R_0}\frac{\left(k_\Delta^+ - k_\Delta^-\left(\frac{R_1}{R_0}\right)^{\sqrt{1+4\lambda_\Delta^{\mathbb{S}^1}}}\right)}{\left(\frac{R_1}{R_0}\right)^{\sqrt{1+4\lambda_\Delta^{\mathbb{S}^1}}} - 1}\omega_{\lambda_\Delta^{\mathbb{S}^1}}.$$
- By definition of $\Lambda_o^{\mathbb{S}}$, $r \in (R_0, R_1)$, $h(R_0) = 0$ and $h(R_1) = 1$, hence
$$\Lambda_o^{\mathbb{S}}(\omega_{\lambda_\Delta^{\mathbb{S}}}) = \frac{-\sigma_e}{R_0}\left(\frac{R_1}{R_0}\right)^{-k_\Delta^-}\frac{\sqrt{1 + 4\lambda_\Delta^{\mathbb{S}^1}}}{\left(\frac{R_1}{R_0}\right)^{\sqrt{1+4\lambda_\Delta^{\mathbb{S}^1}}} - 1}\omega_{\lambda_\Delta^{\mathbb{S}}}.$$

This concludes the proof. □

The operator Λ in the case of a flat periodic membrane

We consider now the case of a flat periodic membrane $(\mathbb{R}/(L\mathbb{Z}))^2$. More precisely, the domain Ω is defined by

$$\Omega = (\mathbb{R}/(L\mathbb{Z}))^2 \times (-H, H) \subset \mathbb{R}^3$$

where H and $L > 0$ are strictly positive constants.

The membrane is defined by $\Gamma = (\mathbb{R}/(L\mathbb{Z}))^2 \times \{0\} \subset \Omega$ and $\partial\Omega = \partial\Omega^+ \cup \partial\Omega^-$ where

$$\begin{aligned}\partial\Omega^+ &= (\mathbb{R}/(L\mathbb{Z}))^2 \times \{H\},\\ \partial\Omega^- &= (\mathbb{R}/(L\mathbb{Z}))^2 \times \{-H\}.\end{aligned}$$

The exterior and interior of the cell are modeled as

$$\begin{aligned}\mathcal{O}_e &= \{(x, y, z) \in \Omega \,|\, z > 0\}\\ \mathcal{O}_c &= \{(x, y, z) \in \Omega \,|\, z < 0\}\end{aligned}$$

respectively. In this setting, the electric potential around the membrane U satisfies (2.14) with the boundary condition

$$g(t, \cdot) = g^{\pm}(t, \cdot) \text{ on } \partial\Omega^{\pm},$$

where g^+ and g^- are given smooth enough functions of $\partial\Omega^+$ and $\partial\Omega^-$ respectively. We also get the similar diagonalisation result as in the spherical sphere.

Lemma 30 (Eigenmodes of the operator Λ for the flat torus $(\mathbb{R}/(L\mathbb{Z}))^2$)**.** *The operator Λ – denoted by $\Lambda^{\mathbb{T}}$ in the case of a flat torus – is diagonalisable in the same basis as the periodic Laplace operator $-\Delta_{\mathbb{T}}$. For $\mathbf{k} = (\mathbf{k}_1, \mathbf{k}_2) \in \mathbb{Z}^2$, let $4\pi^2\|\mathbf{k}\|^2/L^2$ and $\omega_{\mathbf{k}}(x, y) = \exp\big((2i\pi/L)(\mathbf{k}_1 x + \mathbf{k}_2 y)\big)$ be the eigenpair of $-\Delta_{\mathbb{T}}$ in Γ then*

$$\Lambda^{\mathbb{T}}\omega_{\mathbf{k}} = \lambda^{\mathbb{T}}_{\mathbf{k}}\omega_{\mathbf{k}},$$

where

$$\lambda^{\mathbb{T}}_{\mathbf{k}} = \begin{cases} \dfrac{1}{H}\dfrac{\sigma_c\sigma_e}{\sigma_c + \sigma_e}, & \text{if} \quad \mathbf{k} = 0,\\ \dfrac{2\pi|\mathbf{k}|}{L\tanh(\frac{2\pi}{L}H|\mathbf{k}|)}\dfrac{\sigma_c\sigma_e}{\sigma_c + \sigma_e}, & \text{otherwise.}\end{cases}$$

Proof. We proceed in the same way as in the case of the sphere. Denote by $\Lambda^{\mathbb{T}}_c$, $\Lambda^{\mathbb{T}}_e$, and $\Lambda^{\mathbb{T}}_o$ the operators (2.15) in this flat periodic setting. It is also convenient to split $\Lambda^{\mathbb{T}}_o$ into $\Lambda^{\mathbb{T},+}_o$ and $\Lambda^{\mathbb{T},-}_o$ defined as

$$\Lambda^{\mathbb{T},+}_o : \begin{aligned} H^{1/2}(\partial\Omega^+) &\to H^{-1/2}(\Gamma)\\ g &\mapsto -\sigma_e\partial_z v_{|_{\Gamma^+}}\end{aligned}, \text{ where } v \text{ is the solution to } \begin{cases}\nabla\cdot\sigma_e\nabla v = 0, \text{ in } \mathcal{O}_e,\\ v_{|_\Gamma} = 0,\\ v_{|_{\partial\Omega^+}} = g^+\end{cases}$$

$$\Lambda_o^{\mathbb{T},-} : H^{1/2}(\partial\Omega^-) \to H^{-1/2}(\Gamma) \\ g \mapsto \sigma_c \partial_z v_{|_{\Gamma^-}}$$, where v is the solution to $\begin{cases} \nabla \cdot \sigma_c \nabla v = 0, \text{ in } \mathcal{O}_c, \\ v_{|_\Gamma} = 0, \\ v_{|_{\partial\Omega^-}} = g^-. \end{cases}$

Then, from (2.16) we infer

$$\Lambda^{\mathbb{T}} = \Lambda_c^{\mathbb{T}}(\Lambda_e^{\mathbb{T}} + \Lambda_e^{\mathbb{T}})^{-1}\Lambda_e^{\mathbb{T}}, \text{ and } G = \frac{1}{\sigma_e + \sigma_c}\left(\sigma_c \Lambda_o^{+,\mathbb{T}} g^+ - \sigma_e \Lambda_o^{-,\mathbb{T}} g^-\right).$$

We diagonalise the above operators and conclude by means of the above relations. All the above problems associated to the operators $\Lambda_o^{\mathbb{T},\pm}$, $\Lambda_c^{\mathbb{T}}$ and $\Lambda_e^{\mathbb{T}}$ can be solved similarly due the symmetry of the domain. In all cases, we apply separation of variables, that is, we assume that solution has the following ansatz $v(x,y,z) = h(z)\omega_{\mathbf{k}}(x,y)$ (like for the sphere, $f = \omega_{\mathbf{k}}$). This results in the following ordinary differential equation (ODE)

$$\frac{d^2 h_{\mathbf{k}}}{dz^2} - \left(\frac{2\pi}{L}\right)^2 |\mathbf{k}|^2 h_{\mathbf{k}} = 0,$$

whose solution is of the form

$$h_{\mathbf{k}}(z) = \begin{cases} A_{\mathbf{k}} \sinh\left(\frac{2\pi}{L} z|\mathbf{k}|\right) + B_{\mathbf{k}} \cosh\left(\frac{2\pi}{L} z|\mathbf{k}|\right), & \text{if } \mathbf{k} \neq 0, \\ A_0 z + B_0, & \text{if } \mathbf{k} = 0. \end{cases}$$

We determine the coefficients $A_{\mathbf{k}}$ and $B_{\mathbf{k}}$ in each case according to the definition of the operators. More precisely,

- In the case of the operator $\Lambda_e^{\mathbb{T}}$, one has the conditions $h_{\mathbf{k}}(0) = 1$ and $h_{\mathbf{k}}(H) = 0$.
- In the case of the operator $\Lambda_c^{\mathbb{T}}$ one has the conditions $h_{\mathbf{k}}(0) = 1$ and $h_{\mathbf{k}}(-H) = 0$.
- In the case of the operator $\Lambda_0^{\mathbb{T},+}$ one has the conditions $h_{\mathbf{k}}(0) = 0$ and $h_{\mathbf{k}}(H) = 1$.
- In the case of the operator $\Lambda_0^{\mathbb{T},-}$ one has the conditions $h_{\mathbf{k}}(0) = 0$ and $h_{\mathbf{k}}(-H) = 1$.

The simple calculations (left to the reader) lead to the expressions given by the lemma. □

We use this setting to approximate what locally happens near the poles of the cell when we zoom in.

Spherical vs flat membranes

Definition 31 (Time constant and (dis–)charging times the transmembrane voltage)**.** *We define the time constant of the membrane as*

$$\tau^\Lambda = \frac{C_m(0)}{S_m(0) + \min_{\lambda \in \mathfrak{S}(\Lambda)\setminus\{0\}}(\lambda)}, \tag{2.18}$$

where $\mathfrak{S}(\Lambda)$ is the spectrum of Λ.

The charging (resp. discharging) time of the TMV subjected to a constant unidirectional electric field of magnitude $\mathbf{E} = E\mathbf{z}$, that is $g^+ = EH = -g^-$, is defined as $5\tau^\Lambda$, corresponding in the linear regime to 99% of the complete charge (resp. discharge) of the membrane.

Simple calculations lead to the following property.

Property 32 (Time constants of the TMV for spherical vs flat membranes)**.** *Using the expressions of the eigenvalues of the operators $\Lambda^{\mathbb{S}}$ and $\Lambda^{\mathbb{T}}$ given in Lemma 28 and Lemma 30 respectively , one gets*

- *In the case of a spherical membrane, one has*

$$\min_{\lambda\in\mathfrak{S}(\Lambda)\setminus\{0\}}(\lambda)=\lambda_1^{\mathbb{S}}=\frac{1}{\frac{2R_0}{\sigma_c}+\frac{R_0}{\sigma_e}\frac{(R_1/R_0)^3-1}{1+2(R_1/R_0)^3}}\sim_{R_1\to+\infty}\frac{\sigma_e}{R_0}\frac{2}{1+2\frac{\sigma_e}{\sigma_c}}.$$

Therefore the time constant $\tau^{\mathbb{S}}$ of a spherical membrane in $\mathbb{R}^3$ is given by

$$\tau^{\mathbb{S}}\sim_{R_1\to+\infty}\frac{C_m(0)}{S_m(0)+\frac{1}{R_0}\frac{2\sigma_e\sigma_c}{\sigma_c+2\sigma_e}}.$$

- *In the case of a flat torus,*

$$\tau^{\mathbb{T}}=\frac{C_m(0)}{S_m(0)+\frac{1}{H}\frac{\sigma_c\sigma_e}{\sigma_c+\sigma_e}}.$$

Remark 33. *In order to consider the periodic flat membrane as a zoomed-in flat patch of the spherical cell model, it is thus necessary to match their time constants accordingly. This means that to compare both settings, we need to adjust the height H of the box as*

$$H=\frac{R_0}{2}\left(\frac{\sigma_c+2\sigma_e}{\sigma_c+\sigma_e}\right). \tag{2.19}$$

In molecular dynamics simulations of membrane electroporation, the dimension of the simulation boxes are a few nanometers thick (see for instance papers by Tieleman or Tarek [85, 88, 11, 84]), while the cell radius is about 5 to 10 μs. According to the above estimation, the corresponding time constant $\tau^{\mathbb{T}}_{\mathrm{MD}}$ of the TMV in molecular dynamics simulation is thus about 3 order of magnitude smaller than the time constant $\tau^{\mathbb{S}}_{\mathrm{vesicle}}$ of the TMV for spherical bilipid membrane (also call vesicle)

$$\tau^{\mathbb{T}}_{\mathrm{MD}}\sim 10^{-3}\,\tau^{\mathbb{S}}_{\mathrm{vesicle}}.$$

Based on this observation, and due to the coupling between water content and TMV, we believe that this dramatic difference on the time constant of the TMV prevents molecular dynamics simulations to give quantitative information on the membrane electroporation, even though they provide interesting qualitative description of the phenomenon.

The following property provides a bound on the Fourier coefficients of the steady TMV in a membrane containing water.

Property 34 (Steady TMV in porated membrane)**.** *Let $\bar{\phi}$ be a smooth phase order parameter constant in time on $\Gamma = (\mathbb{R}/(L\mathbb{Z}))^2$. Let $(p,q) \in (0,1] \times [0,1)$ be the proportion of pure water (resp. pure lipid) phases inside the flat membrane, and let s_0 be the mean of $S_m(\bar{\phi})$:*

$$p := \frac{1}{|\Gamma|}\int_{\{\bar{\phi}=1\}} dx, \qquad q := \frac{1}{|\Gamma|}\int_{\{\bar{\phi}=0\}} dx, \quad \bar{S}_m = \frac{1}{|\Gamma|}\int_\Gamma S_m(\bar{\phi})\, dx.$$

Denote by ϵ the term $\epsilon = 1-p-q \in (0,1)$. Let v^∞ be the stationary solution of equation (2.16) with a constant source term $g^+ = EH = -g^-$:

$$(S_m(\phi) + \Lambda)v^\infty = \frac{\sigma_e\sigma_e}{\sigma_c+\sigma_e}E. \tag{2.20}$$

Assume v^∞ that can be expanded in Fourier by

$$v^\infty(\mathbf{x}) = \sum_{\mathbf{k}\in\mathbb{Z}^2} \xi_{\mathbf{k}} \exp\left(\frac{2i\pi}{L}\mathbf{k}\cdot\mathbf{x}\right), \qquad \text{for a.e. } \mathbf{x}\in\Gamma.$$

Then one has the following estimate for $\mathbf{k}\in\mathbb{Z}^2$:

$$|\xi_{\mathbf{k}}| \le \frac{\sqrt{p(1-p)(S_m(1)-S_m(0))^2 + \epsilon S_m^2(1)}}{\bar{S}_m + \frac{2\pi|\mathbf{k}|}{L\tanh(2\pi|\mathbf{k}|H/L)}\frac{\sigma_e\sigma_c}{\sigma_e+\sigma_c}} \|v^\infty\|_{L^2,d\mu}, \tag{2.21}$$

where $d\mu := dx/|\Gamma|$ is the probability measure so that

$$\forall \psi \in L^2(\Gamma), \qquad \|\psi\|_{L^2,d\mu} := \left(\frac{1}{|\Gamma|}\int_\Gamma |\psi(x)|^2\, dx\right)^{1/2}.$$

Remark 35 (Influence of the patch size)**.** *Letting L go to zero in (2.21), all the other parameter being fixed, shows that the Fourier coefficients $\xi_{\mathbf{k}}$ the decreases linearly with L. Therefore small patches tend to flatten the TMV artificially even if we keep the same proportion of water in the membrane. This heuristic calculation suggests that large patches of flat membrane are needed so that flat torus can be seen as a zoom of the spherical setting.*

Proof. The squared L^2 distance between s_0 and S_m for the probability measure is bounded by

$$\begin{aligned}\left\|S_m(\bar{\phi}) - \bar{S}_m\right\|^2_{L^2,d\mu} &= \left\|S_m(\bar{\phi})\right\|^2_{L^2,d\mu} - \bar{S}_m^2 \\ &\le S_m^2(1)p + S_m^2(0)q + S_m^2(1)\epsilon - \bar{S}_m^2 \\ &\le (S_m(1)-S_m(0))^2 p(1-p) + \epsilon S_m^2(1).\end{aligned} \tag{2.22}$$

Applying the operator $(\bar{S}_m+\Lambda)^{-1}$ to the static equation (2.20) leads to

$$(\bar{S}_m+\Lambda)^{-1}(S_m(\bar{\phi})-\bar{S}_m)v^\infty + v^\infty = \frac{2\sigma_c\sigma_e}{\sigma_e+\sigma_c}\frac{E}{\bar{S}_m + \frac{1}{H}\frac{\sigma_c\sigma_e}{\sigma_c+\sigma_e}}.$$

Taking the L^2 dot-product for the probability measure $d\mu$ with $\exp\left(\frac{2i\pi}{L}\mathbf{k}\cdot\mathbf{x}\right)$ and using (2.22) ends the proof.

□

2.4 The nonlinear coupled system and its stability analysis

Putting the TMV equation and the order parameter equation results in the following joint problem on Γ, we obtain

$$\partial_t \phi - D_0 \triangle_\Gamma \phi = -\alpha W^{'}(\phi) + \frac{\alpha}{2} C_m^{'}(\phi) v^2, \quad \forall x \in \Gamma, \forall t > 0, \tag{2.23a}$$

$$C_m(\phi)\partial_t v + (S_m(\phi) + \Lambda)v = G, \quad \forall x \in \Gamma, \forall t > 0, \tag{2.23b}$$

$$v|_{t=0} = v_\diamond, \quad \phi|_{t=0} = \phi_\diamond, \text{on } \Gamma. \tag{2.23c}$$

Let $(\bar{\phi}, \bar{v})$ be two constant solutions to (2.23) such that $\bar{\phi} < 0.5 - 3a_2/8a_1$. For small perturbations $\mu_\diamond, \varepsilon_\diamond$ of these initial conditions, we assume there exists a unique solution $(t,x) \mapsto (\phi(t,x), v(t,x))$. Let $\mu(t,x) := v(t,x) - \bar{v}$ and $\varepsilon(t,x) := \phi(t,x) - \bar{\phi}$, and set $\mu(0) = \mu_\diamond$ and $\varepsilon(0) = \varepsilon_\diamond$. Inserting these expressions into (2.23) and linearising results in the following system

$$\partial_t \begin{bmatrix} \varepsilon \\ \mu \end{bmatrix} = \begin{bmatrix} D_0 \triangle_\Gamma - \alpha \mathcal{W}_m^{''}(\bar{\phi}) + \frac{\alpha}{2} C_m^{''} \bar{v}^2 & \alpha C_m^{'}(\bar{\phi})\bar{v} \\ -\frac{S_m^{'}(\bar{\phi})\bar{v}}{C_m(\bar{\phi})} & -\frac{S_m(\bar{\phi})+\Lambda}{C_m(\bar{\phi})} \end{bmatrix} \begin{bmatrix} \varepsilon \\ \mu \end{bmatrix}. \tag{2.24}$$

In both the case of $\Gamma = \mathbb{S}$ or $\Gamma = (\mathbb{R}/(L\mathbb{Z}))^2$ the operators $\triangle_\Gamma$ and Λ are diagonalisable in the same L^2 basis. We can thus further simplify the problem by looking at the decomposition of ε and δ in its Fourier modes (or spherical harmonics).

Remark 36. *Due to $(\bar{\phi}, \bar{v})$ being constant, all of the operators in each entry of the square matrix in (2.24) commute.*

We denote by $\varepsilon(t) = \sum \varepsilon_n(t)\omega_n$ and $\mu(t) = \sum \mu_n(t)\omega_n$ the Fourier (or harmonic) decomposition of the solution. Then splitting the above linearized problem along each frequency (ε_n, μ_n) results in the following

$$\partial_t \begin{bmatrix} \varepsilon_n \\ \mu_n \end{bmatrix} = \underbrace{\begin{bmatrix} -D_0\lambda_n^{\triangle} - \alpha \mathcal{W}_m^{''}(\bar{\phi}) + \frac{\alpha}{2} C_m^{''}(\bar{\phi})\bar{v}^2 & \alpha C_m^{'}(\bar{\phi})\bar{v} \\ -\frac{S_m^{'}(\bar{\phi})\bar{v}}{C_m(\bar{\phi})} & -\frac{S_m(\bar{\phi})+\lambda_n^{\Lambda}}{C_m(\bar{\phi})} \end{bmatrix}}_{:=A_n} \begin{bmatrix} \varepsilon_n \\ \mu_n \end{bmatrix}$$

where $\lambda_n^{\triangle}$ and λ_n^{Λ} are the n-th eigenvalues of $-\Delta_\Gamma$ and Λ respectively.

Linear instability occurs if there exists an integer n (associated to non-constant eigenfunctions) such that A_n has an eigenvalue with positive real part. This is the case if and only if $\det(A_n) < 0$ or $\mathrm{Tr}(A_n) > 0$ for some n. We assume that the conductivity of the membrane does not change much for $\bar{\phi} \in [0, 0.4]$ (see Section 2.5.4), we expect that $|S_m^{'}(\bar{\phi})| \ll 1$. Therefore, the easiest condition to verify is $\det(A_n) < 0$ (for some n). In fact, we get exactly

$$\mathcal{W}_m^{''}(\bar{\phi}) + \frac{D_0}{\alpha}\lambda_n^{\triangle} + \frac{S_m^{'}(\bar{\phi})C_m^{'}(\bar{\phi})}{S_m(\bar{\phi}) + \lambda_n^{\Lambda}}\bar{v}^2 < \frac{C_m^{''}(\bar{\phi})}{2}\bar{v}^2.$$

If $S_m^{'}(\bar{\phi})$ is small enough for $\bar{\phi} \in [0, 0.4]$, we simplify this constraint by

$$C_m^{''}(\bar{\phi}) > \frac{2}{\bar{v}^2}\mathcal{W}_m^{''}(\bar{\phi}) + \frac{2}{\bar{v}^2}\frac{D_0}{\alpha}\lambda_n^{\triangle} + \rho, \quad \text{in units } [\text{F.m}^{-2}],$$

for some (small) $\rho > 0$. Using the expression of $\mathcal{W}_m$ given in (2.5), we infer

$$C_m^{''}(\bar{\phi}) > \frac{8a_1}{\bar{v}^2}\left(\left(6\bar{\phi}^2 - \left(6 - \frac{3a_2}{a_1}\right)\bar{\phi} + \left(1 - \frac{3a_2}{2a_1}\right)\right) + \frac{D_0}{4a_1\alpha}\lambda_n^{\triangle}\right) + \rho.$$

In practice $a_2 \ll a_1$ and $\frac{D_0}{4a_1\alpha} \sim (\delta^h)^2$ which is the membrane thickness (see Section 2.5) this suggests the following simple sufficient condition allowing to study the effect of each parameter in our model

$$C_m^{''}(\bar{\phi}) > \frac{8a_1}{\bar{v}^2}\left(6\bar{\phi}^2 - 6\bar{\phi} + 1 + (\delta^h)^2\lambda_n^{\triangle}\right) + \rho. \tag{2.25}$$

Remark 37. *Dividing the above inequality (2.25) by $C_m(\bar{\phi})$ shows that the emergence of instabilities is driven by $\frac{4a_1}{\frac{1}{2}C_m(\bar{\phi})\bar{v}^2}$, which is the ratio of the barrier energy of the double-well potential $\mathcal{W}_m$ and the electrostatic energy of the membrane. In addition the parameter α impacts on the size of the initial instabilities created. This can be seen through the size of the highest eigenmodes (highest in the sense of the value of $|\vec{n}|$) that are linearly unstable.*

- *In the flat periodic case the eigenvalues of the surface Laplace-Beltrami read*

$$\lambda_{\vec{n}}^{\triangle} = \frac{4\pi^2|\vec{n}|^2}{L^2}, \text{ if } \Gamma = (\mathbb{R}/(L\mathbb{Z}))^2,$$

We take the largest eigenvalue $\lambda_{\vec{n}}$ such that $(\delta^h)^2\lambda_{\vec{n}}^{\triangle} \sim 1$, which results in the following

$$\frac{L}{|\vec{n}|} \sim 2\pi\delta^h. \tag{2.26}$$

As in the periodic case the $\vec{n}$-th eigenfunction is of wavelength $L/|\vec{n}|$, therefore linear instabilities reach eigenmodes of the lengthscale of the membrane thickness. This supports the idea that the size of pores created by the influence of the electric field are expected to initially be of the length scale of the membrane thickness.

- *In the case of a spherical cell we get a similar result. Here the Laplace-Beltrami eigenvalues read*

$$\lambda_n^{\triangle} = \frac{n(n+1)}{R_0^2}, \text{ if } \Gamma = \mathbb{S}, \text{ the sphere of radius } R_0.$$

Here, the notion of wavelength of an eigenfunction is not directly applicable, however qualitatively, for higher values of n the eigenfunctions associated to $\lambda_n^{\triangle}$ oscillate more rapidly. Another way to see this is the following, for a given eigenvalue $\lambda_n^{\triangle}$, there is a spherical

harmonic which divides the sphere in $2\lfloor n/2 \rfloor (1 + \lceil n/2 \rceil)$ *regions with alternating signs (also known as nodal domains), see [48] for more information. Again, if we take the largest value of* n *such that* $(\delta^h)^2 \lambda_n^{\triangle} \sim 1$*, then we get*

$$\frac{R_0^2}{n(n+1)} \sim (\delta^h)^2$$
$$\frac{|\Gamma|}{4\pi n(n+1)} \sim (\delta^h)^2.$$

Therefore, we can see that there is at least one spherical harmonic with a nodal domain of size comparable to $(\delta^h)^2$ *which is linearly unstable. We conclude similarly as in the flat membrane case, and we obtain a similar estimation of the initial size of pores.*

2.5 Choice of membrane parameters

The aim of this section is to obtain reasonable estimates for the parameters in our model. Indeed, some of these parameters are not physiological, meaning that they cannot be directly measured. Therefore, we would like to infer a priori value ranges allowing realistic simulation. To this end, we are going to link our free-energy (2.2) to the energy model proposed by Chizmadzhev *et al.*, from which the models of Krassowska, Weaver *et al.* are derived [41, 90, 93, 42].

2.5.1 Determination of the double-well potential coefficients

In the theory proposed by Abidor, Chizmadzhev and Weaver [1, 16, 91], the water pore is assumed to be a cylinder embedded in a sea of lipid. The introduced the notion of hydrophobic pores, defined as the pores with radius smaller that a pore parameter $r^\star$. It was introduced to account for the fluctuation of lipids which does not generate water pathways in the membrane. Pores of radius above $r^\star$ are defined as hydrophilic (see Figure 2.3) and enables the water to pass through the membrane.

Energy functional (2.2) (when $v = 0$) can be thought of as a generalisation of the standard energy model for hydrophilic pores (2.27). Interestingly, the use of reaction-diffusion on the water content enables us to describe the interaction between neighboring pores, which was not possible in the previous approach, since the pores were considered somehow isolated from each other. In order to compare the both approaches, it is instructive to consider the physical units of each term of the membrane free-energy (2.2).

As ϕ is dimensionless then the unit for κ is the energy unit [J] and the coefficients a_1 and a_2 have surface tension units [J.m^{-2}]. We thus compare these terms with the linear and surface tension terms from the hydrophilic pore energy in [91]. Let $r^\star > 0$ be the radius at which hydrophobic pores are more energetically favorable than hydrophilic pores (see [91, 64] for a description of $r^\star$, in the literature its value is estimated to be $r^\star := 0.5$[nm]), then for

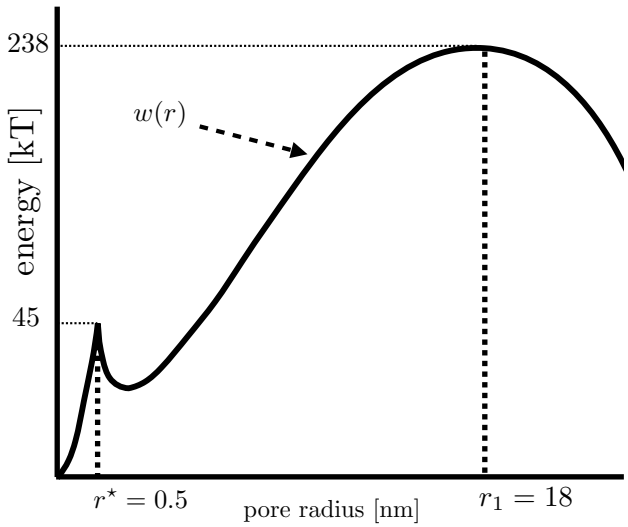

Figure 2.3: Energy needed to create a pore of radius r according to Weaver and Chizmadzhev appraoch. A pore is considered to be hydrophilic if its radius r is bigger than $r^\star$, otherwise it is considered to be hydrophobic pore (see [91, 64]).

any radius $r > r^\star > 0$ the energy needed to create a pore (see Figure 2.3) of that radius is

$$w(r) = 2\pi\gamma r - \pi\sigma r^2 + \frac{C}{r^4}, \quad \forall r > 0, \qquad \text{(hydrophilic pore energy)}, \tag{2.27}$$

where γ is the linear tension of the edge of a pore and σ the surface tension of the membrane. The last term represents the steric repulsion of the lipid heads in the edge of a pore. In practice it prevents (hydrophilic) pores from being too small which would be too energetically costly. In order to make the link with our energy functional more concrete, we are going to consider the case of an "ideal" smooth pore. This allows us to compare each term in (2.27) with the terms in our energy functional. Let ϕ_p be a smooth circular pore of radius $r_0 > 0$ with a small interface (where $\phi \in (0,1)$) of size $\delta^h \ll r_0$ (see Figure 2.4a). The energy difference between an intact membrane $\phi \equiv 0$ and a membrane with such a pore ϕ_p is given by

$$\begin{aligned}\mathcal{E}(\phi_p, 0) - \mathcal{E}(0,0) &= \frac{\kappa}{2}\int_\Gamma |\nabla\phi_p|^2 + \int_{\text{interface}} \big(\mathcal{W}_m(\phi_p) - \mathcal{W}_m(0)\big)dx - \int_{\text{interior}} \mathcal{W}_m(0)dx, \\ &= \frac{\kappa}{2}\int_\Gamma |\nabla\phi_p|^2 + \pi((r+\delta^h)^2 - r^2)\big(\bar{\mathcal{W}}_m - \frac{a_2}{2}\big) - \pi r^2\frac{a_2}{2},\end{aligned} \tag{2.28}$$

where $\bar{\mathcal{W}}_m$ is the mean value of $x \in \Gamma \mapsto \mathcal{W}_m(\phi_p(x))$ inside the pore interface. As ϕ_p takes values in $[0,1]$ for all $x \in \Gamma$, we deduce that $\bar{\mathcal{W}}_m \in [0, W_m(1/2 + 3a_2/2a_1)]$. Let $\gamma_0 := \bar{\mathcal{W}}_m - a_2/2$, then (2.28) can be rewritten as

$$\mathcal{E}(\phi_p, 0) - \mathcal{E}(0,0) = 2\pi r_0\big(\delta^h\gamma_0\big) - \pi r_0^2\frac{a_2}{2} + \left(\frac{\kappa}{2}||\nabla\phi_p||^2_{L^2(\Gamma)} + \pi(\delta^h)^2\gamma_0\right). \tag{2.29}$$

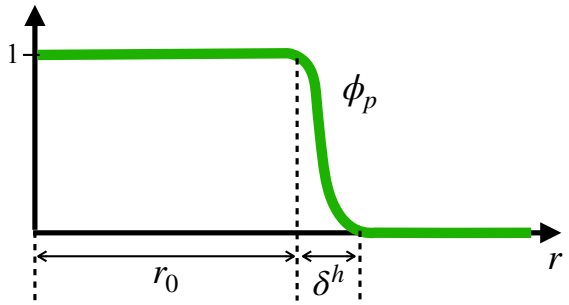

(a) Profile of the order parameter ϕ_p.

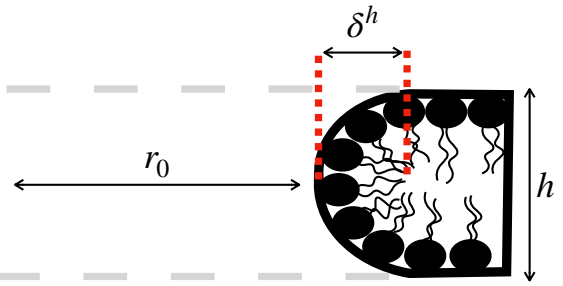

(b) Representation of half the cross section of ϕ_p.

Figure 2.4: Ideal smooth circular pore ϕ_p of radius $r_0 > 0$ in a flat membrane Γ centered at the origin. The rotational symmetry of the setting allows us to describe the pore as a function $r \mapsto \phi_p(r)$ where r is the distance to the origin. The thickness of the lipid bilayer is denoted by $h > 0$. The interface is of size $\delta^h > 0$ such that $\delta^h \ll r_0$.

Looking at (2.29), the parallel between our energy functional and (2.27) becomes clear. We already know that a_1 and a_2 represent surface tensions and we therefore deduce that $\delta^h \gamma_0$ corresponds to the linear tension of the pore's edge γ from (2.27), and similarly for the term $a_2/2$ and σ from (2.27). This results in the following system of equations

$$\bar{\mathcal{W}}_m - \frac{a_2}{2} = \frac{\gamma}{\delta^h}, \text{ and } a_2 = 2\sigma,$$

where a_1 and a_2 are the unknowns. The size δ^h of the interface for a typical pore can be roughly estimated. The size of δ^h intuitively should be comparable with half the membrane thickness $h/2$ (see Figure 2.4b). In order to determine the value of a_1 expressed in terms of the model proposed in [91], we need to invert the following nonlinear equation

$$\bar{\mathcal{W}}_m = \frac{\gamma}{\delta^h} + \sigma,$$

where $\bar{\mathcal{W}}_m$ depends on a_1, a_2 and the shape of ϕ_p inside the interface.

As a first approximation, we estimate the value of $\bar{\mathcal{W}}_m$ by assuming that $r \mapsto \phi_p(r)$ changes almost linearly inside the interface (meaning that $\frac{d\phi_p}{dr}(r) \sim 1/\delta^h$ inside the interface). This results in the following rough estimate

$$\bar{\mathcal{W}}_m \sim \int_0^1 a_1\phi^2(1-\phi)^2 + a_2(\phi + 1/2)(\phi - 1)^2 d\phi = \frac{a_1}{30} + \frac{a_2}{4}.$$

Replacing this expression in the above equations results in the following values

$$a_1 = 30\frac{\gamma}{\delta^h} + 15\sigma, \text{ and } a_2 = 2\sigma.$$

The last term in (2.29) will play a similar role to the steric repulsion term when a pore is too small. In the next paragraph, we continue to estimate all the values of the model before presenting the table summarizing the values used.

2.5.2 Parameters influencing membrane dynamics under null TMV

We can now estimate the values of a_1 and a_2, in addition to the kinetic coefficient α. These values depend only on the cell membrane and so we consider $v \equiv 0$ throughout this section. To estimate the values of a_1 and a_2, we use the values of linear and surface tension from [41]. To estimate α, we can roughly approximate it by using Property 22 in Section 2.2.3. We take the asymptotic relation bounding the size of the anti-phase interface (δ_n^h instead of δ^h) from that property to be an equality and we obtain the following rough estimate

$$\alpha = \frac{D_0}{4a_1(\delta^h)^2} \quad [\mathrm{m}^2\mathrm{J}^{-1}\mathrm{s}^{-1}].$$

In practice, given estimates for a_1, a_2, D_0 and δ^h, we estimate α via the above formula and then verify the conditions from Property 22.

2.5.3 Summary of parameters

We summarize the choice of parameters used in our simulations in Table 2.1 and 2.2. The conductivity of an intact membrane (lipid conductivity σ_l) is estimated by looking at its characteristic time of charge

$$\tau_m = \frac{C_m(0)}{S_m(0) + \dfrac{2\sigma_e\sigma_c}{R_0(\sigma_c + 2\sigma_e)}}, \quad \text{for an intact spherical membrane, with } C_m(0) = \varepsilon_0\varepsilon_l/h,$$

where h is the membrane thickness, $\varepsilon_0\varepsilon_l$ the lipid permittivity, σ_c and σ_e the conductivities of the cell interior and exterior respectively, and R_0 is the cell radius. According to experimental observations (we refer the reader to [76, 77] and references therein), the value of τ_m ranges between 0.1 μs and 1 μs.

	Value	Description	Reference
D_0	2×10^{-12} m^2.s^{-1}	lateral diffusion of lipids in the cell membrane	[51]
σ	10^{-6} J.m^{-2}	surface tension of the lipid-bilayer	[41]
γ	1.8×10^{-11} J.m^{-1}	pore edge energy	[41]
ϵ_0	8.85×10^{-12} F.m^{-1}	vacuum permittivity	[59]
ϵ_w	80	relative water permittivity	[91]
ϵ_l	2	relative lipid permittivity	[91]
σ_c	1 S.m^{-1}	interior medium conductivity	[77, 76]
σ_e	1.5 S.m^{-1}	exterior medium conductivity	[76, 77]
σ_l	3×10^{-5} S.m^{-1}	lipid membrane conductivity	[19, 41]
σ_w	1 S.m^{-1}	pore conductivity	[19, 41]
h	5×10^{-9} m	membrane thickness	[41]

Table 2.1: Physical parameters of the cell electroporation model.

	Value	Description	Section
δ^h	10^{-9} m	pore edge size	(Section 2.5.1)
α	9.26×10^6 m^2.J^{-1}.s^{-1}	kinetic coefficient of our model	(Section 2.5.2)
a_1	5.44×10^{-1} J.m^{-2}	measures energy barrier between the stable states	(Section 2.5.1)
a_2	2.0×10^{-6} J.m^{-2}	measures the surface tension of the membrane	(Section 2.5.1)

Table 2.2: Estimated parameters specific to our model. We consider them up to order of magnitude, as they are taken to be rough approximations deduced from our analysis. That is why they may not verify the exact formulas used to defined them.

Remark 38. *It is worth noting that with these choices of parameters, the coefficient* $\sqrt{\frac{4a_1\alpha L^2}{D_0}}$ *is large and* $\frac{3a_2}{4a_1}$ *small. Therefore, the asymptotic results, presented in Property 22, hold.*

2.5.4 Choice of the conductance and capacitance model

In this section, we look at one behaviour of our model according to the model choices for S_m and C_m. Previous models require the values of these functions for the lipid ($\phi = 0$) state or the pore state ($\phi = 1$). In this continuous setting, we have a modeling choice to make to extend these properties to "mixed" states between lipid and pore (for example $\phi = 1/2$). For both S_m and C_m, the main approach will be to interpolate between the values of the function for the stable states. Of course, whatever the choice of interpolation, our model is only concerned by the values in a neighbourhood of $\phi \in [0, 1]$. We can for example consider linear interpolations and still consider S_m and C_m to be bounded if we just apply appropriate cutoff functions outside the region of interest.

Membrane conductance model

The choice of S_m directly impacts on the amplitude of the transmembrane voltage v. In order to interpolate between the conductivity of the membrane (lipid conductivity) and the conductivity of a pore, we consider the following sigmoid function

$$S_m(\psi) = \frac{\sigma_m(\psi)}{h}, \quad \text{where} \quad \sigma_m(\psi) = \frac{1 + \tanh(k_0(\psi - \phi_{\text{th}}))}{2}(\sigma_w - \sigma_l) + \sigma_l, \quad \forall \psi \in \mathbb{R},$$

where σ_l and σ_w are the lipid and water conductivities respectively. The factor $k_0 > 0$ determines the steepness of the transition between these two conductivities and the value of $\phi_{\text{th}} \in [0, 1]$ is the water content threshold of the transition. The effect of electroporation on the cell membrane tends to suddenly and dramatically increases its conductivity. As ϕ evolves continuously in time and we dot not expect a gradual change in membrane conductivity during its evolution, this translates into a steep transition for S_m. In other words k_0 cannot be too small if we wish to model this effect correctly. As for an appropriate value for ϕ_{th}, this will depend on the value of k_0 to some extent, although it is intuitive to impose $\phi_{\text{th}} \sim 1/2$ as it is an instability mid point between the two stable states of the double well energy potential $\mathcal{W}_m$. In the following we set $k_0 = 100$.

2.5.5 Influence of the capacitance model

In contrast to S_m, C_m directly affects the order parameter ϕ as it is directly responsible (along with the TMV) for pore formation, which is why we must also consider the membrane dynamics in this analysis.

Looking at the Allen-Cahn equation (2.23a), to promote water entering the membrane, we need $C_m'(\phi) > 0$ (at least for $\phi \in [0, 1/2]$). Furthermore, we do not expect that the membrane order parameter ϕ uniformly increases as the TMV increases. The model of Looyenga given in (2.3) ensures that so that constant solutions to the joint problem (2.23) are (linearly) unstable and that $C_m'(\phi) > 0$.

2.6 Conclusion

We have proposed a new model of membrane permeabilisation based on the free-energy of the membrane. The problem consists in a surface reaction-diffusion of the water content of the membrane coupled to the nonlocal equation on the transmembrane voltage as described by the system equation (2.23). Thanks to the analysis of the eigenvalue of the nonlocal operator on the transmembrane voltage, we have compared the time constants in the spherical and the flat periodic settings. This fine analysis enables us to state that in order to have comparable time constants in both spherical and flat settings, it is necessary to have a flat periodic setting with a height of the order of the sphere radius as shown in Equation (2.19).

This observation explains why the time constants obtained in the molecular dynamic simulations (in which the height box of simulation is a few tens of nanometers) are most likely too short compared with cell membrane electroporation.

From the modeling view point the free-energy of the membrane could be complexified. Indeed, Breton and Mir have shown that the intense electric field generates an oxidation of the lipids. This means that in addition to the pore, a new species of oxidised lipid is created. The interfaces oxidised-nonoxidised lipids could increase the permeability of the membrane, and thus could explain the long duration of the permeabilised state of the membrane [12].

Moreover, as presented in the stability analysis section, there is an important interplay between the membrane potential $\mathcal{W}_m$ and the modeling choice of $\phi \mapsto C_m(\phi)$. Seeing as we chose the $\mathcal{W}_m$ for the sake of simplicity, a more physically sensible model should be possible with a more appropriate choice of membrane potential and maybe a different capacitance model. This choice will have little effect on the pore evolution once the membrane is discharged, so we can expect the same pore sealing behavior. These perspectives will be addressed in Chapter 5.

Chapter 3

Numerical simulation of our phase-field model

3.1 Introduction

Until recently, only molecular dynamic simulations (MD) were used to illustrate the emergence of water pathway (called pores) in lipid bilayer subjected to short electric field of high intensity. However the huge computational cost of MD imposes a small simulation box (a few tens of nanometers large), a computation time of less than one hundred nanoseconds and an electric field magnitude of several hundred megavolts (much higher than in experiments), making it difficult to link to experimental observations. Another drawback of MD is its link to "effective" electrical properties of the membrane such as capacitance and conductance which cannot be easily extracted from the simulations. In the previous chapter, we propose a phase-field model of lipid bilayer electroporation that link the water content of the membrane to the electrical properties of the membrane, enabling to link the nanoscopic phenomenon of pore creation and the microscopic description of membranes submitted to high electric field of similar magnitudes as in the experiments. Roughly speaking, the model consists of a 3D electric quasi-static equation describing the potential combined with a 2D Allen-Cahn equation for the water content [36]. Somehow the model provides the physical grounds of the phenomenological model proposed by Leguèbe *et al.* a decade ago [46] while also allowing to simulate realistic physicial conditions.

This chapter is devoted to the simulation of System 2.23 presented in Chapter 2. In Section 3.2 we present the numerical challenges that arise naturally in this problem, some of which become even more difficult in the case of a sphere. In Section 3.3, we present an order 1 (in time) numerical scheme to simulate the coupled system of partial differential equations. Then we improve it to obtain a scheme – presented in Section 3.4 – with second-ordre temporal accuracy. Then, we perform a standard numerical test for the impoved scheme to verify the second-order accuracy. Finally, in Section 3.5, we perform some experimental simulations to measure the effects of different parameters on the result predicted by our model.

3.2 Numerical challenges and simulation setting

The computational challenge of the phase-field model proposed in Chapter 2 lies on the fact that the characteristic size of the pores is on the length scale of a few nanometers. The pore edges are of particular importance, and these are even smaller than pores so this means that to simulate the cell membrane (or a patch of membrane) requires the use of a very fine mesh with a resolution equivalent to about one nanometer in length. Additionally, even in the case of a very small patch of membrane, the distance between the electrodes needed in order to make a reasonable comparison with the electric behavior of a spherical cell is on the same order of magnitude as the radius of that cell. As a result, considering a straightforward coupling of the 3D/2D model is computationally unfeasible, even for small membrane patches. Even with adaptive meshing the size of the system containing the membrane patch is too large to be solved in reasonable time (just the file size of the meshes easily surpasses 2 GB in storage).

Interestingly, thanks to Dirichlet-to-Neumann operators, the 3D/2D model is reduced to a coupled system of two dimensional non-local partial differential equations, written on the cell membrane, which is a smooth two dimensional compact manifold without boundary. This has the computational benefit of reducing the dimension of the problem and so the size of the mesh. There is also the added benefit that both the Laplace-Beltrami $\triangle_\Gamma$ and the Dirichlet-to-Neumann operator Λ are diagonalizable in the same basis in both of the scenarios considered in Chapter 2. However, this simplification does not trivialize the problem as there are still some computational challenges that need to be addressed.

First, we focus on the evolution equation for the TMV in the case of a periodic membrane patch of characteristic length $L > 0$ represented as the flat torus $\Gamma = (\mathbb{R}/L\mathbb{Z})^2$. In practice, given two functions $G\colon \mathbb{R}^+ \to \mathbb{R}$ (piecewise smooth), and $\phi\colon \mathbb{R}^+ \times \Gamma \to [0,1]$ (smooth in time and space), we wish to construct a numerical scheme for the following equation on the transmembrane voltage v:

$$\begin{cases} C_m(\phi)\partial_t v + S_m(\phi)v + \Lambda^{\mathbb{T}} v = \frac{2\sigma_e\sigma_c}{\sigma_e+\sigma_c}E, \text{ in } \Gamma, \forall t > 0, \\ v(0,\cdot) = 0, \text{ in } \Gamma. \end{cases}$$

Remark 39. *The function E represents the intensity of the electric field pulse being applied. Using the notation of lemma 30 for the source term G, we can see that*

$$E(t) := \frac{g^-(t) - g^+(t)}{2H},$$

where $g^\pm$ are constant in space.

We list some of the difficulties associated to this problem, some of which automatically render some standard numerical approaches unsuitable. It is important to note, that the purpose of this list is twofold. First, it shows the numerical difficulty of the problem. Second, it also convinces the reader that the main ideas in our scheme are reasonably "optimal" in the sense that further improvements (which minimize computation time) are probably more

a matter of engineering (parallelising and optimizing code) rather than a clever reformulation of the problem.

The numerical difficulties in solving the TMV equation are:

1. **Explicit scheme:** The non local operator $\frac{1}{C_m(\phi)}\Lambda^{\mathbb{T}}$ is of order one and so one could imagine just using some sort of explicit numerical scheme. In reality this is not practical as the characteristic length of a patch is on the scale $L \sim 10^{-7}$ [m], and so in Lemma 30 we can see its amplifying effect on the operator $\Lambda^{\mathbb{T}}$. The fact that $1/C_m(\phi) \in [10, 400]$ does not help either. In short, the size of the problem naturally imposes a strong CFL condition which makes using an explicit scheme a less desirable option.

2. **Implicit scheme:** The above point motivates the need for an implicit scheme, to gain stability. This requires two clarifications.

   First, the multiplicative operator $v \mapsto \frac{S_m(\phi)}{C_m(\phi)}v$ can be neglected for now (meaning we can eventually consider a numerical scheme which is explicit on this term). This is natural, as it is a bounded operator and so it is not problematic, and even if this decreases the accuracy of our scheme, for now the scheme stability takes precedence.

   Second, given $0 < \delta t \ll 1$, we need to invert the operator $I_{\mathrm{d}} + \frac{\delta t}{C_m(\phi)}\Lambda^{\mathbb{T}}$, which is an operator which cannot be diagonalised in the same basis as $\Lambda^{\mathbb{T}}$. We know that $\Lambda^{\mathbb{T}}$ is diagonalisable, and its definition imposes that we can only calculate it by means of its diagonalized form (at least if we wish to keep this problem two dimensional). As it is diagonalized in the same basis as the Laplacian, then applying $\Lambda^{\mathbb{T}}$ to a function entails using its Fourier series decomposition. As a result, if we were to discretize $\Lambda^{\mathbb{T}}$ in the canonical basis (in space and not in frequency), we would get a convolution operator (as it is a multiplication operator in the Fourier basis), which is a full matrix.

   Of course, this poses a problem as $f \mapsto \frac{1}{C_m(\phi)}f$ is multiplication operator and so in general it does not commute with $\Lambda^{\mathbb{T}}$. In fact, this operator in the Fourier basis takes the form of a convolution operator, which when discretized also translates into a full matrix.

   In conclusion, an implicit numerical scheme is necessary and it is not trivial to implement as both of the operators above seem to be at odds with one another. Needless to say, brute-forcing an inversion of full matrices at each discrete time step is not a realistic approach and so some other approach has to be used.

3. **Fast inversion:** The full inversion procedure of the operator $\frac{1}{C_m(\phi)}\Lambda^{\mathbb{T}}$ needs to be fast.

   Unlike the Laplacian $\triangle$ which can be factorized once by means of Cholesky factorisation and then inverted in this form at each time step, our operator depends on time and so it changes at each time step. This means that the entire computational cost has to be paid at each iteration.

This requirement, like the ones mentioned above, is non-negotiable. It, may possibly be overlooked if the function ϕ is somehow constant. However, this scenario is not of interest to us.

4. **High time resolution:** The characteristic time of charge of a cell is smaller than 1 [μs] and once the membrane is porated its characteristic time of discharge is a fraction of that. In the case of high conductivity of the intracellular and extracellular media, the effect of the electric field is amplified, further increasing the magnitude of $\partial_t v$. This is due to the multiplicative factor $\frac{\sigma_c \sigma_e}{\sigma_e + \sigma_c}$ which appears in the source term. As a result, this means that the problem naturally requires a high resolution in time to simulate.

   When dealing with nanopulses, as the electric field magnitude is particularly high (on the scale of 10^6 [V.m^{-1}]), the time step δt needed is really small (on the scale of 10^{-10} [V.m^{-1}]).

5. **Sign preserving scheme:** The numerical scheme of choice should ideally preserve the sign of the TMV. By this we mean that if the initial condition of the TMV is positive and the source term is null then the solutoin should stay positive for all time. This is particularly important when the membrane discharges as we expect the TMV to decrease to zero while remaining everywhere strictly positive (or negative, depending on the direction of the electric field).

   Of course, in the list of priorities, this property is last. Realistically speaking, when the TMV is small enough (in absolute value) its sign does not make a big difference. In particular, when considering a spherical cell we expect the parts of the cell facing the electrodes applying the PEF treatment to have opposite charge.

The list above is not particular to the case of a periodic membrane patch. In the case of a spherical cell, the same points apply. The first point may be less of a factor as the characteristic length in that case is the radius of the sphere which is usually in the length scale of $10 - 50$ [μs]. However, the number of points in the discretization of the sphere is orders of magnitude larger than for a patch, so other problems come into play.

We now focus on the semi-linear equation on the order parameter ϕ, again in the case of a bi-periodic membrane patch $\Gamma = (\mathbb{R}/L\mathbb{Z})^2$. Given a smooth $v\colon \mathbb{R}^+ \times \Gamma \to \mathbb{R}$ we wish to construct a numerical scheme for the following equation:

$$\begin{cases} \partial_t \phi - D \triangle_\Gamma \phi = -\alpha \mathcal{W}'(\phi) + \frac{\alpha}{2} C_m'(\phi) v^2, \text{ in } \Gamma, \forall t > 0, \\ \phi(0, \cdot) = 0. \end{cases}$$

For the most part, this equation is not so problematic as the one before. It is a local equation and so there is a choice between discretizing the unbounded operator $\triangle_\Gamma$ or diagonalizing it. Furthermore, the operator $\triangle_\Gamma$ does not depend on time and so it is possible to alleviate the cost of direct solvers used to invert $I_\mathrm{d} + \delta t \triangle_\Gamma$ at each iteration. Finally, there is a fair amount of literature on the subject of this equation, in particular regarding numerical schemes (for example, see [74, 50, 27, 96, 73]).

Solving the order parameter equation adds a last numerically difficulty:

6. **High mesh resolution:** As explained in Chapter 2 the solutions to the Allen-Cahn involve regions where they are essentially constant (with values near 0 or 1), with sharp interfaces between these regions. In practice, the numerical representations of these solutions usually require a higher space resolution near these interfaces than in the rest of the domain. Depending on the use case of the equation, this can be achieved by means of adaptive meshing or by just considering parameters in the equation which result in a bigger size of interface.

   In our case, we expect pores to appear in random places in the membrane, therefore adaptive meshing techniques are not a practical solution. Thus, we need a high space resolution in the whole domain and the size of the discretization is determined by the estimated size of the interface (which is naturally small).

   This condition, translates into very refined meshes (even for small patches of membrane). So, when considering a numerical scheme, its computational cost will play an important role as there is a high minimum-resolution required for any simulation. In practice, we expect one of these interfaces (which represents a pore edge) to be in the order of magnitude of 10^{-9} [m] (see Chapter 2) this is why $L \sim 10^{-7}$ [m] in our simulations.

From the above two lists, we can see that the main difficulty when dealing with both equations coupled together, is the combination of high resolution in time needed from one equation and high resolution in space needed from the other equation. For long pulses (longer than 50 [μs]), and big membrane patches (larger than 100 [μm^2]) this problem seems hard. Indeed, some of the solutions we found in the case of a membrane patch do not easily transfer to the spherical case.

Remark 40. *In the rest of this chapter, Γ and Λ respectively denote the boundary $(\mathbb{R}/\mathbb{Z})^2$ and the operator $\Lambda^{\mathbb{T}}$ from Section 2.3, unless otherwise indicated.*

3.3 Order 1 numerical scheme

In this section, we present a simple and fast numerical scheme to approximate the solution (v, ϕ) of the following rescaled partial differential equation

$$\partial_t \phi - \frac{D\tau}{L^2}\Delta_\Gamma \phi = -\tau\alpha \mathcal{W}'(\phi) + \frac{\tau\alpha}{2} C_m'(\phi) v^2, \text{ in } \Gamma, \forall t > 0, \tag{3.1a}$$

$$\frac{C_m(\phi)}{\tau}\partial_t v + S_m(\phi) v + \Lambda v = G, \text{ in } \Gamma, \forall t > 0, \tag{3.1b}$$

$$v(0, \cdot) = 0, \text{ in } \Gamma, \tag{3.1c}$$

$$\phi(0, \cdot) = 0, \text{ in } \Gamma, \tag{3.1d}$$

where $\tau > 0$ represents some characteristic time and $L > 0$ is the characteristic size of the membrane patch.

The idea is to try to solve each equation separately so that we can tackle the difficulties of each equation independently of the other. Once both equations can be solved independently then we coupled them by a taking the dependence of one equation on the other to be explicit.

Remark 41. *This approach to constructing a numerical scheme was mainly done to get the model up and running in code, so that we could verify the behavior of our model without caring too much for order of accuracy. It turns out, that the numerical schemes we used, naturally worked together in the case of the coupled problem and were then improved upon later on. We decided to present our scheme in this way (instead of just the final improved scheme) as it shows the ideas we used in a more understandable manner.*

3.3.1 Scheme to solve the Allen-Cahn equation

We start with the scheme for the equation of the evolution of the order parameter.

$$\begin{aligned}&\partial_t\phi - \frac{D_0\tau}{L^2}\Delta_\Gamma\phi = -4\tau\alpha a_1\phi(\phi-1)(\phi-1/2+3a_2/4a_1) + \frac{\tau\alpha}{2}C_m'(\phi)v^2, \text{ in }]0,+\infty[\times\Gamma,\\ &\phi(t=0)=\phi^0,\end{aligned}$$

where $x \in \Gamma \mapsto v(x)$ is constant in time. We solve this equation by using an operator splitting scheme (for an example see [50]). The surface Γ is discretised with a Cartesian grid.

Let $t^n > 0$ denote a point in time and $\delta t > 0$ denote a time step. We define Φ^n as the spatial discretisation of $\phi(t^n,\cdot)$ in our cartesian grid. At time $t^{n+1} := t^n + \delta t$ the numerical approximation Φ^{n+1} of $\phi(t^{n+1},\cdot)$ is obtained by numerically solving the following ordinary differential equation (ODE) at each node of the square grid $(x_p,y_q)_{\{p,q\}} \in \Gamma$

$$\frac{d\phi}{dt} = -4\tau\alpha a_1\phi(\phi-1)(\phi-1/2+3a_2/4a_1) + \frac{\tau\alpha}{2}C_m'(\phi)v^2, \quad t\in(t^n,t^{n+1}), \tag{3.2a}$$

$$\phi(t^n,(x_p,y_q)) = (e^{\delta t\triangle}\Phi^n)(x_p,y_q), \tag{3.2b}$$

where the term $e^{\delta t\triangle}$ in the initial condition, is the heat semigroup which can be explicitly calculated by diagonalising the Laplacian in Fourier domain. Concretely, if

$$\phi(t^n,\vec{x}) = \sum_{\vec{k}\in\mathbb{Z}^2} c_{\vec{k}} e^{2i\pi\vec{k}\cdot\vec{x}}, \quad \forall\vec{x}\in\Gamma, \tag{3.3}$$

then

$$e^{\delta t\triangle}\phi(t^n,\vec{x}) = \sum_{\vec{k}\in\mathbb{Z}^2} \left(e^{-\delta t 4\pi^2|\vec{k}|^2\frac{\tau D_0}{L^2}} c_{\vec{k}}\right) e^{2i\pi\vec{k}\cdot\vec{x}}.$$

The above calculation can be obtained explicitly for Φ^n by means of the Fast Fourier Transform (FFT). Once $e^{\delta t\triangle}\Phi^n$ is calculated, Equation (3.2) is numerically solved by means of a

Taylor method of order two. This approach is easy to implement and particularly fast to solve. It can be summarized as follows. Given Φ^n we obtain Φ^{n+1} in the following way

$$\begin{cases} \Phi^* = \mathrm{FFT}^{-1} \cdot \left(e^{-(\delta t) 4\pi^2 |\vec{k}|^2 \frac{\tau D_0}{L^2}} \right)_{\vec{k}} \cdot \mathrm{FFT}(\Phi^n), \\ \Phi^{n+1} = \Phi^* + \delta t F(\Phi^*)(1 + \frac{\delta t}{2} F'(\Phi^*)), \end{cases}$$

with

$$F : y \mapsto -4\tau\alpha a_1 y(y-1)(y - 1/2 + 3a_2/4a_1) + \frac{\tau\alpha}{2} C_m'(y) v^2. \tag{3.4}$$

Applying a Strang Splitting scheme to the above fractional step method gives order 2 accuracy in time [56]. Although when coupling both problems we may lose the second order of accuracy it does help with the constant factors multipling the error and it does not increase the computational cost by much. The Strang Splitting scheme we use takes the following form

$$\begin{cases} \Phi^* = \mathrm{FFT}^{-1} \cdot \left(e^{-(\frac{\delta t}{2}) 4\pi^2 |\vec{k}|^2 \frac{\tau D_0}{L^2}} \right)_{\vec{k}} \cdot \mathrm{FFT}(\Phi^n), \\ \Phi^{**} = \Phi^* + \delta t F(\Phi^*)(1 + \frac{\delta t}{2} F'(\Phi^*)), \\ \Phi^{n+1} = \mathrm{FFT}^{-1} \cdot \left(e^{-(\frac{\delta t}{2}) 4\pi^2 |\vec{k}|^2 \frac{\tau D_0}{L^2}} \right)_{\vec{k}} \cdot \mathrm{FFT}(\Phi^{**}), \end{cases}$$

Remark 42. *Operator splitting schemes are fairly standard as far as numerical schemes of the Allen-Cahn equation go. That is why this equation was the least problematic of the two in the coupled system.*

3.3.2 Scheme to solve the transmembrane voltage

Due to the rescaling, the equation on the TMV is given by

$$C_m(\phi)\partial_t v + \tau(S_m(\phi) + \Lambda)v = \tau G, \quad \forall t > 0, \quad \forall x \in \Gamma, \tag{3.5a}$$

$$v(0) = v_\diamond, \tag{3.5b}$$

where the operator Λ is described by the same eigenvalues as before (see Section 2.3), but with eigenfunctions

$$\omega_{(k_1,k_2)}(x,y) := e^{2i\pi(k_1 x + k_2 y)}, \quad \forall (k_1,k_2) \in \mathbb{Z}^2, \quad \forall x \in \Gamma.$$

Assume that the function $x \in \Gamma \mapsto \phi(x)$ is constant in time, as well as G (this choice is done mainly for simplicity). We denote by λ_0 the smallest eigenvalue of Λ, which we remind is given by the following formula (see Section 2.3)

$$\lambda_0 = \frac{1}{H} \frac{\sigma_e \sigma_c}{\sigma_c + \sigma_e}.$$

Let V^n denote the spatial discretisation of $v(t^n, \cdot)$, then to obtain the numerical approximation V^{n+1} of $v(t^{n+1}, \cdot)$ we numerically solve the following scheme (Strang operator splitting scheme already applied):

$$\frac{V^* - V^n}{\delta t/2} + \frac{\tau}{2}\frac{1}{C_m(\phi)}(\Lambda - \lambda_0)(V^* + V^n) = 0, \tag{3.6}$$

$$V^{**} = e^{-\tau\delta t\left(\frac{S_m(\phi)+\lambda_0}{C_m(\phi)}\right)}V^* + \frac{G}{S_m(\phi)+\lambda_0}\left(1 - e^{-\tau\delta t\left(\frac{S_m(\phi)+\lambda_0}{C_m(\phi)}\right)}\right), \tag{3.7}$$

$$\frac{V^{n+1} - V^{**}}{\delta t/2} + \frac{\tau}{2}\frac{1}{C_m(\phi)}(\Lambda^{\mathbb{T}} - \lambda_0)(V^{n+1} + V^{**}) = 0, \tag{3.8}$$

where $\Lambda^{\mathbb{T}} - \lambda_0^{\mathbb{T}}$ is a nonnegative symmetric operator. We remark that (3.7) corresponds to the ordinary differential equation (ODE) part of the splitting (exact formula for the solution of the ODE), while (3.6) and (3.8) correspond to the unbounded part of the splitting.

In order to invert equations (3.6) and (3.8) we use a Conjugate Gradient (CG) method [35]. For example, in the case of (3.6) this is possible by rewriting the linear problem as

$$AY = B$$

where

$$\begin{aligned} Y &:= \sqrt{C_m(\phi)}V^*, \\ A &:= \left(Id + \frac{\tau\delta t}{2}\frac{1}{\sqrt{C_m(\phi)}}\left(\Lambda^{\mathbb{T}} - \lambda_0^{\mathbb{T}}\right)\frac{1}{\sqrt{C_m(\phi)}}\right), \text{ and} \\ B &:= \left(\sqrt{C_m(\phi)} - \frac{\tau\delta t}{2}\frac{1}{\sqrt{C_m(\phi)}}\left(\Lambda^{\mathbb{T}} - \lambda_0^{\mathbb{T}}\right)\right)V^n. \end{aligned}$$

As A is symmetric positive definite operator (matrix) we can apply CG to solve this equation. Lastly, V^* is then recovered by dividing the solution Y by $\sqrt{C_m(\phi)}$.

Like for the case of the Allen-Cahn equation, this scheme should have an accuracy of order 2 in time.

Clarifications of this method

There are a few ideas to unpack in this scheme. First of all, the use of the splitting method.

As we described in Section 3.2, we are searching for an implicit scheme. We could at first just take a standard implicit scheme of order 1. This translates to inverting the following linear system:

$$(C_m(\phi) + \tau\delta t(S_m(\phi) + \Lambda))V^{n+1} = C_m(\phi)V^n + \tau\delta t G.$$

If we were to write this system in matrix form, it would involve the inversion of a full matrix. Therefore using a direct solver is not an option. As the problem is already symmetric we could use the conjugate gradient method to solve this linear system. However, in its current form,

this system is a badly conditionned. In practice $C_m(\phi) \sim 10^{-2}$ [F.m^{-2}], $S_m(1) \sim 10^9$ [S.m^{-2}] and $S_m(0) \sim 10^4$ [S.m^{-2}] therefore unless the characteristic time τ is small enough (or equivalently, δt is small enough) the condition number of the system is too large and this affects the convergence of the CG solver. We therefore precondition it while keeping it symmetric. By multiplying the above linear equation by $\sqrt{C_m(\phi) + \tau\delta t S_m(\phi)}$ and changing variables we get

$$\left(I_{\mathrm{d}} + \frac{\tau\delta t}{\sqrt{C_m(\phi) + \tau\delta t S_m(\phi)}}\Lambda\frac{1}{\sqrt{C_m(\phi) + \tau\delta t S_m(\phi)}}\right)\underbrace{\sqrt{C_m(\phi) + \tau\delta t S_m(\phi)}V^{n+1}}_{\text{new variable}} = B$$

where

$$B = \frac{C_m(\phi)V^n + \tau\delta t G}{\sqrt{C_m(\phi) + \tau\delta t S_m(\phi)}}.$$

We would then use the CG solver by using at each step of the algorithm the FFT (and its inverse) in order to quickly apply the non local operator Λ and the other operator $v \mapsto \frac{v}{\sqrt{C_m(\phi)+\tau\delta t S_m(\phi)}}$.

Although this solution seems reasonable, in practice it is extremely slow and solving the above linear problem is also numerically unstable in general. The reason for this seems to be, again, the membrane conductivity function $S_m(\phi)$. Again, if τ (or δt) is not small enough, then usually numerical errors accumulate and the solver does not converge.

The operator is too complicated to precisely explain how this happens although our intuition is the following. Just like in the case of a (discretized) Laplacian in a poisson equation (which is ill-conditioned), this system is also ill-conditioned. However, in the case of the Poisson equation, usually the source term typically is smooth (or at least not too heterogeneous), which implies that most of its higher eigenmodes are small. In this case, as the source term is divided by $\sqrt{C_m(\phi) + \tau\delta t S_m(\phi)}$ it means that if δt is not too small then, where there is a pore, there is a sharp transition in the source term. This activates high eigenmodes of the source term and so the natural ill-condition of the system kicks in.

Remark 43. *It is probable that this is not the only effect that takes place and maybe it could be fixed with some other preconditioning but further investigation of this approach seemed fruitless and so we looked at a different approach.*

At this point we consider a splitting scheme separating the unbounded term from the bounded conductive term. This explains our choice for the operator splitting scheme, which still allows our scheme to obtain order 2 accuracy in time (by using Strang splitting). It is also a natural choice as the both operators $v \mapsto \frac{S_m(\phi)}{C_m(\phi)}v$ and $v \mapsto \frac{1}{\sqrt{C_m(\phi)}}\Lambda\frac{1}{\sqrt{C_m(\phi)}}v$ produce two semigroups with different characteristic timescales.

Remark 44. *This was one of the motivating uses for this type of fractional methods. That is, to solve differential equations with operators with characteristic times of different scales of magnitude.*

The other noticeable idea in the scheme we presented above is removing the smallest eigenvalue λ_0 from Λ. This helps mantain the positivity of the scheme, the positivity really only enters into play in the PDE part of the splitting as the other split gives an exact solution (which always preserves positivity). This property has been tested for various forms of G and ϕ, all with remarkably positive results.

3.3.3 Coupled problem

A simple scheme to solve the system of partial differenatial equations is then obtained by combining the last two solvers. Meaning that, for a discrete numerical approximations (Φ^n, V^n) of $(\phi(t^n, \cdot), v(t^n, \cdot))$ we calculate the approximate solution (Φ^{n+1}, V^{n+1}) at time t^{n+1} by applying the above two solvers but replacing v by V^n in Equation (3.4) and $S_m(\phi)$ and $C_m(\phi)$ by $C_m(\Phi^n)$ and $S_m(\Phi^n)$ respectively in (3.6 - 3.8).

Concerning the properties of the schemes, both of them are of order 2 accuracy in time for their respective equations. Of course, no matter the order of accuracy of each scheme, when combined in this explicit manner we expect to the accuracy to be of order one when solving the coupled system of equations. Before continuing to the next section we finish this one by explaining how our schemes answer the difficulties listed at the beginning of this chapter:

1–2 Each independent solver is stable. The only caveat is that if δt is not small enough, then the CG solver becomes numerically unstable. Still, there is a net gain in the size we can take of δt before this numerical instability kicks in, at least we have seen it in our simulations.

3 The scheme for the TMV equation is quite fast. On average each iteration takes less than 9 iterations before the CG solver converges, and so we think we have a good enough preconditioner for the linear solver. The fact that we use the FFT also plays a big role in keeping the computation costs low. This is the most costly part of the scheme in this scenario as the ODE solver is explicit.

4 As a bonus, we do get the positivity property although this has only been tested for numerically. A proof of this is out of the scope of this work.

6 Regarding the scheme for the equation of the order parameter, because we do not discretize the Laplacian operator, the scheme is exact in space. This gives us the confidence to take only the necessary resolution in space to simulate the membrane and no more.

A more accurate scheme is presented in the next section to help with the high time resolution needed to simulate the problem.

3.4 Full order 2 numerical scheme

In this section we present an improved numerical scheme for the coupled system of equations. It is a natural extension of the last one presented in the last section and so we focus on clear

description of the scheme and not so much on the ideas behind it (they are essentially the same as in the order 1 scheme).

3.4.1 Scheme description

Let $T > 0$ denote final time of simulation for the equation (3.1), which we rewrite here for the convenience of the reader,

$$\partial_t \phi - \frac{D\tau}{L^2}\Delta_\Gamma \phi = -\tau\alpha \mathcal{W}'(\phi) + \frac{\tau\alpha}{2} C_m'(\phi) v^2, \text{ in } \Gamma, \forall t \in [0,T], \tag{3.9a}$$

$$\partial_t v + \frac{\tau S_m(\phi)}{C_m(\phi)} v + \frac{\tau}{C_m(\phi)} \Lambda v = \frac{\tau G}{C_m(\phi)}, \text{ in } \Gamma, \forall t \in [0,T], \tag{3.9b}$$

$$\phi(0,\cdot) = 0, \text{ in } \Gamma, \tag{3.9c}$$

$$v(0,\cdot) = 0, \text{ in } \Gamma. \tag{3.9d}$$

Let $N_t \in \mathbb{N}$, we divide the time interval in subintervals of size $\delta t := \frac{T}{N_t+1}$ so that $t^n := \frac{nT}{N_t+1}$, for $n = 0, \dots, N_t+1$. Similarly, let $N_x \in \mathbb{N}$, we consider the cartesian grid made of the points $(x_1^i, x_2^j) := (\frac{i}{N_x+1}, \frac{j}{N_x+1})$ where $i,j = 0,\dots,N_x$. We denote by $\left(\Phi_{i,j}^n\right)_{i,j}$ and $\left(V_{i,j}^n\right)_{i,j}$ the numerical approximations of $\phi(t^n, x_1^i, x_2^j)$ and $v(t^n, x_1^i, x_2^j)$ respectively. Finally, let $G_{i,j}^n := G(t^n, x_1^i, x_2^j)$ and $G^n = \left(G_{i,j}^n\right)_{i,j}$ be the numerical discretisation of the source term G and let $e^{\delta t D \Delta_\Gamma}$ denote the heat semigroup in $\Gamma = (\mathbb{R}/\mathbb{Z})^2$ evaluated at time δt. Given Φ^n and V^n, we consider the following fractional step scheme

$$\begin{cases} \Phi^* = e^{\delta t D \triangle_\Gamma} \Phi^n, \\ \frac{V^* - V^n}{\delta t} + \frac{1}{2}\left(\frac{1}{C_m(\Phi^*)}\left(\Lambda^{\mathbb{T}} - \lambda_{\vec{0}}^{\mathbb{T}}\right)V^* + \frac{1}{C_m(\Phi^n)}\left(\Lambda^{\mathbb{T}} - \lambda_{\vec{0}}^{\mathbb{T}}\right)V^n\right) = \frac{1}{2}\left(\frac{G^n}{C_m(\Phi^n)} + \frac{G^{n+1}}{C_m(\Phi^*)}\right) \end{cases} \tag{3.10}$$

$$\begin{cases} \begin{bmatrix} \Phi^{n+1} \\ V^{n+1} \end{bmatrix} = \begin{bmatrix} \Phi^* \\ V^* \end{bmatrix} + \delta t F\left(\begin{bmatrix} \Phi^* \\ V^* \end{bmatrix}\right) + \frac{\delta t^2}{2} \mathbb{J}F|_{(\Phi^*, V^*)} \cdot F\left(\begin{bmatrix} \Phi^* \\ V^* \end{bmatrix}\right) \end{cases} \tag{3.11}$$

where the function F is given by

$$F : \begin{bmatrix} \phi \\ v \end{bmatrix} \mapsto \begin{bmatrix} -\alpha \mathcal{W}'(\phi) + \frac{\alpha}{2} C_m'(\phi) v^2 \\ -\frac{(S_m(\phi) + \lambda_{\vec{0}}^{\mathbb{T}})}{C_m(\phi)} v \end{bmatrix},$$

and its Jacobian, $\mathbb{J}F$, is given by

$$\begin{bmatrix} \phi \\ v \end{bmatrix} \mapsto \begin{bmatrix} -\alpha \mathcal{W}''(\phi) + \frac{\alpha}{2} C_m''(\phi) v^2 & \alpha C_m'(\phi) v \\ -\left(\frac{S_m'(\phi) C_m(\phi) - C_m'(\phi)(S_m(\phi) + \lambda_{\vec{0}}^{\mathbb{T}})}{C_m^2(\phi)}\right) v & \frac{S_m(\phi) + \lambda_{\vec{0}}^{\mathbb{T}}}{C_m(\phi)} \end{bmatrix}.$$

Therefore we solve each of the following problems with second order accuracy:

$$\partial_t \begin{bmatrix} \phi \\ v \end{bmatrix} = \begin{bmatrix} D\triangle_{\mathbb{T}} & 0 \\ 0 & -\frac{1}{C_m(\phi)}(\Lambda^{\mathbb{T}} - \lambda_{\vec{0}}^{\mathbb{T}}) \end{bmatrix} \begin{bmatrix} \phi \\ v \end{bmatrix} + \begin{bmatrix} 0 \\ \frac{G}{C_m(\phi)} \end{bmatrix} \tag{3.12}$$

$$\frac{d}{dt}\begin{bmatrix}\phi\\ v\end{bmatrix} = F\left(\begin{bmatrix}\phi\\ v\end{bmatrix}\right). \tag{3.13}$$

Again, a Strang splitting scheme then should allow us to get second order accuracy in time. The first part of the fractional step scheme, Eq. (3.10), can be solved as a decoupled problem. In fact, we can apply the heat semigroup to solve the equation of the first coordinate in Eq. (3.12) by means of the Fast Fourier Transform. Once Φ^n and Φ^* are known, then solving for V^* is done by means of a CG algorithm used along with the FFT, as before. The idea is to symmetrise the second equation in (3.10) by rewriting it as a problem on a new variable $Y := \sqrt{C_m(\Phi^*)}V^*$ as follows

$$\left[Id + \frac{\delta t/2}{\sqrt{C_m(\Phi^*)}}(\Lambda^{\mathbb{T}} - \lambda_{\vec{0}}^{\mathbb{T}})\frac{1}{\sqrt{C_m(\Phi^*)}}\right]Y = B$$

where

$$B = \sqrt{C_m(\Phi^*)}\left[\left[Id - \frac{\delta t/2}{C_m(\Phi^n)}(\Lambda^{\mathbb{T}} - \lambda_{\vec{0}}^{\mathbb{T}})\right]V^n + \frac{\delta t}{2}\left[\frac{G^n}{C_m(\Phi^n)} + \frac{G^{n+1}}{C_m(\Phi^*)}\right]\right].$$

The second part of the scheme, Eq. (3.11), is a second order Taylor scheme for the ordinary differential equation (ODE) shown in Eq. (3.13).

Remark 45. *As is usual for iterative solvers, in the CG algorithm we use a residue tolerance according to the expected error of our scheme. In this case we expect second order accuracy in time at most. Therefore, we take the residue tolerance threshold to be of the form* $CG_{threshold} := \max(10^{-2}(N_t)^{-3}, 5\cdot 10^{-8})$.

Let $U^n := (\Phi^n, V^n)$, we rewrite the fractional step scheme presented above as

$$\begin{aligned} U^* &= \mathcal{N}_{\text{PDE}}(U^n, t^n, \delta t), \quad \text{representing the one-step numerical method of Eq. (3.10)},\\ U^{n+1} &= \mathcal{N}_{\text{ODE}}(U^*, \delta t), \quad \text{representing the one-step numerical method of Eq. (3.11)}, \end{aligned}$$

then, our choice of Strang splitting can be written as

$$\begin{cases} U^* = \mathcal{N}_{\text{PDE}}(U^n, t^n, \frac{\delta t}{2}),\\ U^{**} = \mathcal{N}_{\text{ODE}}(U^*, \delta t),\\ U^{n+1} = \mathcal{N}_{\text{PDE}}(U^{**}, t^n + \frac{\delta t}{2}, \frac{\delta t}{2}). \end{cases} \tag{3.14}$$

Remark 46. *In the above scheme, the numerical method* $\mathcal{N}_{PDE}$ *will use the source term* G *evaluated at times* t^n, t^{n+1} *and* $t^{n+\frac{1}{2}} := t^n + \frac{\delta t}{2}$.

3.4.2 Convergence test

All the parameters and modeling choices for functions are given in Tables 3.1 and 3.2.

	Value	Description	Reference
D_0	2×10^{-12} [$m^2.s^{-1}$]	lateral diffusion of lipids in the cell membrane	[51]
ϵ_0	8.85×10^{-12} [$F.m^{-1}$]	vacuum permittivity	[59]
ϵ_w	80	relative water permittivity	[91]
ϵ_l	2	relative lipid permittivity	[91]
σ_c	1 [$S.m^{-1}$]	interior medium conductivity	[77, 76]
σ_e	1.5 [$S.m^{-1}$]	exterior medium conductivity	[76, 77]
σ_l	3×10^{-5} [$S.m^{-1}$]	lipid membrane conductivity	[19, 41]
σ_w	1 [$S.m^{-1}$]	pore conductivity	[19, 41]
h	5×10^{-9} [m]	membrane thickness	[41]
δ^h	10^{-9} [m]	pore edge size	Section 2.5.1
α	9.26×10^6 [$m^2.J^{-1}.s^{-1}$]	kinetic coefficient of our model	Section 2.5.2
a_1	5.44×10^{-1} [$J.m^{-2}$]	measures energy barrier between the stable states	Section 2.5.1
a_2	2.0×10^{-6} [$J.m^{-2}$]	measures the surface tension of the membrane	Section 2.5.1
E	3.2×10^6 [$V.m^{-1}$]	Electric field magnitude of applied electric pulse.	
R_0	10^{-5} [m]	Cell radius.	

Table 3.1: Physically relevant values of parameters used in the simulations.

Modeling choices in our model	
$H := \frac{R_0}{2}\frac{\sigma_c+2\sigma_e}{\sigma_c+\sigma_e}$	Distance between electrodes.
$\vartheta_1 : \phi \mapsto 0.5(1+\tanh(-15(\phi-1)))$	Adhoc smooth cutoff function.
$\vartheta_2 : \phi \mapsto 0.5(1+\tanh(13(\phi-1)))$	Adhoc smooth cutoff function.
$C_m : \phi \mapsto \frac{\varepsilon_0}{h}\left(\left[\epsilon_l^{1/3} + \phi(\epsilon_w^{1/3} - \epsilon_l^{1/3})\right]^3 \vartheta_1(\phi) + \epsilon_w \vartheta_2(\phi)\right)$	Membrane capacitance.
$S_m : \phi \mapsto \frac{1}{2h}((\sigma_w - \sigma_l)(1+\tanh(100(\phi-0.5))) + 2\sigma_l)$	Membrane surface conductivity.
$\mathcal{W} : \phi \mapsto a_1\phi^2(1-\phi)^2 + a_2(\phi+0.5)(\phi-1)^2$	Membrane energy potential.
$G_0 : (x_1, x_2) \mapsto \frac{2\sigma_e\sigma_c E}{\sigma_e+\sigma_c}$	Source term from constant electric field.
$G : (t, x_1, x_2) \mapsto \mathbb{1}_{[0,T_p]}(t) \cdot G_0(x_1, x_2)$	Source term of duration T_p.

Table 3.2: For the purposes of testing it is only important that they be smooth although they are also a natural choice for numerical experimenting (as explained in Chapter 2).

Let $\vec{p} = (p_0, p_1, p_2), \vec{q} = (q_0, q_1, q_2) \in \mathbb{R} \times \mathbb{Z}^2$. To test the convergence of (3.14) in our setting we add an appropriate source terms to (3.9) so that the following functions

$$\begin{bmatrix}\phi_0 \\ v_0\end{bmatrix} = \frac{1}{2}\begin{bmatrix}1+\sin(2\pi(p_0 t + p_1 x_1 + p_2 x_2)) \\ 1+\cos(2\pi(p_0 t + q_1 x_1 + q_2 x_2))\end{bmatrix}$$

are an exact solution to the problem. This results in the following equation

$$\begin{cases} \partial_t \phi - \frac{\tau D}{L^2}\Delta_\Gamma \phi = -\alpha\tau \mathcal{W}'(\phi) + \frac{\tau\alpha}{2} C_m'(\phi) v^2 + S_{\vec{p}}, \quad \forall x \in \mathbb{T},\, \forall t > 0, \\ \partial_t v + \tau\left(\frac{S_m(\phi)}{C_m(\phi)} + \frac{1}{C_m(\phi)}\Lambda^{\mathbb{T}}\right) v = \frac{\tau S_{\vec{q}}}{C_m(\phi)}, \quad \forall x \in \Gamma,\, \forall t > 0, \\ v_{|t=0} = \frac{1+\cos(2\pi(q_1 x_1 + q_2 x_2))}{2}, \quad \phi_{|t=0} = \frac{1+\sin(2\pi(p_1 x_1 + p_2 x_2))}{2}, \quad \forall x \in \mathbb{T}. \end{cases}$$

where the functions $S_{\vec{p}}$ and $S_{\vec{q}}$ are given by

$$\begin{aligned} S_{\vec{p}} &: (x,t) \mapsto \partial_t \phi_0(t,x) - \frac{\tau D}{L^2}\Delta_\Gamma \phi_0(t,x) + \tau\alpha \mathcal{W}'(\phi_0(t,x)) - \frac{\tau\alpha}{2} C_m'(\phi_0(t,x)) v_0^2(t,x), \\ S_{\vec{q}} &: (x,t) \mapsto C_m(\phi_0(t,x))\partial_t v_0(t,x) + \tau S_m(\phi_0(t,x)) v_0(t,x) + \tau \Lambda^{\mathbb{T}} v_0(t,x). \end{aligned}$$

We incorporate the additional source terms into the above scheme (3.14) by replacing G by $S_{\vec{q}}$ and by adding $S_{\vec{p}}$ to the ODE splitting (thereby considering a nonautonomous ODE instead of (3.13)). Let $S^n_{\vec{q},i,j} := S_{\vec{q}}(t^n, x_1^i, x_2^j)$ and $S^n_{\vec{q}} = \left(S^n_{\vec{q},i,j}\right)_{i,j}$ be the numerical discretisation of the source $S_{\vec{q}}$. Our concrete fractional step testing scheme is written as

$$\tilde{\mathcal{N}}_{\text{PDE}} \leftarrow \begin{cases} \Phi^* = e^{\delta t \Delta_\Gamma}\Phi^n, \\ \frac{V^* - V^n}{\delta t} + \frac{1}{2}\left(\frac{1}{C_m(\Phi^*)}\left(\Lambda^{\mathbb{T}} - \lambda_{\vec{0}}^{\mathbb{T}}\right)V^* + \frac{1}{C_m(\Phi^n)}\left(\Lambda^{\mathbb{T}} - \lambda_{\vec{0}}^{\mathbb{T}}\right)V^n\right) = \frac{1}{2}\left(\frac{S^n_{\vec{q}}}{C_m(\Phi^n)} + \frac{S^{n+1}_{\vec{q}}}{C_m(\Phi^*)}\right) \end{cases}$$

$$\tilde{\mathcal{N}}_{\text{ODE}} \leftarrow \left\{ \begin{bmatrix} \Phi^{n+1} \\ V^{n+1} \end{bmatrix} = \begin{bmatrix} \Phi^* \\ V^* \end{bmatrix} + \delta t \tilde{F}\left(t^n, \begin{bmatrix} \Phi^* \\ V^* \end{bmatrix}\right) + \frac{\delta t^2}{2}\left[\partial_t \tilde{F}\left(t^n, \begin{bmatrix} \Phi^* \\ V^* \end{bmatrix}\right) + \mathbb{J}\tilde{F}_{|(t^n, \Phi^*, V^*)} \cdot \tilde{F}\left(t^n, \begin{bmatrix} \Phi^* \\ V^* \end{bmatrix}\right)\right] \right.$$

where the function $\tilde{F}$ is given by

$$F : \left(t, \begin{bmatrix} \phi \\ v \end{bmatrix}\right) \mapsto \begin{bmatrix} -\alpha\mathcal{W}'(\phi) + \frac{\alpha}{2} C_m'(\phi) v^2 + S_{\vec{p}}(t) \\ -\frac{(S_m(\phi) + \lambda_{\vec{0}}^{\mathbb{T}})}{C_m(\phi)} v \end{bmatrix}.$$

Now our testing scheme consists of applying the above numerical methods $\tilde{\mathcal{N}}_{\text{PDE}}$ and $\tilde{\mathcal{N}}_{\text{ODE}}$ in the same manner as in (3.14).

Remark 47. *Unlike in the scheme (3.14), in addition to U^* and δt, $\tilde{\mathcal{N}}_{ODE}$ will also depend on t^n.*

We can now continue with some numerical results. In Figure 3.1 we show some numerical evidence of second order convergence in time. This is in accordance with what we expect from a Strang splitting scheme.

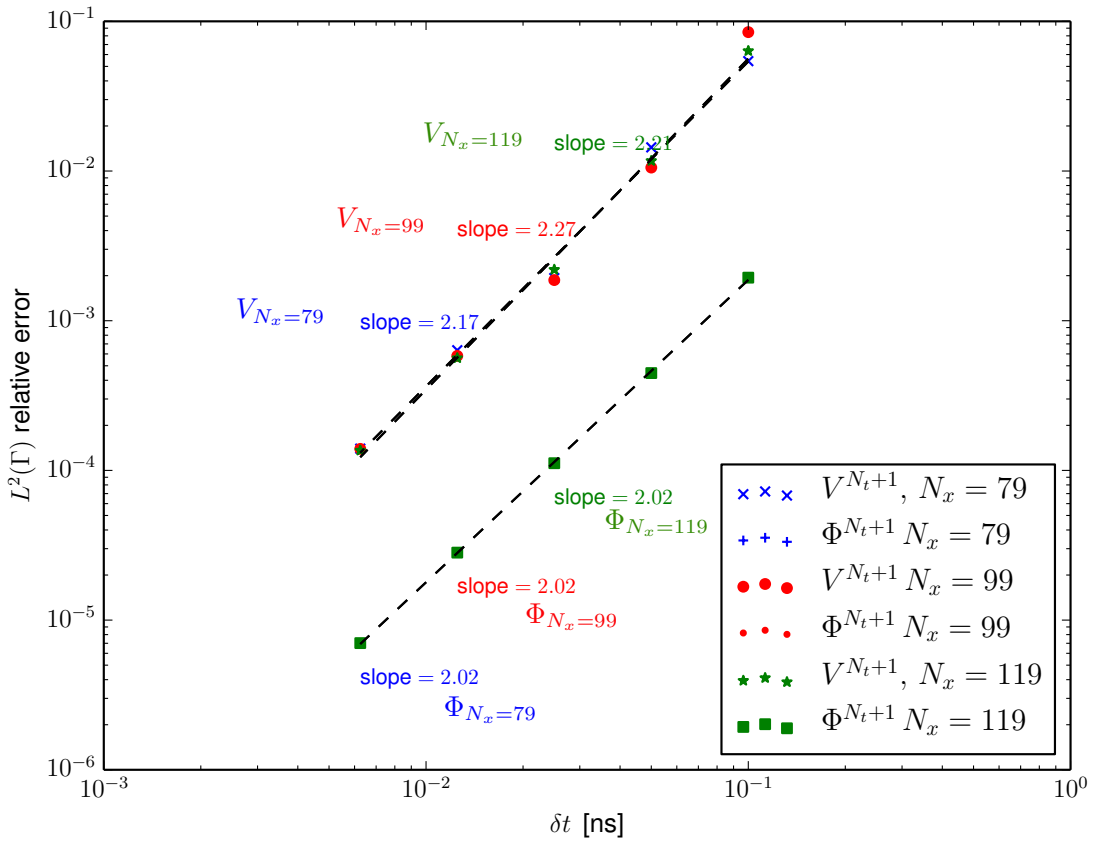

Figure 3.1: Convergence test for $\vec{p} = (0.2, 2, 0)$ and $\vec{q} = (1, 0, 3)$. In this test the characteristic length of the membrane is $L = 500$ [nm] and the final time of the simulation is $t^{N_t+1} = 1$ [ns].

Remark 48. *As we diagonalise both $\triangle_\Gamma$ and Λ^Γ, the error due to the usual discrete approximation of differential operators does not appear. In other words, the error in consistency of our scheme depends only on the size of δt. We show evidence for this by testing our scheme for numerical convergence in time for different values in N_x, see Figure 3.1.*

3.5 Numerical Experiments

In the rest this chapter we run some numerical experiments of our model under physically realistic conditions.

3.5.1 Simulation of coupled system

We simulated a flat bi-periodic membrane of size $L = 200$ [nm], see Figure 2.2-Right, under the influence of a 12 [ns] square pulse of a uniform electric field of intensity $|E| = 3.2 \times 10^6$ [V.m^{-1}]. After the membrane discharges its TMV we continue to simulate it for another 10 [μs]. We

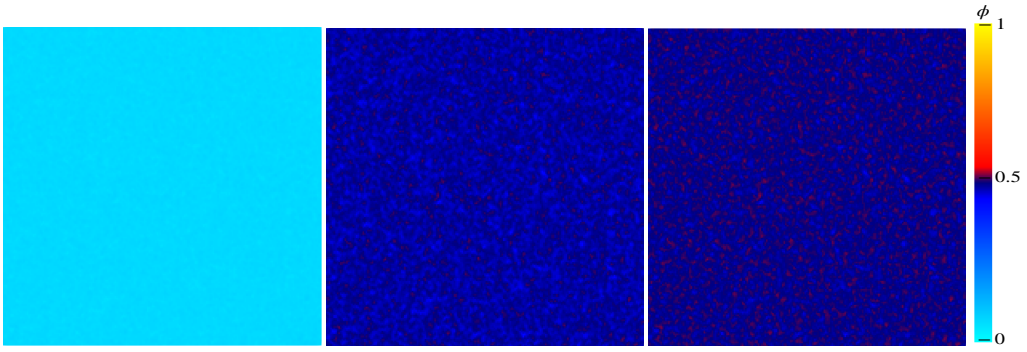

(a) ϕ at $t = 12$ [ns]. (b) ϕ at $t = 27.5$ [ns]. (c) ϕ at $t = 30$ [ns].

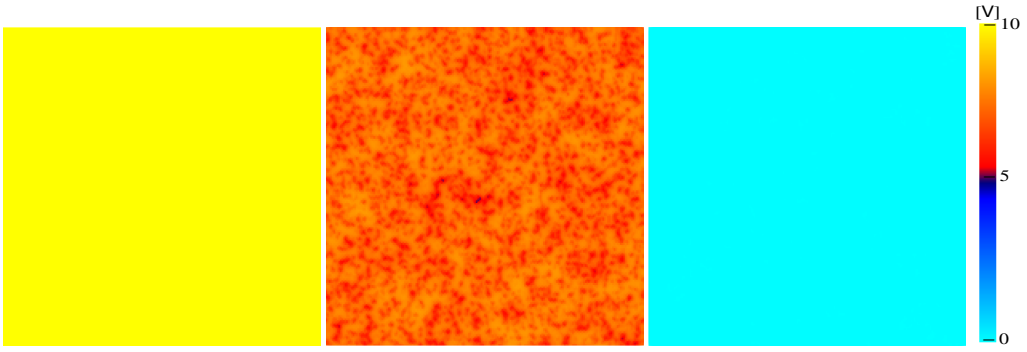

(d) v at $t = 12$ [ns]. (e) v at $t = 27.5$ [ns]. (f) v at $t = 30$ [ns].

Figure 3.2: Simulations of System (3.9). The upper row of corresponds to the membrane order parameter ϕ while the bottom row are the associated TMV.

pick as the initial condition

$$\phi_\diamond : (x, y) \mapsto \mu(x, y) \tag{3.15}$$

where $|\mu| < 1.5 \cdot 10^{-2}$ is a Gaussian random noise (which has been smoothed for numerical stability purposes).

We can see in Figure 3.2 the evolution of the TMV shortly after the initial electric pulse. During the initial charge time the TMV increases almost linearly, until about $t = 12$ [ns]. At this time, the electric field is turned off but the membrane remains charged. It then discharges as a capacitor, slowly over time, while the order parameter continues to evolve under the influence of the remaining TMV. At around $t = 27$ [ns] the conductive effect of the membrane enters into play. At this point, the membrane is still charged but now discharges mainly through the high conductivity spots that result from the affected order parameter ($\phi > 1/2$). These places can be seen more easily in Figure 3.2e in the distribution of the TMV on the membrane. However, as the membrane charge is small, the membrane discharges within nanoseconds of this configuration taking place. This sudden discharge of the TMV leads us to consider that electroporation has occurred, although a clear membrane configuration as the one described in Property 22 does not take place but until about 1 μs later. This is in accordance with the time estimate described in that property. The initial

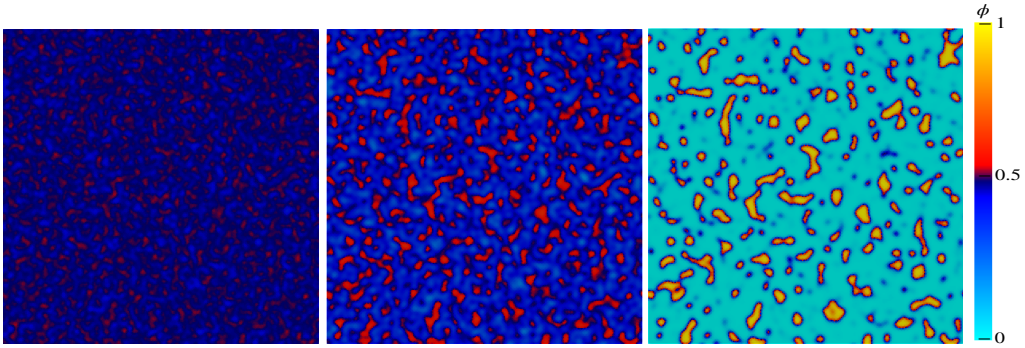

(a) ϕ at $t = 0.235$ [μs]. (b) ϕ at $t = 0.635$ [μs]. (c) ϕ at $t = 1.435$ [μs].

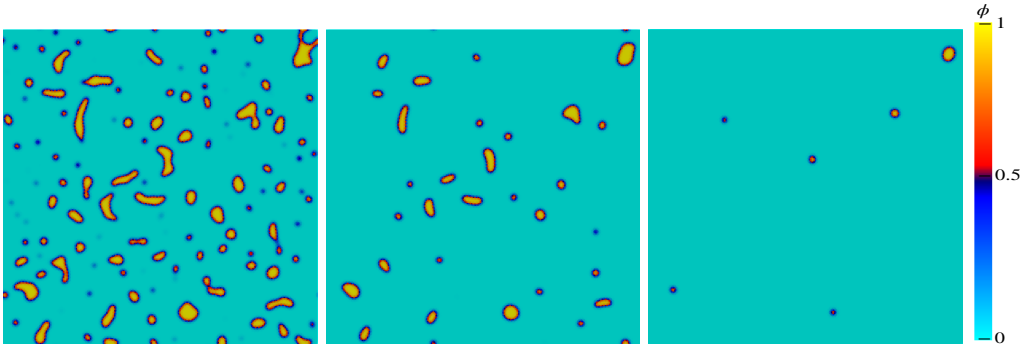

(d) ϕ at $t = 2.435$ [μs]. (e) ϕ at $t = 5.035$ [μs]. (f) ϕ at $t = 10.035$ [μs].

Figure 3.3: Continuing the evolution of the membrane order parameter ϕ for 10 [μs] after the end of the pulse delivery.

perturbation of the membrane grows (between $t = 0$ [ns] and $t = 30$ ns) resulting in a stronger perturbation in accordance with linear instability analysis done in Section 2.4.

Remark 49. *In fact, were we to take an affine function for $\phi \mapsto C_m(\phi)$, this behavior would be completely lost. This is not only suggested by the linear instability analysis but we also tested for it in practice.*

In this setting the membrane is almost completely discharged by $t = 33$ [ns]. From that point on, the transmembrane voltage does not play a significant role and only the Allen-Cahn equation drives the membrane dynamics.

The lifetime of pores depends on their size. After the pulse, the pores remain open for several microsecond as shown in Figure 3.3. It is worth noting that the pore closure is driven by the mean curvature, as stated for the Allen-Cahn equation by Bellettini [6]. This has to be linked to Kroeger *et al.* paper in which a curvature-driven pore closure is proposed [42]. That is why we see the pores becoming rounder as they shrink in size in Figure 3.3.

Remark 50. *With respect to computational efficiency, we report that the entire simulation took about 3 hours and a half in a computer armed with a 2.4 GHz Dual-Core Inter Core i5 processor. The first 35 [ns] of simulation took a little more than 3 hours and the rest of the time was used to simulate the next 10 [μs]. For the first 35 [ns] we used a time step of $\delta t = 0.02$ [ns] and for the rest of the simulation $\delta t = 15$ [ns]. We highlight the fact that our implementation has not been fully optimized nor parallelized. This is a crucial point to increasing the size L of the membrane patch we can simulate. We do not forsee any unsurmountable problems for this as one part of the splitting is solving an ODE at each point of the grid, and the other is mainly done with FFT.*

3.5.2 Evolution of the electric properties of the membrane

To better visualize the dielectric breakdown of the membrane, in this section we plot the electric properties of the membrane as they evolve in time, instead of the order parameter ϕ, as in the section above. Replicating the same numerical experiment as in the Section 3.5.1, we show the evolution of the electric properties of the membrane during the pulse until it discharges in Figure 3.4.

The creation of pores can be more easily read in the graph showing the conductivity of the membrane due to the small locations where there is a huge spike in conductivity $S_m(\phi)$. In contrast, we see that the capacitance of the membrane changes more uniformly in space. We do highlight the fact that the change in capacitance is not negligible. This can be seen more clearly in Figure 3.5, where we plot the evolution in time of the mean relative capacitance of the membrane.

In fact, we can see in Figure 3.5 three notable characteristic stages of the membrane during and shortly after the electric pulse delivery. The first 12 [ns], the membrane charges due to the constant intensity pulse (3.2×10^6 [V.m^{-1}]) being applied. During this stage the behavior of the membrane is almost linear as there is little change in the order parameter and the pulse duration is much smaller than the characteristic time of charge of the membrane.

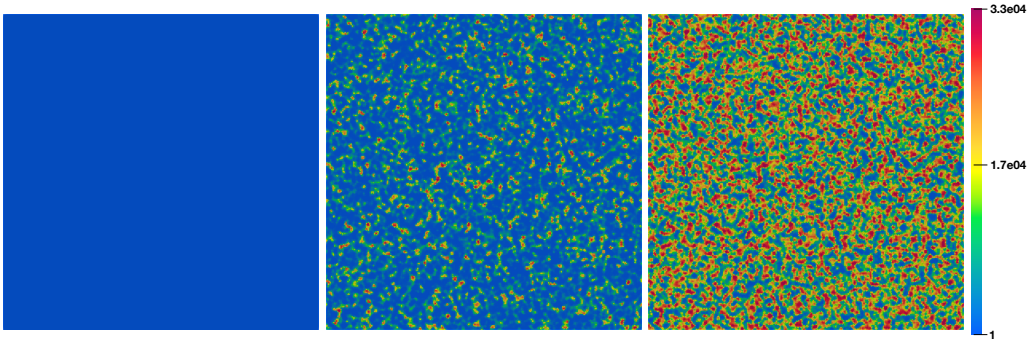

(a) $\frac{S_m(\phi)}{S_m(0)}$ at $t = 12$ [ns]. (b) $\frac{S_m(\phi)}{S_m(0)}$ at $t = 27$ [ns]. (c) $\frac{S_m(\phi)}{S_m(0)}$ at $t = 32.5$ [ns].

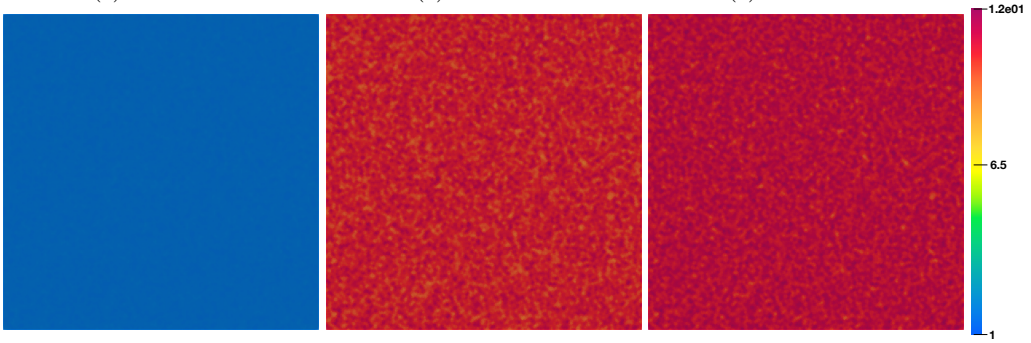

(d) $\frac{C_m(\phi)}{C_m(0)}$ at $t = 12$ [ns]. (e) $\frac{C_m(\phi)}{C_m(0)}$ v at $t = 27$ [ns]. (f) $\frac{C_m(\phi)}{C_m(0)}$ at $t = 32.5$ [ns].

Figure 3.4: Evolution of the relative electric properties during the membrane charge and discharge stage.

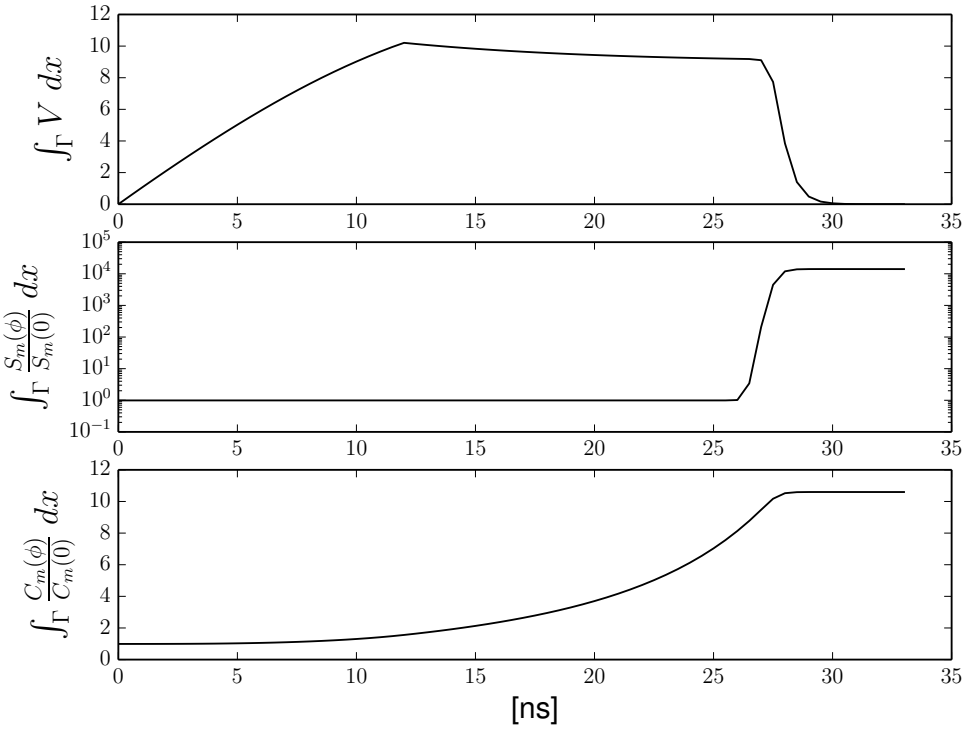

Figure 3.5: This shows the evolution of the mean electric properties of the membrane over time. It shows the same time frame used in Figure 3.4. Due to the different orders of magnitude in the membrane conductivity, we show the plot of $t \mapsto \int_\Gamma \frac{S_m(\phi)}{S_m(0)} \mathrm{d}x$ in logarithmic scale.

Just after the pulse ends, at 12 [ns], the membrane starts discharging, the cusp in the plot of $t \mapsto \int_\Gamma V$ is due to the discontinuity of the electric field (we turn the electric pulse off instantaneously). This discharging is primarily the membrane acting as a capacitor (the membrane conductivity is still not important enough). It is important to note that during this discharge, the membrane capacitance changes considerably. The third stage is when dielectric breakdown takes place (at around 27 [ns]) and there is a sudden membrane discharge. This can be seen clearly in the plots as both the conductivity suddenly increases and the TMV plummets at the about the same time.

3.5.3 Effect of membrane size on the TMV

In this section, we numerically show the influence the characteristic length L of the membrane has on the shape of the TMV. To this end, we decouple problem (3.9) and only focus on the effect of the membrane order parameter ϕ on the TMV. The basic setup is to consider a membrane with one smooth round stationary pore in the center. This membrane is under the effect of a constant electric field of magnitude E (see Table 3.1), therefore source term G is the one used in Table 3.2. The explicit order parameter we consider in Figure 3.6 is given by

$$\phi_{\text{pore}} : (x_1, x_2) \mapsto 1 - \tanh(5(\sin^2(\pi(x_1 - 0.5)) + \sin^2(\pi(x_2 - 0.5)))^2). \tag{3.16}$$

The results of can be seen in Figure 3.6. We can see the effect of the membrane size in the distribution of the TMV. The smaller the size of the membrane the flatter the TMV tends to be. In fact, for the bigger membrane not only is is the maximum value of the TMV bigger than in the smaller membrane, the minimum value is also smaller than in the smaller membrane. This suggests that taking $L > 0$ too small may artificially alter the behavior of the TMV and therefore that of the membrane. This effect can be easily explained if we periodically extend the smaller membrane patch to cover the same area of the bigger patch. As the bigger membrane is four times bigger than the smaller area, the periodic extension of the order parameter above is given by

$$\phi_{4\,\text{pores}}(x_1, x_2) = 1 - \tanh(5(\sin^2(\pi(2x_1 - 0.5)) + \sin^2(\pi(2x_2 - 0.5)))^2). \tag{3.17}$$

With this extension now we have two order parameters defined in membrane of the same size and can therefore compare the resulting TMV. The result of this simulation can be seen in Figure 3.7. In this case, we get four repeated copies of the TMV distribution we get in Figure 3.6 with one pore in a membrane of size $L = 100$ [nm].

In fact, we can see that the larger the value of L the more membrane configurations that are possible (think of the membrane as an actual infinite plane due to the periodic boundary conditions). This shows a correct way to compare two flat membrane patches of different sizes L. We consider a big enough periodic extension of each of the membranes so that both extended membranes have the same dimensions (this could potentially mean we consider the whole plane). Then, we can compare the state of both membranes at this scale, as we consider two patches of the same size. This means that if the value of L is

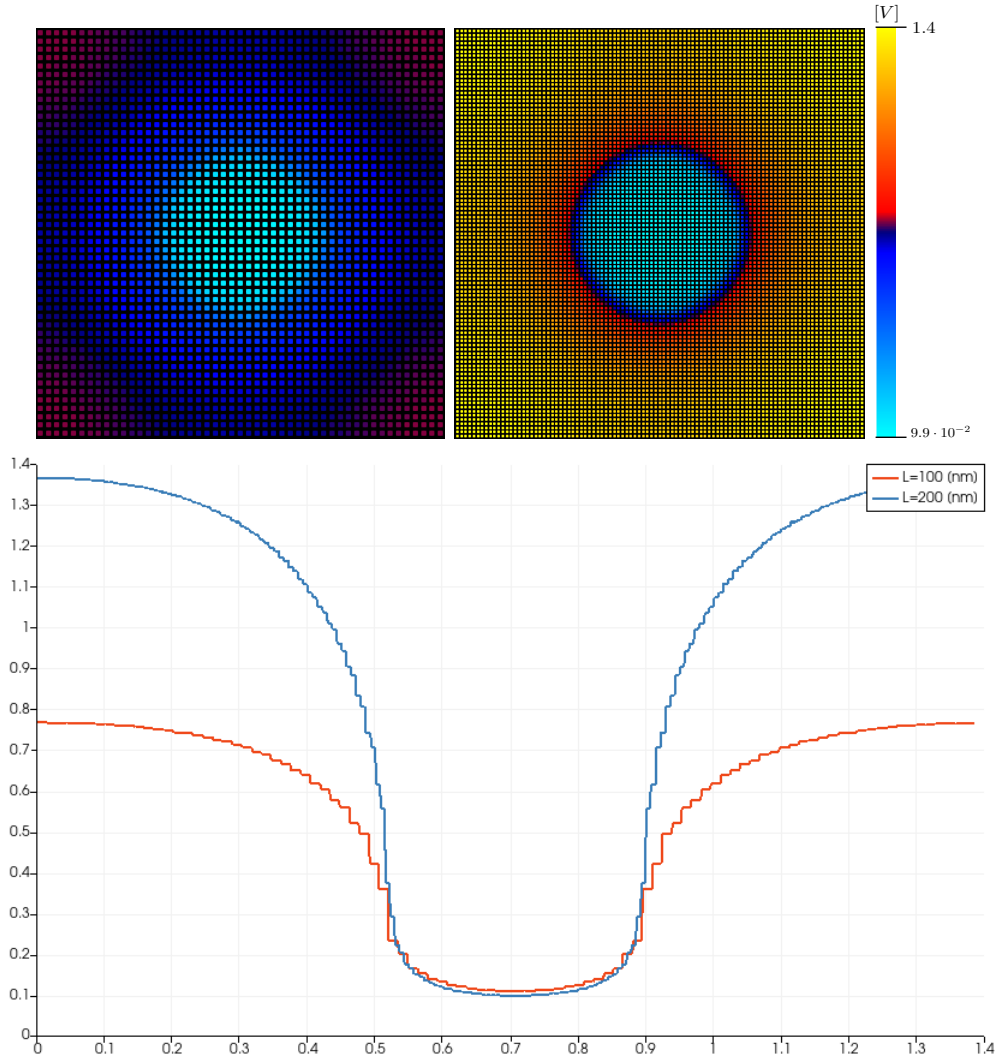

(a) Diagonal cut (lower left corner to upper right corner) of these two simulations.

Figure 3.6: We simulate the charging of the membrane with order parameter given by (3.16) and with null TMV as initial condition for 15 [ns]. This seems enough to get close enough to the stationary state of the TMV. The resolution for each simulation is the same, by this we mean that $\frac{1+N_x}{L}$ is the same in both cases. The upper left image shows the TMV associated to membrane of length $L = 100$ [nm], and $N_x = 49$. Its diagonal cut is displayed in the bottom graph as the red curve. The upper right image shows TMV associated to membrane of length $L = 200$ [nm], and $N_x = 99$. Its diagonal cut is displayed in the bottom graph as the blue curve.

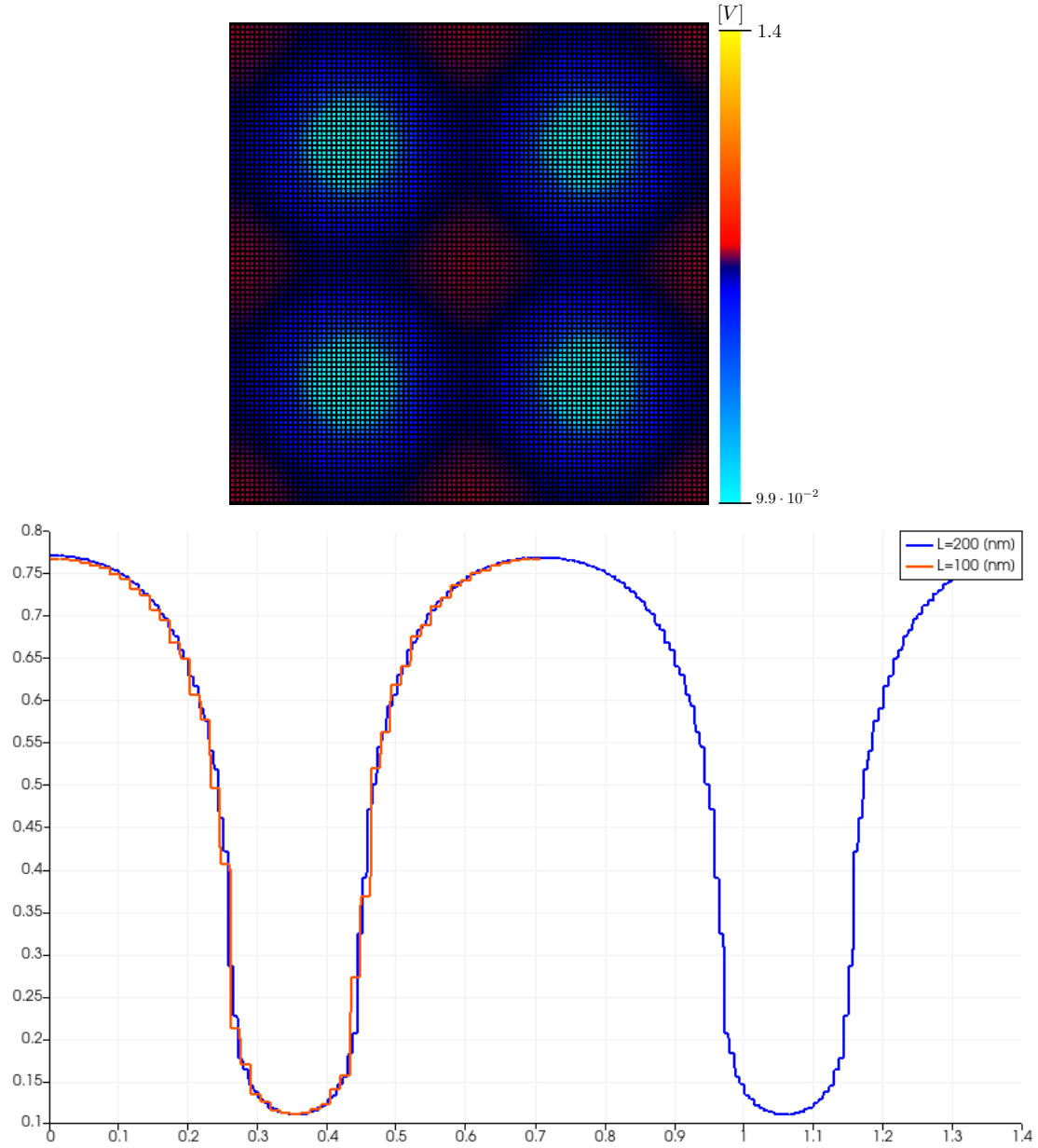

Figure 3.7: We simulate the charging of the membrane with null TMV as initial condition for 15 [ns]. We consider the same setup as in Figure 3.6, but the order parameter ϕ is given by Eq. (3.17) this time. The upper image shows the TMV associated to membrane of length $L = 200$ [nm] ($N_x = 99$). We compare this solution with the numerical solution we got before (small patch, $L = 100$ [nm] in Figure 3.6). The diagonal cut of this simulation is shown in blue in the graph below the simulation. It is compared with the diagonal cut from TMV obtained for $L = 100$ [nm] in Figure 3.6 (shown in red, as in the graph in Figure 3.6).

too small, whenever the membrane has one pore it is equivalent to a large plane with many small pores which tend to flatten the resulting TMV. Larger values of L lead to potentially more heterogeneous membrane configurations, which then implies more heterogeneous TMV configurations. This illustrates the point made in Chapter 2, where we suggest that the best option for this model is to take L as large as possible. If an interaction between the membrane and the TMV results in a flat TMV profile when $L \gg 1$, it would be a natural consequence of the model and not an artificial effect resulting from a using a not big enough patch. Of course, the notion of what is a big enough patch is not evident from what we have shown until now. An appropriate size L of a patch would probably be something on the lengthscale of the cell, although this intuition would have to be verified numerically by simulating the whole cell membrane (for example in the case of a spherical cell).

3.5.4 Sensitivity Analysis of our model

In this section we simulate (3.9) applying a square pulse of duration $T_p = 12$ [ns] (see Table 3.2) to a membrane patch of size $L = 200$ [nm] ($N_x = 199$). After membrane discharge (when the TMV is of order 10^{-4} or smaller), we continue our simulation but only considering the order parameter equation (under the assumption of null TMV). This can be done with the same splitting operator scheme, only it is just applied to the evolution equation on ϕ. Most plots in this section start 50 [ns] after the start of the square pulse (by this time the membrane has already been discharged). The only time this isn't the case corresponds to the tests for different conductivities of the intracellular and extracellular media. This is because, depending on the conductivity the membrane discharge can have much later (at around 100 [ns]) or sooner (at around 21 [ns]).

We show a sensitivity analysis of the electroporation model to some of its variables. The non-linearity of the problem along with the high number of parameters in the model forces us to consider only a part of the parameter space. We fix one set of parameters (see Table 3.1 and 3.2), and then we test the sensitivity of the model to changes in values around this fixed set. We denote this fixed set as the base case, and we display the results associated to this fixed in black in all the graphs. Due to the complexity of comparing different simulations, we compare the evolution of the membrane where $\{\phi > 0.5\}$ for each simulation. By this, we mean that we look at plot of the function

$$t \mapsto \int_{\Gamma \cap \{\phi > 0.5\}} \phi(t, x) dx$$

for different parameter values in each test.

Noise sensitivity

To test for noise sensitivity, we fix one realisation of a Gaussian noise $\Pi_{\text{rough}} \sim \mathcal{N}(0, 1)$ on $\mathbb{T}$. We then smooth it a bit by applying the heat semigroup for a short period of time (this is done for numerical stability purposes). We denote the smoothed noise by Π_{smooth}. Finally

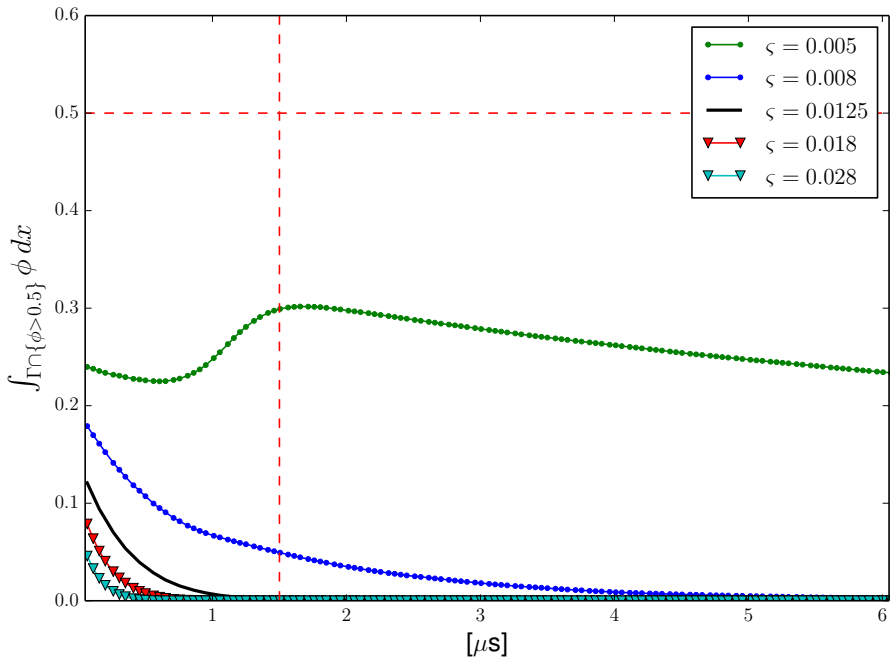

Figure 3.8: Noise sensitivity test for different values of ς. The same realisation of a Gaussian noise on $\mathbb{T}$ is used, to faithfully compare between different simulations. We mark with dots the curves above the base case and with triangles curves below the base case (in black).

we consider the initial condition to be given by

$$\phi_\diamond(x) = \varsigma \Pi_{\text{smooth}}(x),\ \forall x \in \mathbb{T}$$

where $\varsigma > 0$ and where ς^2 corresponds to the variance of the noise. We fix (arbitrarily) $\varsigma = 0.0125$ to correspond to the base case of parameters. The results of this test can be seen in Figure 3.8. We can see that adding more noise results in less water entering the membrane. This is due to small defects being created early on after the pulse and so the membrane discharges quickly before any big enough pore can be created. In the extreme case $\varsigma = 0$ the order parameter uniformly increases until it equals one everywhere.

Remark 51. *We highlight the red vertical line that we marked at* 1500 $[ns]$ *in Figure 3.8 and 3.9. This roughly corresponds to the time at which the membrane order parameter is mainly composed of two regions where either* $\phi = 0$ *or* $\phi = 1$ *and only a small portion of the membrane corresponding to transition layers between them. This is consistent with the properties presented in Chapter 2.*

Pore conductivity

Next, we tested the sensitivity of the model to the conductivity of the fluid filling pores in the membrane. The results of this test can be seen in Figure 3.9. Naturally, the lower

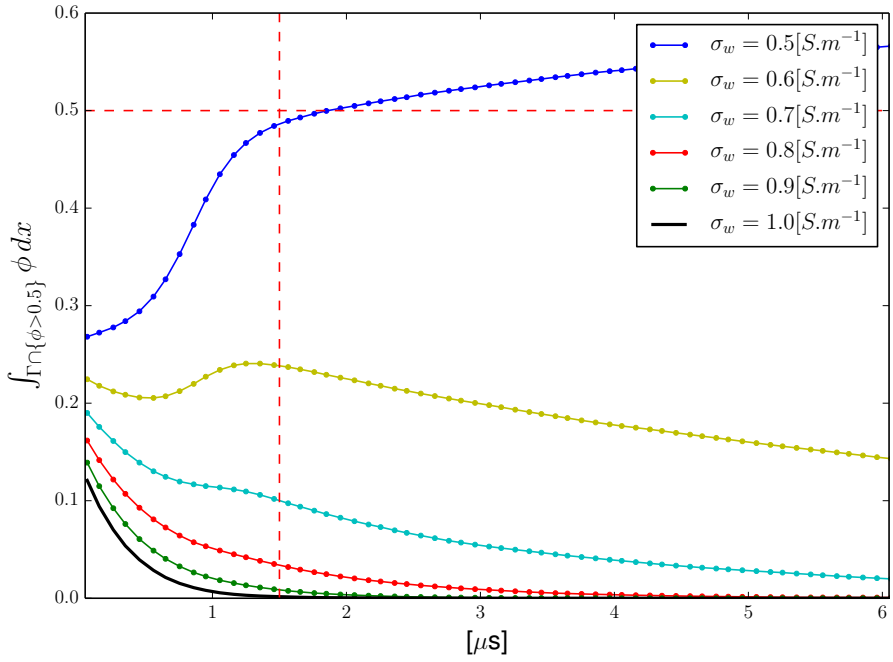

Figure 3.9: Given the same perturbed initial condition (noise associated to the base case) we run simulations for different values of pore conductivities. We mark with dots the curves above the base case and with triangles curves below the base case (in black).

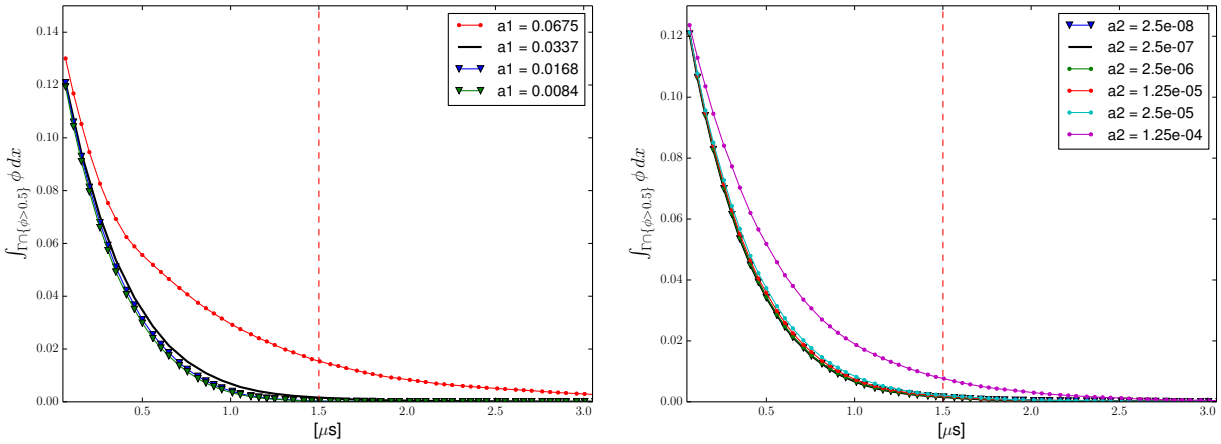

Figure 3.10: Sensitivity tests to changes in the line tension a_1 and the surface tension a_2 of our model.

the conducitvity of the fluid filling the pores in a membrane the longer the membrane takes to discharge. As a result, the effect of the TMV on the membrane continues to act for longer, creating more membrane defects. In terms of membrane damage, it seems to be a nonlinear effect (in terms of amount of water entering the membrane). In the case where $\sigma_w = 0.5$ [S.m^{-1}], most of the membrane is replaced by water, and the membrane patch eventually disappears. This is most likely an extreme outcome of our model resulting from the setting we consider (small biperiodic membrane patch). We cannot say that this result should be interpreted as membrane rupture as usually the damage in the whole cell is not uniform, and so this behavior would not happen all over a cell.

Line tension and surface tension

The next two tests concerns the line tension and surface tension terms a_1 and a_2. These values were roughly estimated in Chapter 2, and so we test the robustness of the model to variations in these values. The results are shown in Figure 3.10.

It seems that the increase in value of a_1 increases the amount of water (although by a small amount) which enters the membrane, although this is counter-intuitive as a higher value of a_1 means higher energy barrier between the two stable states $\phi = 1$ and $\phi = 0$. This is a side-effect of sorts, as in high-intensity nanosecond pulses (as is our current base case) the membrane easily quickly charges up to values largely surpassing what is needed to overcome the energy barrier of the potential $\mathcal{W}$. Therefore, increasing a_1 plays a bigger role on the time scale of pore formation and the length scale of small pores that can be created (according to the properties of the Allen-Cahn equation we presented in Chapter 2). In fact, although it may seem this parameter has little influence on the model it actually changes the size of the pore edge quite significantly, to the point that if this value increases too much, a higher resolution in space is needed to simulate the system.

Remark 52. *One reason we do not simulate higher values of a_1 is due to the effect it has on*

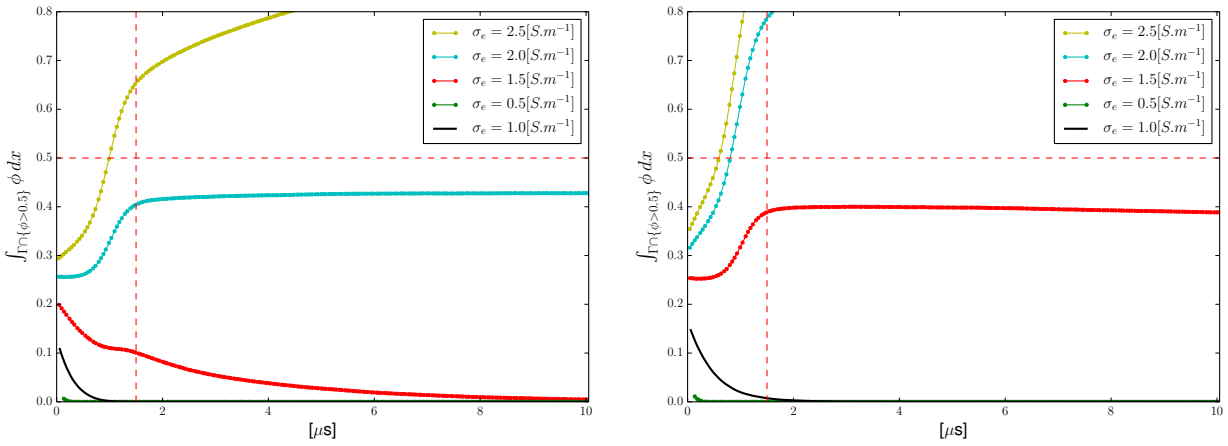

(a) $\sigma_c = 1$ [S.m^{-1}] (b) $\sigma_c = 1.25$ [S.m^{-1}]

Figure 3.11: Sensitivity test to changes in the conductivity of the extracellular medium. In graph **(a)** the interior conductivity is given by $\sigma_c = 1$ [S.m^{-1}]. In graph **(b)** the interior conductivity is given by $\sigma_c = 1.25$ [S.m^{-1}].

the length scale of the pore edge (transition layer between $\phi = 1$ and $\phi = 0$). Higher values of a_1 demand higher resolution N_x (which can be numerically expensive) to accurately capture the evolution of the membrane. We remark that testing the sensitivity of our model to the kinetic coefficient α has a similar effect.

We highlight the low sensitivity of our model to changes in surface tension. This is consistent with what we expect of a cell membrane, as surface tension does not play an important role on electroporation. This seems to be the case in all models of electroporation so far.

Extracellular and intracellular conductivity

Lastly we test the effect the conductivity of the exterior and interior media have on the dynamics of the membrane. In our current setting the interior and exterior media are only differentiated by their conductivity. Because of this, we focus more of our tests on the exterior conductivity. The results of our tests are shown in Figure 3.11.

These parameters can be seen to have an important effect on the behavior of the system. In fact, if we plot the evolution of the electrical properties of the system during the pulse delivery until membrane discharge we get different behaviors. This is shown for two cases in Figure 3.12.

Two simulations seem to have stable pores in Figure 3.11 as the proportion of membrane does not seem to change much in 8 [μs]. This is mainly due to the big amount of damage done to the membrane patch. It is not clear that this same behaviour would be replicated in a spherical cell (or maybe in a bigger patch). This can be seen in Figure 3.13, where we show the membrane 1.5 [μs] after the the start of the pulse and then at the end of their evolution

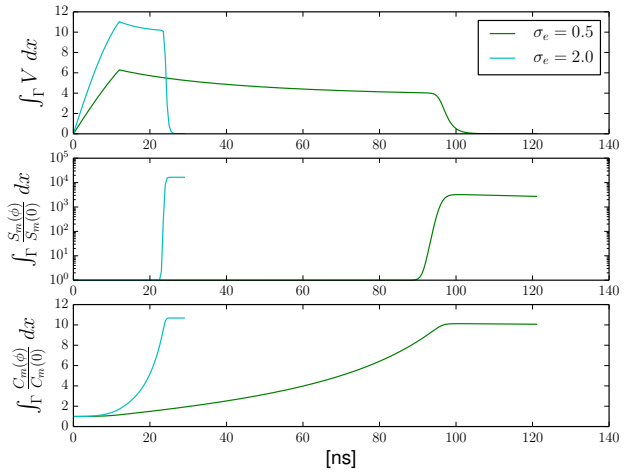

(a) $\sigma_c = 1$ [S.m^{-1}]

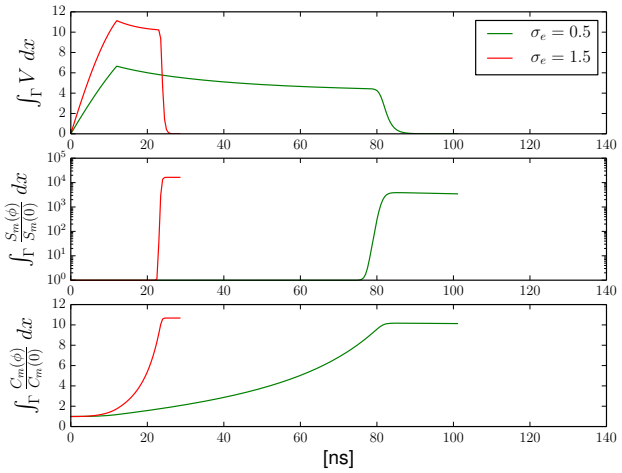

(b) $\sigma_c = 1.25$ [S.m^{-1}]

Figure 3.12: Two graphs of the simulations done in Figure 3.11 in two cases. The graphs in **(a)** corresponds to Figure 3.11a. The graphs in **(b)** corresponds to Figure 3.11b. Both simulations correspond to the period between the start of the pulse and the membrane discharge.

after 10 [μs]. This just shows that at long life of pores in the membrane is probably more an artifact of this setting (we do not expect pores to be so big) than an actual behavior we expect to see in the membranes.

With this test, we finish this chapter of the thesis.

3.6 Conclusion

We propose a robust and efficient numerical scheme to solve System 3.1. The corresponding numerical scheme deals with all the numerical difficulties presented at the beginning of the chapter. Its efficiency allows to make many numerical tests like the influence of the size of the membrane patch and sensitivity analysis to various parameters.

Concerning the perspectives, they mainly concern transferring this numerical scheme to the spherical cell setting (instead of a membrane patch), see Chapter 5 for details. For now, we would like to compare our model to the more classical KN-model thanks to the numerical scheme in an experimental situation.

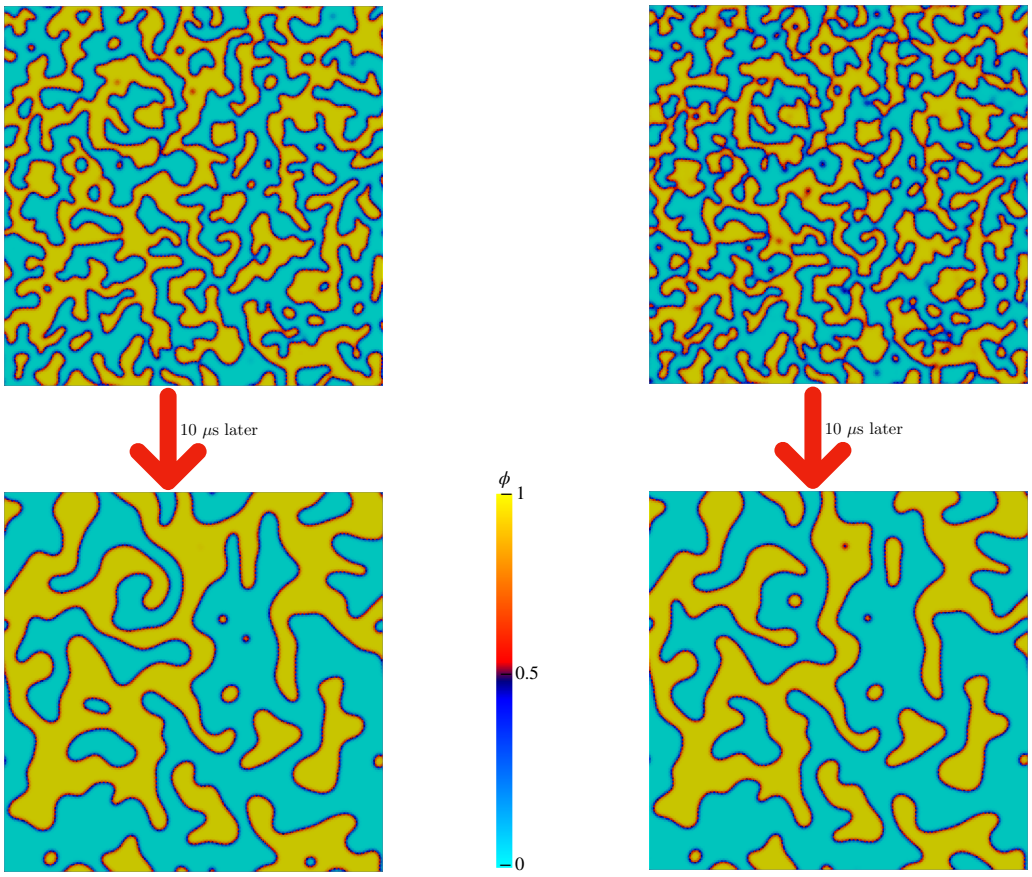

(a) $\sigma_c = 1$ [S.m^{-1}], $\sigma_e = 2$ [S.m^{-1}]. (b) $\sigma_c = 1.25$ [S.m^{-1}], $\sigma_e = 1.5$ [S.m^{-1}].

Figure 3.13: Figure **(a)** corresponds to the blue line in Figure 3.11a. Figure **(b)** corresponds to the red line in Figure 3.11b.

Chapter 4

Simulations in an experimental context

In this chapter, we run numerical simulations of the KN model (see Chapter 1, Section 1.3.4) and our phase-field model introduced in Chapter 2 in a physically relevant setting. We confront these models with data obtained from experimental results. Our goal is to find an explanation for a surprising phenomenon observed experimentally in [77], where it was shown that the effectiveness of electroporation decreases when the conductivity of the exterior medium of the cell increases and when the number of applied pulses is low.

We first explain the experimental context in which this phenomenon was observed and present two hypotheses which could explain it. Next, we look at a simulation protocol, equivalent to the experimental setup, which takes into account these two hypotheses. We show the different behaviors the KN model predicts and how this model could test the two hypotheses we presented. Next, we do the same for the phase-field model. First we simulate this model in a simplified setting (where we ignore lateral diffusion effects in the membrane) for a wide range of parameters. Then, basing ourselves on these results, we simulate the more general setting for a couple of parameter sets that are representative of the two hypotheses we wish to test.

Finally, we compare the numerical results from the KN model and the phase-field model and we propose a plausible explanation for the phenomenon experimentally observed in [77]. Notably, we show that the KN model is not sensitive to change in extracellular conductivity (at least in the case of strong nanosecond pulses) and that phase field model improves upon this by showing two distinct behaviors depending on the extracellular conductivity. We conclude this chapter by putting forward a hypothesis which could explain this surprising experimental result.

4.1 Experimental setting

The experimental setup was the same in both [76, 77]. Electric pulses were applied to a culture of Chinese hamster lung cell line DC-3F. The external medium conductivity was controlled by using two different media:

- S-MEM corresponds to a Minimum Essential Medium (MEM, 11380-037 Life Technolo-

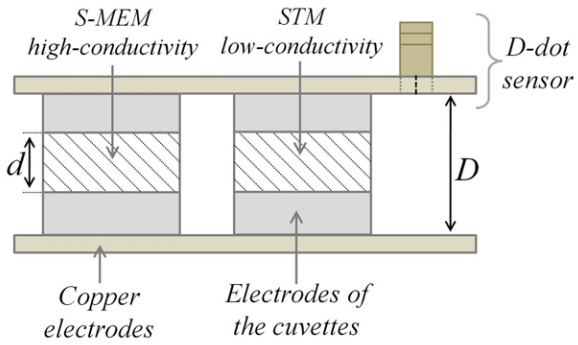

Figure 4.1: Scheme of the experimental setup used in [76, 77]. The distance between electrodes is $d = 4.19 \pm 0.02$ [mm]. This illustration is taken from [76].

gies) modified for the cultivation of cells in suspension and with a **high-conductivity** of 1.5 [S.m^{-1}] ;

- STM corresponds to a medium composed of 250 [mM] sucrose, 10 [mM] Tris HCl pH 7.0 and 1 [mM] $MgCl_2$ and with a **low-conductivity** of 0.1 [S.m^{-1}].

The applied electric field is measured with a D-dot sensor attached to the experimental device. A diagram of the experiment setup for the pulse delivery is shown in Figure 4.1.

In the experimental procedure, cells are placed in a cuvette between two electrodes containing the controlled medium. Electric pulses are then applied to the cell suspension. After the pulses, the cells are left to rest at room temperature for 10 minutes.

Bleomycin – a cytotoxic drug – is added to the medium to detect reversible electroporation. The cell groups without bleomycin in the medium are called control groups. After the pulse delivery, the viability of the cells is evaluated using a quantitative cloning assay. The two groups of cell suspensions are used to quantify the effectiveness of electroporation by measuring cell viability.

Among the electroporation protocols, there are:

Protocol 1 the application of a single 100 [μs] pulse with an electric field intensity between 85 and 145 [kV.m^{-1}],

Protocol 2 the application of a low number of 12 [ns] pulses (between 1 and 10) with an electric field intensity of 14.2 [MV.m^{-1}],

Protocol 3 the application of a low number of 102 [ns] pulses (between 1 and 30) with a field intensity of 3.2 [MV.m^{-1}],

Protocol 4 and a high number of 12 [ns] pulses (between 100 and 1000) with a field intensity of 3.2 [MV.m^{-1}].

Table 4.1 summarizes the different experiments.

Protocol	Pulse count	Pulse Duration	Intensity	Conductivity	Effectiveness
1	1	100 [μs]	[85, 145] [kV.m^{-1}]	0.1 [S.m^{-1}]	high
	1	100 [μs]	[85, 145] [kV.m^{-1}]	1.5 [S.m^{-1}]	low
Not defined	8	100 [μs]	[50, 120] [kV.m^{-1}]	0.1 [S.m^{-1}]	similar
	8	100 [μs]	[50, 120] [kV.m^{-1}]	1.5 [S.m^{-1}]	similar
2	≤ 3	12 [ns]	14.2 [MV.m^{-1}]	0.1 [S.m^{-1}]	high
	≤ 3	12 [ns]	14.2 [MV.m^{-1}]	1.5 [S.m^{-1}]	low
3	≥ 100	12 [ns]	3.2 [MV.m^{-1}]	0.1 [S.m^{-1}]	low
	≥ 100	12 [ns]	3.2 [MV.m^{-1}]	1.5 [S.m^{-1}]	high
4	≤ 10	102 [ns]	3.2 [MV.m^{-1}]	0.1 [S.m^{-1}]	high
	≤ 10	102 [ns]	3.2 [MV.m^{-1}]	1.5 [S.m^{-1}]	low

Table 4.1: Table summarizing the results reported in [76, 77]. The effectiveness of electroporation is denoted as low or high just to compare these results. Quantitative results can be found in these articles.

The take home message from these two articles is that higher extracellular conductivity increases the effectiveness in cell electroporation of nanosecond pulses when a high number of pulses are applied. Remarkably, the opposite behavior is observed when a low number of pulses are applied. This can be seen in both the bleomycin group and in the control group. The last column of Table 4.1 summarizes the effectiveness.

Remark 53. *Particular attention is paid to limiting the number of electrical pulses applied to avoid possible accumulation effects due to a high number of electrical pulses. This could lead to a saturation phenomenon.*

These results are counter-intuitive. If we look at the linear TMV model in the case of a sphere (Lemma 27 taking $\phi \equiv 0$ and constant in time), for example in the case of a 12 [ns] square pulse (see Figure 4.2), we can see that the maximum TMV felt by the membrane is about four times bigger when $\sigma_e = 1.5$ [S.m^{-1}] compared to $\sigma_e = 0.1$ [S.m^{-1}]. Therefore the effectiveness of cell electroporation is naturally expected to be higher if the exterior medium conductivity is higher, even for a single pulse.

We highlight two hypotheses presented in [77] that could explain this counter-intuitive behavior:

- The first one states that extracellular conductivity may influence the conductivity of the pores created by an electric pulse. As a result there is a quicker discharge of the membrane in the higher conductivity medium and so the induced pores in the membrane cannot attain too large of a size.

- The second hypothesis suggests that the influence of the sugar content in the low conductivity medium could affect the state of the membrane by influencing some of its mechanical properties (bending rigidity and stretching coefficients of the membrane). In other words, a lower TMV would then be enough to electroporate the cell membrane.

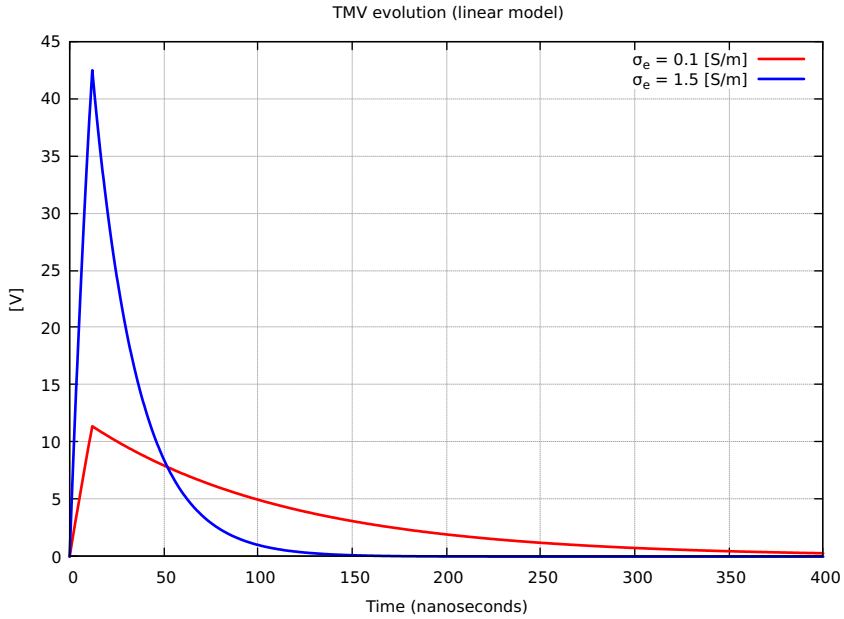

Figure 4.2: Resulting TMV at the pole of a cell of radius $R = 5$ [μm] (take $\theta = 0$ in Figure 1.7) from a square electric pulse of 12 [ns] of intensity $E = 14.2$ [MV.m^{-1}].]

In light of these hypotheses, in the next sections, we are going to study the behavior the KN model has for different parameters but subject to one of the experimental protocols (Protocol 2) presented above. The goal is to find a suitable explanation for the counter-intuitive behavior resulting from experiments. We first explain the simulation protocol which mimics the experimental setting used in [77] to get the results in Table 4.1.

4.2 Simulation protocol

For our simulations, we consider the periodic membrane patch setting introduced in Chapter 2 (see Figure 2.2-Right) and also used in Chapter 3. Regardless of the model we use (KN model or phase-field model), the PDE determining the TMV in this setting is given by

$$C_m \partial_t v + (S_m + \Lambda) v = G, \text{ in } \Gamma := (\mathbb{R}/\mathbb{Z})^2 \tag{4.1a}$$

$$v(t = 0, \cdot) = 0, \tag{4.1b}$$

where Λ is described in Lemma 30 and the source term G associated to the applied electric field (of intensity E) is given by

$$G = \frac{2\sigma_e \sigma_c E}{\sigma_e + \sigma_c}.$$

A $t_{\text{pulse}} := 12$ [ns] square electric pulse is applied to this system so that

$$G : t \mapsto \frac{2\sigma_e \sigma_c}{\sigma_e + \sigma_c} E_{\mathbb{T}} \cdot \mathbb{1}_{[0, t_{\text{pulse}}/\tau]}(t), \tag{4.2}$$

where $E_{\mathbb{T}}$ is the electric field intensity of the pulse applied. To test the effect of the different extracellular conductivities we simulate both cases $\sigma_e \in \{0.1\ [\mathrm{S.m^{-1}}], 1.5\ [\mathrm{S.m^{-1}}]\}$.

In order to compare our simulations to the spherical setting, two constraints coming from the linear electric model (as described in 2.3.2) are taken into account. The first constraint is on the height of the simulation box

$$H = \frac{R}{2}\frac{\sigma_c + 2\sigma_e}{\sigma_c + \sigma_e}, \tag{4.3}$$

where R is the radius of the Chinese hamster lung cells. This constraint makes the characteristic time of both the spherical membrane and the flat periodic membrane match; similarly, to match the amplitude of the TMV amplitude in both settings as $t \to +\infty$ we obtain the following constraint

$$E_{\mathbb{T}} = \frac{3(\sigma_e + \sigma_c)}{2(\sigma_c + 2\sigma_e)} E_{\mathbb{S}}, \tag{4.4}$$

where $E_{\mathbb{S}} = 14.2\ [\mathrm{MV.m^{-1}}]$ is the electric field intensity applied to the spherical setting and $E_{\mathbb{T}}$ is the electric field intensity needed in the flat periodic case to compare both scenarios.

Remark 54. *Taking these constraints into account in our simulations is important as σ_e is not constant across simulations. In particular, when $\sigma_c = 1\ [S.m^{-1}]$, depending on the value of σ_e, $E_{\mathbb{T}}$ ranges from $0.937E_{\mathbb{S}}$ to $1.375E_{\mathbb{S}}$:*

$$E_{\mathbb{T}}(\sigma_e = 0.1) = 1.375 \cdot E_{\mathbb{S}},$$
$$E_{\mathbb{T}}(\sigma_e = 1.5) = 0.937 \cdot E_{\mathbb{S}}.$$

The following simulation replicates the experimental protocol 2 and it is defined as follows: verifying the above two constraints, we apply a single 12 [ns] square electric pulse (resulting in (4.2)) on the membrane under two different extracellular conductivities $\sigma_e \in \{0.1\ [\mathrm{S.m^{-1}}],\ 1.5\ [\mathrm{S.m^{-1}}]\}$. Depending on the model we are studying – KN model, phase-field ODE (introduced later) and phase-field PDE – we couple to Equation (4.1a) the associated ODE or PDE. When simulating a system of ODEs we run the simulation until $T = \frac{10\ [\mu s]}{\tau}$. When simulating a system of PDEs we run the simulation of the complete system until the membrane is discharged (TMV is smaller than 10^{-3}) after which we just run that model with a null TMV (this is just the Allen-Cahn equation in the case of the phase-field model).

Remark 55. *All simulations of ODE systems are done using the ODE solver of the package* `Scipy.integrate` *of* `Python` *(function* `odeint`*), with a Runge-Kutta 4 adaptive scheme.*

In order to test the first hypothesis we will consider the two following modeling choices for the conductivity of aqueous solution in pores:

$$\sigma_w = \frac{\sigma_e + \sigma_c}{2}, \tag{4.5}$$

$$\frac{1}{\sigma_w} = \frac{1}{\sigma_e} + \frac{1}{\sigma_c}. \tag{4.6}$$

	Value	Description
α	10^9 [$m^2.s^{-1}$]	pore creation rate coefficient
q	2.56	coefficient linked to pore creation
N_m	1.5×10^9 [m^{-2}]	equilibrium pore density at zero TMV
V_{ep}	0.258 [V]	characteristic voltage of electroporation
S_m	2 [$S.m^{-2}$]	membrane conductivity
C_m	$3.54 \cdot 10^{-3}$ [$F.m^{-2}$]	membrane capacitance
σ_c	1 [$S.m^{-1}$]	interior medium conductivity
L	200 [nm]	characteristic length of membrane patch
R	$5 \cdot 10^{-6}$ [m]	cell radius
E	$14 \cdot 10^6$ [V.m]	pulsed electric field intensity

Table 4.2: Reference parameters used for the KN model.

The first choice (4.5), is a simple intuitive model where we consider a linear interpolation between the extracellular and intracellular conductivities. The second choice (4.6) can be thought of as an analogy between the membrane and a circuit of resistances in series.

4.3 KN model behavior

This section is dedicated to the simulation of the KN model to confront it to the results shown in Table 4.1. The KN model was briefly introduced in Chapter 1, however for the convenience of the reader we rewrite it below. We express it in the setting of a periodic membrane patch as we are also interested in comparing this model to the phase-field model.

$$\frac{dN}{dt}(t,x) - \tau\alpha e^{(v/V_{ep})^2}\left(1 - \frac{N(t,x)}{N_m e^{q(v/V_{ep})^2}}\right) = 0,\ t > 0,\ x \in \Gamma, \tag{4.7a}$$

$$\partial_t v + \frac{\tau(S_m + S_p(v)\cdot N)}{C_m}v + \frac{\tau\Lambda}{C_m}v = \frac{\tau G}{C_m},\ \text{in } \Gamma, \forall t \in [0,T], \tag{4.7b}$$

$$N(0,\cdot) = N_m,\ \text{in } \Gamma, \tag{4.7c}$$

$$v(0,\cdot) = 0,\ \text{in } \Gamma. \tag{4.7d}$$

where the reference values for α, q, V_{ep} and N_m are constants whose values can be found in Table 4.2, and τ is the characteristic time used for simulating purposes only.

Simulation Protocol

We test the first hypothesis by simulating the two modeling choices from Equations (4.5) and (4.6). The second hypothesis is tested by varying the coefficients α and V_{ep} around the reference set of parameters.

Results

The results of our simulations to test the first hypothesis, using the reference parameters, are shown in Figures 4.3, 4.4 and 4.5.

Figure 4.3 first shows the behavior of the solutions of the KN model under the consideration that the conductivity of the fluid filling a pore does not depend on the intracellular and extracellular conductivities. This is the usual consideration taken in the literature [19, 18, 77]. It is thought of as a reference simulation.

Figures 4.4 and 4.5 show the behavior of the solutions of the KN model under the two different modeling choices (4.6) and (4.5). As in our phase field model we see a net increase in the damage done to the membrane, here measured by the number of pores being created in the membrane patch.

Roughly speaking, regardless of the modeling choice for σ_w, this model predicts a sharp increase in the TMV along with an instant creation of pores in the membrane. The TMV then plateaus at ~ 1 [V] for the rest of the electric pulse and finally rapidly drops due to the present number of pores. This similarity in electrical behavior means that this model does not seem to differentiate between the conductivity of the extracellular conductivities.

We now continue with the numerical experiment where we vary the parameters α and V_{ep}. The results of this experiment as shown in Figures 4.7 and 4.6.

We can see again that when using (4.6), there is a net increase in the amount of pores being created regardless of the extracellular conductivity. With this model we can find a set of parameters (α, V_{ep}) such that more pores are created at lower extracellular conductivity. However, because both membranes are considerably affected by electroporation at this point, it is highly unlikely that this would explain the marked difference in the effectiveness of electroporation observed experimentally.

According to this model, pore population remains stable for a long time (more than 100 [μs]). Therefore regardless of the hypothesis we consider, this model predicts effective electroporation while using any of the two media, STM or SMEM.

4.4 Phase-field model behavior

In this section we now test the phase-field model to the experimental data. Before continuing with this section we fix a reference set of parameters around which we will study the behavior of this model. This set of parameters is given in Table 4.3.

4.4.1 ODE System

A first approach is to study the idealized scenario where the membrane initial condition is $\phi(t = 0, \cdot) = 0$. This consideration neglects diffusive effects in the membrane and so it allows us to test a wide range of the parameters as our model is simplified to an ODE system.

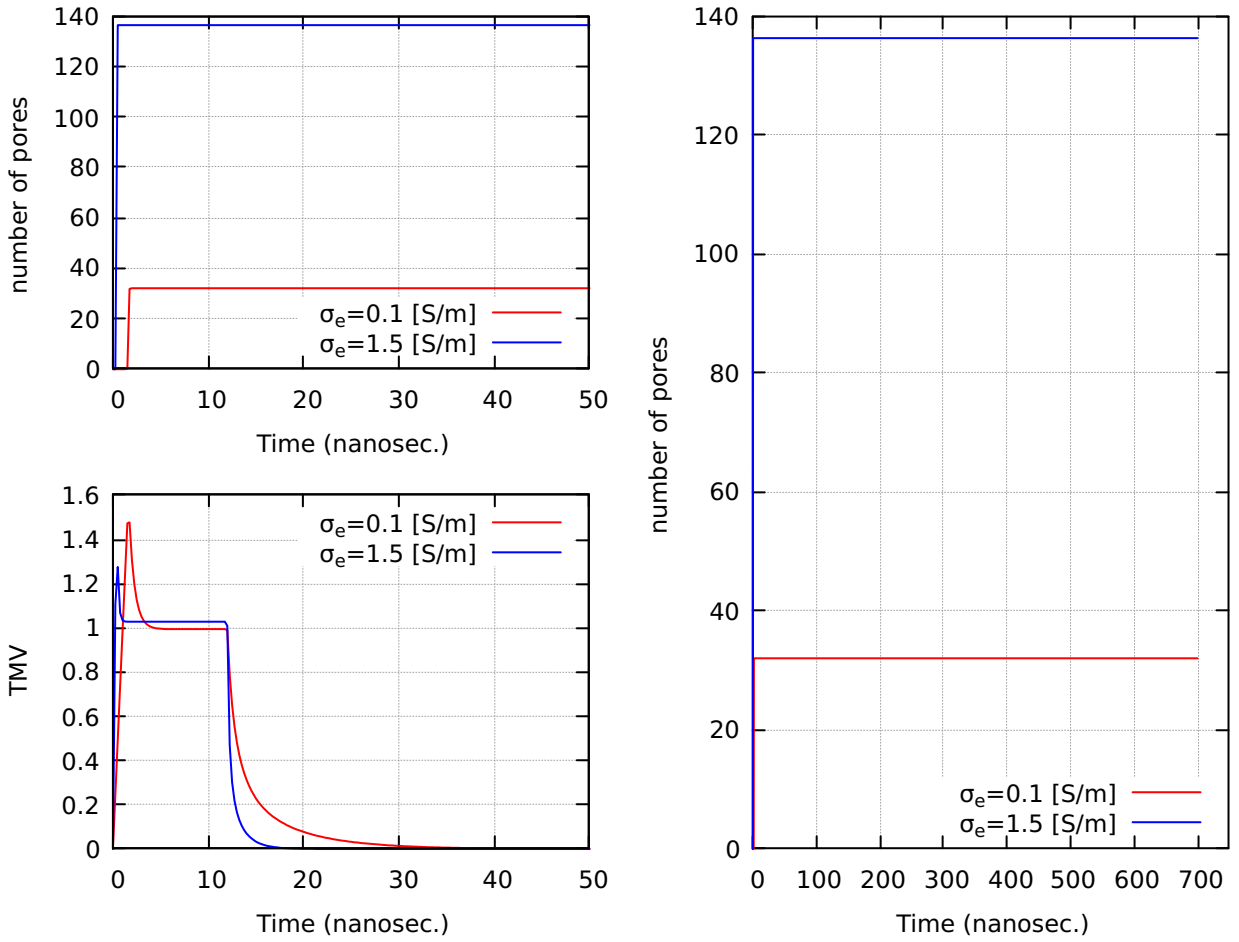

Figure 4.3: Time evolution of the solutions of the KN model using the reference parameters given in Table 4.2 and modeling fluid conductivity filling a pore independent on the intracellular and extracellular conductivities. A 12 [ns] square pulse of magnitude $E = 14.2$ [MV.m^{-1}] is applied to two systems with different extracellular conductivity. The two plots on the left show the evolution of the system during the charge and discharge of the membrane.

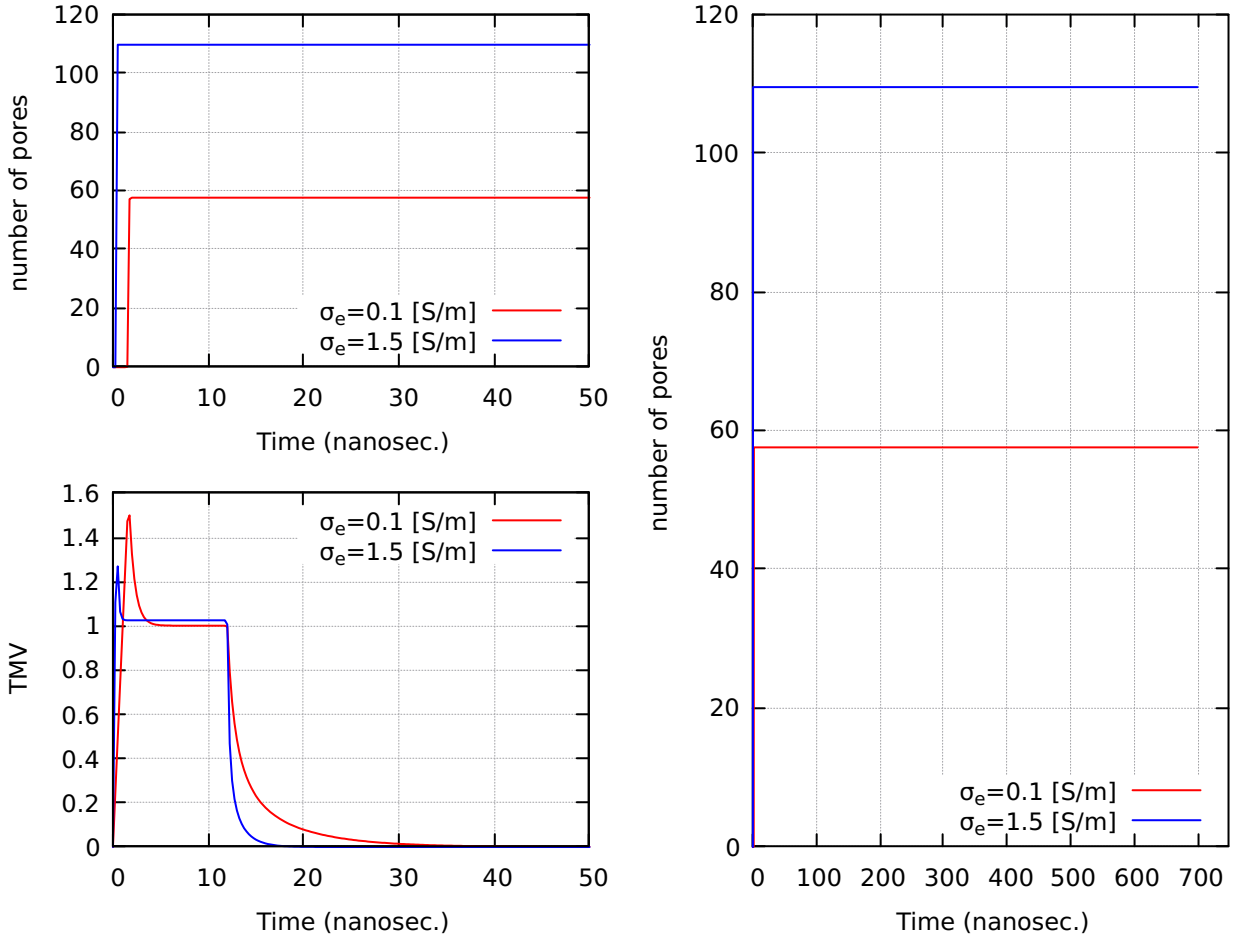

Figure 4.4: Time evolution of the solutions of the KN model using the reference parameters given in Table 4.2 and modeling pore conductivity with (4.5). A 12 [ns] square pulse of magnitude $E = 14.2$ [MV.m^{-1}] is applied to two systems with different extracellular conductivity. The two plots on the left show the evolution of the system during the charge and discharge of the membrane.

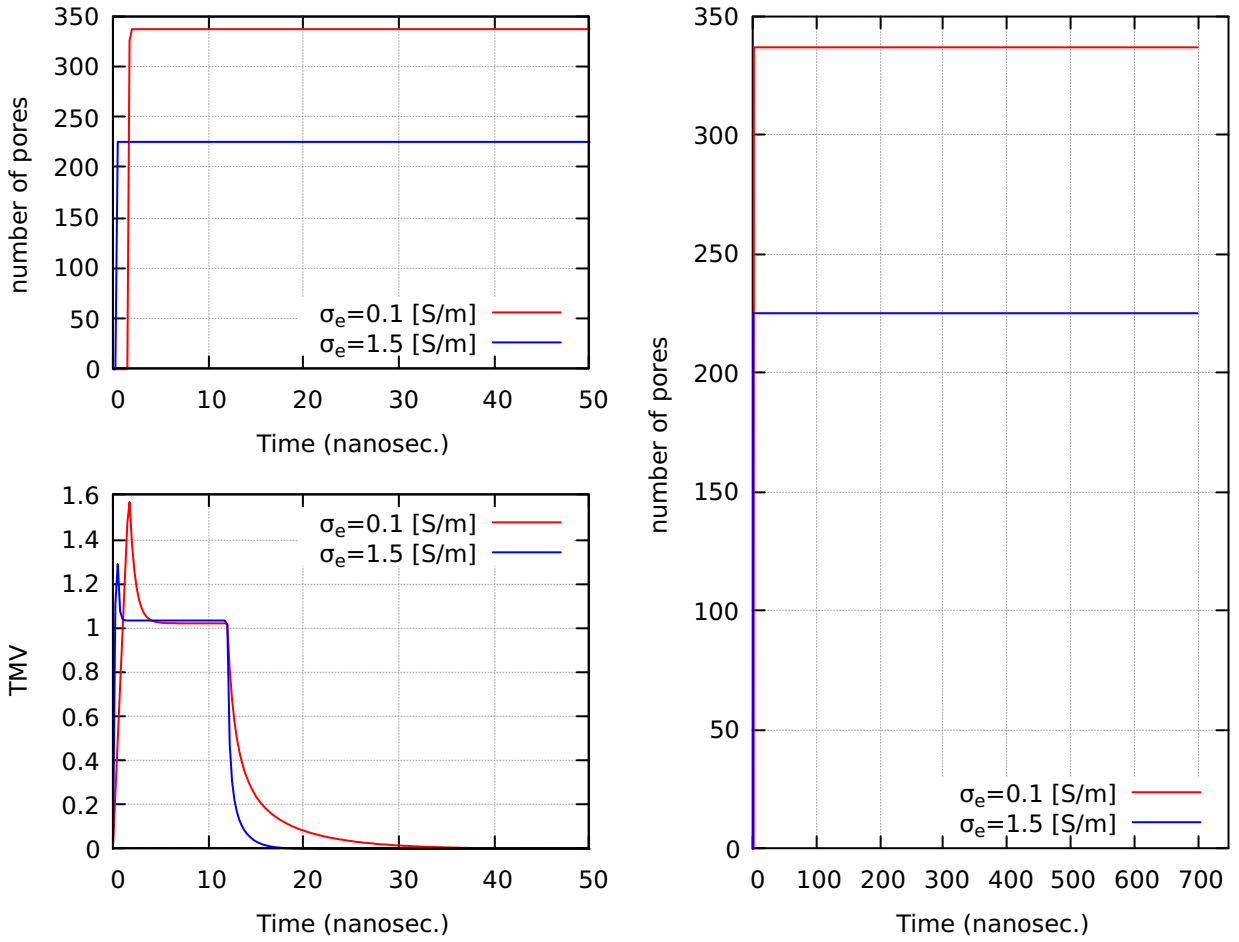

Figure 4.5: Time evolution of the solutions of the KN model using the reference parameters given in Table 4.2 and modeling pore conductivity with (4.6). A 12 [ns] square pulse of magnitude $E = 14.2$ [MV.m^{-1}] is applied to two systems with different extracellular conductivity. The two plots on the left show the evolution of the system during the charge and discharge of the membrane.

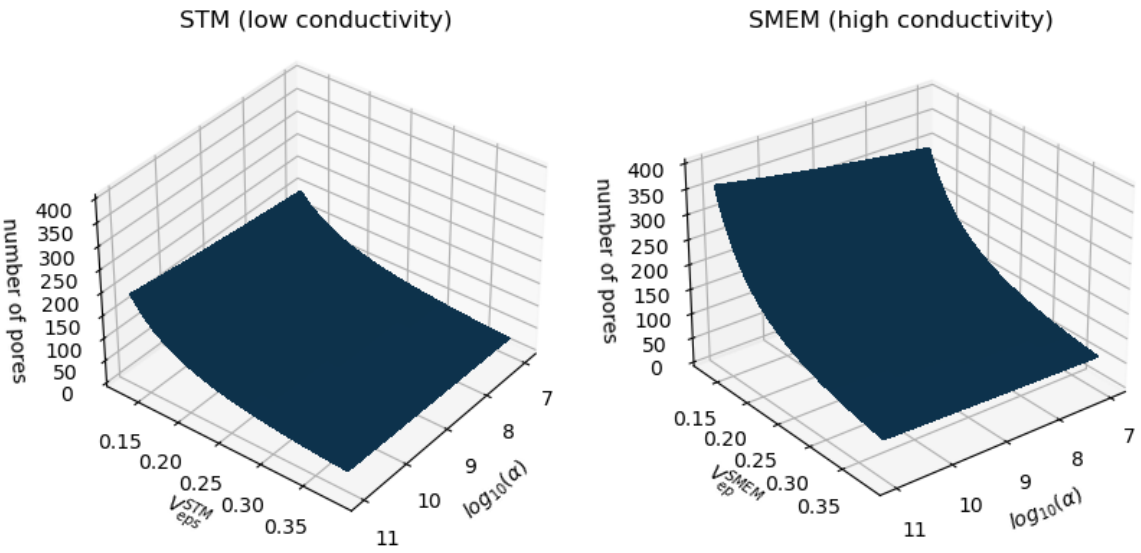

Figure 4.6: Final state of L^2N (at time $t = 2$ [μs]) for different values of α and V_{ep} after being influenced by a 12 [ns]. Pore conductivity (4.5).

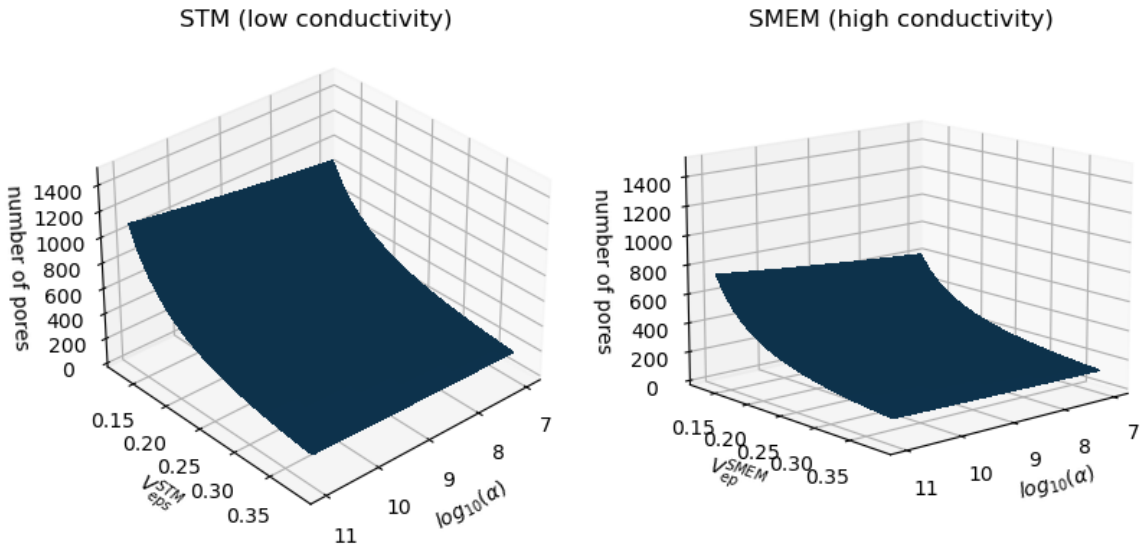

Figure 4.7: Final state of L^2N (at time $t = 2$ [μs]) for different values of α and V_{ep} after being influenced by a 12 [ns]. Pore conductivity (4.6).

	Value	Description
D_0	2×10^{-12} [$m^2.s^{-1}$]	lateral diffusion
ϵ_0	8.85×10^{-12} [$F.m^{-1}$]	vacuum permittivity
ϵ_w	80	relative water permittivity
ϵ_l	2	relative lipid permittivity
σ_c	1 [$S.m^{-1}$]	interior medium conductivity
σ_l	10^{-8} [$S.m^{-1}$]	lipid membrane conductivity
h	5×10^{-9} [m]	membrane thickness
δ^h	10^{-9} [m]	pore edge size
α	$1.852 \cdot 10^7$ [$m^2.J^{-1}.s^{-1}$]	kinetic coefficient
a_1	$5.44 \cdot 10^{-1}$ [$J.m^{-2}$]	measures membrane linear energy
a_2	$2.0 \cdot 10^{-6}$ [$J.m^{-2}$]	measures membrane surface tension
E	$14 \cdot 10^6$ [$V.m^{-1}$]	pulsed electric field intensity.
R	$5 \cdot 10^{-6}$ [m]	cell radius
L	200 [nm]	characteristic length of membrane patch.
k_1	20	manages interporlation between σ_l and σ_w.
S_m	$\phi \mapsto \frac{\sigma_w - \sigma_l}{2h}(1 + \tanh(k_1(\phi - \frac{1}{2}))) + \frac{\sigma_l}{h}$	membrane surface conductivity.

Table 4.3: Reference values of parameters. The model behavior is studied around this predefined set.

Indeed in this setting, System (3.9) reads as the following ODE system

$$\frac{d\phi}{dt} = -\tau\alpha\mathcal{W}'(\phi) + \frac{\tau\alpha}{2}C_m'(\phi)v^2, \forall t \in [0,T], \tag{4.8a}$$

$$\frac{dv}{dt} = -\frac{\tau S_m(\phi)}{C_m(\phi)}v - \frac{\tau}{C_m(\phi)}\frac{\sigma_e\sigma_c}{\sigma_e+\sigma_c}\frac{1}{H}v + \frac{\tau G}{C_m(\phi)}, \forall t \in [0,T], \tag{4.8b}$$

$$\phi_{|t=0} = 0, \tag{4.8c}$$

$$v_{|t=0} = 0, \tag{4.8d}$$

where τ is a time rescaling constant and $2H$ denotes the distance between the electrodes in the periodic membrane setting.

The motivation for this approach is that by considering a system of ODEs we can sweep a wide range of parameters to get a rough idea of the behavior of our model. This also helps our intution when we choose a reference set of parameters to test the second hypothesis with a full PDE simulation.

Results

We test the first hypothesis by considering the conductivities of the fluid filling the pores σ_w to depend on the intracellular and extracellular conductivities. The simplest concrete modeling choice is to consider the mean value between these two values, in other words we consider the constraint (4.5). The numerical solution of the ODE system, using the reference parameters and this choice for σ_w, is shown in Figure 4.8.

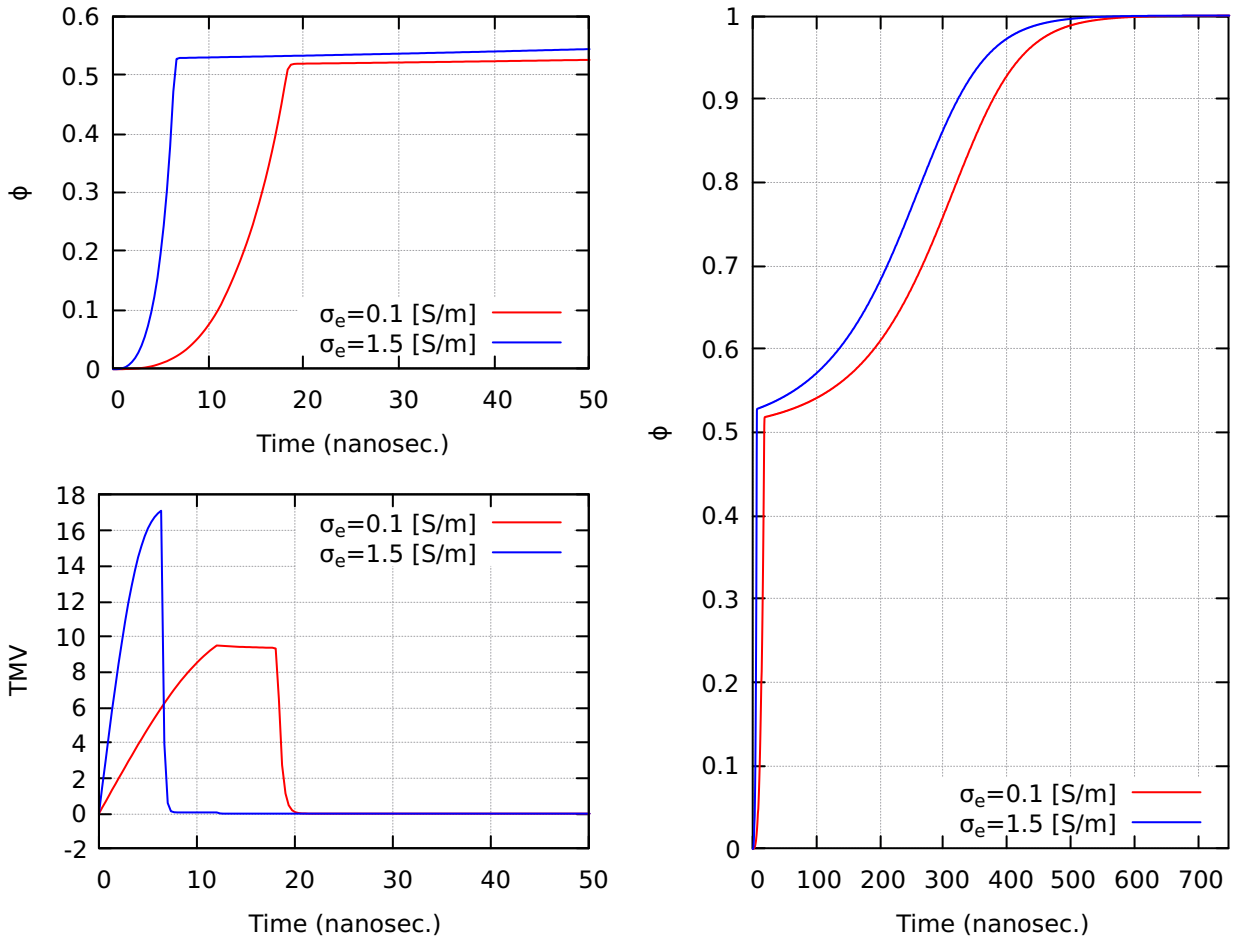

Figure 4.8: Time evolution of (4.8). Parameters fixed using Table 4.3. Pore conductivity defined by (4.5). Square pulse of magnitude $E = 14.2$ [MV.m^{-1}] and 12 [ns]. Red (resp. blue): extracellular conductivity $\sigma_e = 0.1$ [S/m] (resp. $\sigma_e = 1.5$ [S/m]). Left-Top (resp. Left-Bottom): ϕ (resp TMV) during the first nanoseconds (charge and discharge of the membrane). Right: ϕ until a stable state is reached.

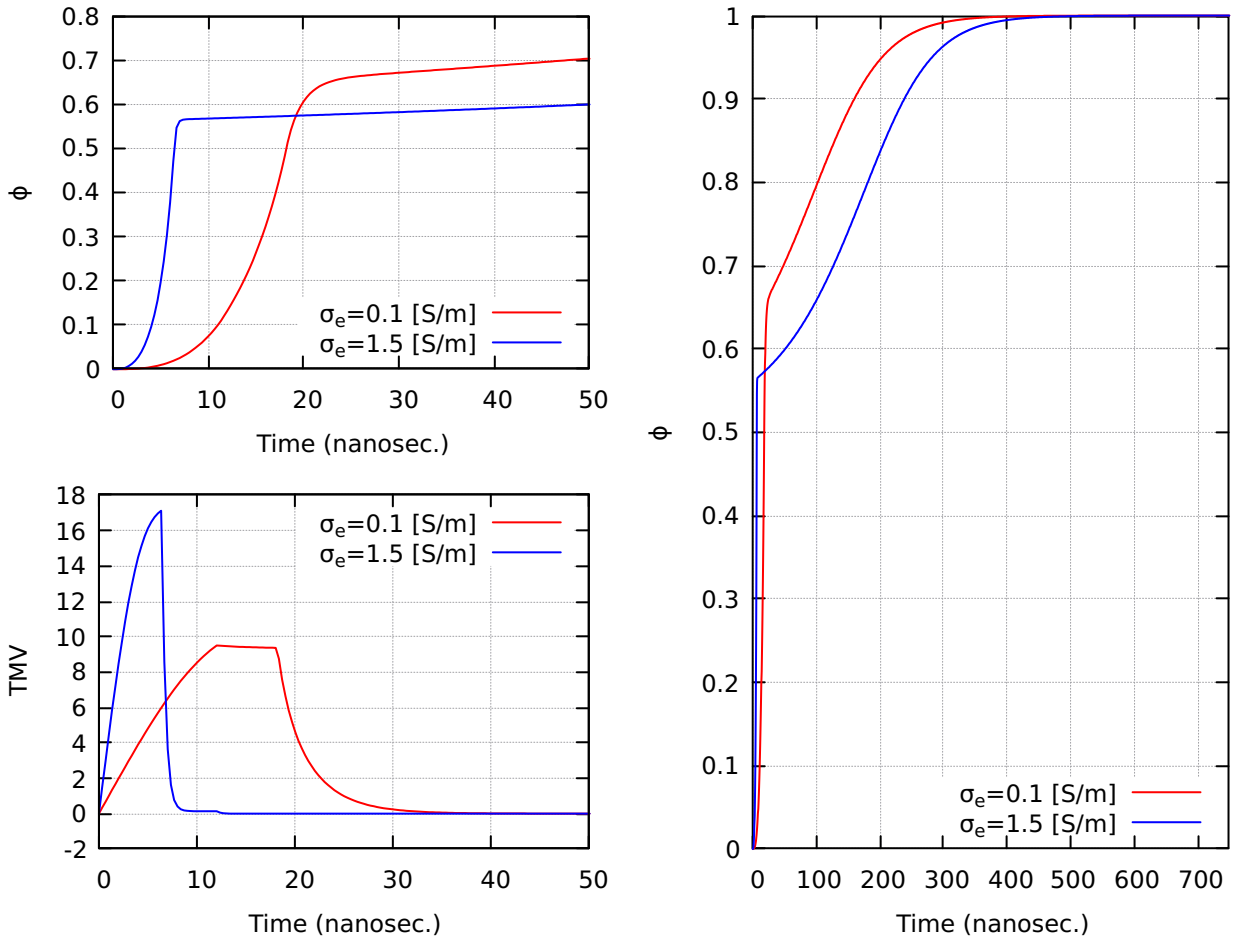

Figure 4.9: Time evolution of (4.8). Parameters fixed using Table 4.3. Pore conductivity defined by (4.6). Square pulse of magnitude $E = 14.2$ [MV.m^{-1}] and 12 [ns]. Red (resp. blue): extracellular conductivity $\sigma_e = 0.1$ [S/m] (resp. $\sigma_e = 1.5$ [S/m]). Left-Top (resp. Left-Bottom): ϕ (resp TMV) during the first nanoseconds (charge and discharge of the membrane). Right: ϕ until a stable state is reached.

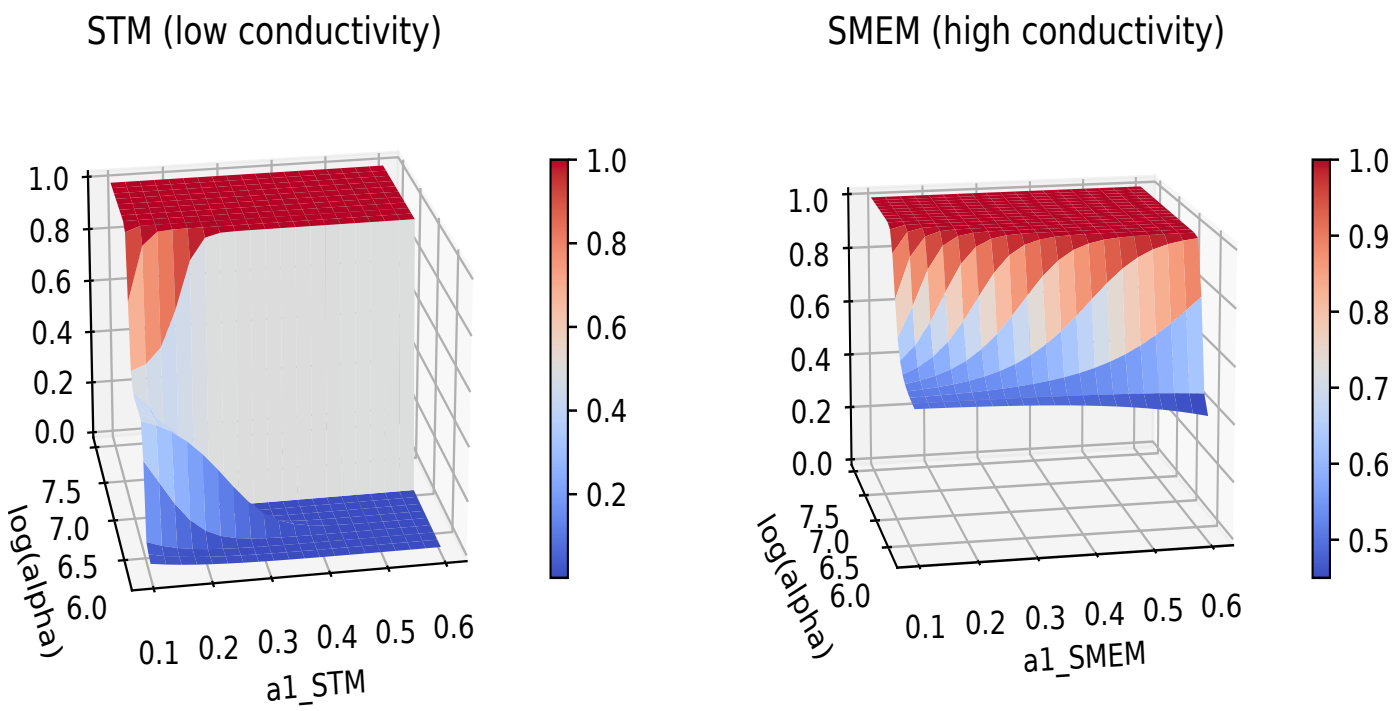

Figure 4.10: Final state of order parameter ϕ (at time $t = 10$ [μs]) for different values of a_1 and α. Pore conductivity (4.5).

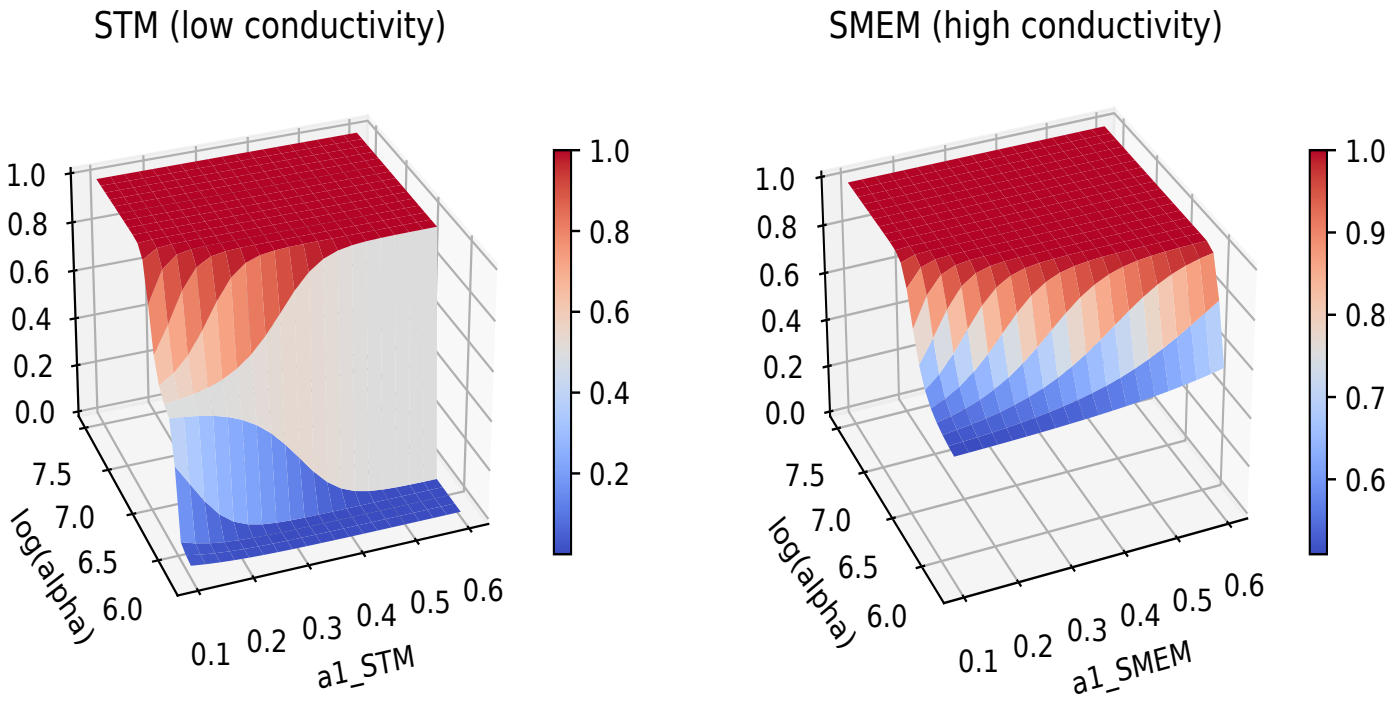

Figure 4.11: Final state of order parameter ϕ (at time $t = 10$ [μs]) for different values of a_1 and α. Pore conductivity (4.6).

For both extracellular conductivities, the membrane charges like a capacitor and discharges, for the most part, due to dielectric breakdown. The main difference between when considering STM and SMEM is the time that the respective membrane remains charged, e.g., when the TMV is greater than 2 [V] (this is an arbitrary but reasonable threshold value). When using STM (low extracellular conductivity), the time of membrane charging is much larger than when using SMEM. As a result, the TMV is not as high as in the SMEM case and the dielectric breakdown is not immediate. In fact, the membrane remains charged for some time after the end of the pulse (it discharges like a capacitor during this time) before dielectric breakdown occurs, so the total time that the TMV remains high is longer than when the extracellular conductivity is lower.

We also simulate the second choice to modeling the conductivity of the fluid entering the membrane (4.6). The behavior of the system with this modeling choice is shown in Figure 4.9. In this case, the behavior is similar to the one shown before, however we can see that due to the smaller value of σ_w, the discharge time is increased and thus the influence of TMV on the order parameter ϕ persists after dielectric breakdown (when $\phi > 0.5$). Thus, it is clear that this additional effect leads to a net increase in the water entering the membrane compared to the other choices (4.5). In other words, this modeling choice is only likely to increase the effectiveness of membrane electroporation for both media (SMEM and STM) in this model.

These two graphs are intended to illustrate the general behavior of the reference values. For values close enough to these parameters, we expect similar behavior in similar time periods, so when considering different parameters, we are mainly interested in the final state of the order parameter. A wide range of parameters can lead to different behaviors (ϕ never reaches $\phi = 0.5$, for example). In general, the membrane either experiences dielectric breakdown and then discharges rapidly, or dielectric breakdown does not occur ($\phi(t) < 0.5$ for all $t > 0$) and the membrane then discharges slowly like a capacitor until it returns to the stable initial state $\phi = 0$.

The second hypothesis presented in Section 4.1 is tested by simulating (4.8) using different values of a_1. Intuitively, we could imagine that the effect of sugar in the STM on the membrane could manifest as a lower energy barrier in the membrane potential $\mathcal{W}$. In other words, the value of a_1 could be lower when using STM than when using $SMEM$. Therefore, to test this hypothesis we test different values of a_1 around its reference value. As the value of α is determined from the value of a_1 (see Chapter 2), we also vary α around its reference value as well. To get a more complete description of the effect of these two parameters on the outcome of our simulations, we make them vary independently. The results of this numerical experiment are shown in Figures 4.10 and 4.11.

To interpret these results, we fix a value of α and then find a $a1_{\text{STM}}$ smaller than $a1_{\text{SMEM}}$ such that then final state of ϕ in STM is higher than the final state of in SMEM. It is clear that even a moderate decrease in the value of a_1 when using the low conductivity medium (STM) does not compensate for the higher TMV resulting from the higher conductivity medium. Of course, this does not take into account spatial effects that appear when we consider the full PDE.

We highlight that for the modeling choice (4.6) the final state of the order parameter ϕ is equal to 1 for more parameter choices (a_1, α) as expected than for the other modeling choice (4.5). For this reason, we will focus more on the use of (4.5) when simulating the full PDE system.

It should be noted that a more dramatic change in parameters is not shown because it strongly contradicts the pore-edge estimates made in Chapter 2. To counteract this effect on the estimate, we would also need to change the value of the lateral diffusion coefficient.

4.4.2 PDE System

We continue to test the hypotheses presented at the beginning of this chapter by simulating the complete PDE system (3.9), which we rewrite here

$$\partial_t \phi - \frac{D\tau}{L^2}\triangle\phi = -\tau\alpha\mathcal{W}'(\phi) + \frac{\tau\alpha}{2}C_m'(\phi)v^2, \text{ in } \Gamma, \forall t \in [0,T], \tag{4.9a}$$

$$\partial_t v + \frac{\tau S_m(\phi)}{C_m(\phi)}v + \frac{\tau}{C_m(\phi)}\Lambda v = \frac{\tau G}{C_m(\phi)}, \text{ in } \Gamma, \forall t \in [0,T], \tag{4.9b}$$

$$\phi(0,\cdot) = M_{\text{noise}}(1 + \Pi_{\text{smooth}}), \text{ in } \Gamma, \tag{4.9c}$$

$$v(0,\cdot) = 0, \text{ in } \Gamma, \tag{4.9d}$$

where $\Gamma = (\mathbb{R}/\mathbb{Z})^2$, M_{noise} corresponds to the noise magnitude, and Π_{smooth} is smoothed out (by applying the periodic heat kernel like in Chapter 3) realization of the a Gaussian noise and rescaled so that $\|\Pi_{\text{smoot}}\|_\infty = 1$. We already know from the sensitivity test done in Chapter 3 that higher noise magnitude results in less water entering the membrane induced by the pulsed electric field. As a physically sensible amount of noise in the membrane (determined by M_{noise}) is unclear, we test for a few values of noise magnitude in our simulations.

Results

Here we show the numerical solution of the time evolution of the unknowns of the PDE system for a limited set of parameters. Dealing with a large set (as in the case of the ODE system) is more computationally expensive and more difficult to study (and impractical to display). We will therefore favor choosing a few representative set of parameters instead of a wide range (as in the case of the ODE system). Additionally, for practical reasons, we restrict ourselves to the linear pore conductivity model (4.5).

First, we show the behavior using the reference values of the parameters for different values of M_{noise}. The behavior of the membrane charging and discharging is shown in Figures 4.13 and 4.12. The behavior of the membrane just after the membrane is completely discharged, see Figure 4.14.

We can see two different behaviors arise depending on the different extracellular conductivities. This can be seen during the time period when the electric field pulse influences the membrane and also later on, once the membrane is discharged and enters a metastable state.

During the electric pulse, it is clear that a higher extracellular conductivity results in a higher TMV during the membrane charging phase. Other than this, there is the additional

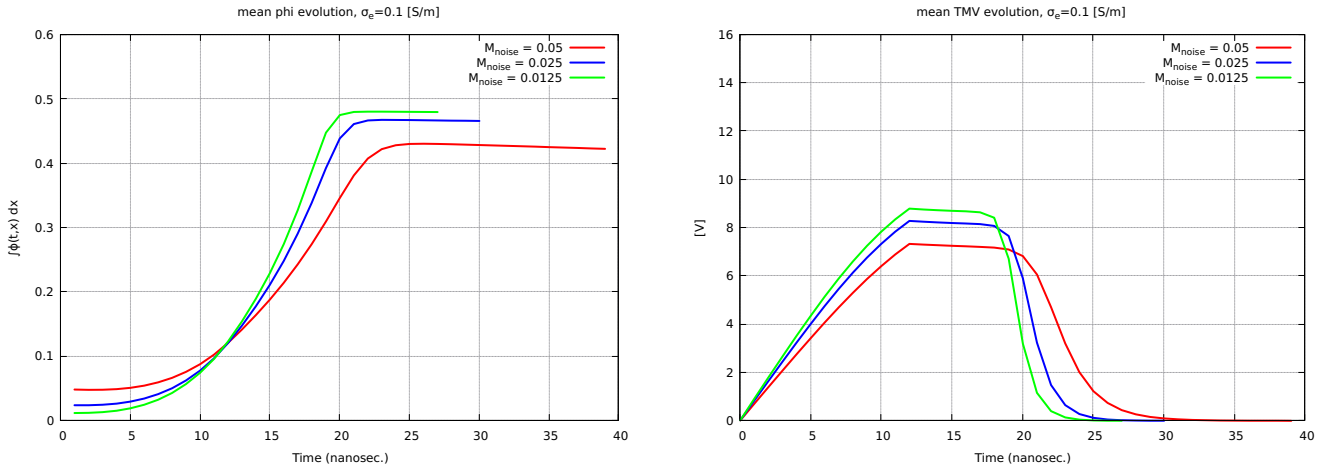

Figure 4.12: Mean behavior of the solutions of the PDE system (during pulse delivery) using the reference parameters, $\sigma_e = 0.1$ [S.m^{-1}] and $\sigma_w = (\sigma_e + \sigma_c)/2$. The different colors correspond to different values of M_{noise}. Simulations are stopped when the mean TMV is smaller than 10^{-3} [V].

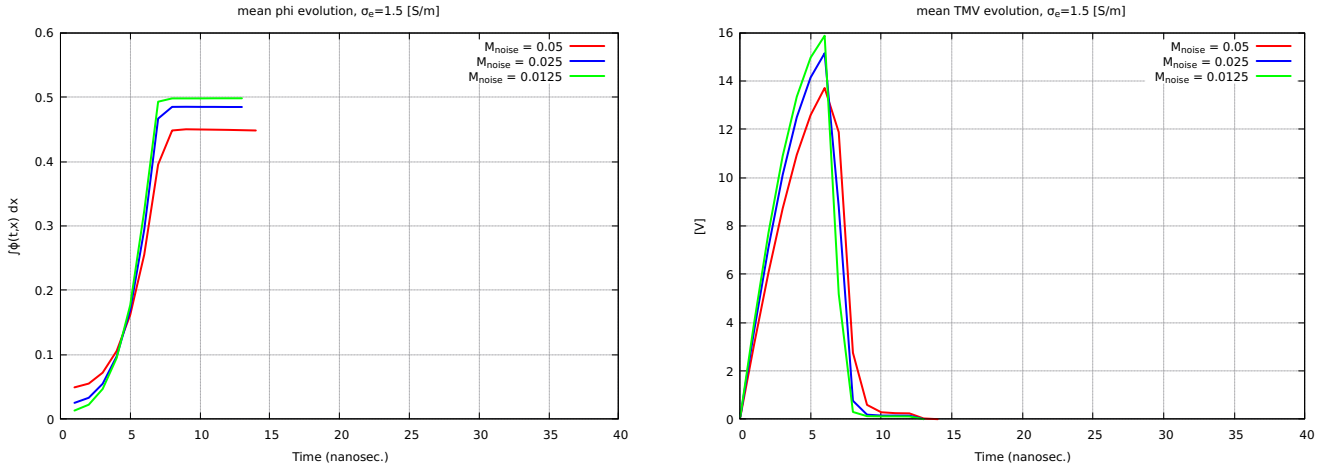

Figure 4.13: Mean behavior of the solutions of the PDE system (during pulse delivery) using the reference parameters, $\sigma_e = 1.5$ [S.m^{-1}] and $\sigma_w = (\sigma_e + \sigma_c)/2$. The different colors correspond to different values of M_{noise}. Simulations are stopped when the mean TMV is smaller than 10^{-3} [V].

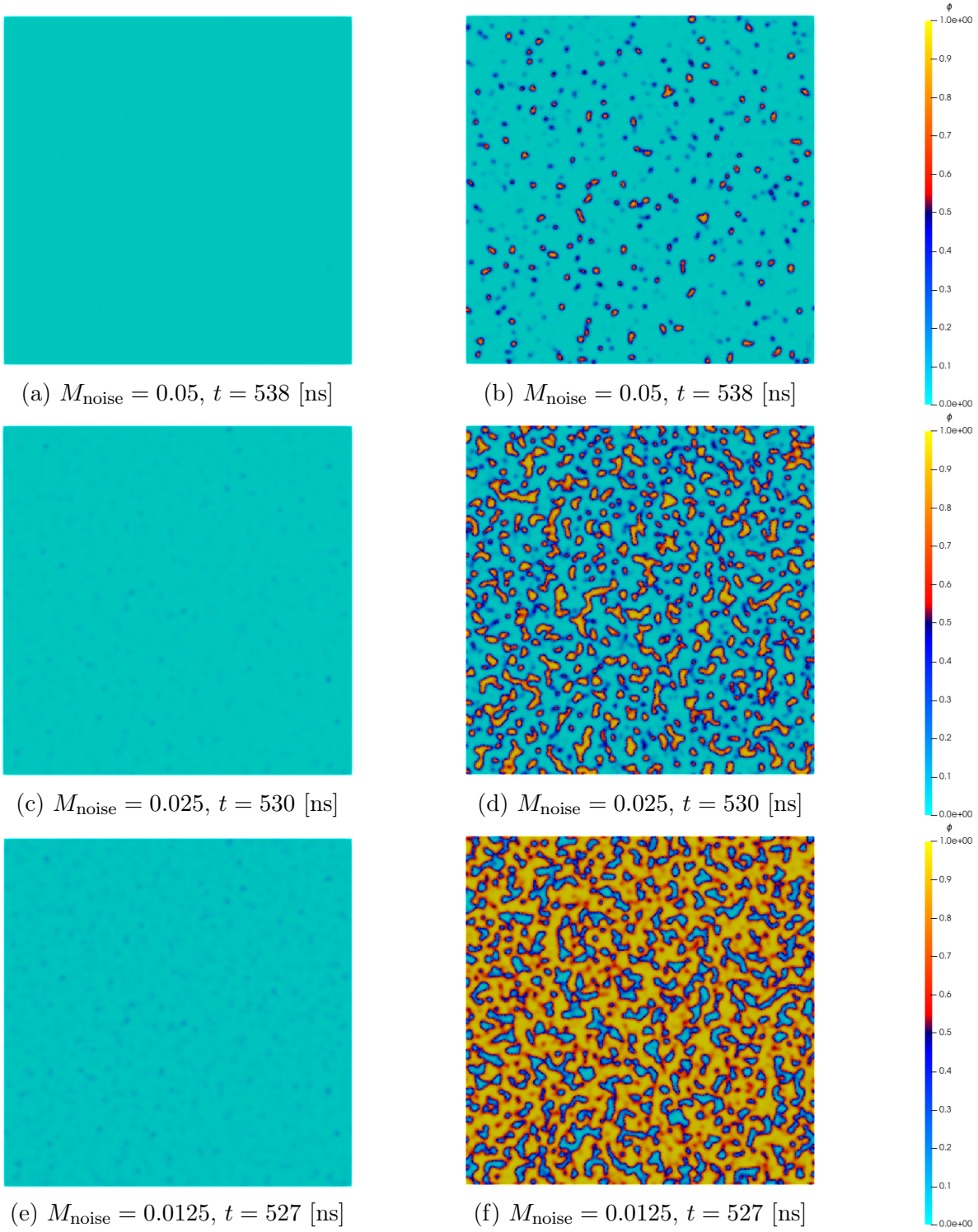

(a) $M_{\text{noise}} = 0.05$, $t = 538$ [ns]

(b) $M_{\text{noise}} = 0.05$, $t = 538$ [ns]

(c) $M_{\text{noise}} = 0.025$, $t = 530$ [ns]

(d) $M_{\text{noise}} = 0.025$, $t = 530$ [ns]

(e) $M_{\text{noise}} = 0.0125$, $t = 527$ [ns]

(f) $M_{\text{noise}} = 0.0125$, $t = 527$ [ns]

Figure 4.14: Numerical resolution of the PDE system using the reference parameters after membrane discharge (simulations associated to Figures 4.12 and 4.13). The left column shows results corresponding to $\sigma_e = 0.1$ [S.m^{-1}], the right column corresponds to $\sigma_e = 1.5$ [S.m^{-1}]. In both cases, $\sigma_w = (\sigma_e + \sigma_c)/2$.

distinction that at higher conductivity, dielectric breakdown happens before the pulse delivery ends. As a result the membrane remains charged for a much shorter time than in lower extracellular conductivity. This is the case for all the levels of noise we used.

Remark 56. *We highlight that during the membrane charging phase the behavior of the mean values of our simulation are qualitatively similar to the ODE simulation shown in Figure 4.8.*

After the membrane is discharged, the membrane enters its metastable state where the difference between water and the membrane state in the membrane is more clearly defined. During this time, there is a clear difference of the electric pulse effect at higher extracellular conductivity.

There are two visible differences from our results. The first is the amount of water that enters the membrane. At higher conductivity, there is visibly more water entering the membrane (at all levels of noise). The second observable difference is the sensitivity of the effectiveness of electroporation to the noise magnitude. It seems that at higher conductivity, the amount of water entering increases much more dramatically when the noise magnitude decreases. In fact, as an extreme example, when $M_{\text{noise}} = 0.0125$, and $\sigma_e = 1.5$ [S.m^{-1}] we can see that most of the membrane is water (this would normally be interpreted as irreversible electroporation).

Now, in order to test the second hypothesis which could explain this phenomenon, is to also alter the values a_1 and D_0. Decreasing the value of a_1 lowers the energy barrier between the two stable states of the order parameter and thus a lower TMV is required to tilt the energy potential into a single stable state ($\phi \equiv 1$). In order to preserve the qualitative properties of the order parameter (see Chapter 2) we also proportionally decrease the diffusion coefficient. This ensures that there is little change to the pore edge size. The physical significance of this change is not so important for the moment as we are only interested in exploring the behaviors our model can capture. Additionally, as we study values near the reference set of parameters established before, the resulting change in the diffusion coefficient is never so important as to require further justification (from a modeling standpoint).

The parameters changed in order to test the second hypothesis are shown in Table 4.4. The results are shown in Figures 4.15 and 4.16.

	Value	Description
D_0	5×10^{-13} [m^2.s^{-1}]	lateral diffusion
a_1	$1.36 \cdot 10^{-1}$ [J.m^{-2}]	measures membrane linear energy

Table 4.4: Values selected to test the second hypothesis. The other parameters are fixed at the reference values (see Table 4.3). Both of these values correspond to one fourth of the respective reference values.

In this setting, we are testing both the first and second hypothesis. That is, we consider that the conductivity of the fluid entering the membrane depends on both the intacellular and extracellular media, and because of the sugar content in STM (low conductivity medium)

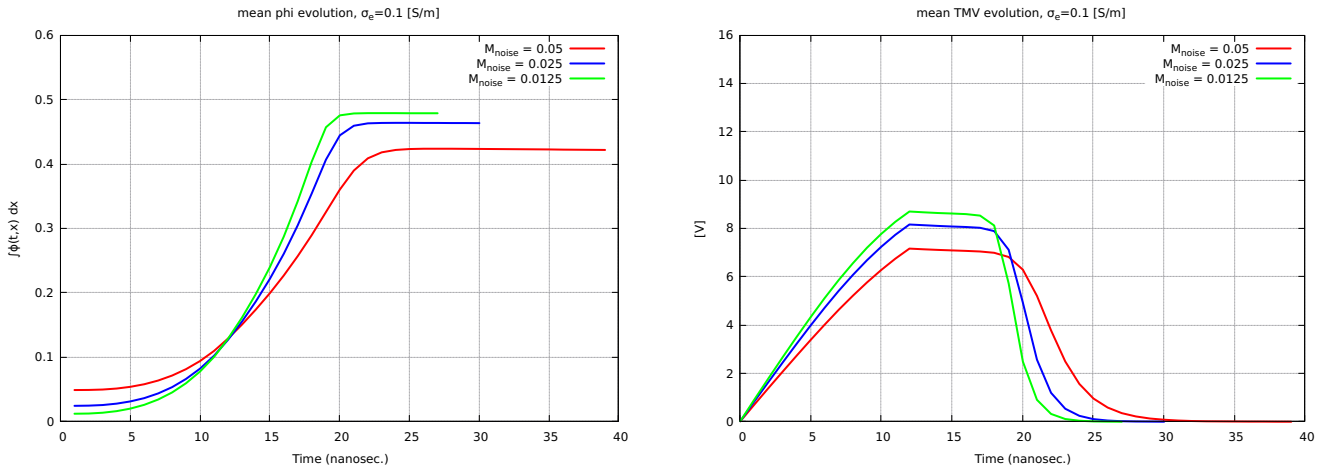

Figure 4.15: Mean behavior of the solutions of the PDE system (during pulse delivery) using a modified set of parameters (adapted at the second hypothesis), $\sigma_e = 0.1$ [S.m^{-1}] and $\sigma_w = (\sigma_e + \sigma_c)/2$. The different colors correspond to different values of M_{noise}. Simulations are stopped when the mean TMV is smaller than 10^{-3} [V].

the mechanical properties of the membrane change at low conductivity. It is clear when comparing Figure 4.16 with the second column in Figure 4.14, that the experimental counter-intuitive results of [77] cannot be explained only using these two hypotheses, as there is a significant increase in the amount of water entering the membrane at higher extracellular conductivity.

We emphasize that this result also holds for other similar values of a_1 and D_0. We do not show them for practical reasons, but the reader should be easily convinced of the clear difference in the results by comparing Figures 4.16 and 4.14.

4.5 Conclusion

We have shown the different behaviors that the KN model and the phase field model can explain. From our results, it appears that the two hypotheses proposed by Silve *et al.* works are not the main cause of the marked difference in the effectiveness of electroporation as a function of the extracellular medium at a low number of delivered pulses. Our numerical simulations suggest that the change in the conductivity of the pores as a function of the extracellular conductivity (first hypothesis) has no effect on the amount of water entering the membrane (unless the change is dramatic). If the conductivity of aqueous solution in pores σ_w (depending on the use of STM or SMEM) ranged from 0.3 to 1.5 [S.m^{-1}] then the expected result (independent of the model) is qualitatively similar to when σ_w does not depend on the external medium of the cell (for example $\sigma_w = 1$ [S.m^{-1}]). If we additionally consider the second hypothesis (as manifested in each of the models), we see that it cannot explain these results either. It is possible that these two hypotheses play a role in this

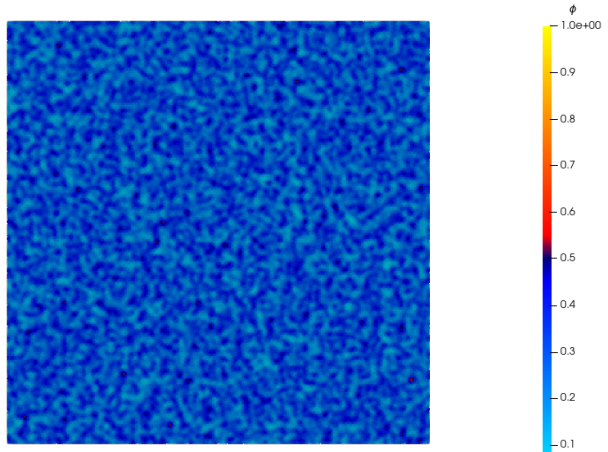

(a) $M_{\text{noise}} = 0.05$, $t = 538$ [ns]

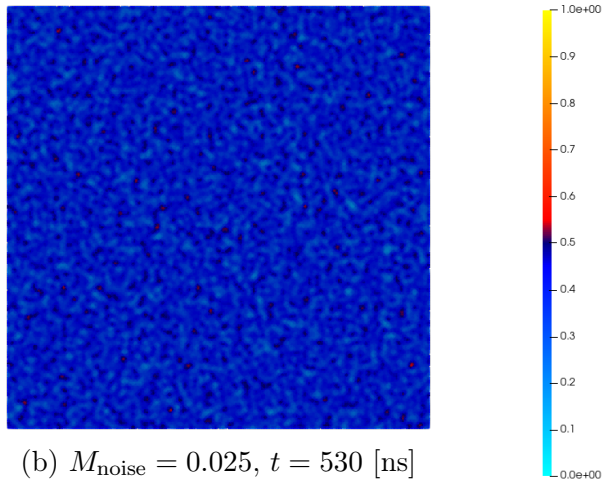

(b) $M_{\text{noise}} = 0.025$, $t = 530$ [ns]

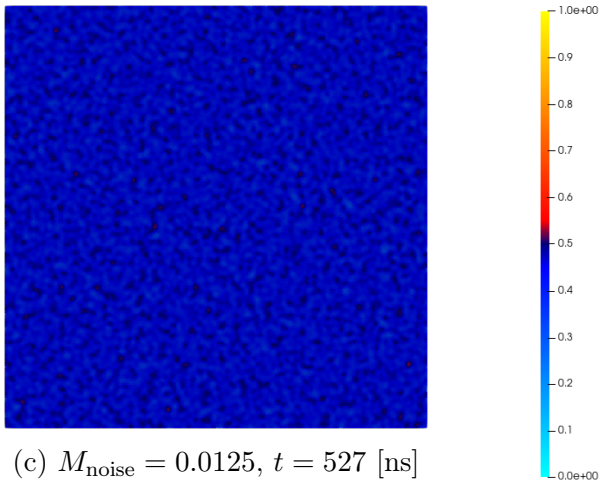

(c) $M_{\text{noise}} = 0.0125$, $t = 527$ [ns]

Figure 4.16: Numerical resolution of the PDE system using a modified version of the parameters for D_0 and a_1 (see Table 4.4) after membrane discharge (simulations associated to Figure 4.15). These results correspond to $\sigma_e = 0.1$ [S.m^{-1}] and $\sigma_w = (\sigma_e + \sigma_c)/2$.

phenomenon, but our simulations suggest that they are not the main driver. This leads to the idea that the increased permeability of the cell membrane is not necessarily related to the amount of water entering the cell membrane.

It is clear that the KN model makes little difference between the two experimental media (STM and SMEM). This can be explained by the dependence on V_{ep} of the equation governing the evolution of N. Since nanosecond pulses use strong electrical pulses, we would normally expect (using the linear model) the value of TMV to reach much larger values than for longer pulses with weaker electrical pulse delivery. This means that if we do not drastically change the parameters of the KN model (using the second hypothesis), we should expect a large amount of pores to be generated regardless of the conductivity of the extracellular medium. Once the pores are created and the membrane is discharged, the long lifetime predicted by this model would further challenge the surprising results observed in [77].

In summary, although the KN model provides an explanation for the electroporation phenomenon, it appears to be at odds with the experimental results. If the increased permeability of the membrane due to electroporation is a consequence of the long lifetime of the pores, then we should not expect the results of Silve's group [77] to hold. If the increased membrane permeability is due to some other effect, then the fact that this model does not distinguish between high and low extracellular conductivity, means that this hypothesis probably cannot be tested with this model.

The phase-field model, on the other hand, improves on the KN model by showing a clear difference in the effect of extracellular conductivity on the dynamics of the membrane order parameter and TMV. More importantly, it shows a significant difference in the duration that the membrane remains charged at a high TMV. It appears that higher conductivity causes a kind of premature dielectric breakdown that discharges the membrane, protecting it from the rest of the electrical pulse. Furthermore, since we assume that membranes close within a few microseconds, it is clear that considering only the amount of water entering the membrane cannot explain the behavior observed experimentally by Silve *et al.* [77].

The phase-field model results suggest that another effect may play a role in the phenomenon observed in [77]. These results seem to indicate that this phenomenon could be due to the change in the membrane as a result of the long exposure of the membrane to a high TMV. This implies that the effectiveness of electroporation at lower conductivities (and a low number of nanopulses) is not primarily related to the amount of water entering the membrane. We therefore hypothesize that the increase in electroporation effectiveness is due to an oxidation effect of the membrane resulting from the long time period it remains charged. Once the membrane is oxidized, the permeability associated with this new state of the membrane should last much longer than the expected lifetime of a pore and would thus explain the results observed in [77].

Chapter 5

Conclusion and perspectives

5.1 Conclusion

In this work, a new phase field model of electroporation based on physical principles was presented. It consists of the Allen-Cahn equation for the membrane water content and a nonlocal differential equation for the transmembrane voltage.

As for the mathematical aspects, a fine analysis of the involved nonlocal Dirichlet-to-Neumann operators was performed in two basic configurations, allowing the comparison of the time constants of the phenomenon between spherical and flat membranes. Furthermore, a comprehensive linear stability analysis of our model was conducted. In addition to these very interesting results and to estimate the parameters of the model, a comparison of the energy functional of our model with the energy functionals of other physical models was performed.

As for the numerical aspects, a highly efficient numerical scheme of order 2 in time was developed and implemented, harnessing the Fast Fourier Transform and a Strang Splitting scheme. This robust technique significantly enhances computational efficiency, facilitating a sensitivity analysis of the parameters of the model.

Lastly we compare our model to the KN-model in a realistic scenario using experimental data in the case of nanosecond pulses applied to a cell suspension. As a result, we show that – unlike the classical KN-model – our model behaves differently as observed in the experiments to different pulse durations and to different number of pulses. Furthermore, we highlight that the short pore-lifetime our model predicts is compatible with the experimental observations done by Silve *et al.* regarding the influence of extracellular conductivity on electroporation effectiveness when a small number of pulses are applied. Indeed, it could explain the different timescales for which the cell membrane is conductive and for which the membrane is permeable.

Despite all these qualities, our model has room for improvement. From a modeling point of view, our model does not allow to link higher extracellular conductivity to lower electroporation effectiveness in the case of small number of pores. From a numerical simulation point of view, we still need to obtain a reasonable simulation which takes into account a

whole cell and not just a periodic membrane patch. These limitations are discussed in the following sections.

5.2 Perspectives

We conclude with some of the directions in which we plan to take the electroporation model we have presented in this work. We present two aspects. First, the further development of our model to account for the more complex aspects of electroporation. Second, a strategy to tackle the simulation of the spherical cell model.

5.2.1 Extensions and changes to our model

Lipid oxidation

As we explained in Chapter 1, an important aspect of cell electroporation is the characteristic timescales involved. When a cell is electroporated, the duration of increased permeability of the membrane cannot be explained by only considering pore dynamics. According to our model, the lifetime of a pore is not much more than 10 μs, so we do not expect that it is the only cause of the increased membrane permeability. This conclusion is consistent with what has already been observed in molecular dynamics simulations [40], since the pores close almost immediately there as well (they do not even come close to 1 μs lifetimes in these simulations).

A theory has been proposed for distinguishing conductivity between the highly conductive and highly permeable states of the membrane. This involves the chemical alteration of the lipid membrane due to lipid oxidation as a result of the elevated TMV, which is a consequence of the applied electric field.

This distinction could explain the unintuitive phenomenon observed in [77] in which a small number of nanosecond electric pulses are less effective at a higher extracellular conductivity. The hypothesis is that a sudden increase in TMV promotes "premature" pore creation and therefore the membrane discharges fast enough to avoid membrane damage from prolonged exposure to an elevated TMV.

The addition of this oxidized or altered membrane could be modeled in a couple of ways. A possible extension of our model to take into account lipid oxidation consists in associating a new energy potential $\mathcal{W}_{\text{oxi}}$ to oxidised phospholipids and then describe the state of the membrane by means of an additional order parameter ρ, which describes the degree of oxidation of the membrane. For example we could conceive of having an energy functional of the form

$$\mathcal{E}(\phi, \rho, v) = \frac{\kappa}{2} \int_\Gamma \|\nabla \phi\|^2 + \int_\Gamma \mathcal{W}_{\text{oxi}}(\phi) f_{\text{sig}}(\rho) + \mathcal{W}(\phi)(1 - f_{\text{sig}}(\rho)) - \frac{1}{2} \int_\Gamma C_m(\phi, \rho) v^2$$

where $f_{\text{sig}} : \mathbb{R} \to [0, 1]$ is a sigmoid function to be chosen to interpolate between the two states of the membrane (oxidised or not). Additionally, the order parameter ρ would follow

a reaction-diffusion equation on the membrane. This would capture the oxidation process of phospholipids and the lateral diffusion of the oxidised phospholipids in the membrane.

Another option would be to consider a Cahn-Hilliard model which distinguishes two phases, normal membrane and oxidised membrane. This would involve adding another order parameter, ψ, which would also evolve according to an energy functional similar to the one associated to ϕ. By this we mean that there would be a similar $H_0^1(\Gamma)$ norm and a membrane energy potential, but with an extra term to model the oxidation process. Of course, this would behave completely differently to the first option we proposed, as the Cahn-Hilliard equation has a tendency to accumulate each phase into different regions, as opposed to a diffusion equation which does the opposite.

These different modeling choices do not represent trivial research. Indeed, both ideas, membrane diffusion and accumulation (in the form of rafts, as indicated in Chapter 1), are potentially valid ways to model membrane dynamics.

Choice of potential $\mathcal{W}$

In our model, we chose the membrane potential $\mathcal{W}$ as a fourth-degree polynomial because it was the simplest function that satisfied all the requirements we needed. This arbitrary choice can be justified by the fact that in Allen-Cahn dynamics the exact shape of the potential has no real influence on the evolution of the membrane parameter. This is especially true when the initial condition has significantly different sections where the order parameter has the two different stable values ($\phi \in \{0, 1\}$). In this case, the evolution of the order parameter is related to the mean curvature of the interphase sections.

However, in our case we have a completely different setup. We start with an order parameter that is essentially a stable phase ($\phi \sim 0$), and then water enters the membrane due to the TMV influence. In this part of the evolution, the actual form of the potential $\mathcal{W}$ is indeed important, as we have shown with the linear instability analysis. We could therefore argue that there is still some work to be done to determine an appropriate (and physically inspired) shape for the membrane potential. Creating a "better" membrane potential is easily accomplished using simple polynomials, but more refined analysis should probably be performed to motivate the exact choice. This is one of the places where molecular dynamics simulation results shoud prove to be useful.

Minor adjustments

Other than this, some modeling choices still need further development. For example, modeling the noise affecting the membrane order parameter ϕ is still not well understood. Furthermore, it has a considerable effect at least for the application nanosecond pulses. Another example is the electrical conductivity of membrane $\phi \mapsto S_m(\phi)$ and a model for the conductivity of the fluid entering the membrane σ_w. We show a couple of examples in Chapter 4, but a more definite choice would help control the number of parameters we can fix when numerically testing different hypotheses by simulating this model.

5.2.2 Numerical scheme for a spherical cell setting

A pore edge is somehow comparable in size to the width of the cell membrane $h \sim 10^{-9}$ $[m]$ and the characteristic length of a cell membrane is comparable with the cell radius $R_0 \sim 10^{-5}$ $[m]$. Then to capture the evolution of pores in a spherical cell setting we would need a discretized membrane with an amount of nodes of around

$$\frac{R_0^2}{h^2} \sim 10^8.$$

At this scale, simulating without parallelization or without dedicated use of a GPU is unfeasible. Other than this, the fact that we are not in a periodic setting anymore means that we can no longer base our numerical scheme the in the speed of the FFT algorithm. We propose to tackle this simulation problem in the following manner.

As explained in Chapter 3, our scheme is optimized for this problem, as a result we essentially keep the same splitting scheme for the spherical case but we now need to change the way of solving each of the split problems.

We propose an approach of solving the heat equation in the first split by discretizing the Laplace operator. This seems to be an appropriate choice as the amount of nodes we have to consider implies a large amount of spherical harmonics we would need to consider when diagonalising the operator (this quickly becomes unfeasible). Moreover, as we do not have the speed from the FFT algorithm diagonalising the Laplacian operator loses most of its advantages. Solving the linear system resulting from this problem can be done in the GPU by means of an iterative solver based on Krylov spaces (like the one we use in Chapter 3), although there could be other more appropriate solvers at our disposal.

The problem concerning the non-local Dirichlet-to-Neumann operator Λ also cannot be solved by means of diagonalization because of the large amount of nodes involved. It also cannot be done otherwise as we would then have to solve a 3D problem. One solution to this impasse, is to keep our current CG solver but to artificially project the solutions onto a reasonably big eigenspace of Λ but which remains moderate in size so that computations do not take too long.

As we have seen in our simulations the amount of increased conductivity seems to strongly flatten the TMV. This suggests that if we were to consider, say the eigenspaces of Λ associated to its first fifty eigenvalues (in the spherical setting), it could be enough for our simulation purposes. This is not an ideal solution from a numerical analysis standpoint, but it is an easy and practical solution to the computational challenges involved in our problem. Furthermore, this type of computation is possible to do in parallel.

Lastly, the ODE split can be solved in parallel as there is no space component. Later on, an adaptive mesh could be use to speed up computations, as we do not expect much to happens at the equator of the cell (where the normal vector is orthogonal to the applied electric field).

Bibliography

[1] I. Abidor, V. Arakelyan, L. Chernomordik, Y. Chizmadzhev, V. Pastushenko, and M. Tarasevich. Electric breakdown of bilayer lipid membranes: I. the main experimental facts and their qualitative discussion. Journal of Electroanalytical Chemistry and Interfacial Electrochemistry, 104, 1979.

[2] M. Alfaro, D. Hilhorst, and H. Matano. The singular limit of the Allen-Cahn equation and the FitzHugh-Nagumo system. Journal of Differential Equations, 245(2), 2008.

[3] S. M. Allen and J. W. Cahn. A microscopic theory for antiphase boundary motion and its application to antiphase domain coarsening. Acta Metallurgica, 27(6), 1979.

[4] S. Asavasanti, W. Ristenpart, P. Stroeve, and D. M. Barrett. Permeabilization of plant tissues by monopolar pulsed electric fields: effect of frequency. J. Food Sci., 76(1):E98–111, Jan. 2011.

[5] A. Barnett. The current-voltage relation of an aqueous pore in a lipid bilayer membrane. Biochimica et Biophysica Acta (BBA) - Biomembranes, 1025(1), 1990.

[6] G. Bellettini. Lecture optnotes on mean curvature flow: Barriers and singular perturbations. Lecture optnotes (Scuola Normale Superiore). Scuola Normale Superiore, Pisa, Italy, 2014 edition, 2014.

[7] R. Benz, F. Beckers, and U. Zimmermann. Reversible electrical breakdown of lipid bilayer membranes: a charge-pulse relaxation study. J. Membr. Biol., 48(2), 1979.

[8] P. Bertuccio, G. Alicandro, M. Malvezzi, G. Carioli, P. Boffetta, F. Levi, C. La Vecchia, and E. Negri. Cancer mortality in europe in 2015 and an overview of trends since 1990. Annals of Oncology, 30(8):1356–1369, 2019. Triple-negative breast cancer - clinical results and biomarker analysis of GeparNuevo study.

[9] F. Boyer. Analyse numérique des EDP elliptiques - univ-toulouse.fr. `https://www.math.univ-toulouse.fr/~fboyer/_media/enseignements/m2_anedp/cours_m2_anedp_fboyer.pdf`.

[10] A. J. Bray. Theory of phase-ordering kinetics. Adv. Phys., 51(2), 2002.

[11] M. Breton, L. Delemotte, A. Silve, L. M. Mir, and M. Tarek. Transport of siRNA through lipid membranes driven by nanosecond electric pulses: an experimental and computational study. J. Am. Chem. Soc., 134(34), 2012.

[12] M. Breton and L. M. Mir. Investigation of the chemical mechanisms involved in the electropulsation of membranes at the molecular level. Bioelectrochemistry, 119, 2018.

[13] J. W. Cahn and J. E. Hilliard. Free energy of a nonuniform system. I. interfacial free energy. J. Chem. Phys., 28(2), 1958.

[14] C. Y. Calvet and L. M. Mir. The promising alliance of anti-cancer electrochemotherapy with immunotherapy. Cancer Metastasis Rev., 35(2):165–177, June 2016.

[15] J. P. Castillo, H. Rui, D. Basilio, A. Das, B. Roux, R. Latorre, F. Bezanilla, and M. Holmgren. Mechanism of potassium ion uptake by the Na(+)/K(+)-ATPase. Nat. Commun., 6:7622, July 2015.

[16] Y. Chizmadzhev, F. Cohen, A. Shcherbakov, and J. Zimmerberg. Membrane mechanics can account for fusion pore dilation in stages. Biophysical Journal, 69(6), 1995.

[17] P. De Weer, D. C. Gadsby, and R. F. Rakowski. Voltage dependence of the Na-K pump. Annu. Rev. Physiol., 50(1):225–241, 1988.

[18] K. A. DeBruin and W. Krassowska. Electroporation and shock-induced transmembrane potential in a cardiac fiber during defibrillation strength shocks. Ann. Biomed. Eng., 26(4), 1998.

[19] K. A. DeBruin and W. Krassowska. Modeling electroporation in a single cell. I. effects of field strength and rest potential. Biophys. J., 77(3):1213–1224, Sept. 1999.

[20] K. A. DeBruin and W. Krassowska. Modeling electroporation in a single cell. II. effects of ionic concentrations. Biophys. J., 77(3), 1999.

[21] S. Dev and G. Hofmann. Electrochemotherapy—a novel method of cancer treatment. Cancer Treatment Reviews, 20(1):105–115, 1994.

[22] R. Dimova and C. Marques, editors. The giant vesicle book the giant vesicle book. Productivity Press, New York, NY, 2019.

[23] A. Ern and J.-L. Guermond. Finite elements II. Texts in applied mathematics. Springer International Publishing, Cham, 2021.

[24] J.-M. Escoffre, T. Portet, L. Wasungu, J. Teissié, D. Dean, and M.-P. Rols. What is (still not) known of the mechanism by which electroporation mediates gene transfer and expression in cells and tissues. Mol. Biotechnol., 41(3), 2009.

[25] L. C. Evans, H. M. Soner, and P. E. Souganidis. Phase transitions and generalized motion by mean curvature. Communications on Pure and Applied Mathematics, 45(9), 1992.

[26] A. Farina, Y. Sire, and E. Valdinoci. Stable solutions of elliptic equations on Riemannian manifolds. J. Geom. Anal., 23(3), 2013.

[27] X. Feng and A. Prohl. Numerical analysis of the Allen-Cahn equation and approximation for mean curvature flows. Numer. Math. (Heidelb.), 94(1):33–65, Mar. 2003.

[28] D. Fraggedakis, M. Mirzadeh, T. Zhou, and M. Z. Bazant. Dielectric breakdown by electric-field induced phase separation. Journal of The Electrochemical Society, 167(11), 2020.

[29] S. K. Frandsen, M. Vissing, and J. Gehl. A comprehensive review of calcium electroporation—a novel cancer treatment modality. Cancers, 12(2), 2020.

[30] R. W. Glaser, S. L. Leikin, L. V. Chernomordik, V. F. Pastushenko, and A. I. Sokirko. Reversible electrical breakdown of lipid bilayers: formation and evolution of pores. Biochimica et Biophysica Acta (BBA) - Biomembranes, 940(2), 1988.

[31] M. Golzio, J. Teissie, and M.-P. Rols. Direct visualization at the single-cell level of electrically mediated gene delivery. Proc. Natl. Acad. Sci. U. S. A., 99(3), 2002.

[32] A. Gothelf, L. M. Mir, and J. Gehl. Electrochemotherapy: results of cancer treatment using enhanced delivery of bleomycin by electroporation. Cancer Treat. Rev., 29(5), 2003.

[33] B. Greenebaum and F. Barnes, editors. Biological and medical aspects of electromagnetic fields. CRC Press, 2018.

[34] L. C. Heller and R. Heller. In vivo electroporation for gene therapy. Human Gene Therapy, 17(9):890–897, 2006. PMID: 16972757.

[35] M. R. Hestenes, E. Stiefel, et al. Methods of conjugate gradients for solving linear systems. Journal of research of the National Bureau of Standards, 49(6), 1952.

[36] P. Jaramillo-Aguayo, A. Collin, and C. Poignard. Phase-field model of bilipid membrane electroporation. Journal of Mathematical Biology, 87(1):18, 2023.

[37] O. Kavian, M. Leguèbe, C. Poignard, and L. Weynans. "Classical" Electropermeabilization Modeling at the Cell Scale. Journal of Mathematical Biology, 68, 2014.

[38] M. D. Kluger, I. Epelboym, B. A. Schrope, K. Mahendraraj, E. M. Hecht, J. Susman, J. L. Weintraub, and J. A. Chabot. Single-institution experience with irreversible electroporation for T4 pancreatic cancer: First 50 patients. Ann. Surg. Oncol., 23(5):1736–1743, May 2015.

[39] D. Kondepudi and I. Prigogine. Modern thermodynamics. John Wiley & Sons, Nashville, TN, 2 edition, 2014.

[40] T. Kotnik, L. Rems, M. Tarek, and D. Miklavčič. Membrane electroporation and electropermeabilization: Mechanisms and models. Annu. Rev. Biophys., 48(1):63–91, May 2019.

[41] W. Krassowska and P. D. Filev. Modeling electroporation in a single cell. Biophys. J., 92(2), 2007.

[42] J. H. Kroeger, D. Vernon, and M. Grant. Curvature-driven pore growth in charged membranes during charge-pulse and voltage-clamp experiments. Biophys. J., 96(3), 2009.

[43] J. Kulbacka, A. Choromańska, J. Rossowska, J. Weżgowiec, J. Saczko, and M.-P. Rols. Cell Membrane Transport Mechanisms: Ion Channels and Electrical Properties of Cell Membranes, pages 39–58. Springer International Publishing, Cham, 2017.

[44] S. Lang. Fundamentals of differential geometry. Graduate Texts in Mathematics. Springer, New York, NY, 1 edition, Sept. 2001.

[45] N. I. Lebovka, M. I. Bazhal, and E. Vorobiev. Pulsed electric field breakage of cellular tissues: visualisation of percolative properties. Innov. Food Sci. Emerg. Technol., 2(2):113–125, June 2001.

[46] M. Leguèbe, A. Silve, L. Mir, and C. Poignard. Conducting and permeable states of cell membrane submitted to high voltage pulses: Mathematical and numerical studies validated by the experiments. Journal of Theoretical Biology, 360, 2014.

[47] Z. A. Levine and P. T. Vernier. Life cycle of an electropore: field-dependent and field-independent steps in pore creation and annihilation. J. Membr. Biol., 236(1):27–36, July 2010.

[48] J. Leydold. On the number of nodal domains of spherical harmonics. Topology, 35, 1996.

[49] J. Li, W. Tan, M. Yu, and H. Lin. The effect of extracellular conductivity on electroporation-mediated molecular delivery. Biochimica et Biophysica Acta (BBA) - Biomembranes, 1828(2), 2013.

[50] Y. Li, H. G. Lee, D. Jeong, and J. Kim. An unconditionally stable hybrid numerical method for solving the allen-cahn equation. Computers & Mathematics with Applications, 60(6), 2010.

[51] G. Lindblom and G. Oradd. Lipid lateral diffusion and membrane heterogeneity. Biochimica et Biophysica Acta (BBA) - Biomembranes, 1788(1), 2009.

[52] H. Looyenga. Dielectric constants of heterogeneous mixtures. Physica, 31(3), 1965.

[53] S. Mahnič-Kalamiza, E. Vorobiev, and D. Miklavčič. Electroporation in food processing and biorefinery. J. Membr. Biol., 247(12):1279–1304, Dec. 2014.

[54] J. Malmivuo and R. Plonsey. Bioelectromagnetism. Oxford University Press, New York, NY, July 1995.

[55] R. C. G. Martin, 2nd, K. McFarland, S. Ellis, and V. Velanovich. Irreversible electroporation in locally advanced pancreatic cancer: potential improved overall survival. Ann. Surg. Oncol., 20 Suppl 3(S3):S443–9, Dec. 2013.

[56] R. I. McLachlan and G. R. W. Quispel. Splitting methods. Acta Numerica, 11, 2002.

[57] D. Miklavcic and L. Towhidi. Numerical study of the electroporation pulse shape effect on molecular uptake of biological cells. Radiology and Oncology, 44(1):34–41, 2010.

[58] L. M. Mir. Electroporation-Based Gene Therapy: Recent Evolution in the Mechanism Description and Technology Developments, pages 3–23. Springer New York, New York, NY, 2014.

[59] P. J. Mohr, B. N. Taylor, and D. B. Newell. CODATA recommended values of the fundamental physical constants: 2006. Rev. Mod. Phys., 80(2), 2008.

[60] Molview. `https://molview.org/`.

[61] P. D. Mottoni and M. Schatzman. Geometrical evolution of developed interfaces. Trans. Am. Math. Soc., 347(5):1533, May 1995.

[62] C. Muller. Spherical Harmonics. Lecture optnotes in mathematics. Springer, Berlin, Germany, 1966 edition, 1966.

[63] M. Nakao and D. C. Gadsby. Voltage dependence of Na translocation by the Na/K pump. Nature, 323(6089):628–630, 1986.

[64] J. C. Neu and W. Krassowska. Asymptotic model of electroporation. Phys. Rev. E, 59, 1999.

[65] W. K. Neu and J. C. Neu. Theory of Electroporation, pages 133–161. Springer US, Boston, MA, 2009.

[66] V. P. Nikolski and I. R. Efimov. Electroporation of the heart. EP Europace, 7(s2):S146–S154, 01 2005.

[67] V. F. Pastushenko, Y. A. Chizmadzhev, and V. B. Arakelyan. Electric breakdown of bilayer lipid membranes. J. Electroanal. Chem. Interfacial Electrochem., 104:53–62, Jan. 1979.

[68] A. Pazy. Semigroups of linear operators and applications to partial differential equations. Applied mathematical sciences. Springer, New York, NY, 1983 edition, 2012.

[69] R. Perrussel and C. Poignard. Asymptotic expansion of steady-state potential in a high contrast medium with a thin resistive layer. Applied Mathematics and Computation, 221:48–65, 2013.

[70] M. Sack, J. Sigler, S. Frenzel, C. Eing, J. Arnold, T. Michelberger, W. Frey, F. Attmann, L. Stukenbrock, and G. Müller. Research on industrial-scale electroporation devices fostering the extraction of substances from biological tissue. Food Eng. Rev., 2(2):147–156, June 2010.

[71] H. J. Scheffer, K. Nielsen, M. C. de Jong, A. A. van Tilborg, J. M. Vieveen, A. R. Bouwman, S. Meijer, C. van Kuijk, P. M. van den Tol, and M. R. Meijerink. Irreversible electroporation for nonthermal tumor ablation in the clinical setting: A systematic review of safety and efficacy. Journal of Vascular and Interventional Radiology, 25(7):997–1011, 2014. Special Issue: Interventional Oncology.

[72] M. Scuderi, J. Dermol-Černe, C. Amaral da Silva, A. Muralidharan, P. E. Boukany, and L. Rems. Models of electroporation and the associated transmembrane molecular transport should be revisited. Bioelectrochemistry, 147(108216):108216, Oct. 2022.

[73] A. Shah, M. Sabir, M. Qasim, and P. Bastian. Efficient numerical scheme for solving the Allen-Cahn equation. Numer. Methods Partial Differ. Equ., 34(5):1820–1833, Sept. 2018.

[74] J. Shen and X. Yang. Numerical approximations of allen-cahn and cahn-hilliard equations. Discrete Contin. Dyn. Syst, 28(4):1669–1691, 2010.

[75] A. Silve, A. GuimerÃ Brunet, B. Al-Sakere, A. Ivorra, and L. Mir. Comparison of the effects of the repetition rate between microsecond and nanosecond pulses: Electropermeabilization-induced electro-desensitization? Biochimica et Biophysica Acta (BBA) - General Subjects, 1840(7), 2014.

[76] A. Silve, I. Leray, M. Leguèbe, C. Poignard, and L. M. Mir. Cell membrane permeabilization by 12-ns electric pulses: Not a purely dielectric, but a charge-dependent phenomenon. Bioelectrochemistry, 106, 2015.

[77] A. Silve, I. Leray, C. Poignard, and L. M. Mir. Impact of external medium conductivity on cell membrane electropermeabilization by microsecond and nanosecond electric pulses. Sci. Rep., 6(1), 2016.

[78] J. C. Skou. The Na-K pump. Physiology (Bethesda), 7(3):95–100, June 1992.

[79] K. C. Smith, R. S. Son, T. Gowrishankar, and J. C. Weaver. Emergence of a large pore subpopulation during electroporating pulses. Bioelectrochemistry, 100, 2014.

[80] K. C. Smith and J. C. Weaver. Active mechanisms are needed to describe cell responses to submicrosecond, megavolt-per-meter pulses: Cell models for ultrashort pulses. Biophysical Journal, 95(4):1547–1563, 2008.

[81] E. B. Sözer, Z. A. Levine, and P. T. Vernier. Quantitative limits on small molecule transport via the electropermeome - measuring and modeling single nanosecond perturbations. Sci. Rep., 7(1):57, Mar. 2017.

[82] A. Sugrue, E. Maor, A. Ivorra, V. Vaidya, C. Witt, S. Kapa, and S. Asirvatham. Irreversible electroporation for the treatment of cardiac arrhythmias. Expert Review of Cardiovascular Therapy, 16(5):349–360, 2018. PMID: 29595355.

[83] M. Tarek. Membrane electroporation: a molecular dynamics simulation. Biophys. J., 88(6):4045–4053, June 2005.

[84] M. Tarek. Atomistic simulations of electroporation of model cell membranes. Adv. Anat. Embryol. Cell Biol., 227, 2017.

[85] D. P. Tieleman. The molecular basis of electroporation. BMC Biochem., 5, 2004.

[86] B. Todorova, L. Adam, S. Culina, R. Boisgard, F. Martinon, A. Cosma, M. Ustav, T. Kortulewski, R. Le Grand, and C. Chapon. Electroporation as a vaccine delivery system and a natural adjuvant to intradermal administration of plasmid DNA in macaques. Sci. Rep., 7(1):4122, June 2017.

[87] B. Valič, M. Golzio, M. Pavlin, A. Schatz, C. Faurie, B. Gabriel, J. Teissié, M.-P. Rols, and D. Miklavčič. Effect of electric field induced transmembrane potential on spheroidal cells: theory and experiment. European Biophysics Journal, 32(6):519–528, Oct. 2003.

[88] P. T. Vernier, Z. A. Levine, Y.-H. Wu, V. Joubert, M. J. Ziegler, L. M. Mir, and D. P. Tieleman. Electroporating fields target oxidatively damaged areas in the cell membrane. PLOS ONE, 4(11), 2009.

[89] P. T. Vernier, Y. Sun, and M. A. Gundersen. Nanoelectropulse-driven membrane perturbation and small molecule permeabilization. BMC Cell Biol., 7(1):37, Oct. 2006.

[90] J. Weaver. Electroporation of biological membranes from multicellular to nano scales. IEEE Transactions on Dielectrics and Electrical Insulation, 10(5), 2003.

[91] J. C. Weaver and Y. Chizmadzhev. Theory of electroporation: A review. Bioelectrochemistry and Bioenergetics, 41(2), 1996.

[92] J. C. Weaver and R. A. Mintzer. Decreased bilayer stability due to transmembrane potentials. Phys. Lett. A, 86(1):57–59, Oct. 1981.

[93] J. C. Weaver, K. C. Smith, A. T. Esser, R. S. Son, and T. Gowrishankar. A brief overview of electroporation pulse strength duration space: A region where additional intracellular effects are expected. Bioelectrochemistry, 87, 2012.

[94] J. C. Weaver and P. T. Vernier. Pore lifetimes in cell electroporation: Complex dark pores?, 2017.

[95] C. Wilhelm, M. Winterhalter, U. Zimmermann, and R. Benz. Kinetics of pore size during irreversible electrical breakdown of lipid bilayer membranes. Biophys. J., 64(1):121–128, Jan. 1993.

[96] J. Zhang and Q. Du. Numerical studies of discrete approximations to the Allen–Cahn equation in the sharp interface limit. SIAM J. Sci. Comput., 31(4):3042–3063, Jan. 2009.